# High Temporal Resolution Functional Magnetic Resonance Imaging at 7 Tesla

PAR

## Mayur NARSUDE

EPFL

ÉCOLE POLYTECHNIQUE
FÉDÉRALE DE LAUSANNE

Suisse
2014

*To my mother*

*&*

*To my wife*

# Acknowledgements

I would like to start my acknowledgements by thanking my thesis advisor Professor Rolf Gruetter for his support, constant encouragement, his time, and dedication to work. His guidance helped me all the time of my research and writing of this thesis. I have always appreciated the professional and friendly atmosphere he has provided to the researchers at CIBM.

Thank you José! I consider myself very fortunate to have you as a mentor/co-advisor for my PhD study. You never were tired of explaining MR physics to me and always came up with interesting ideas. I always liked the fact that you not only guided me to get the results but also made sure that I present them well at conferences/meetings. Thank you for everything. I could not have imagined a better mentor.

The parallel imaging *'guru'* in the lab – Dan! Thank you for helping me with the reconstruction of 'drastically' accelerated EPI images and g-factor calculations, without which the most prolific chapter of this thesis was not possible. I wish you good luck with the 'overproof' GRAPPA. Thank you also, Wietske, for your valuable guidance for performing fMRI experiments. Your profound experience in fMRI data processing is an asset for the lab and has helped me considerably to get all the fMRI results presented in this thesis.

I always enjoyed listening to Tobi's whole-hearted laughter coming from cafeteria every morning of the last four years. Thank you for helping me in making my sequences actually run on the scanner! Benoit, the french man, I miss the poker nights you used to arrange. Thanks for that and also for being a cheerful neighbour in the lab. Thank you for great moments we shared, Florent, while sharing the office space for nearly four years. Rajika you were as good a flatmate as you were an officemate. You made sure not to miss the slightest opportunity to document a few of my most hilarious moments.

I met so many wonderful people during the course of my PhD that this acknowledgement would go on forever. To name a few people from CIBM: Andrea, Lali, Lijing, Nicolas (a few of the figures in my thesis are his courtesy), Joao senior, Joao Junior, Diana, Emine, Masaumeh, Ozlem, Jessica, Bernard, Najath, Nathalie, Hongxia, Cedric, Mor, Christina, . . . I have enjoyed my time working at CIBM because of lively colleagues like you all. This acknowledgements to the 'office-mates' would not be complete without mentioning a few of my ex-colleagues – Tom-tom, Pavel, Maryna, Ruud, Mélanie, Tian, Bene, Kieran, and Arthur! Thank you all for the wonderful time I had so far!!

On the 'non-office' front, I would first like to thank Patil family from Bern for providing a home-away-from-home in Switzerland to us. We enjoyed being at your place and attending

# Preface

Functional magnetic resonance imaging (fMRI) is one of the most sought applications of magnetic resonance imaging. Over 3000 papers are published every year using this methodology, with its users ranging from psychologists, clinicians and neuroscientists to neurobiologists and physiologists.

2D-EPI has been the main sequence used in functional imaging studies over the last 20 years. Yet, the search for more efficient ways to sample the MR signal is still a very active field of research, with the main trend being that one should sample faster. This despite the known slow nature of the BOLD effect.

In our lab, over the last years, there has been a coordinated effort to implement and study the properties of 3D based EPI techniques. While the motivation has been clear from the start: "3D based acquisitions benefit from higher spatial SNR per unit of time than the standard 2D-EPI", we quickly noticed that this advantage in spatial SNR was not translated into temporal SNR. Unfortunately, temporal SNR is the measure that describes the sensitivity to changes in the MR signal observed in fMRI studies.

While we had shown that post-processing techniques using information about the physiology of the subject allowed to recover some of the lost temporal SNR, there was a need to simply reduce the number of independent acquisitions that are needed to encode the 3D volume. This has been the focus of (the now Dr.) Mayur Narsude's research: How to bring the temporal sampling down to a rate comparable to the major physiological processes we are, thankfully, continuously going through? How to make the acquisitions faster while not introducing significant artifacts?

These two questions were very successfully addressed by Mayur Narsude during his PhD and are now presented systematically in this thesis. Most of this work was presented in international high profile conferences, published in the most relevant journals of our field and, more importantly, has now started to be used by other groups demonstrating the impact of his contributions.

José P. Marques

# Abstract

Speed has always been a critical consideration in magnetic resonance imaging (MRI), promising dramatic gains in imaging speed, a reduction in motion and susceptibility artifacts, and ultimately increased throughput for clinical studies. In the context of functional magnetic resonance imaging (fMRI), MRI pulse sequences designed to increase the speed and spatial resolution have always been a topic of intense research to furnish demands of increased sampling rates and statistical power. This thesis presents several new approaches to increase temporal resolution of a three dimensional (3D) echo planar imaging (EPI) sequence and explores the benefits of using high temporal resolution for both event-related brain activation and resting state networks fMRI studies.

In the first approach, a new $k$-space traversal strategy for segmented 3D EPI is introduced which we termed as 3D reduced excitation EPI (3D RE-EPI). In this approach, two partitions are encoded per radio frequency (RF) excitation, effectively reducing the number of excitations used to acquire a 3D EPI dataset by a factor of two. With this strategy, whole-brain images with a nominal voxel size of 2 mm isotropic could be acquired with a temporal resolution under half a second, using traditional parallel imaging acceleration upto 4x in the partition-encoding direction and using novel data acquisition speed-up of 2x. With 8x data acquisition speed-up in the partition-encoding direction, 3D RE-EPI produced acceptable image quality without introduction of noticeable additional artifacts. Due to increased temporal signal-to-noise ratio (tSNR) and better characterization of physiological fluctuations, the new strategy allowed detection of more resting state networks compared to standard multi-slice two dimensional (2D) EPI and segmented 3D EPI.

The approach above suffered from geometry factor (g-factor related) signal-to-noise ratio (SNR) losses, while using very high parallel imaging acceleration factor. To achieve substantial increase in the temporal resolution while maintaining low g-factors when high parallel imaging acceleration factors are used, the combination of segmented 3D EPI using 2D controlled aliasing with generalized autocalibrating partially parallel acquisitions (GRAPPA) was implemented in the next approach termed 3D-EPI-CAIPI. Functional MRI data with whole-brain coverage, a voxel size of 2 mm isotropic and a temporal resolution of 371 ms was acquired with acceptable image quality. 10-fold parallel imaging accelerated 3D-EPI-CAIPI data was shown to lower g-factor losses by as much as 10% with respect to segmented 3D EPI at 7 Tesla. Additional resting state networks were detected using 3D-EPI-CAIPI compared to a comparable standard 2D EPI acquisition. This was attributed to the improved statistics due to an increased number of volumes acquired in a given duration and because of the improved

characterization of physiological signal fluctuations. Functional MRI with 400 ms temporal resolution allowed the detection of time-to-peak variations in temporal, occipital and frontal cortices hemodynamic responses due to multisensory facilitation of the order of ~ 200 ms.

In the final demonstration, a 2D RF pulse was combined with 3D-EPI-CAIPI for achieving circularly symmetric Gaussian localized excitation. An example of restricted field-of-view acquisition with a spatial resolution of 1.5 mm isotropic and subsecond temporal resolution at 7 Tesla was demonstrated using spiral excitation 3D-EPI-CAIPI. The potential of spiral excitation 3D-EPI-CAIPI in localized fMRI studies of brain regions (e.g. brainstem), which are highly susceptible to various bulk motion and physiological processes related artifacts but contain important small brain nuclei, is discussed.

To conclude, this thesis introduces several novel techniques to increase temporal resolution of fMRI. Besides building theoretical foundations for these techniques, their applications for studying human brain functional connectivity, event-related brain activation and the ability to characterize physiological signal fluctuations at ultra-high field strength (7 Tesla) are evaluated.

*Key words*:

magnetic resonance imaging, functional magnetic resonance imaging, echo planar imaging, temporal resolution, $k$-space, parallel imaging, GRAPPA, controlled aliasing, CAIPIRINHA, localized RF excitation

# Résumé

La vitesse a toujours été un facteur critique dans l'imagerie par résonance magnétique (IRM), promettant des progrès spectaculaires dans la vitesse d'imagerie, une réduction du mouvement et des artefacts de susceptibilité, et en fin de compte l'augmentation du débit pour les études cliniques. Dans le contexte d'imagerie par résonance magnétique fonctionnelle (IRMf), les séquences d'IRM conçues pour augmenter la vitesse et la résolution spatiale ont toujours été un sujet de recherche intense pour fournir une augmentation des taux d'échantillonnage et de puissance statistique. Cette thèse présente plusieures nouvelles approches pour augmenter la résolution temporelle de la séquence d'imagerie écho planar (EPI) tridimensionnelle (3D) et explore les avantages d'utiliser une haute résolution temporelle à la fois durant l'activation du cerveau liées à l'événement et durant des études IRMf de l'état de repos.

Dans la première approche, une nouvelle stratégie de remplissage de l'espace réciproque ($k$-space) de traversée pour la séquence 3D EPI segmentée est introduite, que nous avons appelée 3D EPI par excitation réduite (3D RE-EPI). Dans cette approche, deux partitions sont codées par excitation radiofréquence (RF), ce qui réduit efficacement le nombre d'excitations utilisées pour acquérir un ensemble de données 3D EPI par un facteur deux. Avec cette stratégie, des images du cerveau entier avec une taille de voxel nominale de 2mm isotropique peuvent être acquises avec une résolution temporelle inférieure à une demi-seconde, grâce à l'accélération de l'imagerie parallèle traditionnelle jusqu'à 4x dans la direction de codage de partition et utilisant une nouvelle méthode d'acquisition de données accélérée 2x. Avec une acquisition de données accélérée 8x dans la direction de l'encodage de partition, 3D RE-EPI produit des images de qualité acceptable sans introduire d'artefacts additionnels notables. En raison de l'augmentation du rapport signal-sur-bruit temporel (TSNR) et une meilleure caractérisation des fluctuations physiologiques, la nouvelle stratégie a permis la détection de plusieurs réseaux de l'état de repos par rapport à une séquence multi-coupe standard à deux dimensions (2D) EPI et une séquence EPI 3D segmentée.

L'approche ci-dessus est affectée par le facteur de géométrie (facteur g lié) des pertes rapport signal-sur-bruit (SNR), tout en utilisant un très haut facteur d'accélération d'imagerie parallèle. Pour obtenir une augmentation substantielle en résolution temporelle tout en maintenant les facteurs g faibles et en utilisant une haute accélération parallèle de formation d'image, la combinaison de 3D EPI segmenté en utilisant 2D avec aliasing contrôlée et des acquisitions partiellement parallèles avec autocalibration généralisée (GRAPPA) a été mise en œuvre dans la suivante approche appelée 3D-EPI-CAIPI. Des données d'IRM fonctionnelle couvrant l'ensemble du cerveau, avec une taille de voxel de 2 mm isotrope et une résolution temporelle

de 371 ms ont été acquises avec une qualité d'image acceptable. Des données en imagerie parallèle 10 fois accéléré 3D-EPI-CAIPI ont montré une diminution de pertes du facteur g de 10% par rapport à EPI 3D segmentée à 7 Tesla. Des réseaux supplémentaire de l'état de repos ont été détectés en utilisant 3D-EPI-CAIPI à un niveau comparable à une acquisition EPI 2D. Cela a été attribué à l'amélioration des statistiques en raison d'une augmentation du nombre des volumes acquis pour une durée fixée et en raison de l'amélioration de la caractérisation de fluctuations de signaux physiologiques. L'IRM fonctionnelle avec une résolution temporelle de 400 ms a permis la détection des variations de temps à crête dans les réponses hémodynamiques temporales, occipitales et corticales dues à la facilitation multisensorielle de l'ordre de ~ 200ms.

Dans la démonstration finale, une impulsion RF 2D a été combinée avec 3D-EPI-CAIPI pour atteindre une excitation gaussienne localisée circulairement symétrique. Un exemple d'acquisition de domaine restreint de vision avec une résolution spatiale de 1.5mm isotropique et une résolution temporelle inférieures à la seconde à 7 Tesla a été démontrée à l'aide d'une excitation en spirale 3D EPI. Le potentiel d'excitation en spirale 3D EPI dans les études IRMf localisées tout en prenant avantage de la puissance statistique élevée et la capacité pour caractériser les fluctuations du signal physiologiques en raison du taux d'échantillonnage élevé est discutée.

Pour conclure, cette thèse présente plusieurs nouvelles techniques pour augmenter la résolution temporelle de l'IRMf. Outre la construction de fondements théoriques de ces techniques, leurs applications pour étudier la connectivité fonctionnelle du cerveau humain, l'activation du cerveau liée à l'événement et la capacité à caractériser les fluctuations du signal physiologique à champ ultra-élevé (7 Tesla) sont évaluées.

*Mots clefs* :

imagerie par résonance magnétique, imagerie par résonance magnétique fonctionnelle, imagerie écho planar, résolution temporelle, $k$-space, imagerie parallèle, GRAPPA, aliasing contrôlée, CAIPIRINHA, excitation RF localisée

# Contents

# Contents

# Contents

# List of Figures

# List of Tables

# Important Symbols & Abbreviations

| | |
|---|---|
| $\Delta\omega$ | Frequency range |
| $\Delta E$ | Energy level difference between the two spin states |
| $\Delta k$ | Distance between two $k$-space points |
| $\Delta z$ | Slice thickness |
| $\gamma$ | Gyromagnetic ratio |
| $\text{TI}_{\text{null}}$ | Inversion time at which magnetization is nulled |
| $\text{TE}_{\text{eff}}$ | Effective echo time |
| $\nu_0$ | Larmor frequency in $MHz/T$ |
| $\omega_0$ | Larmor frequency in $rad/s \cdot T$ |
| $\omega_{\text{centre}}$ | Center frequency |
| $\rho$ | Spin density |
| $\tau$ | Duration of the RF pulse |
| $\mathbf{B}_0$ | Main magnetic field |
| $\mathbf{B}_1$ | Electromagnetic field for excitation |
| $\mathbf{B}_{\text{eff}}$ | Effective magnetic field |
| $\mathbf{E}$ | Electrical field |
| $\mathbf{M}$ | Net magnetic moment |
| $\theta_E$ | Ernst Angle |
| $G_x$ | Linear magnetic field gradient along the $x$-axis |
| $G_y$ | Linear magnetic field gradient along the $y$-axis |
| $G_z$ | Linear magnetic field gradient along the $z$-axis |

**List of Tables**

| | |
|---|---|
| fMRI | functional Magnetic Resonance Imaging |
| FOV | Field Of View |
| FOX | Field Of Excitation |
| FSE | Fast Spin Echo |
| FWHM | Full-Width-Half-Maximum |
| GE | Gradient Echo |
| GE-EPI | Gradient Echo EPI |
| GLM | General Linear Model |
| GRE-EPI | GRadient Echo EPI |
| HDR | HaemoDynamic Response |
| ICA | Independent Component Analysis |
| IR-EPI | Inversion Recovery EPI |
| MELODIC | Multivariate Exploratory Linear Optimized Decomposition into Independent Components |
| MNI | Montreal Neurological Institute |
| MP2RAGE | Magnetization Prepared 2 Rapid Acquisition Gradient Echoes |
| MR | Magnetic Resonance |
| MRI | Magnetic Resonance Imaging |
| MRS | Magnetic Resonance Spectroscopy |
| NIRS | Near InfraRed Spectroscopy |
| NMR | Nuclear Magnetic Resonance |
| PF | Partial Fourier |
| pMRI | parallel Magnetic Resonance Imaging |
| PNS | Peripheral Nerve Stimulation |
| PPA | Partial Parallel Acquisition |
| PSF | Point Spread Function |
| rBW | readout BandWidth |

## List of Tables

rCBF          regional cerebral blood flow

RE-EPI        Reduced Excitations Echo Planar Imaging

RF            Radio Frequency

ROI           Region Of Interest

RSN           Resting State Network

Sa2RAGE       Saturation-prepared with 2 RApid Gradient Echoes

SAR           Specific Absorption Rate

SE            Spin Echo

SE-EPI        Spin Echo EPI

SMS           Simultaneous MultiSlice

SNR           Signal-to-Noise Ratio

SOS           Sum Of Squares

SPM           Statistical Parametric Mapping

TI            Inversion time

tSNR          temporal Signal-to-Noise Ratio

VD-AUTO-SMASH  Variable Density AUTO-SMASH

# 1 Introduction

Nuclear magnetic resonance (NMR), over the last several decades, has revolutionized many different scientific fields including study of our own internal system i.e. the interior of the human body and its functioning. Few of its prominent *in-vivo* applications realized so far include anatomical imaging (magnetic resonance imaging, MRI), localized composition characterization (Magnetic Resonance Spectroscopy, MRS), cellular structure assessment (Diffusion Tensor Imaging, DTI) and cerebral activity mapping (functional magnetic resonance imaging, fMRI). While MRI offered a detailed imaging of the brain, fMRI enabled an unprecedented insight in the healthy brain to understand its functioning. It paved the way for high resolution, real-time, and dynamic assessment of the brain function which re-defined the approach to modern day psychological and neuroscientific studies.

This chapter begins with a brief historical introduction to magnetic resonance imaging. Next, the motivation and purpose behind the preparation of this manuscript is explained, highlighting the importance of imaging speed for dynamic studies. The chapter ends with a briefing on the contents of different chapters in this thesis.

## 1.1   Historical Perspective

The pioneering work for MRI's incredible journey was done way back in 1930's by Rabi to demonstrate that an oscillating magnetic field could induce transitions between levels associated to the spin state of various nuclei in an applied magnetic field [1]. Later in December 1945, Purcell, Torrey and Pound at MIT detected weak radio-frequency signals generated by the nuclei of atoms in 1 kg of paraffin wax [2]. Bloch, Hansen and Packard performed similar experiments on a sample of water to observe re-emission of the resonant radio-frequency power absorbed from the transmit coil by the nuclei of the water protons [3, 4]. Although Rabi's work[I] was crucial as the initial demonstration of NMR, the conceptual advances demonstrated

---

[I]Rabi was awarded the Physics Nobel prize in 1944 "for his resonance method for recording the magnetic properties of atomic nuclei".

by Bloch and Purcell paved the way to modern NMR and MRI[II]. In later years, Torrey [5] and Hahn [6] independently demonstrated the feasibility of pulsed NMR as originally suggested by Bloch and observed free Larmor precession. Hahn further used pulsed NMR to generate and observe spin echoes[7].

The next couple of decades witnessed NMR penetrating through many areas of Physics and Chemistry as a powerful investigative tool which include many diverse subjects starting from brain, bones etc. to oil wells, Antarctic ice etc. The first two dimensional image (of two glass tubes filled with water) was produced in 1973 by Lauterbur from a series of one dimensional projections obtained using a magnetic field gradient [8]. Soon after demonstration of first MRI images, the technique was given a massive boost by ground-breaking developments performed by Mansfield in Nottingham[III], which allowed use of slice selection [9] and fast acquisition schemes [10] to generate images in lesser amount of time. Ernst et al. took a step forward to develop *NMR-Fourier-Zeugmatography*[IV] which is a technique still used in modern day MRI to generate images within clinically acceptable time durations [11, 12].

Today, MRI is used to image most of the human organs and has proved itself as an indispensible diagnostic tool for modern day medical science. The main distinguishable virtue of MRI, when compared to other medical imaging modalities, is its non-invasive nature. Unlike x-rays or PET/SPECT, there are no harmful ionizing radiations or radioactive isotopes used with magnetic resonance imaging. With technological advances in all verticals, e.g. increase in main magnetic field strengths, stronger gradient hardware offering high slew-rate, innovative data acquisition schemes, it has become possible to image subtler anatomical details with unprecedented soft-tissue contrast. The data acquisition of MRI is fairly flexible to accommodate diagnostic needs and offers a wide range of parameters which one can modify to obtain desired contrast. The journey of MRI has now come to a time point where this less than a century old technology can provide information about very small anatomical/physiological details with excellent spatial/temporal resolution.

## 1.2   Motivation and Purpose of This Work

During an MRI experiment, the speed of data acquisition is one of the critical parameters, not only because of the reasons related to patient comfort but also because faster data acquisition enables study of many high-speed physiological phenomena such as brain functional studies, blood perfusion studies, and cardiac imaging. With ever-growing scientific community, the thirst to increase data acquisition speed seems never-ending. Inevitably, the speed of data acquisition comes at the cost of compromises on image quality. Over the years since its

---

[II]Bloch and Purcell were awarded the 1952 Physics Nobel prize "for their development of new methods for nuclear magnetic precision measurement and discoveries in connection therewith"

[III]These pioneering contributions were jointly rewarded by the 2003 Nobel prize in Medicine "for their discoveries concerning magnetic resonance imaging".

[IV]Ernst was awarded the Nobel prize in Chemistry in 1991 "for his contributions to the development of the methodology of high resolution nuclear magnetic resonance spectroscopy".

inception, various research groups have focused on achieving higher acquisition speed with minimum compromise on the quality of the images.

Echo planar imaging, first conceptualized in 1977 by sir Peter Mansfield [13], is still a universally accepted data acquisition technique for obtaining high temporal resolution datasets. The technique was mostly under-utilized since it was first proposed, mainly owing to its high susceptibility to various artifacts. Due to advances in hardware technology, especially magnetic field gradient hardware which offer higher slew-rates and amplitudes, it has now become possible to acquire two dimensional echo planar image within few tens of milliseconds. Increments in magnetic field strengths have offered increase in signal to noise ratio, thus opening opportunities to improve image quality for a given scan time or to reduce scan time while maintaining acceptable image quality for a given spatial resolution.

In the late 1990's, researchers realized that the speed of data acquisition in MRI can further be increased even without further advances in the magnetic gradient hardware [14–16]. The birth of phased array coils [17] had commenced an era which witnessed unprecedented increase in the speed of data acquisition [18–21]. Because multiple receiver coils in a phased array work in *parallel* to acquire data, the time of data acquisition is reduced by the number of receiver coils. A number of research groups focused their attention in exploiting this parallel imaging technique by developing a wide range of reconstruction algorithms to create images as faithfully as possible using acquired data [14–16, 22, 23].

The research work presented through this thesis makes a humble attempt to demonstrate a few innovative methodologies to further increase the speed of data acquisition using a three dimensional echo planar imaging (3D EPI) technique. In depth qualitative and quantitative assessment of the usefulness of these methods is performed while making sure that the image quality of the acquired images is still within acceptable limits. Along with gradient pulses, excitation RF pulses are also tweaked to excite only the volume of interest and thus enabling acquisition of high spatial and temporal resolution datasets of localized brain regions. A few application studies are performed to demonstrate benefits of high temporal resolution scans for functional study of the brain.

## 1.3 Thesis Outline

The work presented in this thesis was conducted by the author in four years of his Ph.D. at the Centre d'Imagerie BioMédicale (CIBM) in Lausanne, Switzerland. The CIBM is a joint effort of the Ecole Polytechnique Fédérale de Lausanne (EPFL) as well as the universities and hospitals in both Lausanne and Geneva (UNIL/UNIGE and CHUV/HUG). The focus of the center is neuroscience, namely brain diseases, metabolic diseases (e.g. diabetes) and oncology.

In the following, a brief overview over the content of the different chapters of this thesis is given.

- **Chapter 2** starts with description of the basic phenomenon of NMR. After establishing the Larmor resonance condition with a combination of classical and quantum mechanical treatments, the NMR phenomenon is provided a macroscopic view through the *Bloch equation.* Later in the chapter, a brief introduction to the hardware components of a typical magnetic resonance scanner is given. Lastly, important safety considerations for designs and use of magnetic resonance scanners are discussed.

- **Chapter 3** begins with the explanation of the spatial encoding in MRI and effect of the application of gradients and RF pulses on $k$-space sampling positions. Fundamental pulse sequence types used in routine MRI such as *spin echo* sequence and *gradient echo* sequence are discussed next. Multi-echo variants of spin echo and gradient echo pulse sequences are dealt very briefly. Different types of contrast mechanisms achievable are discussed next which have found a plethora of applications in clinical MRI studies. The chapter concludes with an introduction to *functional magnetic resonance imaging* (fMRI) which is the main area of application for acquisition methods developed during the preparation of this thesis.

- **Chapter 4** explains different variants of EPI pulse sequence at the beginning. Compared to conventional spin-echo and gradient-echo imaging, EPI is more prone to a variety of artifacts. These commonly encountered artifacts of echo planar images and their cures are discussed next. In the later part of the chapter, a new $k$-space traversal strategy for 3D EPI is presented that encodes two partitions per RF excitation, effectively reducing the number of excitations used to acquire a 3D EPI dataset by half.

- **Chapter 5** begins with discussion of founding concepts of *parallel MRI*, in which the role of coil arrays in pMRI is explained first. A mathematical treatment of the image aliasing arising due to under-sampling of $k$-space is provided next, followed by parallel imaging reconstruction algorithms used to resolve such image aliasing. Explanation of pMRI algorithms begins with a simplified example and quickly moves towards explaining more advanced parallel imaging techniques. Though a wide range of pMRI techniques have been developed by various research groups, the scope of the discussion here is limited to only a few (namely SMASH, SENSE, and GRAPPA) which lay a sufficient foundation to understand other pMRI variants. Later part of the chapter explains the use of controlled aliasing during pMRI acquisition to improve the image SNR by making effective use of coil sensitivity variations provided by array coils.

- **Chapter 6** demonstrates the combination of 3D EPI sequence and controlled aliasing to benefit from reduced spatially varying noise amplifications commonly encountered during parallel imaging reconstruction. The chapter concludes with proving the benefits of high temporal acquisitions through few examples applications to functional MRI studies performed on the human brains.

- **Chapter 7** starts with expanding $k$-space interpretation to the excitation phase of a pulse sequence. Next, $k$-space interpretation of 2D RF excitation is explained by first understanding the $k$-space approach of analyzing RF excitation through 1D selective excitation analysis. Once the founding concepts for 2D RF pulse and its $k$-space interpretation are explained, 2D RF excitation pulse in combination with controlled aliasing enabled 3D EPI readout moodule is demostrated for high resolution localized fMRI acquisition.

- **Chapter 8** provides a consolidated summary and future outlook of the principal findings of this thesis.

# References

[1] I. I. Rabi, J. R. Zacharias, S. Millman, and P. Kusch. A new method of measuring nuclear magnetic moment. *Phys. Rev.*, 53:318–318, Feb 1938.

[2] E. M. Purcell, H. C. Torrey, and R. V. Pound. Resonance absorption by nuclear magnetic moments in a solid. *Phys. Rev.*, 69:37–38, Jan 1946.

[3] F. Bloch, W. W. Hansen, and Martin Packard. Nuclear induction. *Phys. Rev.*, 69:127–127, Feb 1946.

[4] F. Bloch, W. W. Hansen, and M. Packard. The nuclear induction experiment. *Phys. Rev.*, 70:474–485, Oct 1946.

[5] H. C. Torrey. Transient nutations in nuclear magnetic resonance. *Phys. Rev.*, 76:1059–1068, Oct 1949.

[6] E. L. Hahn. Nuclear induction due to free larmor precession. *Phys. Rev.*, 77:297–298, Jan 1950.

[7] E. L. Hahn. Spin echoes. *Phys. Rev.*, 80:580–594, Nov 1950.

[8] P. C. Lauterbur. Image formation by induced local interactions: Examples employing nuclear magnetic resonance, 1973.

[9] A N Garroway, P K Grannell, and P Mansfield. Image formation in nmr by a selective irradiative process. *Journal of Physics C: Solid State Physics*, 7(24):L457, 1974.

[10] P Mansfield and A.A Maudsley. Planar spin imaging by {NMR}. *Journal of Magnetic Resonance (1969)*, 27(1):101 – 119, 1977.

[11] R. R. Ernst and W. A. Anderson. Application of fourier transform spectroscopy to magnetic resonance. *Review of Scientific Instruments*, 37(1):93–102, 1966.

[12] JR Mallard, JM Hutchison, W Edelstein, M Foster, and R Ling. Nmr imaging. *Proc*, pages 680–681, 1979.

## REFERENCES

[13] P Mansfield. Multi-planar image formation using nmr spin echoes, 1977.

[14] Klaas P. Pruessmann, Markus Weiger, Markus B. Scheidegger, and Peter Boesiger. Sense: Sensitivity encoding for fast mri. *Magnetic Resonance in Medicine*, 42(5):952–962, 1999.

[15] Daniel K. Sodickson and Warren J. Manning. Simultaneous acquisition of spatial harmonics (smash): Fast imaging with radiofrequency coil arrays. *Magnetic Resonance in Medicine*, 38(4):591–603, 1997.

[16] Mark A. Griswold, Peter M. Jakob, Robin M. Heidemann, Mathias Nittka, Vladimir Jellus, Jianmin Wang, Berthold Kiefer, and Axel Haase. Generalized autocalibrating partially parallel acquisitions (grappa). *Magnetic Resonance in Medicine*, 47(6):1202–1210, 2002.

[17] P. B. Roemer, W. A. Edelstein, C. E. Hayes, S. P. Souza, and O. M. Mueller. The NMR phased array. *Magnetic Resonance in Medicine*, 16(2):192–225, 1990.

[18] J. W. Carlson. An algorithm for nmr imaging reconstruction based on multiple rf receiver coils. *Journal of Magnetic Resonance*, 74(2):376–380, 1987.

[19] Michael Hutchinson and Ulrich Raff. Fast mri data acquisition using multiple detectors. *Magnetic Resonance in Medicine*, 6(1):87–91, 1988.

[20] J. Kelton, R. M. Magin, and S. M. Wright. An algorithm for rapid acquisition using multiple receiver coils. In *Proceedings 8th Annual SMRM*, page 1172, 1989.

[21] J. B. Ra and C. Y. Rim. Fast imaging using subencoding data sets from multiple detectors. *Magnetic Resonance in Medicine*, 30(1):142–145, 1993.

[22] PeterM. Jakob, MarkA. Grisowld, RobertR. Edelman, and DanielK. Sodickson. Auto-smash: A self-calibrating technique for smash imaging. *Magnetic Resonance Materials in Physics, Biology and Medicine*, 7(1):42–54, 1998.

[23] Robin M. Heidemann, Mark A. Griswold, Axel Haase, and Peter M. Jakob. Vd-auto-smash imaging. *Magnetic Resonance in Medicine*, 45(6):1066–1074, 2001.

# 2 Theoretical Backgrounds

*Nuclear Magnetic Resonance* (NMR) [24–27] is the study of the magnetic properties (and energies) of nuclei. The interaction of electromagnetic waves with the elementary particles can be observed when the nuclei are placed in a (strong) external magnetic field. In essence, NMR is exactly what its name says: the study of nuclei in a magnetic field at their resonance frequency. NMR is the consequence of a physical property of atomic nuclei called '*spin*' which causes an interaction with an externally applied magnetic field.

In this chapter the basic phenomenon of NMR is described. After establishing the Larmor resonance condition with a combination of classical and quantum mechanical descriptions, the NMR phenomenon is provided a macroscopic view through the *Bloch equation.* Later in the chapter, a brief introduction to the hardware components of a typical magnetic resonance scanner is given. Lastly, important safety considerations for designs and use of magnetic resonance scanners are discussed.

## 2.1 Nuclear Magnetic Resonance (NMR)

### 2.1.1 Classical Description

The NMR phenomenon cannot be completely explained by classical physics, though classical physics is often used to create a familiar frame of reference in which the existence of a spin angular momentum can be visualized.

A rotating object, carrying an electrical charge $q$ and rotating with a constant angular velocity $v$ about a fixed point at a distance $r$, generates a magnetic field, characterized by the magnetic dipole moment $\mu$:

$$
\begin{aligned}
\mu &= [\text{current}]\,[\text{area}] \\
&= \left[ \frac{q\mathbf{v}}{2\pi\mathbf{r}} \right] \pi\mathbf{r}^2
\end{aligned}
\tag{2.1}
$$

---

Majority of this chapter is adapted from the books [28], [29], and [30].

Substituting $\mathbf{L} = m\mathbf{vr}$, we get

$$\boldsymbol{\mu} = \left(\frac{e}{2m}\right)\mathbf{L} = \gamma\mathbf{L} \tag{2.2}$$

where $\gamma$ is the (classical) *gyromagnetic ratio* and $\mathbf{L}$ is the angular momentum vector. In an external magnetic field $\mathbf{B}_0$, the rotating object will feel a torque $T$ (or rotational force) given by:

$$\mathbf{T} = \boldsymbol{\mu} \times \mathbf{B}_0 \tag{2.3}$$

Using the relation $T = \left(\frac{d\mathbf{L}}{dt}\right)$ and combining with Equation (2.2) and (2.3) gives:

$$\left(\frac{d\boldsymbol{\mu}}{dt}\right) = \gamma\boldsymbol{\mu} \times \mathbf{B}_0 \tag{2.4}$$

Due to the constant angular velocity, the amplitude of $\mu$ is constant. Equation (2.4) therefore suggests that $\mu$ changes its orientation relative to $\mathbf{B}_0$. An alternate expression of $\mu$ precessing about $\mathbf{B}_0$ can be given by:

$$\left(\frac{d\boldsymbol{\mu}}{dt}\right) = \boldsymbol{\mu} \times \boldsymbol{\omega}_0 \tag{2.5}$$

Combining Equations (2.4) and (2.5) results in the famous *Larmor equation*:

$$\boldsymbol{\omega}_0 = \gamma\mathbf{B}_0 \tag{2.6}$$

or

$$\boldsymbol{\nu}_0 = \left(\frac{\gamma}{2\pi}\right)\mathbf{B}_0 \tag{2.7}$$

The *Larmor frequency* $\omega_0$ or $\nu_0$ is thus directly proportional to the applied magnetic field $\mathbf{B}_0$ and also to the gyromagnetic ratio $\gamma$, which is characteristic for the nucleus under investigation. Table 2.1 provides values for some commonly used nuclei. In water, the hydrogen proton has a gyromagnetic ratio of approximately $\gamma = 2.68 \cdot 10^8 \frac{rad}{s \cdot T}$.

| nucleus | spin | natural abundance [%] | gyromagnetic ratio [$10^6 \frac{rad}{s \cdot T}$] | Larmor frequency at 7T [MHz] |
|---------|------|-----------------------|---------------------------------------------------|------------------------------|
| $^1$H | 1/2 | 100 | 267.522 | −298.04 |
| $^2$H | 1 | 0.015 | 41.066 | −45.75 |
| $^{12}$C | 0 | 98.9 | - | - |
| $^{13}$C | 1/2 | 1.1 | 67.283 | −74.96 |
| $^{16}$O | 0 | 100 | - | - |

**Table 2.1:** *Selection of nuclear isotopes found in living tissue and/or of importance for MRI and their physical properties.*

### 2.1.2 Quantum Mechanical Description

Quantum mechanics states that the total angular momentum **L** of elementary particles (protons, neutrons or electrons) is quantized and its amplitude is given by:

$$L = \left(\frac{h}{2\pi}\right)\sqrt{I(I+1)} \tag{2.8}$$

where $I$ is the spin quantum number and it can only be an integer or a half-integer and $h$ is Planck's constant. Being a vector, angular momentum has a direction associated with it which is specified by a second quantum number $m$, which can only have certain discrete orientations with respect to a given direction. Quantum mechanics shows that $m$ can have $2I + 1$ values, given by:

$$m = I, \ I-1, \ I-2, \ \dots, \ -I \tag{2.9}$$

For elementary particles, the spin quantum number $I$ equals $1/2$. For nuclei, $I$ can be calculated by using the atomic mass and the charge number. Below rules apply during calculation:

- For nuclei with an odd mass number, $I$ is half-integral ($1/2$, $3/2$, $5/2$, ..., e.g. $^{1}$H, $^{13}$C, $^{15}$N, $^{23}$Na, $^{31}$P).
- For nuclei with an even mass number and an even charge number, $I$ is zero (e.g. $^{12}$C, $^{16}$O, $^{32}$S).
- For nuclei with an even mass number and an odd charge number, $I$ is an integer number (1, 2, ..., e.g. $^{2}$H, $^{14}$N).

Since $m$ is a discrete quantum number [see Equation (2.9)], the energy levels attained by a particle when placed an external magnetic field **B**$_0$ are also quantized. For a particle of spin $I = 1/2$, there are only two energy levels ($m = -1/2$ and $+1/2$) and the energy difference between the two states, $\Delta E$, is given by (see Figure 2.1):

$$\Delta E = \gamma \left(\frac{h}{2\pi}\right) B_0 \tag{2.10}$$

The resonance phenomenon in NMR is achieved by applying an oscillating magnetic field perpendicular to the direction of the external magnetic field **B**$_0$ with a frequency $\nu_0$, such that the energy equals the magnetic energy given by Equation (2.10). In short, the energy of the electromagnetic wave is given by:

$$\Delta E = h\nu_0 \tag{2.11}$$

(a)

(b)
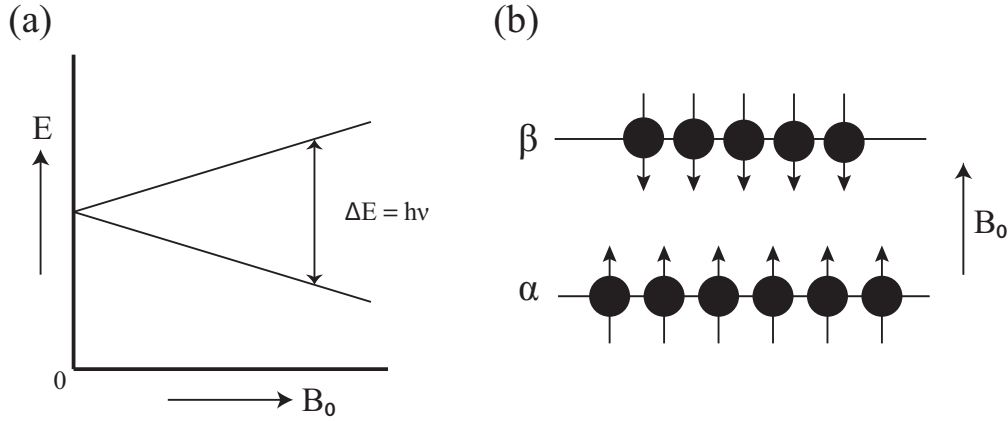


**Figure 2.1:** *(a) The nuclear spin energy for a spin-1/2 nucleus as a function of the external magnetic field strength $B_0$. (b) The lower energy level ($\alpha$ spin state) corresponds to magnetic moments parallel with $B_0$, while spins in the higher energy level ($\beta$ spin state) have an antiparallel alignment with $B_0$. For all currently available magnets, the energy level difference between the two spin states corresponds to electromagnetic radiation in the RF range.*

Combining Equations (2.10) and (2.11) will give the Larmor equation as derived in Section 2.1.1:

$$\nu_0 = \left(\frac{\gamma}{2\pi}\right) B_0 \tag{2.12}$$

Even though the classical and quantum mechanical description of NMR lead to the same result, they play a different role in the understanding of the technique. Quantum mechanics is the only theory which can quantitatively describe the NMR phenomenon. Classical principles are mainly used to visualize the effects of the RF pulses and the magnetic field gradients on macroscopic magnetization vectors.

### 2.1.3 Macroscopic (Net) Magnetization

For elementary particles and atomic nuclei, the angle $\theta$ between $\mu$ and $\mathbf{B}_0$ can no longer be arbitrary as in Section 2.1.1 but is given by:

$$\cos\theta = \frac{m}{\sqrt{I(I+1)}} \tag{2.13}$$

Figure 2.2(a) shows the precession (at the Larmor frequency) of a magnetic moment around an external magnetic field according to classical principles. Quantization of magnetic moment (and magnetic energy) can readily be incorporated in this picture. The nuclei of spin $I = 1/2$ are distributed on the surface of two cones, and rotate about $\mathbf{B}_0$ at the Larmor frequency (Figure 2.2(b)). In the general case of a spin $I$ nucleus, the magnetic moments will be distributed on $2I + 1$ cones at discrete angles $\theta$ as defined by Equation (2.13). For a spin 1/2 nucleus the two spin states $m = +\ 1/2$ ($\mu$ antiparallel to $\mathbf{B}_0$) are often referred to as the $\alpha$ and $\beta$ spin states,
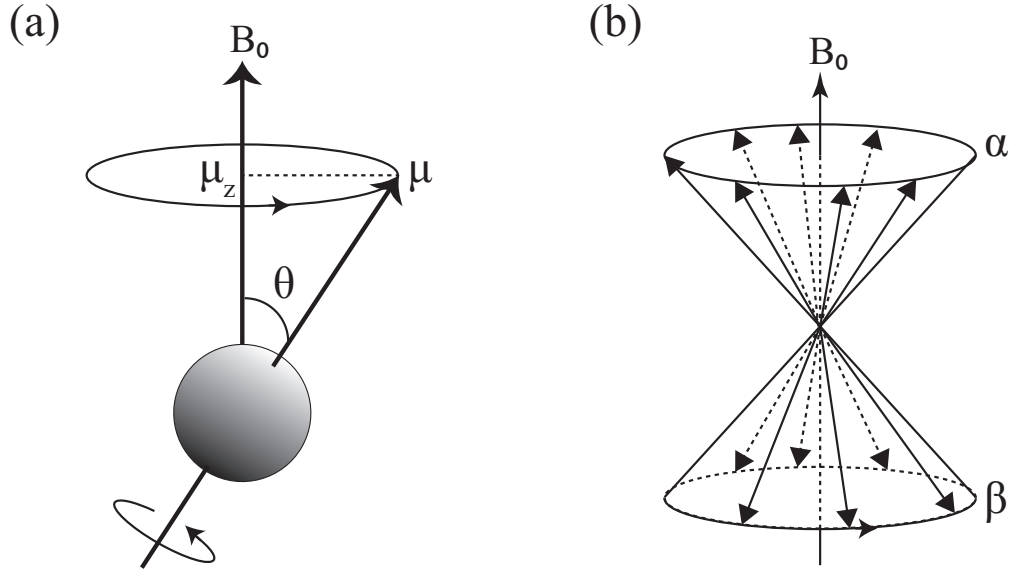
**Figure 2.2:** *(a) A nuclear spin precessing in an external magnetic field $B_0$. The spin magnetic moment $\mu$ precesses about $B_0$, in which the orientation $\theta$ and the amplitude (along z) $\mu_z$ are quantized. (b) In a macroscopic ensemble of nuclear spin-1/2, the spins distribute themselves among two possible orientations according to the Boltzmann equation.*

respectively.

So far, only the behavior of individual nuclear spins has been considered. However, a macroscopic sample contains many spins, which will be randomly distributed on the cones. As a consequence of the small energy difference between the spin states there will be a small difference in the population of these spin states. This population difference can be calculated using the *Boltzmann distribution.* For the situation shown in Figure 2.2(b) the energy difference $\Delta E = h\nu$ gives rise to a population distribution given by:

$$\left(\frac{n_\alpha}{n_\beta}\right) = e^{\Delta E/kT} = e^{h\nu/kT} \tag{2.14}$$

where $n_\alpha$ is the number of spins in the $\alpha$ (low energy) state, $n_\beta$ is the number of spins in the $\beta$ (high energy) state, $k$ is the Boltzmann constant and $T$ is the absolute temperature. Since at normal temperature, $h\nu$ is much less than thermal energy $kT$, the exponent in Equation (2.14) can be simplified through an expansion and truncation of a Taylor series to give:

$$\left(\frac{n_\alpha}{n_\beta}\right) = 1 + \left(\frac{h\nu}{kT}\right) \tag{2.15}$$

The *net magnetic moment,* **M**, of a macroscopic sample is the resultant of the sum over all individual magnetic moments $\mu$. Since the magnetic moments are randomly distributed on the cones, there will be no net component of **M** in the transverse xy plane (see Figure 2.2b).

11

However, due to the population difference there will be a net component $\mathbf{M}$ parallel with $\mathbf{B}_0$ along the +z axis. At thermal equilibrium the magnitude of the longitudinal magnetization, $\mathbf{M}_0$ is:

$$M_0 = \sum \mu_i = n_\alpha \mu_z + n_\beta \mu_z = \gamma \left( \frac{h}{4\pi} \right) (n_\alpha - n_\beta) \tag{2.16}$$

Using Equation (2.15), $(h\nu/kT) \ll 1$ and $n = n_\alpha + n_\beta$ where $n$ is the total number of nuclear spins in the macroscopic sample, the population difference $(n_\alpha - n_\beta)$ is given by:

$$(n_\alpha - n_\beta) \approx \left( \frac{nh\nu}{2kT} \right) \tag{2.17}$$

Therefore, at thermal equilibrium, the amplitude of the macroscopic magnetization vector $\mathbf{M}_0$ is:

$$M_0 = \left( \frac{\gamma h}{2\pi} \right)^2 \left( \frac{nB_0}{4kT} \right) \tag{2.18}$$

For a macroscopic sample containing one million nuclear spins at 37°C ($T = 310.15$ K) and in a magnetic field of 7T, corresponding to $\nu = 300$ MHz, the population difference between the $\alpha$ and $\beta$ spin states is only 23 spins (corresponding to 0.0023%). Since the final received signal is proportional to the population difference, NMR is a rather insensitive technique when compared with other forms of spectroscopy/imaging.

From Equation (2.18) several important features concerning the sensitivity of NMR experiments can be deduced. The quadratic dependence of $\mathbf{M}_0$ on the gyromagnetic ratio $\gamma$ implies that nuclei resonating at high frequency [see Equation (2.12)] also generate relatively intense NMR signals. The gyromagnetic ratios of the most relevant nuclei found in living tissue and/or of importance for MRI and their physical properties are listed in Table 2.1 under Section 2.1.1. The linear dependence of $\mathbf{M}_0$ on the magnetic field strength $\mathbf{B}_0$ implies that higher magnetic fields improve the sensitivity. Finally, the inverse proportionality of $\mathbf{M}_0$ to the temperature $T$ indicates that sensitivity can be enhanced at lower sample temperatures, which obviously is unrealistic for *in vivo* applications.

Describing spin ensembles using the net magnetization vector is extremely useful, in particular for MR imaging. Just as a single magnetic moment (see Equation (2.4)), the net magnetization vector $\mathbf{M}$ also interacts with an external magnetic field according to

$$\frac{\mathrm{d}\mathbf{M}}{\mathrm{d}t} = \gamma \mathbf{M} \times \mathbf{B} \tag{2.19}$$

This description presumes non-interacting protons, which is valid for free water (the scope of this thesis). Hence, the magnetization vector precesses about external fields just as a single magnetic moment. It is sometimes preferable to describe $\mathbf{M}$ as vector sum of the *longitudinal*

*component* ($M_\parallel$) and the *transverse component* ($M_\perp$) so that:

$$\mathbf{M} = M_\parallel \hat{z} + \mathbf{M}_\perp \tag{2.20}$$

where

$$\mathbf{M}_\perp = M_x \hat{x} \cos\omega t + i M_y \hat{y} \sin\omega t \tag{2.21}$$

### 2.1.4 Rotating Frame of Reference and Effective B-field

So far, the phenomena were described in a static reference frame, dubbed *laboratory reference frame* in the MR nomenclature. By convention, it is a right-handed Cartesian coordinate system defined with respect to the MR scanner. In the following discussion of the effects of additional magnetic fields on a spin system, a change of the coordinate system provides very useful simplifications. In the *rotating reference frame*, the z-axis is directed towards the external magnetic field, i.e. towards $\mathbf{B}_0$-field, just as in the laboratory reference frame. While the x- and y-axis are now rotating about the negative z-axis with an angular frequency of $\Omega$, i.e. for positive $\Omega$, the rotation in clockwise. Often, the angular frequency of the rotating frame is set *on-resonance* with the spin system, i.e. rotating at the Larmor frequency, $\mathbf{\Omega} = -\gamma B_0 \hat{z}$.

A given vector $\mathbf{p}$ in the laboratory frame can be transformed to the rotating frame of reference, denoted by the prime ($'$) notation, using the following relation:

$$\mathbf{p}' = \begin{pmatrix} p'_x \\ p'_y \\ p'_x \end{pmatrix} = \begin{pmatrix} \cos\Omega t & -\sin\Omega t & 0 \\ \sin\Omega t & \cos\Omega t & 0 \\ 0 & 0 & 1 \end{pmatrix} \begin{pmatrix} p_x \\ p_y \\ p_x \end{pmatrix} \tag{2.22}$$

To transform in the opposite direction, the transpose of the rotation matrix has to be used.

For the magnetic moment vector $\boldsymbol{\mu}$ rotating about an arbitrary axis, the relation of its derivative in the laboratory frame is

$$\left( \frac{\mathrm{d}\boldsymbol{\mu}}{\mathrm{d}t} \right)' = \frac{\mathrm{d}\boldsymbol{\mu}}{\mathrm{d}t} - \mathbf{\Omega} \times \boldsymbol{\mu} \tag{2.23}$$

Combining Equations (2.4) and (2.23) yields

$$\left( \frac{\mathrm{d}\boldsymbol{\mu}}{\mathrm{d}t} \right)' = \gamma\boldsymbol{\mu} \times + \boldsymbol{\mu} \times \mathbf{\Omega} = \gamma\boldsymbol{\mu} \times \left( \mathbf{B} + \frac{\mathbf{\Omega}}{\gamma} \right) \tag{2.24}$$

The bracketed term on the right is known as the *effective magnetic field* ($\mathbf{B}_{\mathrm{eff}}$):

$$\mathbf{B}_{\mathrm{eff}} = \mathbf{B} + \frac{\mathbf{\Omega}}{\gamma} \tag{2.25}$$

The effective magnetic field is the key concept in the analysis of the magnetization in the
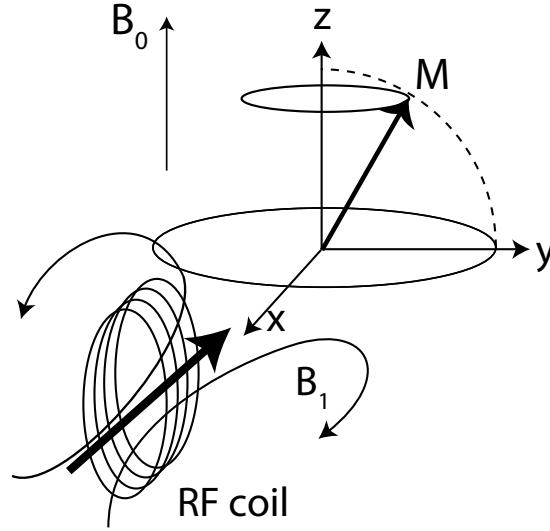
**Figure 2.3:** *After an excitation pulse, the spins are transferred to the transverse plane. Without additional magnetic fields, they subsequently precess at the Larmor frequency which can be detected by means of a single or multiple RF coil(s). The normal vector of the probe area has to lay in the transverse plane to induce a voltage in the coil.*

rotating frame. Notably, setting the rotational frequency of the reference frame to the Larmor precession frequency $\mathbf{\Omega}/\gamma = -\mathbf{B}$, the magnetic moment vector becomes static: $d\boldsymbol{\mu}'/dt = 0$.

### 2.1.5 Radio Frequency Excitation

The longitudinal magnetization established by the spin population energy level differences is almost undetectable. It takes effect on top of the diamagnetism found in a typical sample, which is about four orders of magnitude larger. It is thus impractical to measure. MR spectroscopy and imaging, however, follow a different approach. Instead of measuring the field in z-direction, it is measured perpendicular to z-direction, as illustrated in Figure 2.3. Therefore, the magnetization stored on the longitudinal axis, described by the magnetization vector (see Section 2.1.3), has to be rotated to the xy-plane. For this purpose, a time-dependent magnetic field orthogonal to the main field is employed, denoted as $\mathbf{B}_1$. To excite the spins, the frequency of $\mathbf{B}_1$ has to be matched to the Larmor frequency, which is in the radio frequency range for typical field strengths. The need to match the frequency becomes clearer by visualizing a magnetic moment in the laboratory frame of reference. The magnetic moment precesses about the axis of an external field. If one were to make it rotate about the, say, x-axis, the external field has to be (more or less) static with respect to the precession of the magnetic moment. This is equivalent to match the RF frequency to the Larmor frequency. Consider a time-dependent magnetic field with amplitude $B_1$, without loss of generality linearly polarized
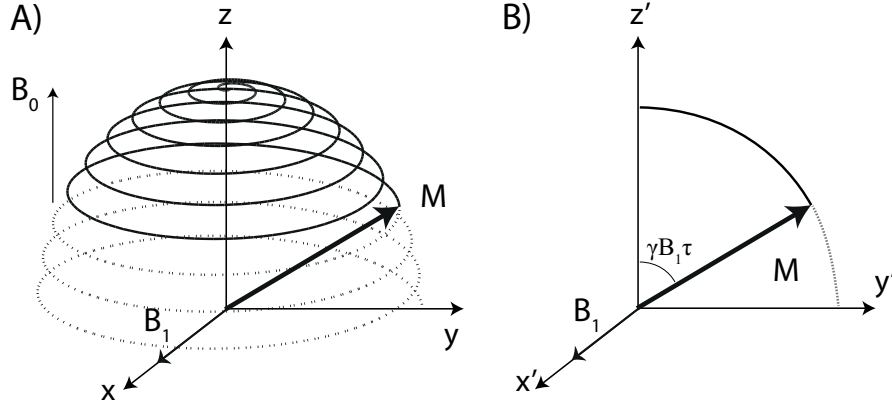
**Figure 2.4:** *Tilting of the longitudinal magnetization using a perpendicular RF (excitation) pulse depicted in (A) the laboratory and (B) the rotating frames of reference. In the latter case, the magnetization vector is assumed to rotate on-resonance, i.e. at the Larmor frequency (which is the rotation frequency of the frame of reference). Consequently, the magnetization vector seems to rotate only about x-axis.*

along the x-axis

$$\mathbf{B}_1 = \begin{pmatrix} B_1 \cos (\omega t) \\ 0 \\ 0 \end{pmatrix} \tag{2.26}$$

Transferring this vector in a reference frame rotating about the z-axis with a (clockwise) angular frequency of $\mathbf{\Omega} = -\omega \hat{z}$ using Equation (2.22) yields

$$\mathbf{B}_1 = \begin{pmatrix} \cos \omega t & -\sin \omega t & 0 \\ \sin \omega t & \cos \omega t & 0 \\ 0 & 0 & 1 \end{pmatrix} \begin{pmatrix} B_1 \cos (\omega t) \\ 0 \\ 0 \end{pmatrix} = \frac{B_1}{2} \begin{pmatrix} \cos (2\omega t) + 1 \\ \sin 2\omega t \\ 0 \end{pmatrix} \tag{2.27}$$

One hence obtains a static $B_1$-component along the x-axis of the rotating frame as well as a component rotating with twice the Larmor frequency. With respect to the magnetization vector's time scale, it is valid to assume that the latter component averages out to zero. Consequently, the magnetization vector starts to rotate about $\hat{x}$. It is important to note that its amplitude is halved [see Equation (2.27)]; i.e. that only half of the energy of the linearly polarized RF field is used to rotate the magnetization vector. This can be overcome by using two coils in the so-called *quadrature configuration* in which case

$$\mathbf{B}_1 = \begin{pmatrix} B_1 \cos (\omega t) \\ B_1 \sin (\omega t) \\ 0 \end{pmatrix} \tag{2.28}$$

15

The magnetization vector rotates about $\mathbf{B}_1$ field until the RF field is switched off. The rotation is characterized by its *flip angle* ($\Delta\theta$):

$$\Delta\theta = \gamma B_1 \tau \tag{2.29}$$

where $\tau$ is the duration of the RF pulse. The process is illustrated for both the laboratory and rotating reference frames in Figure 2.4.

### 2.1.6 Relaxation

As described above, a radiofrequency pulse at the Larmor frequency excites the spin system, hence taking it away from equilibrium. The excitation also aligns the spins in a preferred direction in the transverse plane, creating an ordered state, the coherence. Being in exchange with its environment, the spin system eventually goes back to its thermal equilibrium magnetization, dissipating energy to its surrounding. At the same time, the coherence is lost due to tiny differences in the local magnetic field of the spins. These effects are called *relaxation* and they are governed by two independent mechanisms, resulting in *longitudinal* and *transverse relaxations*.

**Longitudinal Relaxation**

The basis of longitudinal relaxation is energy exchange between protons and their surroundings. The disequilibrium created by the supply of energy via the RF pulse gradually dissipates. This process is irreversible. The phenomenological description of this process is given by the equation

$$\frac{\mathrm{d}M_z}{\mathrm{d}t} = \frac{M_0 - M_z}{T_1} \tag{2.30}$$

where $M_0$ is the *equilibrium longitudinal magnetization* and $T_1$ is the so-called *longitudinal relaxation constant*. The solution of Equation (2.30) is found by integration

$$M_z(t) = M_0 - [M_0 - M_z(0)]\, e^{-t/T_1} \tag{2.31}$$

Where $M_z(0)$ is the longitudinal magnetization right after the RF excitation. $T_1$ is characterized by the chemical environment in which spin resides. Exploiting $T_1$ differences among different tissues one of the basic mechanisms to generate image contrast. $T_1$ is determined by experiment, typical values range from 0.1 to 100 seconds at room temperature.

**Transverse Relaxation**

After excitation, the magnetic moments of a spin ensemble not only return to their equilibrium state, but also they lose coherence at the same time, under the influence of their micro-

environment. Due to the slightly different local magnetic field experienced by each spin, which consequently implies small Larmor frequency deviations, the spins accumulate phase differences. More illustratively, their magnetic moments "fan out" in the transverse plane, the coherence degenerates. Eventually, the transverse components of the magnetic moments are homogeneously distributed on the transverse plane, entirely cancelling out each other. The rate of this effect depends on the micro-environment of the spins; it is hence tissue specific and can serve as a contrast mechanism in MRI.

Closer investigation reveals that the local deviations of the magnetic fields have two different sources, time-dependent and time-independent ones. The time-dependent effects are due to the aforementioned random processes in the proximity of a spin. Their random character renders them irreversible. Magnetic field changes can however also stem from external influences. No magnetic field is perfectly homogeneous and bringing in the sample in it further disrupts the homogeneity. These homogeneities do not, or very slowly, change over time. On a molecular time scale they can hence be considered time-independent and are reversible, typically with spin-echo type sequences, which are introduced later in Section 3.2.1.

Without a dedicated sequence of RF pulses, the two sources of transverse relaxation superpose each other, accelerating the signal decay. The resulting apparent transverse relaxation time constant, $T_2^*$, is composed of the constant of the time-dependent (internal) processes $T_2$, and the one of the external time-independent ones, $T_2'$ and can be described in the following manner:

$$\frac{1}{T_2^*} = \frac{1}{T_2} + \frac{1}{T_2'} \tag{2.32}$$

This implies that $T_2^* \leq T_2$. The $T_2^*$ relaxation is the dominant effect in a simple experiment with one excitation pulse. Such signal decay, i.e. unimpeded by additional gradients or RF pulses, is called a *free induction decay* (FID). Figure 2.5A illustrates the recovery process of the net magnetization after application of an RF excitation pulse in the laboratory reference frame. Figure 2.5B shows the FID of transverse magnetization governed by $T_2^*$ along with restoration of longitudinal magnetization back to its thermal equilibrium state governed by $T_1$.

**The Bloch Equation**

The differential equations describing the behavior of a spin ensemble's magnetization vector in the presence of a magnetic field (see Equation (2.19)) can be combined with the relaxation terms to obtain one vector equation

$$\frac{d\mathbf{M}}{dt} = \gamma \mathbf{M} \times \mathbf{B} - \frac{M_x \hat{x} + M_y \hat{y}}{T_2} - \frac{(M_0 - M_z)\,\hat{z}}{T_1} \tag{2.33}$$

This formula is known as the *Bloch Equation*, named after Felix Bloch [25–27]. It empirically describes many of the effects dealt within MRI and is thus ubiquitously used.
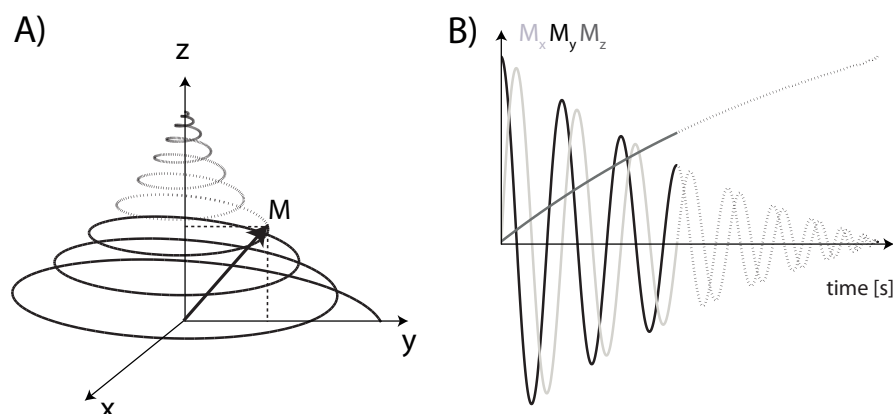
**Figure 2.5:** *(A) After application of an RF excitation pulse, $M_{xy}$ rotates about $B_0$ but undergoes a relaxation process characterized by $T_2^*$, whereas $M_z$ recovery is characterized by $T_1$. (B) Gradual loss of transverse magnetization ($M_x$ and $M_y$) is referred to as the Free Induction Decay and at the same time longitudinal magnetization ($M_z$) is gradually restored back to its thermal equilibrium state.*

### 2.1.7 Chemical Shift

In condensed matter, nuclei are surrounded by atomic or molecular electron clouds which interact with the nuclear spin angular momentum. These interactions are characteristics of the local chemical environment, a discovery which revolutionized chemistry in the 1950s. The ability of nuclear magnetic resonance spectroscopy and imaging to characterize the local chemical environments make them essential tools, in particular for organic chemistry. The consequence of this distinctive characterization is the *chemical shift* [31, 32]. When an external magnetic field is applied, not only the nuclei are interacting with it, but also the electron clouds surrounding the nuclei are perturbed. This interaction generates a magnetic field that counteracts the externally applied field, partly shielding the nucleus from the external field and changing its Larmor frequency. The frequency alteration $\delta$ is characteristic of the electron cloud of the nucleus and its chemical environment. It can be measured by means of NMR.

$$B_{local} = (1-\delta)\, B_0 \tag{2.34}$$

In general, $\delta$ is directional and has to be expressed as a tensor of rank two. Due to thermal motion in the gaseous and fluid phase, however, the anisotropy averages out, rendering $\delta$ scalar. The chemical shift is defined as the difference of the shielding compared to a reference substance:

$$\delta_{cs} = \frac{B_{local} - B_{local}^{ref}}{B_0} = \delta^{ref} - \delta \tag{2.35}$$
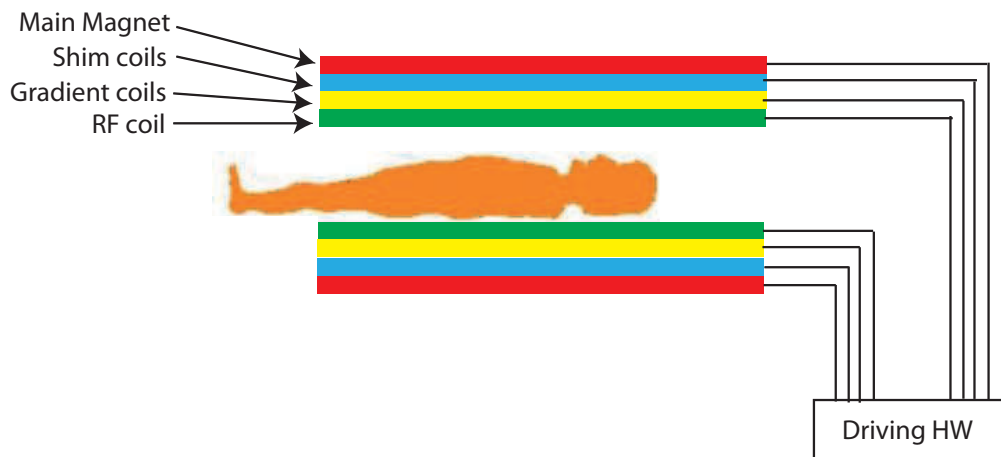
**Figure 2.6:** *A schematic outlining the main components of a MR scanner.*

the strength of $\delta$ strongly depends on the atomic number of the nucleus; it is on the order of a few ppm of the base frequency in protons, but can be up to several hundreds ppm in larger nuclei like $^{13}$C and $^{31}$P. In imaging, however, this effect is rarely exploited, with one exception: the offset of about 3.5 ppm between methylene protons in fat and water protons is of particular interest. In samples where fat significantly contributes to the measured signal, the frequency offset introduced by the chemical shift can lead to severe image distortions, a problem often arising in body imaging, for example.

## 2.2 Hardware components of MR system

A MR scanner is a complex measurement device composed of parts with very different electrical and mechanical characteristics. The main magnet is submerged in liquid helium, necessitating good thermal isolation and a continuous cooling. The gradient system determines the imaging performance to a great extent; here, very high currents have to be switched in a kHz frequency range with high precision. Conversely, the MR signal picked up by the coils creates very low currents at a frequency in the RF range which have to be down-modulated and exactly measured. The whole system comprises several controlling computers, including the console computer interacting with the user, interconnected by a common bus. A schematic diagram of scanner's main components is shown in Figure 2.6. In the following sections, a brief description of the main hardware components of a MR system will be given.

### 2.2.1 The main magnet

While smaller spectrometers, electromagnets or even permanent magnets can be used to generate the main magnetic field, the currents necessary to generate fields over 1 Tesla in a sufficiently large volume are too high for resistive coils. Therefore, superconducting coils have been introduced, allowing very high currents to flow unresistantly. To develop superconduc-

tivity, even today's high-temperature superconducting materials need to be cooled to about 20 Kelvin or below. As a first-order cooling medium, liquid helium is used. Unfortunately, helium is not very abundant and difficult to extract, making it rather costly. Also, the constant cooling demands a considerable maintenance effort and boiled off helium has to be replaced frequently. Currently, common medical human MR scanners employ magnets with field strengths of 1.5 or 3 Tesla. The strongest research animal scanners approach the strength of 20 Tesla, whereas chemical MR machines with very small bores achieve up to 50 Tesla strength.

### 2.2.2 Shim Coils

Besides reaching higher field strengths, one major challenge in building MR magnets are temporal stability and spatial homogeneity constraints. The imaging process requires very stable and homogeneous main magnetic field since even a small disturbance induces artifacts in the acquired images. In applications like functional MRI where small changes are measured over time, the temporal stability of the field is crucial. In addition, the imaging process necessitates a very homogeneous magnetic field in the imaged volume at every point in time. Due to various external influences, this cannot be entirely taken care of in the magnet's design. Therefore, small sheets of metal (*permanent shims*) are distributed in the bore during the tune-up of the scanner, in order to yield a more homogeneous field. By placing an object inside the magnetic field, the latter is also distributed, requiring also a preceding *shimming* procedure for every experiment. To do so, additional *shim coils* create magnetic fields contracting the introduced disturbances. The preceding process of measuring these field disturbances is called *field mapping*.

### 2.2.3 Radio Frequency Coils

The RF coils serve two purposes: (i) emit electromagnetic waves in a frequency range around the Larmor frequency in order to excite the spin system using transmit coil and (ii) detect the tiny resonance signal emitted by the spins after an excitation pulse using receive coil. The same coil can be used for both transmit and receive purposes but are often separate in order to optimize for image quality. Some RF coils transmit and receive in quadrature configuration. This means they produce or detect a circularly polarized field with x and y components of the magnetic field in the laboratory frame. A linear coil which is only able to produce a field along one direction would result in a $\sqrt{2}$ reduction in sensitivity with an effective magnitude in the rotating frame reduced by half.

The excited spins absorb RF energy from a pulse generated by the RF transmit coil. When the pulse is switched off they release energy to be detected by the RF receive coil placed close to the imaging object. Ideally, an RF transmit coil produces a spatially uniform $\mathbf{B}_1$ field at right angles to the static magnetic field $\mathbf{B}_0$. For RF receive coils, ideally Signal-to-Noise Ratio (SNR) obtained with the coil is very high with homogenous receive response over the imaged volume. SNR is influenced by the sensitivity of the coil and the noise associated with the coil. This

(a)　　　　　　　　　　(b)　　　　　　　　　　(c)
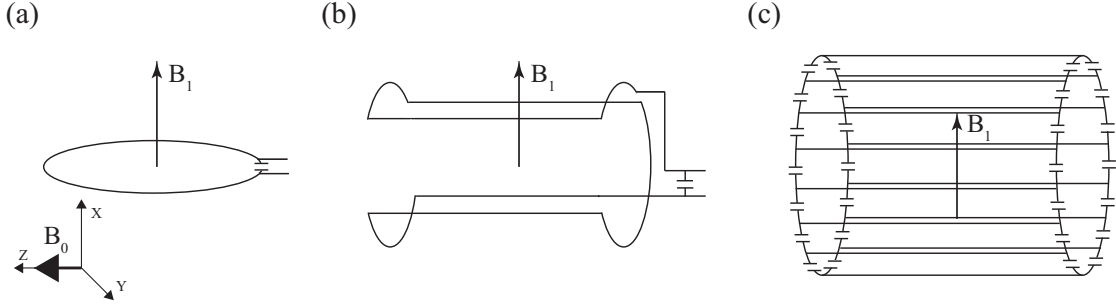


**Figure 2.7:** *Examples of different types of RF coils used in MR experiments: (a) Surface RF coil, (b) Saddle RF coil and (c) Birdcage RF coil*

noise is proportional to the square root of the product of the temperature of the coil $T_c$, the bandwidth of the experiment $\Delta f$ and the effective resistance of the coil $R_{\text{eff}}$

$$noise \propto \sqrt{4kT_c\Delta f R_{\text{eff}}} \tag{2.36}$$

where the value of $R_{\text{eff}}$ is roughly the resistance of the imaging sample $R_{\text{sample}}$ for contemporary imaging experiments. As $R_{\text{sample}}$ is in turn proportional to the volume of region of the body from which the coil receives the signal then SNR decreases with an increase in imaging volume. For this reason, regions which are close to the coil elements show greatest SNR in a typical imaging experiment.

**Types of RF Coils**

The simplest and basic RF coil type is a surface coil as shown in Figure 2.7(a), which is generally used as a receive coil. Surface coils provide excellent SNR in the immediate vicinity of the coil elements but suffer from a limited *field of view* (FOV). Often surface coils can be used in conjunction with one another. In fact it is possible to use two surface coils to produce a quadrature field in the imaging region to mitigate for the aforementioned loss of signal. Typically the coils are designed in a way that the radius of the coil matches the depth to which imaging is required.

A saddle configuration as shown in Figure 2.7(b), on the other hand, uses a pair of coils wrapped on a cylindrical surface. They are made with straight line segments and circular arcs. The field produced is mainly perpendicular to the axis of the saddle and by choosing an appropriate axial length along with the appropriate opening angles for the arcs, the $x^2$, $y^2$ and $z^2$ moments of the $\mathbf{B}_1$ field can be cancelled to reduce $\mathbf{B}_1$-field inhomogeneities.

The Birdcage coil as illustrated in Figure 2.7(c) produces very good radial field homogeneity over the imaging volume and is therefore the most popular coil, particularly for brain imaging. A number of wires are arranged along the cylindrical axis in such a way as to generate a sinusoidal current variation around the circumference of the coil. A big advantage of this coil
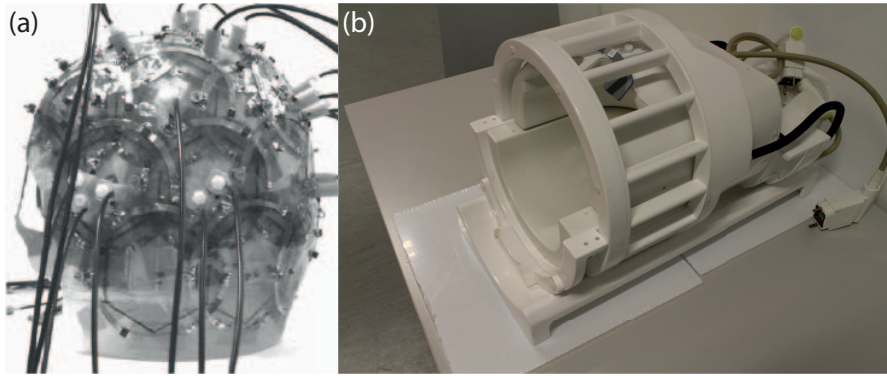
**Figure 2.8:** *A phased array coil composed of 32 individual small surface coils (a) mounted on a fiberglass helmet and (b) in an enclosure for patient safety.*

is the ease at which it facilitates the introduction of a second alternating signal in quadrature to produce a circularly polarized RF field with the advantage of increased sensitivity.

A phased array coil is composed of multiple small surface coils in order to increase coverage and maintain high SNR [33]. The main disadvantage of phased array coils are the requirement of multiple receiver channels pathways which increases both the computational and monetary cost of such coils. There is also a tendency for areas of low sensitivity between the crossover points of the individual coils. An example of an phased array coil revealing individual small surface coils mounted on a fiberglass helmet is shown in Figure 2.8(a)[I] whereas a 32 channel phased array coil in an enclosure is shown in Figure 2.8(b).

### 2.2.4 Gradient Coils

The gradients coils in a MR scanner is comprised of three mutually orthogonal coils, each of which encodes one spatial dimension. As mentioned above, very high currents have to be switched in a very short time in a typical imaging sequence. This often proves to be one of the limiting factors for the speed of the imaging process. Therefore, the gradient system is optimized to switch currents of several amperes on a sub-millisecond time frame. These large rates of change of magnetic field give rise to great electromotive forces, which render the mechanical design of the gradient coils complicated. These same large rates of change of electromotive forces are the reasons for the large audible noise during the measurements, which has an impact on patient comfort and few measurements, e.g. functional imaging involving hearing tasks.

In order to limit the interaction between the gradient coils and external structures & also to reduce the eddy current effects, a two coil system is often used which is known as *self-shielded gradient coils* [35]. Using self-shielded gradients, eddy current effects are reduced by a factor greater than 100 is obtained at the cost of increase in the power supply capability requirement

---

[I]Image source: [34].
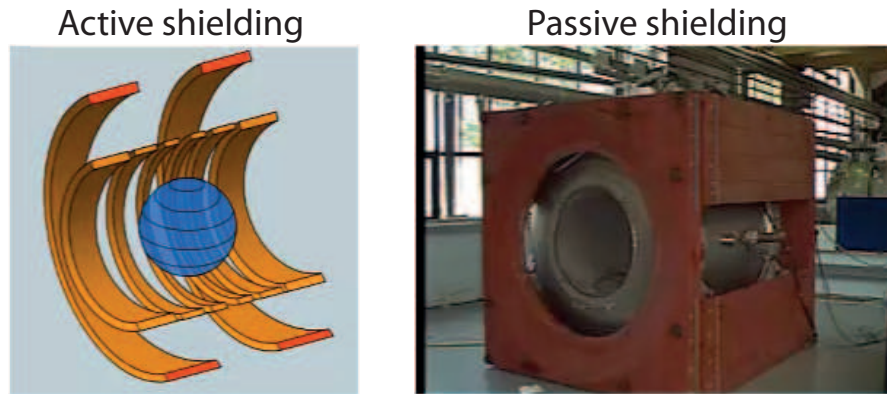
**Figure 2.9:** *Active and Passive shielding of MR scanner*

since in such setups, two coils are required for each gradient axis.

The essential parameters that characterize the performance of the gradients are the maximum achievable *gradient field strength* (mT/m), and the so-called *slew rate*. The slew rate defines the speed at which the gradients can be switched and is given in mT/m·ms. Maximum gradient strengths are normally in the range of 10 to 80 mT/m whereas maximum allowable slew rates are typically 150 mT/m·ms for a whole-body gradient insert and 400 mT/m·ms for a head-only gradient insert. The higher allowable limit for the head-only gradient insert comes because such a gradient insert is less probable to cause cardiac stimulation (see Section 2.2.5) due to lack of coverage. This brings us to the next important topic of discussion which is patient safety.

### 2.2.5 MR Safety

MRI as a non invasive imaging technique is relatively safe. Unlike Computed Tomography (CT) and X-rays, MRI uses non-ionizing radiation, where ionizing radiation may increase the risk of malignancy. At high magnetic field strengths ($\geq$ 7T), nausea, vertigo and a metallic taste are often experienced, particularly when moving the patient in and out of the magnet. Ferromagnetic objects experience a strong attraction when placed at the entrance of the magnet so missile hazards can possibly occur and cause harm to the patient. In addition, few body implants may move in the presence of the magnet. For this reasons, those who possess such implants are excluded from MRI studies so are the people with heart pacemakers.

It is desirable to minimize the area in which these issues occur. This is done by either active or passive shielding as shown in Figure 2.9. Active shielding is accomplished by the addition of a coil pair larger in radius than the interior of the scanner. The current in the shielding coil is opposite to the interior coils and lead to a large reduction in the field outside of the magnet. The disadvantage is that this can result in a reduction of the interior field and hence SNR.

Passive shielding or Ferromagnetic shielding can take the form of building iron into the walls of

the imaging site or including iron in the initial magnet design. The effects of iron on the main field must be calculated in order to properly cancel any main magnetic field disturbances.

### Magnetic Field Gradient Hazards

The fast switching of the currents in the gradient coils induce *eddy currents* in conductive materials in the rest of the scanner.  Conversely, the created eddy currents give rise to a magnetic eddy current field which interferes with the magnetic fields of the gradients.  In modern MR scanners, an automatic pre-emphasis adapts the gradient slopes on the fly in order to minimize eddy current induction. Another induced effect of the rapid gradient currents switching is biological in nature and can manifest in *Peripheral Nerve Stimulation* (PNS) and *Cardiac Stimulation* [36, 37]. PNS can result in a minor tingling sensation as well as muscle twitching but can also become very painful when the gradient magnetic field exposure exceeds the perception level from 50 to 100%. Cardiac stimulation manifests itself as a ventricular vibrations at high exposure levels. In order to avoid such occurrences, limits are set on PNS and cardiac stimulation levels ($< 1.2\ ^A/_m$) as well as on the induced current density ($< 0.4\ ^A/_{m^2}$).

A number of measures have also been introduced to reduce acoustic noise which can exceed the maximum limit of 95 dB for some imaging sequences. These include anti-phase noise in headphones, absorbing rubber foam, altering the coil structure to limit wire displacement while mounting the coil on a rubber surface. Ear protection must be worn at all times by the patient in the scanner in the form of ear plugs.

### Radio Frequency Field Hazards

To excite the spin system in a tissue of interest, enough RF power has to act on them. While emitting electromagnetic waves at RF frequencies in a body, a considerable fraction of the employed energy is absorbed by the tissue.  The deposited energy eventually heats up the tissue, which is possibly harmful if certain limits are exceeded. In order to quantify the energy deposit in the tissue, the *Specific Absorption Rate* (SAR) was introduced. It is defined as the power absorbed per mass of tissue and measured in units of watts per kilogram ($^W/_{kg}$) and calculated as

$$SAR = \int_{\text{body}} \frac{\sigma\, |\, \mathbf{E}\,(\mathbf{r})\,|^2}{\rho\,(\mathbf{r})} \, d\mathbf{r} \tag{2.37}$$

where $\sigma(\mathbf{r})$ is the sample's conductivity at point $\mathbf{r}$, $\mathbf{E}$ the electrical field and $\rho$ the density of the body. International authorities have defined a set of SAR limits for human bodies. There are both global (whole-body) and local limits, the latter defined for a small portion of localized tissue to avoid so-called hot-spots, where the electric field focuses.

Obviously, the integral in Equation (2.37) cannot be calculated for each patient. In lieu thereof, the scanner has a model of a human body which it uses, depending on the age, weight and

gender input from the operator of the scanner, to derive concrete limits. In fact, ensuring that these limits are maintained is one of the most safety-critical tasks of the MR machine.

# References

[24] E. M. Purcell, H. C. Torrey, and R. V. Pound. Resonance absorption by nuclear magnetic moments in a solid. *Phys. Rev.*, 69:37–38, Jan 1946.

[25] F. Bloch, W. W. Hansen, and Martin Packard. Nuclear induction. *Phys. Rev.*, 69:127–127, Feb 1946.

[26] F. Bloch. Nuclear induction. *Phys. Rev.*, 70:460–474, Oct 1946.

[27] F. Bloch, W. W. Hansen, and M. Packard. The nuclear induction experiment. *Phys. Rev.*, 70:474–485, Oct 1946.

[28] Mark E. Haacke, Robert W. Brown, Michael R. Thompson, and Ramesh Venkatesan. *Magnetic Resonance Imaging: Physical Principles and Sequence Design.* Wiley-Liss, June 1999.

[29] Matt A. Bernstein, Kevin F. King, and Xiaohong J. Zhou. *Handbook of MRI Pulse Sequences.* Academic Press, 1 edition, September 2004.

[30] J. Keeler. Understanding NMR spectroscopy, 2002.

[31] W. C. Dickinson. Dependence of the f19 nuclear resonance position on chemical compound. *Phys. Rev.*, 77:736–737, Mar 1950.

[32] W. G. Proctor and F. C. Yu. The dependence of a nuclear magnetic resonance frequency upon chemical compound. *Phys. Rev.*, 77:717–717, Mar 1950.

[33] P. B. Roemer, W. A. Edelstein, C. E. Hayes, S. P. Souza, and O. M. Mueller. The NMR phased array. *Magnetic Resonance in Medicine*, 16(2):192–225, 1990.

[34] G.C. Wiggins, C. Triantafyllou, A. Potthast, A. Reykowski, M. Nittka, and L.L. Wald. 32-channel 3 tesla receive-only phased-array head coil with soccer-ball element geometry. *Magnetic Resonance in Medicine*, 56(1):216–223, 2006.

[35] P.B. Roemer and J.S. Hickey. Self-shielded gradient coils for nuclear magnetic resonance imaging, April 12 1988. US Patent 4,737,716.

[36] J.P. Reilly. Peripheral nerve stimulation by induced electric currents: Exposure to time-varying magnetic fields. *Medical and Biological Engineering and Computing*, 27(2):101–110, 1989.

[37] C. L. G. Ham, J. M. L. Engels, G. T. van de Wiel, and A. Machielsen. Peripheral nerve stimulation during mri: Effects of high gradient amplitudes and switching rates. *Journal of Magnetic Resonance Imaging*, 7(5):933–937, 1997.

# 3 Magnetic Resonance Imaging

In the previous chapter, the global magnetic resonance signal from a sample was described. Magnetic resonance imaging aims at measuring the signal of a specific spin species in discretized sub-volumes of a sample, called *voxels* (for *volume pixels*). The fundamental techniques to conduct this in MRI are *slice selection, frequency encoding* and *phase encoding* which are collectively termed as *spatial encoding* and are described in this chapter. In order to facilitate the comprehension, some assumptions will be made: the application time of an RF-pulse is considered as infinitely short, there are no $B_0$ or $B_1$ inhomogeneities during transmission/reception and the sample is composed only of $^1$H spins.

First, the basics of spatial encoding in MRI and effect of the application of gradients and RF pulses on $k$-space sampling positions will be explained. Fundamental pulse sequence types used in routine MRI such as *spin echo* sequence and *gradient echo* sequence will be discussed next. Multi-echo variants of spin echo and gradient echo pulse sequences will be dealt very briefly and a detailed discussion of gradient echo based multi-echo sequence called *echo planar imaging* (EPI) sequence will be covered in Chapter 4. Different types of contrast mechanisms achievable are discussed next which have found a plethora of applications in clinical MRI studies. The chapter concludes with an introduction to *functional magnetic resonance imaging* (fMRI) which is the main area of application for acquisition methods developed during the preparation of this thesis.

## 3.1 Spatial Encoding

As has been shown in Section 2.1, the equation governing precession frequency of spins is the Larmor equation, $\omega_0 = \gamma \mathbf{B}_0$. Hence, in an NMR experiment a measurement of the frequency of precession of the magnetization gives information on the field experienced by that group of spins. To yield spatial information, this frequency information is exploited by manipulating the external magnetic field in a known way.

---

Only a brief introduction necessary to create the logical flow of this thesis is provided here. Interested readers are advised to refer [38] for an in-depth treatment of imaging pulse sequences.
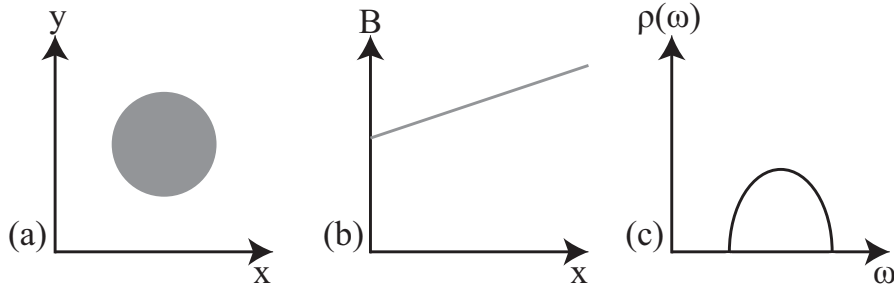
**Figure 3.1:** *Pictorial illustration of gradient encoding used to encode spins along x-axis. (a) xy-plane of a homogeneous cylindrical object, (b) Linear magnetic field gradient applied along the x-axis and (c) Plot of the number of spins at frequency ω*

Consider a linear field gradient $\mathbf{G}_x$ which increases along the $x$-axis, such that the magnetic field along $x$-axis is given by

$$\mathbf{B}_x = \left(B_{0x} + G_x x\right)\hat{x} \tag{3.1}$$

where $G_x$ is the gradient strength. This makes the Larmor equation take following form:

$$\omega\left(x\right) = \gamma\left(B_{0x} + G_x x\right) \tag{3.2}$$

or in its more general three dimensional form

$$\omega\left(\mathbf{r}\right) = \gamma\left(\mathbf{B}_0 + \mathbf{G}\cdot\mathbf{r}\right) \tag{3.3}$$

where $\mathbf{G}$ represents vector sum of the three linear gradient fields

$$\mathbf{G} = \begin{pmatrix} G_x \\ G_y \\ G_z \end{pmatrix} \tag{3.4}$$

By convention, $G_x$, $G_y$ and $G_z$ are linear magnetic field gradients along $x$-, $y$- and $z$-axis respectively. Under a linear field gradient along the $x$-axis, all the spins which lie at a particular value of x will precess at the same frequency. The FID from such a sample will contain components from each of the x values represented by the sample, and the frequency spectrum will therefore represent the number of spins that lie on each of these $x$-planes

$$\rho\left(\omega\right) = \rho\left(x\right) = \int \rho\left(x, y\right)\mathrm{d}y \tag{3.5}$$

where $\rho$ is the spin density of the sample.

The above argument can pictorially be represented as illustrated in Figure 3.1. This simple spectrum therefore gives the spatial information about the object being imaged along one

dimension.

With this understanding of how linear magnetic field gradient creates spatial frequency variation, different spatial encoding methods employed in MRI are discussed next.

### 3.1.1 Slice Selection

MRI falls under tomographical imaging approaches which means it is an approach to imaging by sections. In the case of MRI, these sections correspond to different imaging slices of a solid object (as a human body or a test phantom) which are achieved through a spatial encoding process known as *slice selection*. Conventionally, the slice-selection direction is considered to be along the $z$-axis. Without loss of generality, similar to Equation (3.2) the Larmor frequencies along the slice-selection direction after modulation due to superimposition of a linear magnetic field over the main magnetic field is given by

$$\omega(z) = \gamma \left( B_{0z} + zG_z \right) \tag{3.6}$$

As explained above, this means that a range of precession frequencies over the object along $\hat{z}$ is established. To excite just a subset of these frequencies, an RF pulse containing a certain range of frequencies $\Delta\omega$ around a base frequency $\omega_{\text{centre}}$ is employed, selecting a slice of thickness $\Delta z$:

$$\Delta z = \frac{\Delta\omega}{\gamma G_z} \tag{3.7}$$

Figure 3.2 illustrates this relationship. As it can be seen from Equation (3.7), the slice thickness can be adjusted by either changing the RF pulse bandwidth or the slice-selection gradient amplitude. Furthermore, the position of the slice along the gradient direction is defined by the RF pulse's center frequency $\omega_{\text{centre}}$. This kind of spins excitation by an RF pulse when accompanied by a slice selection gradient is also referred to as *selective excitation*. On the contrary, during *non-selective excitation*, RF pulse is applied in the absence of a gradient along the slice direction.

During the application of the RF pulse and the slice-selection gradient, the spins across the slice (through-plane) precess at different frequencies. They hence accumulate phase differences in addition to the intended selection-effect. To avoid resulting signal loss, the spin phases should be "rewound". To do so, a (slice refocusing) gradient with opposite polarity compared to $G_z$ is applied after the RF pulse (Figure 3.2), cancelling out the through-plane phase differences. In the first approximation, the slice refocusing gradient pulse can be assumed to have half the moment (i.e. the area under the gradient lobe, amplitude × duration assuming a rectangular shape) of the slice-selection gradient. Its exact area is however dependent on the RF pulse shape and can be determined analytically. In most imaging schemes, the slice refocusing gradient is performed concurrent to other imaging gradients and hence this does
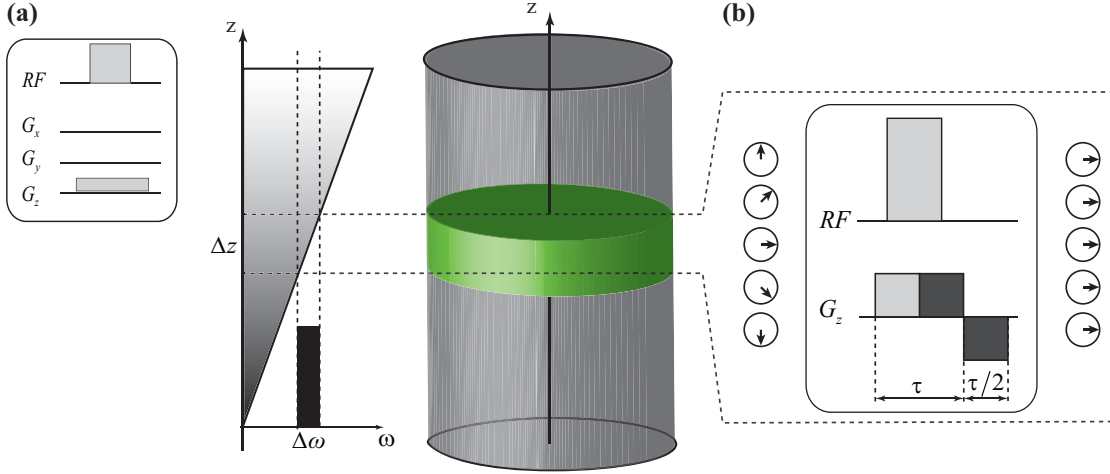
**Figure 3.2:** *Slice selection: (a) A magnetic field gradient is applied along the z-axis, adding a linear component to the existing $\mathbf{B}_0$ that varies linearly with the position on the z-axis. By applying a RF pulse of a particular bandwidth ($\Delta\omega$) and center frequency, a single slice of certain thickness along z-axis is excited. (b) However, at the end of the slice selective gradient, the signal through the slice thickness is slightly dephased. To compensate for this effect, a second gradient is applied along the same axis, with opposite polarity and half the area, which results in the complete rephasing of the signal.*

not have implications on the sequence timing.

To conclude, slice selection is the basis of most two dimensional imaging techniques and is still widely used. The rectangular slice profile shown in Figure 3.2, as defined by the bandwidth of the RF pulse is the ideal scenario. In reality, the sharp cutoff (boxcar shape) at the boundary in the Fourier domain would require an infinitely long sinc RF pulse in the time domain, which obviously is impractical. This factor constrains the perfection of the slice profile and the minimum slice thickness. Thus, three dimensional acquisition schemes (Section 3.1.4) are typically used if very thin slices are desired.

### 3.1.2 Frequency Encoding

Similar to the discussion at the beginning of Section 3.1, a spatial encoding can be established by applying a linear magnetic gradient during the signal sampling. To follow the usual nomenclature, the direction of the readout gradient $G_x$ is defined to be along the $x$-axis. Due to the applied gradient field, the precession frequencies differ along the readout direction during the sampling and the received signal can be expressed as:

$$s(t) = \int_x \rho(x) e^{-i\gamma G_x x t} \mathrm{d}x \tag{3.8}$$

This is equivalent to the Fourier transformation of a projection of the spin densities on the readout axis, the same as described in Figure 3.1. The frequency encoding step is described
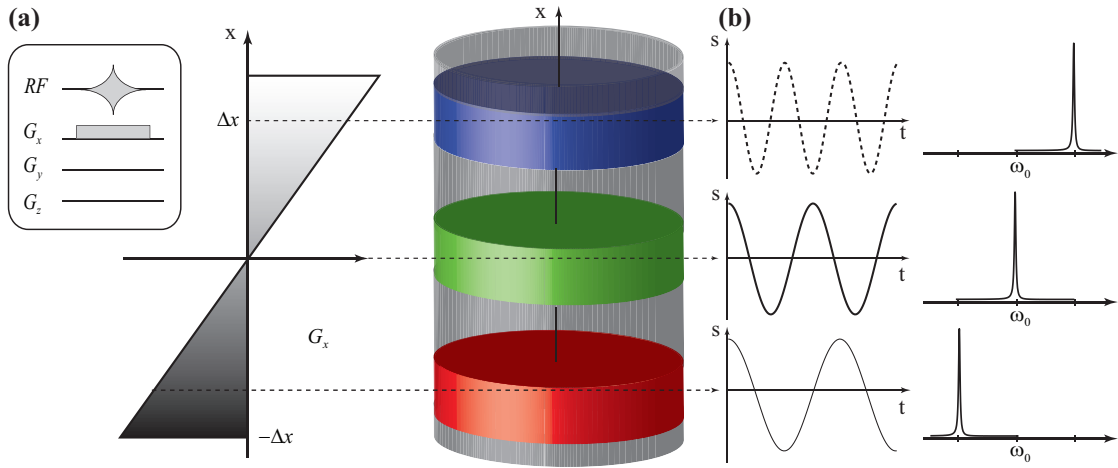
**Figure 3.3:** *Frequency encoding: (a) A magnetic field gradient $G_x$ is applied along the x-axis, adding a linear component to the existing $B_0$ varying linearly with the position on the x-axis. Therefore, nuclei positioned at the center $x = 0$ precess at the Larmor frequency $\omega_0$ and nuclei positioned at $x = \Delta x$ experience a precession frequency equal to $\omega(\Delta x) = \omega_0 + \gamma G_x \cdot \Delta x$, whereas those at $x = -\Delta x$ experience a precession frequency equal to $\omega(-\Delta x) = \omega_0 - \gamma G_x \cdot \Delta x$. (b) The frequency of the acquired signal is linearly proportional to the position of the signal origin along the gradient axis. After Fourier transformation of the signal, it results in the projection of the proton density of the sample along the frequency encoding gradient direction.*

through pictorial illustration in Figure 3.3.

### 3.1.3 Phase Encoding

At this point, we can select a slice and resolve one spatial dimension. A second spatial dimension is encoded in the phases of the spins. A gradient $G_y$ is applied before the frequency encoded readout for a time $\Delta t_y$ along the phase-encoding direction, i.e. along the $y$-axis to follow the nomenclature. For the duration of this gradient, the spins precess at different frequencies along this direction. By the time the gradient is switched off, the spins accumulate a certain phase depending on their position in space. This is illustrated in Figure 3.4 and mathematically expressed as

$$\Delta\phi(y) = \gamma G_y \Delta t_y y \tag{3.9}$$

Although either $G_y$ or $\Delta t_y$ (or both) could be varied to achieve different phase encoding steps, only the amplitude is typically varied. One way of interpreting this is that the phases of spins along $y$-axis now contain information about the frequency differences during the application of $G_y$. This perspective shows the isomorphism between frequency and phase encoding, which is also reflected in the mathematical description of the acquired signal:

$$s(t) = \int_y \int_x \rho(x,y)\, e^{-i\gamma(G_x x t + G_y \Delta t_y y)}\, \mathrm{d}x\mathrm{d}y \tag{3.10}$$

31
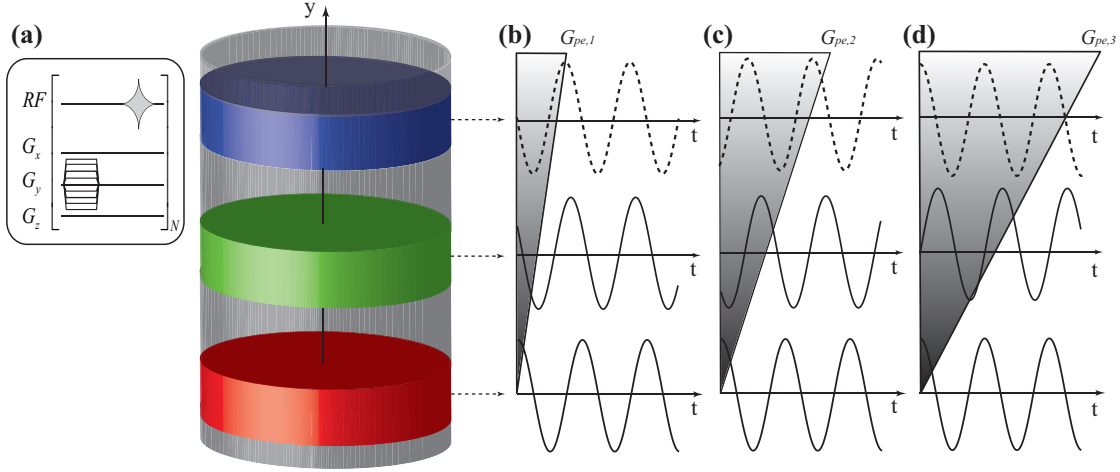
**Figure 3.4:** *Phase encoding: (a) A magnetic field gradient $G_y$ is applied along the y-axis, adding a linear component to the existing $B_0$ varying linearly with the position on the y-axis. (b) The nuclei in the sample experience slightly different external magnetic field which results, at the end of application of the phase encoding gradient, in a linear dephasing proportional to the position along the y-axis. (c-d) The experiment must be repeated with different phase encoding gradient amplitudes (also called phase encoding steps).*

### 3.1.4 Three Dimensional Imaging

As stated in Section 3.1.1, slice selection in two dimensional imaging approaches have significant limitations due to suboptimal slice profile and slice thickness. Conversely, the phase encoding approach is not restricted to only one dimension. Following the same rationale, a second dimension can be encoded by applying an additional phase encoding gradient $G_{y2}$ for a time duration $\Delta t_y$, allowing to omit the slice selection event. Therefore, the whole imaging volume has to be excited either using a thick slice (in that case called a *slab*) or with a non-selective excitation pulse. The received signal is Fourier-encoded in three dimensions:

$$s(t) = \int_z \int_y \int_x \rho(x, y, z) \, e^{-i\gamma(G_x t x + G_y \Delta t_y y + G_{y2} \Delta t_{y2} z)} \, \mathrm{d}x \mathrm{d}y \mathrm{d}z \tag{3.11}$$

Employing frequency encoding together with phase encoding in two dimensions is called three dimensional (3D) imaging since each sampled point in the time domain holds information of the whole 3D volume. Here, the $k$-space has to be traversed also in the third dimension, discretized in $N_{y2}$ phase encoding steps. Consequently, the scan time is increased by a factor of $N_{y2}$. The signal, stemming from the whole volume, is however also increased by a factor of $\sqrt{N_{y2}}$ with respect to the 2D case.
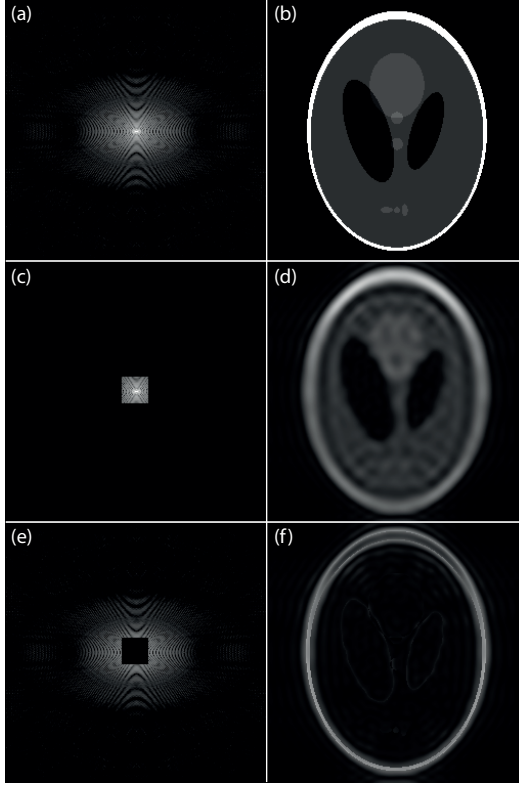
**Figure 3.5:** *(a) k-space representation of a Shepp Logan phantom with* $256 \times 256$ *pixels matrix size; (b) image of the Shepp Logan phantom simulated using MATLAB; (c) only the central* $26 \times 26$ *k-space is preserved while masking outer region values to 0; (d) image obtained after Fourier transformation of the k-space represented in c; (e) the central* $26 \times 26$ *k-space masked to 0 while preserving outer k-space; (f) image obtained after Fourier transformation of the k-space represented in e. Thus, demonstrating that the central region of the k-space (low wave numbers) contains the contrast information whereas the outer region of the k-space (high wave numbers) contains the edge information of the image.*

### 3.1.5   k-Space

The equations describing the received signal, e.g. Equation (3.11) in the case of 3D imaging, are not very intuitive. Therefore, a very helpful notion of the spatial-frequency space in which the MR signal is sampled, has been introduced: the so-called *k-space*, wherein the spatial encoding terms are treated as wave numbers ($k$) in the Fourier space [39, 40]. At each point in time, the $k$-space coordinate is given by

$$\mathbf{k}(t) = \gamma \int_0^t \mathbf{G}(t') \, \mathrm{d}t' \tag{3.12}$$

Where $T$ is the total duration of applied linear gradient **G**. The Fourier-inverse of the $k$-space is the image of the sampled object, represented in the *image space*. As an example, an image of a Shepp Logan phantom simulated in MATLAB and its corresponding $k$-space representation are shown in Figure 3.5(a-b). Noteworthy, the low wave numbers situated in the center of $k$-space hold the low-frequency image information (the contrast) describing majority of the image features (Figure 3.5(c-d)), whereas the high wave numbers situated towards the boundaries of $k$-space hold the high-frequency image information which define the edge information of the image (Figure 3.5(e-f)).

The signal equation in $k$-space terms becomes in the 3D case

$$s(t) = \int_z \int_y \int_x \rho(x, y, z) \, e^{-i2\pi(xk_x(t) + yk_y(t) + zk_z(t))} \, \mathrm{d}x\mathrm{d}y\mathrm{d}z \tag{3.13}$$

According to the theory of Fourier transformations, an infinite amount of wave numbers are necessary to represent a given function in Fourier space. In reality, the $k$-space cannot be sampled to infinity, not only due to obvious scan-time arguments, but also because the MR signal would decay due to relaxation processes described in Section 2.1.6. The $k$-space is rather cut at a certain distance around the $k$-space center. This can be mathematically expressed by multiplication with a boxcar function in Fourier space, which, according to the Fourier theory, translates to a convolution with a sinc function in image space. This has a major implication: it means that the object can never be perfectly sampled; there will always be a slight blurring in the image stemming from the sinc-convolution which is called the *point spread function* (PSF) of the acquisition. Note that relaxation is still neglected in this consideration. In reality, the sampled signal changes during the acquisition due to $T_2/T_2^*$ decay during the acquisition and also due to $T_1$ relaxation and saturation effects throughout the different excitations. This worsens the PSF additionally.

Finally, not only a finite section of the $k$-space is sampled, but also only at discrete time points. Continuous sampling, as suggested by the formulas above, is technically not feasible. Mathematically, the discrete sampling of a signal is expressed as a multiplication with a series of Dirac-delta functions forming a "comb" of sampling points. The time interval between successively sampled $k$-space points is called *dwell time*:

$$f_{\text{sampling}}(t) = \sum_{n=0}^{N} \delta(t - n t_{\text{dwell}}) \tag{3.14}$$

Considering $k$-space sampling along a single dimension, we get

$$s(t)_{\text{discrete}} = s(t) \sum_{n=-N/2}^{N/2} \delta(k - n\Delta k) \tag{3.15}$$

After translating into image space,

$$\rho(x)_{\text{discrete}} = \rho(x) \sum_{n=0}^{N} \delta\left(\frac{x-n}{\Delta k}\right) \tag{3.16}$$

The invariance of the Dirac-delta function implies a periodicity of the image in image space, i.e. the image is periodically repeated at an interval $\frac{1}{\Delta k}$. The distance between two $k$-space points, $\Delta k$, thus defines the *field of view* (FOV) in which an object can be depicted without aliasing:

$$\text{FOV} = N\Delta k = \frac{1}{\Delta k} \tag{3.17}$$

Inserting the definition of $k$, this implies

$$\Delta t_{\text{dwell}} = \frac{1}{\gamma G \, \text{FOV}} \tag{3.18}$$

Equation (3.18) hence defines the minimum dwell time to sample a certain FOV in $k$-space. This is equivalent to the so-called *Nyquist criterion* known from Fourier theory. In practice, we obtain $k$-space values of $s(k_x, k_y)$ at discrete grid by sampling the signal $s$ at appropriate time intervals $\Delta t_{\text{dwell}}$ and for appropriate phase-encoding gradients $nG_y$ with $n = \frac{-N_y}{2}, \ldots, \frac{N_y}{2}$. The discrete time-domain image $S$ is obtained as a discrete inverse Fourier transform

$$S(x, y) = \frac{1}{N_x N_y} \sum_{k_x = \frac{-N_x}{2}}^{\frac{N_x}{2}} \sum_{k_y = \frac{-N_y}{2}}^{\frac{N_y}{2}} s(k_x, k_y) \, e^{i(k_x x + k_y y)} \tag{3.19}$$

where $N_x$ and $N_y$ are the number of sampling points along read- and phase-directions, respectively.

### 3.1.6 Effects of gradients and RF pulses on $k$-space sampling position

Application of gradients on different gradient axes, their amplitude, polarities as well as axis along which RF pulses are applied have direct implication on the sampling positions of the $k$-space. Figure 3.6 exemplifies this relationship between gradient/RF pulses and $k$-space sampling. As the figure illustrates, selective excitation flips the magnetization of a single slice of the sample in $xy$-plane. The phase-encoding gradient amplitude decides the $k$-space line to be sampled during the acquisition. The inversion pulse acts like a mirror placed on one of the $k$-space axes depending on the axis along which inversion pulse is applied, reflecting the $k$-space sampling position around that axis. A negative gradient applied before the frequency encoding gradient sets the initial sample position to the left edge of the $k$-space, and thus the center $k$-space point acquisition will coincide with the maximum echo amplitude. The positive gradient applied along $x$-axis moves the successive $k$-space sample positions from the left edge to the right edge as shown in the figure by arrow heads. Finally, every spatial encoding gradient is rewound at the end of the acquisition, moving the sampling position to the center of the $k$-space.

Different $k$-space sampling schemes are exploited to cover the entire $k$-space giving way to a very active and prolific research arena for MRI, namely the pulse sequence designs which is the subject of discussion for the next section.

## 3.2 The Basic Pulse Sequences

The encoding modules described in the previous section can be used in several combinations to encode the three spatial dimensions of an object. The most common procedure consists of
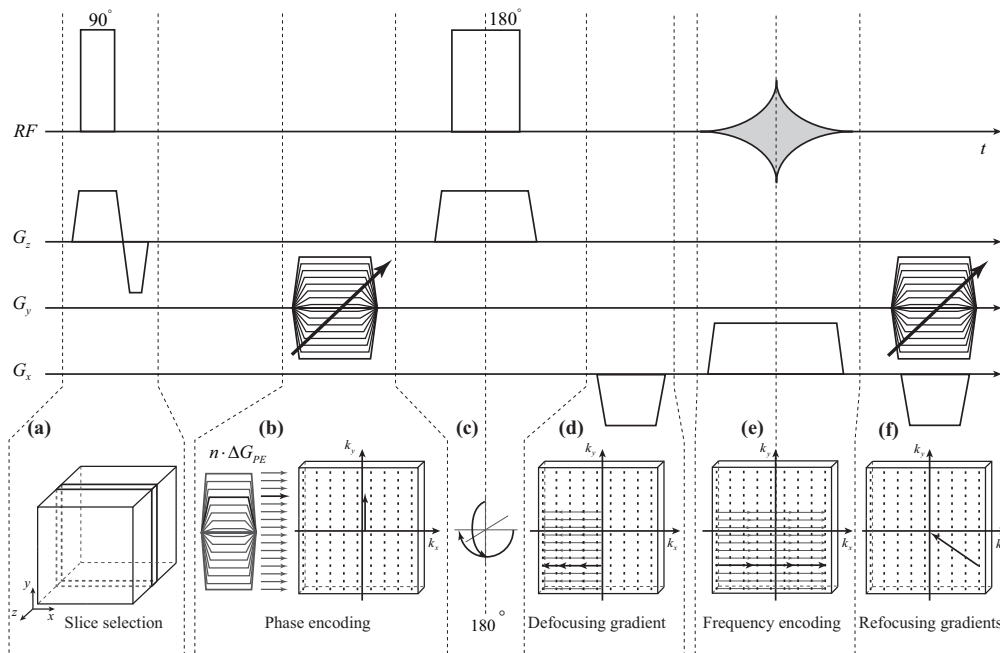
**Figure 3.6:** *Effects of different gradients and RF pulses on $k$-space sampling positions: (a) selective excitation selects a slice, (b) phase-encoding gradient amplitude decides the $k$-space line to be sampled, (c) 180° RF pulse reflects the sampling position about the axis around which RF pulse is applied, (d) defocusing gradient shifts the sampling position to the edge of the $k$-space, (e) frequency-encoding gradient shifts successive sampling positions from one edge to the opposite and finally (f) refocusing gradient shifts the sampling position back to the center of the $k$-space.*
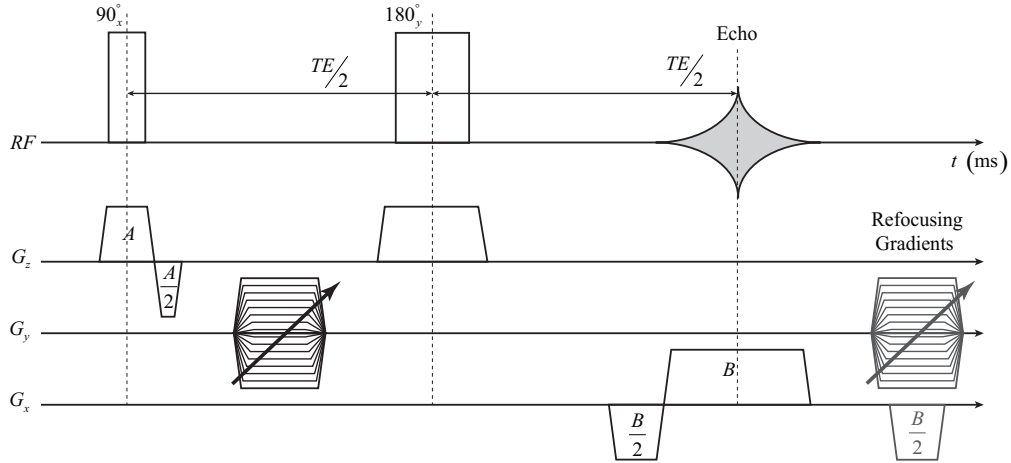
**Figure 3.7:** *Pulse sequence diagram for a spin echo sequence. Following selective excitation with a $90°$ RF pulse, a second $180°$ refocusing RF pulse is applied after a time period $TE/2$ to refocus the dephased magnetization in the $xy$-plane. The delay between the two RF pulses is used to apply the phase encoding gradient. The sequence is repeated with different gradient amplitudes, to sample the entire $k$-space. To encode the last spatial direction, frequency encoding is performed during the signal acquisition. In order to improve the stability of the received signal from one repetition to the next, every gradient must be compensated after the end of each repetition period by applying refocusing gradients. Slice selection is already designed with null gradient moment and thus does not need refocusing gradient.*

making use of all three of them: first selecting a slice during RF excitation and then encoding 2D spatial space with the phase-encoding and the frequency-encoding gradients. This ordered combination of RF pulses, spatial encoding gradients in combination with a readout module makes a *pulse sequence* in MRI. The readout module is used to read an *echo* arising at a time known as *echo time* (TE) in a pulse sequence. An echo differs from an FID in the appearance: The echo is symmetric, i.e. it rises exponentially and reaches its maximum, then decreases exponentially just like an FID.

This section introduces the basic pulse sequences for two separate classes: *spin echo* and *gradient echo* sequences. There are two ways to create an echo from an FID generated after an RF pulse: with a succession of RF-pulse as in case of a spin echo sequence or by applying two successive gradients with opposed polarities as in case of a gradient echo sequence. Most of the other imaging pulse sequences used in MRI are derived out of these two basic types of pulse sequences.

### 3.2.1  Spin Echo Sequence

The spin echo (SE) sequence uses RF pulses to create an echo as shown in Figure 3.7 [41]. After excitation RF pulse (e.g. a $90°$ pulse applied along the $x$-axis), the magnetization is precessing freely in the $xy$-plane and concurrently loses coherence rapidly due to $T_2^*$ relaxation. After a
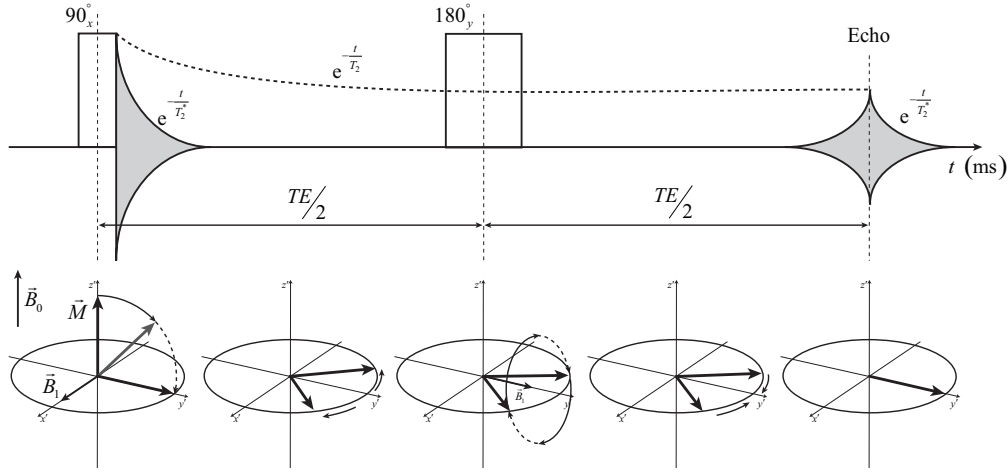
**Figure 3.8:** *Spin echo formation: A 90° excitation pulse is applied, flipping the magnetization in the $xy$-plane and generating a FID. The signal starts to dephase with a time constant $T_2^*$. Nuclei precess at different Larmor frequencies due to differences in the magnetic fields experiences by them due to local magnetic field inhomogeneities. Applying an inversion pulse after a time TE/2 has an effect of rotating the spins about the y-axis. However, the direction of spin precession and speed remains unchanged, rephasing the spins to generate an echo after an additional delay of period TE/2*

few tens of milliseconds, the signal decays considerably, making any acquisition impossible. However, the system's coherence can be rebuilt by applying a refocusing RF pulse (i.e. a 180° pulse applied along $y$-axis) after a delay $\tau$ following the excitation pulse. After an additional delay of equal duration $\tau$, an echo is formed. The addition of two delays i.e. $2\tau$ defines the echo time. The SE formation is explained in a pictorial view in Figure 3.8. The spins dephase at different frequencies during the first delay $\tau$, after the 180° pulse these spins continue to process with the same individual frequencies but in the opposite direction resulting in the beginning of refocusing process and after an equal time period $\tau$, an echo is formed. The SE is exponentially attenuated with a time constant $T_2$ and not $T_2^*$ since magnetic field inhomogeneities effects are cancelled out after application of the refocusing RF pulse.

$$S_{\text{SE}}(\text{TE}) = S(0)\, e^{-\frac{\text{TE}}{T_2}} \tag{3.20}$$

where $S_{\text{SE}}(\text{TE})$ is the maximum signal amplitude of the echo ($t = \text{TE}$) and $S(0)$ is the maximum signal amplitude of the initial FID.

The SE sequence has the additional advantage to leave enough time to apply the spatial encoding gradients. As explained in Section 3.1, slice-select gradient ($G_z$) is used to perform slice encoding during both RF-pulses. Phase encoding gradient ($G_y$) is applied during the first half of the echo time period (i.e. between the two RF pulses) to optimize the time duration of the pulse sequence and hence effectively the total scan time. Finally, the echo formed at time $\text{TE} = 2\tau$ is acquired with the application of a frequency encoding gradient. This
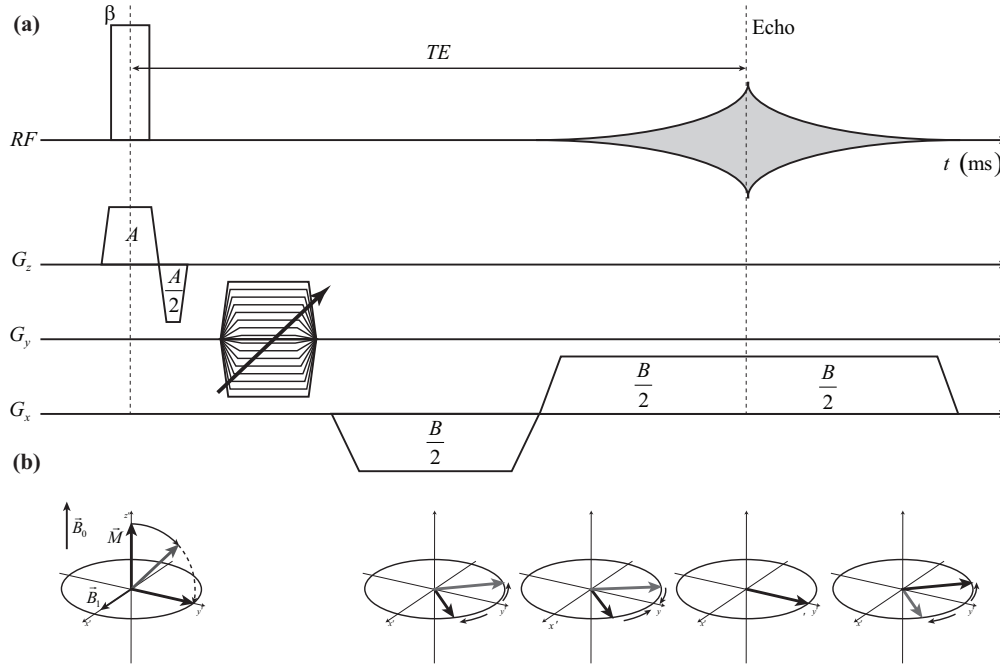
**Figure 3.9:** *Pulse sequence diagram for a gradient echo sequence. Following a selective excitation using a small flip angle RF pulse, phase encoding gradient is applied. The echo is generated by a fast dephasing and rephasing of the signal using two opposite polarity gradients.*

scheme of RF pulses and gradients play-out is repeated with different phase-encoding gradient amplitudes during every repetition to acquire the entire $k$-space and image is reconstructed by Fourier transformation of this acquired $k$-space. The time duration between these successive repetitions i.e. time duration between the center of one excitation RF pulse to the center of the next excitation RF pulse is known as *time to repeat* (TR) and, together with TE and flip angle (FA) it plays an important role in determining final contrast (see Section 3.2.5) of the image.

### 3.2.2 Gradient Echo Sequence

The gradient echo (GE) sequence makes use of a pair of gradients with opposite polarities to first dephase and then rephase the signal, unlike SE sequence described above which makes use of a refocusing RF pulse to refocus the dephased spins to create an echo. In GE sequence, the signal amplitude and the echo decays exponentially with the time constant $T_2^*$. Therefore, a gradient echo is usually applied with very short echo time on the order of a millisecond (e.g. 1-10 ms for *in-vivo* experiments), and with a low flip angle in the case of fast imaging [42].

The spatial encoding in the case of GE follows the same principles as for the SE, i.e. a slice select gradient and excitation RF pulse followed by the phase encoding gradients. The echo is generated by first applying a negative gradient (dephasing gradient) on the read-out axis to dephase the magnetization, rapidly followed by application of a positive gradient with twice the area of the negative gradient. The magnetization is refocused during application of the

39
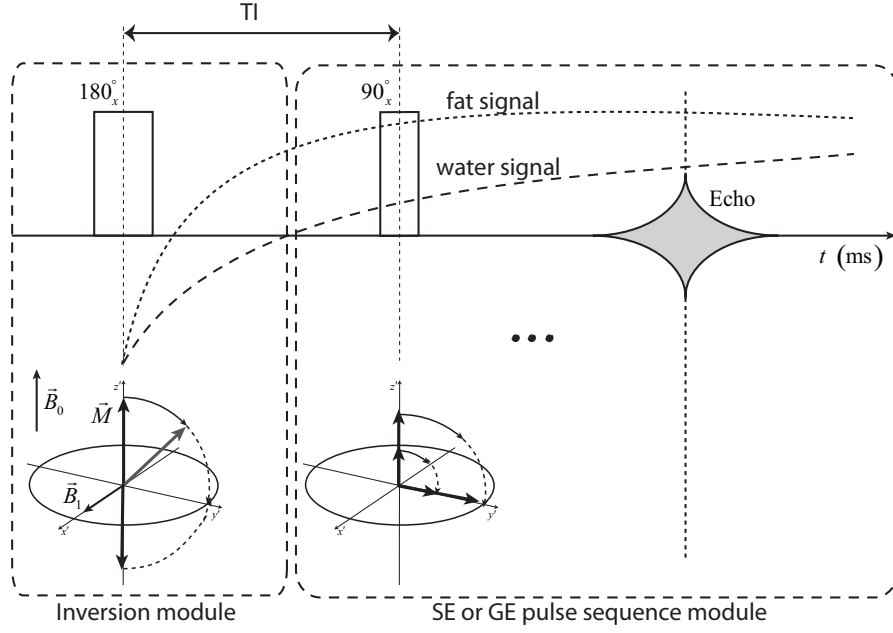
**Figure 3.10:** *Spatial encoding for an inversion recovery sequence. Initially, a* $180°$ *inversion RF pulse inverts the longitudinal magnetization. After time duration TI, any imaging pulse sequence is played to measure the echo and exploit $T_1$-contrast developed due to differences in the $T_1$ values of different tissues.*

positive gradient and creates an echo with its amplitude exponentially attenuated with a time constant $T_2^*$ (Figure 3.9):

$$S_{\text{GE}}(\text{TE}) = S(0) \, e^{-\frac{\text{TE}}{T_2^*}} \tag{3.21}$$

where $S_{\text{GE}}(\text{TE})$ is the maximum signal amplitude of the echo ($t = \text{TE}$) and $S(0)$ is the maximum signal amplitude of the initial FID. During the application of the positive gradient, analog to digital converter (ADC) module is turned on to sample the echo formed and thus to acquire the signal.

### 3.2.3   Inversion Recovery Sequence

As will be seen later in Section 3.2.5, differences between intrinsic characteristics, such as $T_1$ and $T_2$ time constants, among different tissues can be used to generate distinctive image contrasts in MRI. Inversion recovery sequence is used to obtain $T_1$-weighted images more effectively by preparing the longitudinal magnetization using an inversion recovery module before reading the signal (Figure 3.10). This module is simply composed of an inversion pulse that flips the longitudinal magnetization to point along the $-z$-axis, followed by a delay time in which a gradient spoiling (i.e. forcing any residual transverse magnetization to dephase by application of strong gradients) can be executed. During this delay time TI (*inversion time*),

the longitudinal magnetization in the different tissues recovers according to their respective $T_1$ relaxation time constants. Before the next inversion pulse can be played out, the longitudinal magnetization has to return to equilibrium, which results in comparatively long scan times. This is the reason why the readout is usually conducted by means of a multi-echo sequence (Section 3.2.4), sampling several $k$-space lines per TR. Assuming an infinitely long TR, the longitudinal magnetization at time $t$ after the inversion pulse is given by

$$M_z\,(\mathrm{TI}) = M_0 \left( 1 - (1 - \cos\theta_{\mathrm{inv}})\, e^{-t/T_1} \right) \tag{3.22}$$

By substituting $\theta_{\mathrm{inv}} = 180°$ we get

$$M_z\,(\mathrm{TI}) = M_0 \left( 1 - 2 e^{-\mathrm{TI}/T_1} \right) \tag{3.23}$$

Importantly, the magnetization is nulled at the inversion time $\mathrm{TI}_{\mathrm{null}}$

$$\mathrm{TI}_{\mathrm{null}} = T_1 \ln 2 \qquad \mathrm{for} \quad \mathrm{TR} \to \infty \tag{3.24}$$

Signal nulling can be used to suppress unwanted signals in an image, e.g. from the cerebral spinal fluid.

### 3.2.4   Multi-echo sequences

The MR signal can be propagated over several tens of millisecond by generating multiple successive echoes with multiple RF pulses or gradients. Moreover, each echo can be used to sample a different line of $k$-space, thus reducing the total number of sequence repetitions by the number of echoes created within the so-called *echo train length* (ETL). Two techniques are presented in this section: first, the *fast spin echo* (FSE) sequence, which is based on a repetition of 180° pulses to generate successive echoes. Second, the *echo planar imaging* (EPI) sequence, which is based on a repetition of gradient echoes.

**Fast Spin Echo Sequence**

In SE sequences using typical echo times, there is still considerable amount of magnetization left after the spin echo is read. FSE makes use of this fact; instead of refocusing the signal just once, a train of refocusing pulses is employed to produce multiple spin echoes [43, 44]. Thereby, each echo is distinctively phase encoded, so that multiple $k$-space lines can be acquired after a single excitation pulse. This allows for a significant reduction of the measurement time, one of the biggest advantage of FSE sequence over SE sequence.

FSE can be employed either with a 2D or a 3D acquisition scheme. Selective excitations are typically used, whereas the refocusing pulses are non-selective. Using 180° refocusing pulses, however, greatly constraints the achievable ETL due to SAR limitations (see Section 2.2.5), particularly at ultra-high field strengths ($\geq$ 7T).

**Figure 3.11:** *(a) Pulse sequence diagram for gradient echo based echo planar imaging. The time duration from center of the excitation RF pulse to the center of the echo train length defines TE. The decaying envelope of multiple echoes generated is shown on the RF axis. (b-e) k-space sampling scheme that is achieved with EPI sequence. Notice the zigzag nature of the sampling resulting from bipolar readout gradients applied to form train of echoes.*
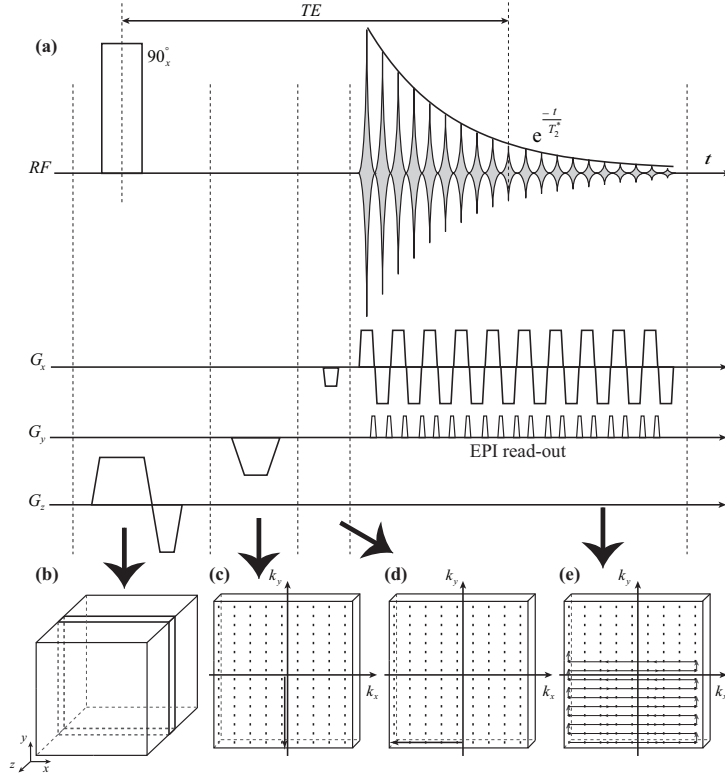
### Echo Planar Imaging Sequence

EPI is one of the fastest acquisition schemes available in MRI. Its temporal performance enables many advanced imaging techniques like fMRI [45, 46], diffusion [47–49] and perfusion imaging [50]. First proposed by Peter Mansfield in the late 1970s [51], it was not usable in practice for a long time, mostly due to its demanding hardware requirements. After a slice-selective excitation, multiple (or all) $k$-space lines are traversed in a zigzag trajectory as depicted in Figure 3.11(e). To do so, a train of bipolar gradient pulses is employed, which can be executed very fast by modern gradient systems. Short gradient "blips" are played out in phase encoding direction between the readouts to move to the next $k$-space line. As in all gradient echo based sequences, the signal is subject to $T_2^*$ decay during the EPI readout. While there is also a spin-echo variant of EPI (see Figure 4.1), Figure 3.11(a) depicts the sequence diagram for the classical gradient-echo EPI.

As the signal decays during the $k$-space traversal, the maximum extent of the $k$-space matrix is limited. With current hardware, one 2D image with a matrix of 128x128 pixels can be sampled in a few tens of milliseconds. Bearing this in mind, it becomes clear that high readout bandwidths have to be employed, leading to very swift gradient switching which explains the high demand on the hardware associated with EPI sequence. The optimal flip angle ($\theta_E$) to attain maximal transverse magnetization under steady state conditions is given by a

relationship known as *Ernst angle relationship*:

$$\theta_E = \arccos\left(e^{-\frac{TR}{T_1}}\right) \tag{3.25}$$

Where $\theta_E$ is the so called *Ernst angle*. TR of EPI is generally much longer than that of a conventional gradient echo pulse sequence due to the use of an ETL as opposed to a single echo sampling. Accordingly, due to the longer TR, flip angle of the excitation pulse for 2D EPI sequence is typically set to 90° to maximize the SNR. To avoid additional $T_1$-weighting, the interval to the re-acquisition of the same slice has to be sufficiently long; usually, a stack of many slices ($\sim 20$) is acquired to sample the image volume, which provides sufficiently long inter-slice intervals. RF pulses are not perfect and a crosstalk between slices, i.e. unwanted excitation of an adjacent slice, cannot be avoided. Therefore, the stack of slices is typically acquired in an interleaved fashion, i.e. adjacent slices are acquired with a maximal temporal distance.

A detailed description of different variants of EPI along with various artifacts and their causes/remedies are discussed in detail in Chapter 4.

### 3.2.5  Image Contrast

Unlike many other medical imaging modalities, the contrast manipulation during an MRI acquisition is highly flexible and dependent upon few parameters prescribed during the acquisition. Basic contrast manipulation parameters at the disposal of an MRI exam include TR, TE, TI if using an inversion recovery sequence and the excitation flip angle ($\theta$). For instance given a standard spin echo MRI sequence, one can increase the $\begin{pmatrix} T_1 \\ T_2 \\ \rho \end{pmatrix}$ weighting by using TR values $\begin{pmatrix} \leq T_1 \\ \gg T_1 \\ \gg T_1 \end{pmatrix}$ and TE values $\begin{pmatrix} \ll T_2 \\ \geq T_2 \\ \ll T_2 \end{pmatrix}$. The actual contrast $C = |S_A - S_B|$ achieved between signals $S_A$ and $S_B$, will depend on the intrinsic $T_1$ and $T_2$ of the two tissues, and on the TR and TE parameters used (Figure 3.12). Since contrast manipulation is one of the greatest strength of MRI over many other existing imaging modalities, discussion of MRI is incomplete without an overview of key approaches to achieve desired contrast.

#### $T_2$ Contrast

$T_2$ weighting is achieved using a spin echo sequence with "longish" TE (to magnify $T_2$ decay differences) and long TR (to minimize $T_1$ recovery differences). The SE sequence is a routine clinical echo sequence as it is less susceptible to inhomogeneities in the magnetic field. SE MRI is particularly well suited to edema as they are sensitive to water content (edema is characterized by increased water content).
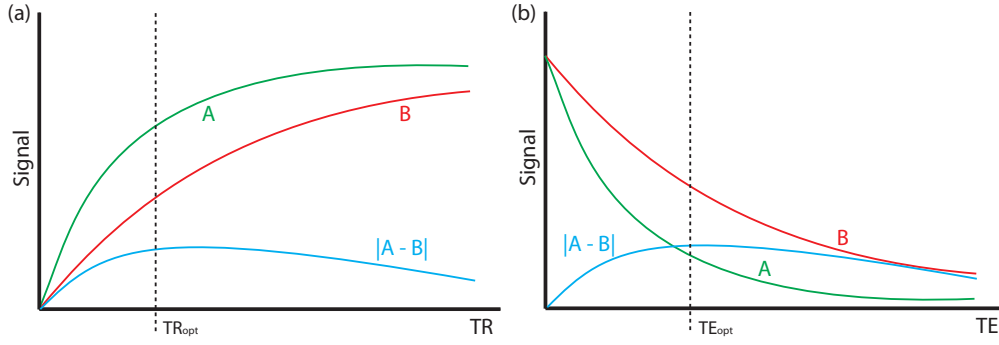
**Figure 3.12:** *(a) $T_1$ recovery curves for two hypothetical tissues A and B are shown in green and red whereas the $T_1$ contrast $C = | S_A - S_B |$ achieved between two signals $S_A$ and $S_B$ is shown in blue. The maximum contrast can be obtained at* $\text{TR} = \text{TR}_{\text{opt}}$ *as shown by dotted line. (b) Similarly, the $T_2$ contrast developed due to difference in $T_2$ decay curves is maximum at* $\text{TE} = \text{TE}_{\text{opt}}$.

### $T_2^*$ Contrast

$T_2^*$ weighting is achieved using a gradient echo sequence with not-so-long TE (to highlight $T_2^*$ effects) and long TR (to minimize $T_1$ differences). Unlike SE sequence, the GE sequence does not have the extra refocusing pulse and so it will be subject to the additional dephasing due to magnetic field inhomogeneities that will combine with the slower $T_2$ decay. In particular, manipulation of $T_2^*$ contrast depends on susceptibility differences between different tissue structures. GE sequences are more prone to susceptibility losses at air/tissue boundaries, but can increase contrast for certain types of anatomical details e.g. venous blood possessing paramagnetic behavior.

### $T_1$ Contrast

$T_1$ weighting is achieved using either a gradient echo or a spin echo sequence but with a short TE (to make differences in $T_2^*$ irrelevant) and short TR (to highlight $T_1$ recovery differences). Due to short TR, sequences used to achieve $T_1$-contrast can be run relatively fast allowing the collection of high resolution 3D datasets. The $T_1$ weighting can be increased with the use of an inversion pulse. The TI is the critical parameter in this case. The inversion is followed with either a gradient or a spin echo sequence.

### $\rho$ Contrast

$\rho$ weighting or also known as *proton density weighting* is essentially a spatial map of spin densities. Proton density weighting is achieved when all the other contrast mechanisms are suppressed i.e. contrasts due to $T_2^*$, $T_2$ and $T_1$ weighting should be minimum or ideally absent. To do so, one may use a spin echo sequence which is naturally $T_2^*$ free or a gradient echo sequence, both with short TE (to minimize $T_2$ contrast) and long TR (to minimize $T_1$ contrast).
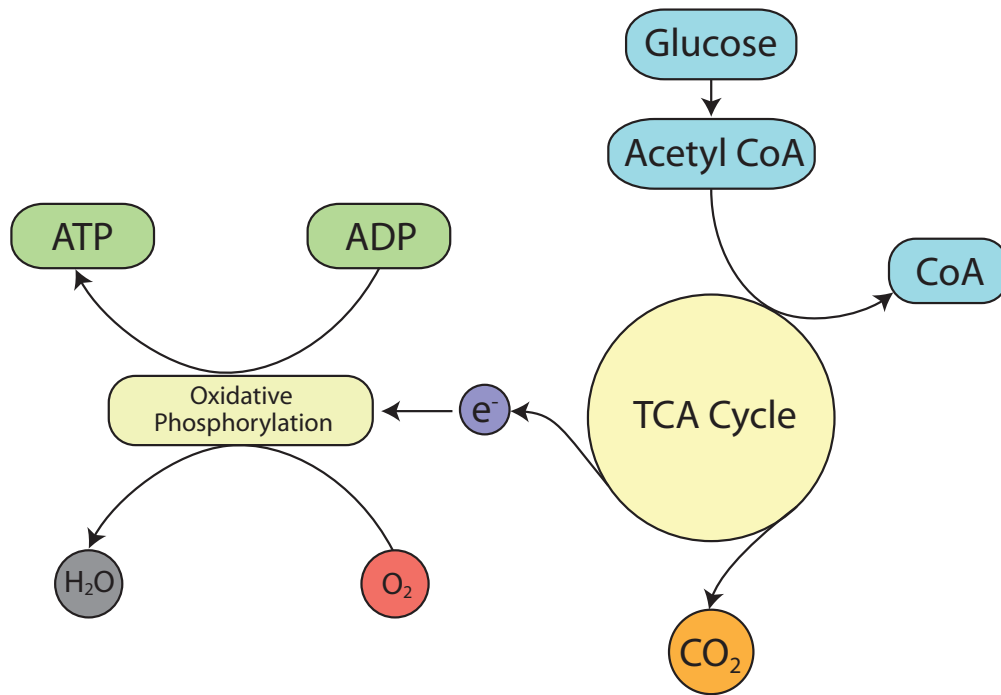
**Figure 3.13:** *Overview of the aerobic metabolism of glucose to ATP following the Kreb's cycle*

Due to suppression of these different contrast weighting mechanisms, the signals acquired from different parts of the object correspond to the amount of spins density present at those locations.

## 3.3 Functional Magnetic Resonance Imaging

The brain, like any other organ in the body requires a steady supply of oxygen in order to metabolise glucose to provide energy. This oxygen is supplied by the component of the blood called haemoglobin. It was demonstrated as long as 1935 that the magnetic properties of haemoglobin depended on the amount of oxygen it carrried [52]. This dependency has given rise to a method for measuring activation using MRI, commonly known as *functional magnetic resonance imaging* (fMRI).

### 3.3.1 Metabolism and Blood Flow in the Brain

The biochemical reactions that transmit neural information via action potentials and neuro-transmitters, all require energy. This energy is provided in the form of ATP, which in turn is produced from glucose by oxidative phosphorylation and the Kreb's cycle (Figure 3.13[I]).

As ATP is hydrolysed to ADP, energy is given up, which can be used to drive biochemical reac-

---

[I]Image source – http://fsl.fmrib.ox.ac.uk/fmri_intro/brief.html

tions that require free energy. The production of ATP from ADP by oxidative phosphorylation is governed by demand, so that the energy reserves are kept constant. That is to say, the rate of this reaction depends mainly on the level of ADP present. This means that the rate of oxygen consumption by oxidative phosphorylation is a good measure of the rate of use of energy in that area.

The oxygen required by metabolism is supplied in the blood. Since oxygen is not very soluble in water, the blood contains a protein that oxygen can bind to, called haemoglobin. The important part of the haemoglobin molecule is an iron atom, bound in an organic structure, and it is this iron atom which gives the blood its color. When an oxygen molecule binds to haemoglobin, it is said to be *oxyhaemoglobin* and on the other hand when no oxygen is bound, it is called *deoxyhaemoglobin.*

To keep up with the high energy demand, oxygen delivery and blood flow to the brain is quite large. Although the brain's weight is only 2% compared to that of the body, its oxygen consumption rate is 20% compared to rest of the other body organs (and the blood flow is 15%). The blood flow per volume of the grey matter, which is a synapse rich area, is about 10 times more than blood flow per volume to the white matter. Regulation of the regional blood flow is poorly understood, but it is known that localized neural activity results in a rapid selective increase in blood flow to that area.

### 3.3.2   Blood Oxygen Level Dependent (BOLD) Contrast

Since regional blood flow is closely related to neural activity, measurement of the *regional cerebral blood flow* (rCBF) is useful in studying brain function. It is possible to measure blood oxygenation level via an interesting contrast mechanism known as *blood oxygen level dependent* (BOLD) contrast.

Deoxyhaemoglobin is a paramagnetic molecule whereas oxyhaemoglobin is diamagnetic. The presence of deoxyhaemoglobin in a blood vessel causes a susceptibility difference between the vessel and its surrounding tissue. Such susceptibility differences cause dephasing of the MR proton signal [53], leading to a reduction in the value of $T_2^*$. In a $T_2^*$ weighted imaging experiment, the presence of deoxyhaemoglobin in the blood vessels causes a reduction in the MR signal in the voxels which contain these vessels [54, 55]. Since oxyhaemoglobin is diamagnetic and does not produce the same dephasing, changes in oxygenation of the blood can be observed as the signal changes in $T_2^*$ weighted images [56–58].

It Would be expected that upon neural activity, since oxygen consumption is increased, that the level of deoxyhaemoglobin in the blood would also increase, and the MR signal would decrease. However what is observed is an increase in signal, implying a decrease in deoxy-haemoglobin. This is because upon neural activity, as well as the slight increase in oxygen extraction from the blood, there is much larger increase in cerebral blood flow, bringing with it more oxyhaemoglobin (Figure 3.14). Thus the bulk effect upon neural activity is a regional
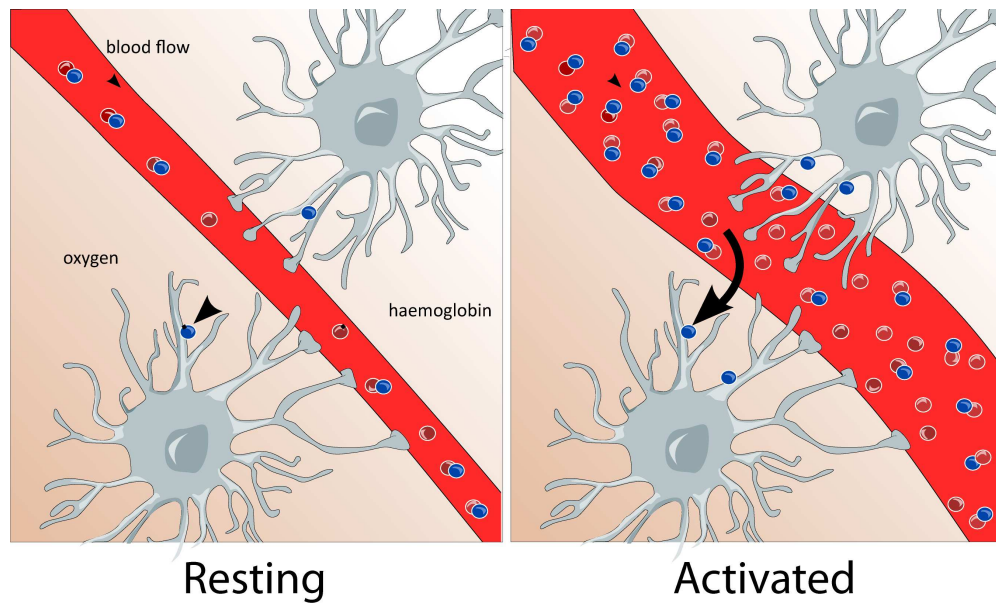
**Figure 3.14:** *Upon activation, oxygen is extracted by the cells, thereby increasing the level of deoxyhaemoglobin the blood. This is compensated for by an increase in blood flow in the vicinity of the active cells, leading to a net increase in oxyhaemoglobin.*

decrease in paramagnetic deoxyhaemoglobin, and an increase in the signal.

The study of these mechanisms are helped by results from PET and near-infrared spectroscopy (NIRS) studies. PET has shown that changes in cerebral blood flow and cerebral blood volume upon activation, are not accompanied by any significant increase in tissue oxygen consumption [59]. NIRS can measure the changes in concentrations of the oxy- and deoxyhaemoglobin, by looking at the absorbency at different frequencies. Such studies have shown an increase in oxyhaemoglobin, and a decrease in deoxyhaemoglobin upon activation. An increase in the total amount of haemoglobin is also observed, reflecting the increase in blood volume upon activation [60].

The time course for the BOLD signal changes is delayed from the onset of the neural activity by a few seconds, and is smooth, representing the changes in blood flow that the technique detects. This is termed the *haemodynamic response* (HDR) to the stimulus. There have been observations of an initial small 'dip' in signal before and after the larger increase in the signal [46, 61], possibly reflecting a transient imbalance between the metabolic activity and blood flow.

### 3.3.3  Functional Mapping using the BOLD Effect

The discovery of the BOLD effect led to many groups trying to map brain activation using the technique. The first MR human brain activation study used an introduced contrast agent to map the visual cortex [62]. Soon after that the BOLD effect was used to map visual and motor

**Figure 3.15:** *Finding the optimal value of TE for the maximum percentage signal change with the BOLD effect*
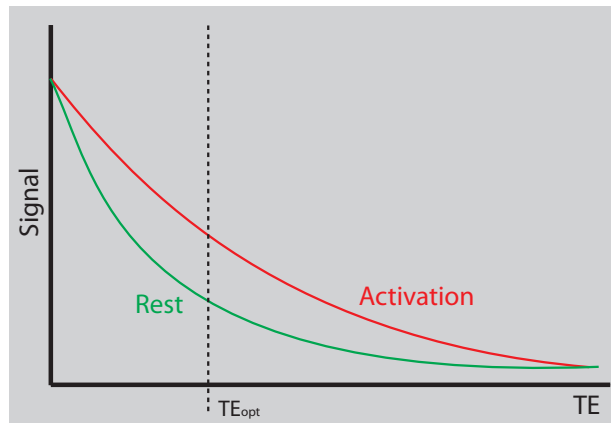
function [45, 63]. References to the many early fMRI experiments can be found in the review articles on the subject [64, 65].

To study brain function using fMRI it is necessary to repeatedly image the brain, whilst the subject is presented with a stimulus or required to carry out some task. The success of the experiment is dependent on three aspects; the scanning sequence used, the design of the stimulus paradigm, and the way the data is analyzed.

The magnitude of the static field used is critical to the percentage signal change obtained on activation. This is because susceptibility differences have a greater signal dephasing effect at higher fields. The earliest fMRI studies were carried out at 1.5 Tesla, but now the forefront research facilities use 3 to 4 Tesla scanners. As field strength increases, the magnitude of the BOLD contrast increases more rapidly than the system noise. Prima facie, it would appear that high field strengths are desirable [66]. However since the adverse effects of image artifacts on the image quality are also enhanced at high field strengths, it becomes challenging to extract the maximum benefits of using high field strength.

The most important aspect of the imaging sequences is that it must produce $T_2^*$ weighted images. This means that a gradient echo is most commonly used, however spin echo sequences still show BOLD contrast because of diffusion effects. Most research is carried out using *Echo Planar Imaging* (EPI) since its fast acquisition rate allows the activation response to short stimuli to be detected. EPI, which is the subject matter of Chapter 4, also has the benefit of reduced artefact from subject motion.

The amount of $T_2^*$ weighting in the image is dependent on the echo time TE. If TE is too short, there will be little difference in the $T_2^*$ curves for the activated state and the resting state, however if TE is too long then there will be no signal from either state. To obtain the maximum signal change for a region with a particular value of $T_2^*$, the optimal value of echo time can be shown to be equal to the $T_2^*$ value of that tissue (Figure 3.15).

The contrast to noise ration of the BOLD signal also depends on voxel size and slice thickness. Smaller voxels have less protons signal due to the reduced number of spins, however larger

voxels may reduce the contrast to noise ratio by partial volume effects. This occurs if the signal changes on activation come from only a small region within the voxel, and so makes less of an impact on the total signal change in that voxel.

During the scanning there are a number of physiological effects that can affect results. These include cardiac pulsation, respiration, and general subject movement. All these problems can be dealt with in two ways, either at the time of scanning or in image post processing. Cardiac or respiratory gating, that is triggering the scanner at one part of the cardiac cycle can be used, although this introduces artifact due to changes in the spin saturation. As will be seen later in Chapters 5 and 6, increasing acquisition rate (temporal resolution) at the time of data acquisitions offers a simple and elegant way to reduce the influence of the physiological signal fluctuations. Postprocessing strategies have been proposed which offer variety of algorithms to deal with this problem [67]. Subject movement can also reduce contrast to noise in fMRI images, and introduce artifacts in the activation maps if the movement is stimulus correlated. This problem is often solved both by restraining the head of the subject and by using a postprocessing registration algorithm.

Another source of artifact in fMRI is the signal coming from draining veins. Since gradient echo images are sensitive to vessels of diameters from micrometers to millimeters, it can be difficult to distinguish between signals from the tissue and that from the veins, which could be some distance away from the activation site [68]. There is also the problem that blood flowing into the imaging slice may be stimulus correlated. One way to reduce the signal from large vessels would be to use a spin echo sequence. This is sensitive to $T_2$ effects only and eliminates the dephasing effects from the large vessels [69, 70]. Using a spin echo sequence will result in some reduction in genuine tissue BOLD signal, so often it is better to acquire a separate set of images which are sensitive to large vessels, and use this to decide whether to reject the signal.

### 3.3.4   Methods of functional MRI

Designing the stimulus paradigm carefully is very important for a fMRI experiment. A lot of experience has come from EEG and PET, but since fMRI has a temporal resolution somewhere between these two techniques, new approaches can be taken. The earliest fMRI experiments were much in the form of PET studies, that is to say a set of resting images were acquired and then a set of activation images, and one set subtracted from the other. However since the BOLD contrast is relatively rapid in its onset and decay (of the order of a few seconds) it is possible to follow time courses for much shorter events occuring more frequently. Besides the stimulus-dependent activity of the brain, the spontaneous activity of the brain can also be studied using fMRI, called *resting state fMRI*. Below we consider both the methods of fMRI experiments which by no means is complete and readers are advised to refer to [71] for a detailed discussion of the topic.

**Block- and Event-related design**

In a block design, two or more conditions are alternated in blocks. Each block will have a duration of a certain number of fMRI scans and within each block only one condition is presented. The state of stimulus delivery is known as the 'on' state whereas absence of stimulus is referred to as the 'off' state. By making conditions differ in only the cognitive process of interest, the fMRI signal that differentiates the conditions should represent this cognitive process of interest. This is known as the *subtraction paradigm* [72]. The increase in fMRI signal in response to a stimulus is additive. This means that the amplitude of the HDR increases when multiple stimuli are presented in rapid succession. When each block is alternated with a rest condition in which the HDR has enough time to return to baseline, a maximum amount of variability is introduced in the signal. As such, the block designs offer considerable statistical power [71, 73]. There are however severe drawbacks to this method, as the signal is very sensitive to signal drift, such as head motion, especially when only a few blocks are used. Another limiting factor is a poor choice of baseline, as it may prevent meaningful conclusions from being drawn. There are also problems with many tasks lacking the ability to be repeated. Since within each block only one condition is presented, randomization of stimulus types is not possible within a block. This makes the type of stimulus within each block very predictable. As a consequence, participants may become aware of the order of the events [71, 73].

Event-related designs allow more real world testing, however, the statistical power of event related designs is inherently low, because the signal change in the BOLD fMRI signal following a single stimulus presentation is small [74].

Both block and event-related designs are based on the subtraction paradigm, which assumes that specific cognitive processes can be added selectively in different conditions. Any difference in blood flow (the BOLD signal) between these two conditions is then assumed to reflect the differing cognitive process. In addition, this model assumes that a cognitive process can be selectively added to a set of active cognitive processes without affecting them [72].

**Resting state fMRI**

*Resting state fMRI* (rs-fMRI) is a method of functional brain imaging that can be used to evaluate regional interactions that occur when a subject is not performing an explicit task [75]. This resting brain activity is observed through changes in blood flow in the brain which creates BOLD signal. Because brain activity is present even in the absence of an externally prompted task, any brain region will have spontaneous fluctuations in BOLD signal. The resting state approach is useful to explore the brain's functional organization and to examine if it is altered in neurological or psychiatric diseases. Resting-state functional connectivity research has revealed a number of networks which are consistently found in healthy subjects, different stages of consciousness and across species, and represent specific patterns of synchronous activity [76, 77].

### 3.3.5 Data Analysis for fMRI

The goal of fMRI data analysis is to detect correlations between brain activation and a task the subject performs during the scan. It also aims to discover correlations with the specific cognitive states, such as memory and recognition, induced in the subject [78]. The BOLD signature of activation is relatively weak, however, so other sources of noise in the acquired data must be carefully controlled. This means that a series of processing steps must be performed on the acquired images before the actual statistical search for task-related activation can begin [79].

Noise is unwanted changes to the MR signal from elements not of interest to the study. The five main sources of noise in fMRI are thermal noise, system noise, physiological noise, random neural activity and differences in both mental strategies and behavior across people and across tasks within a person. Thermal noise multiplies in line with the static field strength, but physiological noise multiplies as the square of the field strength. Since the signal also multiplies as the square of the field strength, and since physiological noise is a large proportion of total noise, higher field strengths above 3 Tesla do not always produce proportionately better images.

Even with the best experimental design, it is not possible to control and constrain all other background stimuli impinging on a subject—scanner noise, random thoughts, physical sensations, and the like. These produce neural activity independent of the experimental manipulation. These are not amenable to mathematical modeling and have to be controlled by the study design.

A person's strategies to respond or react to a stimulus, and to solve problems, often change over time and over tasks. This generates variations in neural activity from trial to trial within a subject. Across people too neural activity differs for similar reasons. Researchers often conduct pilot studies to see how participants typically perform for the task under consideration. They also often train subjects how to respond or react in a trial training session prior to the scanning one [80].

#### Preprocessing

The scanner platform generates a 3D volume of the subject's head every TR. This consists of an array of voxel intensity values, one value per voxel in the scan. The voxels are arranged one after the other, unfolding the three-dimensional structure into a single line. Several such volumes from a session are joined together to form a 4D volume corresponding to a run, for the time period the subject stayed in the scanner without adjusting head position. This 4D volume is the starting point for analysis. The first part of that analysis is preprocessing.

The first step in preprocessing, in the case of a 2D imaging approach, is slice timing correction. The MR scanner acquires different slices within a single brain volume at different times in the case of 2D approach, and hence the slices represent brain activity at different timepoints.

Since this complicates later analysis, a timing correction is applied to bring all slices to the same timepoint reference. This is done by assuming the timecourse of a voxel is smooth when plotted as a dotted line. Hence the voxel's intensity value at other times not in the sampled frames can be calculated by filling in the dots to create a continuous curve. In the case of a 3D imaging apprach, slice timing correction is not required since data acquired is used to fill a 3D $k$-space instead several 2D $k$-spaces and hence the time of acquisition of all the partitions remain the same for 3D imaging approach.

Head motion correction is another common preprocessing step. When the head moves, the neurons under a voxel move and hence its timecourse now represents largely that of some other voxel in the past. Hence the timecourse curve is effectively cut and pasted from one voxel to another. Motion correction tries different ways of undoing this to see which undoing of the cut-and-paste produces the smoothest timecourse for all voxels. The undoing is by applying a rigid-body transform to the volume, by shifting and rotating the whole volume data to account for motion. The transformed volume is compared statistically to the volume at the first timepoint to see how well they match, using a cost function such as correlation or mutual information. The transformation that gives the minimal cost function is chosen as the model for head motion. Since the head can move in a vastly varied number of ways, it is not possible to search for all possible candidates; nor is there right now an algorithm that provides a globally optimal solution independent of the first transformations we try in a chain.

Distortion corrections account for field nonuniformities of the scanner. One method, as described in Section 2.2.2, is to use shimming coils. Another is to recreate a field map of the main field by acquiring two images with differing echo times. If the field were uniform, the differences between the two images also would be uniform. Note these are not true preprocessing techniques since they are independent of the study itself.

In general, fMRI studies acquire both many functional images with fMRI and a structural image with MRI. The structural image is usually of a higher resolution and depends on a different signal, the $T_1$ magnetic field decay after excitation. To demarcate regions of interest in the functional image, one needs to align it with the structural one. Even when whole-brain analysis is done, to interpret the final results, that is to figure out which regions the active voxels fall in, one has to align the functional image to the structural one. This is done with a coregistration algorithm that works similar to the motion-correction one, except that here the resolutions are different, and the intensity values cannot be directly compared since the generating signal is different.

Typical MRI studies scan a few different subjects. To integrate the results across subjects, one possibility is to use a common brain atlas, and adjust all the brains to align to the atlas, and then analyze them as a single group. The atlases commonly used are the Talairach one, a single brain of an elderly woman created by Jean Talairach, and the Montreal Neurological Institute (MNI) one. The second is a probabilistic map created by combining scans from over a hundred individuals. This normalization to a standard template is done by mathematically checking

which combination of stretching, squeezing, and warping reduces the differences between the target and the reference. While this is conceptually similar to motion correction, the changes required are more complex than just translation and rotation, and hence optimization even more likely to depend on the first transformations in the chain that is checked.

Temporal filtering is the removal of frequencies of no interest from the signal. A voxel's intensity change over time can be represented as the sum of a number of different repeating waves with differing periods and heights. A plot with these periods on the x-axis and the heights on the y-axis is called a *power spectrum*, and this plot is created with the Fourier transform technique. Temporal filtering amounts to removing the periodic waves not of interest to us from the power spectrum, and then summing the waves back again, using the inverse Fourier transform to create a new timecourse for the voxel. A high-pass filter removes the lower frequencies, and the lowest frequency that can be identified with this technique is the reciprocal of twice the TR. A low-pass filter removes the higher frequencies, while a band-pass filter removes all frequencies except the particular range of interest.

Smoothing, or spatial filtering, is the idea of averaging the intensities of nearby voxels to produce a smooth spatial map of intensity change across the brain or region of interest. The averaging is often done by convolution with a Gaussian filter, which, at every spatial point, weights neighboring voxels by their distance, with the weights falling exponentially following the bell curve. If the true spatial extent of activation, that is the spread of the cluster of voxels simultaneously active, matches the width of the filter used, this process improves the signal-to-noise ratio. It also makes the total noise for each voxel follow a bell-curve distribution, since adding together a large number of independent, identical distributions of any kind produces the bell curve as the limit case. But if the presumed spatial extent of activation does not match the filter, signal is reduced [80].

**Statistical Analysis**

One common statistical model used for fMRI data analysis is the univariate GLM model, which analyzes each voxel's data separately. The model assumes, at every time point, the HDR is equal to the scaled and summed version of the events active at that point. A researcher creates a design matrix specifying which events are active at any timepoint. One common way is to create a matrix with one column per overlapping event, and one row per time point, and to mark it with a one if a particular event, say a stimulus, is active at that time point. One then assumes a specific shape for the HDR, leaving only its amplitude changeable in active voxels. The design matrix and this shape are used to generate a prediction of the exact HDR of the voxel at every timepoint, using the mathematical procedure of convolution. This prediction does not include the scaling required for every event before summing them.

The basic model assumes the observed HDR is the predicted HDR scaled by the weights for each event and then added, with noise mixed in. This generates a set of linear equations with more equations than unknowns. A linear equation has an exact solution, under most

conditions, when equations and unknowns match. Hence one could choose any subset of the equations, with the number equal to the number of variables, and solve them. But, when these solutions are plugged into the left-out equations, there will be a mismatch between the right and left sides, the error. The GLM model attempts to find the scaling weights that minimize the sum of the squares of the error. This method is provably optimal if the error were distributed as a bell curve, and if the scaling-and-summing model were accurate. For a more mathematical description of the GLM model, see [81].

The GLM model does not take into account the contribution of relationships between multiple voxels. Whereas GLM analysis methods assess whether a voxel or region's signal amplitude is higher or lower for one condition than another, newer statistical models such as multi-voxel pattern analysis (MVPA), utilize that unique contributions of multiple voxels within a voxel-population. In a typical implementation, a classifier or more basic algorithm is trained to distinguish trials for different conditions within a subset of the data. The trained model is then tested by predicting the conditions of the remaining (independent) data. This is most typically achieved by training and testing on different scanner sessions or runs. If the classifier is linear, then the training model is a set of weights used to scale the value in each voxel before summing them to generate a single number that determines the condition for each testing set trial.

### 3.3.6 Resting State fMRI data processing

There are many methods of both acquiring and processing rs-fMRI data, yet there are two methods of analysis that have become the most popular methods for the analysis of functional connectivity in the brain.

**Independent component analysis**

Independent component analysis (ICA) is a useful statistical approach in the detection of resting state networks. ICA separates a signal into non-overlapping spatial and time components. It is highly data-driven and allows for better removal of noisy components of the signal (motion, scanner drift, etc). It also has been shown to reliably extract default mode network as well as many other networks with very high consistency [82].

**Seed-based/Region of interest**

Another method of observing networks and connectivity in the brain is the Seed-Based or region of interest (ROI) method of analysis. In this case, signal from only a certain voxel or cluster of voxels known as the seed or ROI are used to calculate correlations with other voxels of the brain. This provides a much more precise and detailed look at specific connectivity in brain areas of interest [83, 84].

Other methods for characterizing resting-state networks include partial correlation, coherence and partial coherence, phase relationships, clustering, and graph theory [85, 86].

### 3.3.7   Resting State fMRI Applications

Research using resting state fMRI has already proven to have many useful clinical applications, including use in the assessment of many different diseases and mental disorders [87]. Few of the disease condition and corresponding changes in the resting state functional connectivity is listed below:

- Alzheimer's disease: decreased connectivity [88]
- Autism: altered connectivity [89]
- Depression: abnormal connectivity [90–92]
- Schizophrenia: disrupted networks [93]
- Attention deficit hyperactivity disorder (ADHD): Altered "small networks" and Thalamus changes [94]
- Aging brain: disruption of brain systems and motor network [88]
- Epilepsy: disruption and decrease/increase in connectivity [95]
- Parkinson's disease: altered connectivity [96]
- Obsessive Compulsive Disorder:increase/decrease in connectivity [97]
- Pain Disorder: altered connectivity [98, 99]

Other types of current and future clinical applications for resting state fMRI include identifying group differences in brain disease, obtaining diagnostic and prognostic information, longitudinal studies and treatment effects, clustering in heterogeneous disease states, and pre-operative mapping and targeting intervention [100].

## References

[38]  Mark E. Haacke, Robert W. Brown, Michael R. Thompson, and Ramesh Venkatesan. *Magnetic Resonance Imaging: Physical Principles and Sequence Design*. Wiley-Liss, June 1999.

[39]  P. C. Lauterbur. Image formation by induced local interactions: Examples employing nuclear magnetic resonance, 1973.

[40]  R.S. Likes. Moving gradient zeugmatography, December 22 1981. US Patent 4,307,343.

[41]  E. L. Hahn. Spin echoes. *Phys. Rev.*, 80:580–594, Nov 1950.

[42]  Jens Frahm, Axel Haase, and Dieter Matthaei. Rapid NMR imaging of dynamic processes using the FLASII technique. *Magnetic Resonance in Medicine*, 3(2):321–327, 1986.

[43]  J. Hennig, A. Nauerth, and H. Friedburg. Rare imaging: A fast imaging method for clinical mr. *Magnetic Resonance in Medicine*, 3(6):823–833, 1986.

[44] J Hennig. Multiecho imaging sequences with low refocusing flip angles. *Journal of Magnetic Resonance (1969)*, 78(3):397 – 407, 1988.

[45] K K Kwong, J W Belliveau, D A Chesler, I E Goldberg, R M Weisskoff, B P Poncelet, D N Kennedy, B E Hoppel, M S Cohen, and R Turner. Dynamic magnetic resonance imaging of human brain activity during primary sensory stimulation. *Proceedings of the National Academy of Sciences*, 89(12):5675–5679, 1992.

[46] S Ogawa, D W Tank, R Menon, J M Ellermann, S G Kim, H Merkle, and K Ugurbil. Intrinsic signal changes accompanying sensory stimulation: functional brain mapping with magnetic resonance imaging. *Proceedings of the National Academy of Sciences*, 89(13):5951–5955, 1992.

[47] D. Lebihan and E. Breton. Imagerie de Diffusion In Vivo par Résonance Magnétique Nucléaire. *CR Académie des Sciences de Paris*, 301:1109–1112, 1985.

[48] Klaus-Dietmar Merboldt, Wolfgang Hanicke, and Jens Frahm. Self-diffusion {NMR} imaging using stimulated echoes. *Journal of Magnetic Resonance (1969)*, 64(3):479 – 486, 1985.

[49] D. G. Taylor and M. C. Bushell. The spatial mapping of translational diffusion coefficients by the NMR imaging technique. *Physics in Medicine and Biology*, 30(4):345–349, April 1985.

[50] R R Edelman, B Siewert, D G Darby, V Thangaraj, A C Nobre, M M Mesulam, and S Warach. Qualitative mapping of cerebral blood flow and functional localization with echo-planar mr imaging and signal targeting with alternating radio frequency. *Radiology*, 192(2):513–20, 1994.

[51] P Mansfield. Multi-planar image formation using nmr spin echoes, 1977.

[52] L. Pauling. *The Magnetic Properties and Structure of Hemoglobin, Oxyhemoglobin and Carbonmonoxyhemoglobin.* Proc. Nat. Acad. Sci. Oregon State University, 1936.

[53] Keith R. Thulborn, John C. Waterton, Paul M. Matthews, and George K. Radda. Oxygenation dependence of the transverse relaxation time of water protons in whole blood at high field. *Biochimica et Biophysica Acta (BBA) - General Subjects*, 714(2):265 – 270, 1982.

[54] Seiji Ogawa, Tso-Ming Lee, Asha S. Nayak, and Paul Glynn. Oxygenation-sensitive contrast in magnetic resonance image of rodent brain at high magnetic fields. *Magnetic Resonance in Medicine*, 14(1):68–78, 1990.

[55] Seiji Ogawa and Tso-Ming Lee. Magnetic resonance imaging of blood vessels at high fields: In vivo and in vitro measurements and image simulation. *Magnetic Resonance in Medicine*, 16(1):9–18, 1990.

[56] S. Ogawa, T. M. Lee, A. R. Kay, and D. W. Tank. Brain magnetic resonance imaging with contrast dependent on blood oxygenation. *Proceedings of the National Academy of Sciences of the United States of America*, 87(24):9868–9872, 1990.

[57] R Turner, D Le Bihan, C T Moonen, D Despres, and J Frank. Echo-planar time course mri of cat brain oxygenation changes. *Magn Reson Med*, 22(1):159–66, 1991.

[58] Peter Jezzard, Frederick Heineman, Joni Taylor, Daryl Despres, Han Wen, Robert S. Balaban, and Robert Turner. Comparison of epi gradient-echo contrast changes in cat brain caused by respiratory challenges with direct simultaneous evaluation of cerebral oxygenation via a cranial window. *NMR in Biomedicine*, 7(1-2):35–44, 1994.

[59] P. T. Fox, M. E. Raichle, M. A. Mintun, and C. Dence. Nonoxidative glucose consumption during focal physiologic neural activity. *Science*, 241(4864):462–464, July 1988.

[60] A Villringer, J Planck, C Hock, L Schleinkofer, and U Dirnagl. Near infrared spectroscopy (nirs): a new tool to study hemodynamic changes during activation of brain function in human adults. *Neuroscience letters*, 154(1-2):101—104, May 1993.

[61] Thomas Ernst and Jürgen Hennig. Observation of a fast response in functional mr. *Magnetic Resonance in Medicine*, 32(1):146–149, 1994.

[62] Jw Belliveau, Dn Kennedy, Rc Mckinstry, Br Buchbinder, Rm Weisskoff, Ms Cohen, Jm Vevea, Tj Brady, and Br Rosen. Functional mapping of the human visual cortex by magnetic resonance imaging. *Science*, 254(5032):716–719, November 1991.

[63] Peter A. Bandettini, Eric C. Wong, R. Scott Hinks, Ronald S. Tikofsky, and James S. Hyde. Time course epi of human brain function during task activation. *Magnetic Resonance in Medicine*, 25(2):390–397, 1992.

[64] K.K. Kwong. Functional magnetic resonance imaging with echo planar imaging. In Paolo Pavone and Plinio Rossi, editors, *Functional MRI*, Syllabus, pages 73–90. Springer Milan, 1996.

[65] Mark S. Cohen and Susan Y. Bookheimer. Localization of brain function using magnetic resonance imaging. *Trends in Neurosciences*, 17(7):268 – 277, 1994.

[66] R Turner, P Jezzard, H Wen, KK Kwong, D Le Bihan, T Zeffiro, and RS Balaban. Functional mapping of the human visual cortex at 4 and 1.5 tesla using deoxygenation contrast epi. *Magnetic resonance in medicine*, 29(2):277–279, 1993.

[67] Tuong Huu Le and Xiaoping Hu. Retrospective estimation and correction of physiological artifacts in fmri by direct extraction of physiological activity from mr data. *Magnetic Resonance in Medicine*, 35(3):290–298, 1996.

[68] JH Gao, I Miller, S Lai, J Xiong, and PT Fox. Quantitative assessment of blood inflow effects in functional mri signals. *Magnetic resonance in medicine : official journal of the*

## REFERENCES

*Society of Magnetic Resonance in Medicine / Society of Magnetic Resonance in Medicine*, 36(2):314—319, August 1996.

[69] C.R. Fisel, J.L. Ackerman, R.B. Buxton, L. Garrido, J.W. Belliveau, B.R. Rosen, and T.J. Brady. Mr contrast due to microscopically heterogeneous magnetic susceptibility: Numerical simulations and applications to cerebral physiology. *Magnetic Resonance in Medicine*, 17(2):336–347, 1991. cited By (since 1996)225.

[70] J. Hykin, R. Bowtell, P. Mansfield, P. Glover, R. Coxon, B. Worthington, and L. Blumhardt. Functional brain imaging using epi at 3 t. *Magnetic Resonance Materials in Physics, Biology and Medicine*, 2(3):347–349, 1994.

[71] P. Jezzard, P.M. Matthews, and S.M. Smith. *Functional Magnetic Resonance Imaging: An Introduction to Methods*. Oxford medical publications. OUP Oxford, 2001.

[72] T.J. Grabowski and A.R. Damasio. 14 - investigating language with functional neuroimaging. In Arthur W. TogaJohn C. Mazziotta, editor, *Brain Mapping: The Systems*, pages 425 – 461. Academic Press, San Diego, 2000.

[73] Geoffrey K Aguirre and Mark D'Esposito. *Experimental design for brain fMRI*, chapter 3, pages 47–51. Springer-Verlag, Berlin, 1999.

[74] M. D'Esposito, E. Zarahn, and G. K. Aguirre. Event-related functional mri: Implications for cognitive psychology. *Psychological Bulletin*, 125(1), 1999.

[75] Bharat B. Biswal. Resting state fmri: A personal history. *NeuroImage*, 62(2):938 – 944, 2012. 20 {YEARS} {OF} fMRI 20 {YEARS} {OF} fMRI.

[76] Cristina Rosazza and Ludovico Minati. Resting-state brain networks: literature review and clinical applications. *Neurological Sciences*, 32(5):773–785, 2011.

[77] David M. Cole, Stephen M. Smith, and Christian F. Beckmann. Advances and pitfalls in the analysis and interpretation of resting-state fmri data. *Frontiers in systems neuroscience*, 4(April):8, January 2010.

[78] Nikos K. Logothetis. What we can do and what we cannot do with fmri. *Nature*, 453(7197):869–878, June 2008.

[79] S.A. Huettel, A.W. Song, and G. McCarthy. *Functional Magnetic Resonance Imaging*. Number Bd. 1 in Functional Magnetic Resonance Imaging. Sinauer Associates, 2004.

[80] Martin A. Lindquist. The statistical analysis of fmri data. *Statistical Science*, 23(4):439–464, June 2009.

[81] G. Enderlein. Mccullagh, p., j. a. nelder: Generalized linear models. chapman and hall london – new york 1983, 261 s., £ 16,–. *Biometrical Journal*, 29(2):206–206, 1987.

[82] Christian F. Beckmann, Marilena DeLuca, Joseph T. Devlin, and Stephen M. Smith. Investigations into resting-state connectivity using independent component analysis. *Philosophical Transactions of the Royal Society B: Biological Sciences*, 360(1457):1001–1013, May 2005.

[83] Daniel S. Margulies, A.M. Clare Kelly, Lucina Q. Uddin, Bharat B. Biswal, F. Xavier Castellanos, and Michael P. Milham. Mapping the functional connectivity of anterior cingulate cortex. *NeuroImage*, 37(2):579 – 588, 2007.

[84] Koene R. Van Dijk, Trey Hedden, Archana Venkataraman, Karleyton C. Evans, Sara W. Lazar, and Randy L. Buckner. Intrinsic functional connectivity as a tool for human connectomics: theory, properties, and optimization. *Journal of neurophysiology*, 103(1):297–321, January 2010.

[85] Gary H. Glover Catie Chang. Time–frequency dynamics of resting-state brain connectivity measured with fmri. *NeuroImage*, 50(1), 2010.

[86] Andreia V Faria, Suresh E Joel, Yajing Zhang, Kenichi Oishi, Peter C M van Zjil, Michael I Miller, James J Pekar, and Susumu Mori. Atlas-based analysis of resting-state functional connectivity: evaluation for reproducibility and multi-modal anatomy-function correlation studies. *NeuroImage*, 61(3):613—621, July 2012.

[87] F. Holtbernd and D. Eidelberg. Functional brain networks in movement disorders: recent advances. *Current Opinion in Neurology*, 25(4):392–401, 2012.

[88] R. Li, X. Wu, K. Chen, A. S. Fleisher, E. M. Reiman, and L. Yao. Alterations of directional connectivity among resting-state networks in alzheimer disease. *AJNR Am J Neuroradiol*, 34(2):340–345, 2013.

[89] R. A. Müller, P. Shih, B. Keehn, J. R. Deyoe, K. M. Leyden, and D. K. Shukla. Underconnected, but how? a survey of functional connectivity mri studies in autism spectrum disorders. *Cereb Cortex*, 21(10):2233–2243, 2011.

[90] A. Anand, Y. Li, Y. Wang, J. Wu, S. Gao, L. Bukhari, V. P. Mathews, A. Kalnin, and M. J. Lowe. Activity and connectivity of brain mood regulating circuit in depression: a functional magnetic resonance study. *Biological psychiatry*, 57(10):1079–1088, May 2005.

[91] Michael D. Greicius, Benjamin H. Flores, Vinod Menon, Gary H. Glover, Hugh B. Solvason, Heather Kenna, Allan L. Reiss, and Alan F. Schatzberg. Resting-state functional connectivity in major depression: Abnormally increased contributions from subgenual cingulate cortex and thalamus. *Biological Psychiatry*, 62(5):429 – 437, 2007. Neurocircuitry and Neuroplasticity Abnormalities in Mood and Anxiety Disorders.

[92] A. Anand, Y. Li, Y. Wang, M. J. Lowe, and M. Dzemidzic. Resting state corticolimbic connectivity abnormalities in unmedicated bipolar disorder and unipolar depression. *Psychiatry Res.*, 171(3):189–198, 2008.

# REFERENCES

[93] A. Venkataraman, T. J. Whitford, C. F. Westin, P. Golland, and M. Kubicki. Whole brain resting state functional connectivity abnormalities in schizophrenia. *Schizophr Res*, 139(1-3):7–12, 08 2012.

[94] Lucina Q. Uddin, A. M. Clare Kelly, Bharat B. Biswal, Daniel S. Margulies, Zarrar E. Shehzad, D. Shaw, M. Ghaffari, J. Rotrosen, L. A. Adler, F. Xavier Castellanos, and Michael P. Milham. Network homogeneity reveals decreased integrity of default-mode network in ADHD. *Journal of Neuroscience Methods*, 169(1):249–254, 2008.

[95] Wurina, Y. F. Zang, and S. G. Zhao. Resting-state fmri studies in epilepsy. *Neuroscience Bulletin*, 28(4):449–455, 2012.

[96] Alessandro Tessitore, Marianna Amboni, Fabrizio Esposito, Antonio Russo, Marina Picillo, Laura Marcuccio, Maria Teresa Pellecchia, Carmine Vitale, Mario Cirillo, Gioacchino Tedeschi, and Paolo Barone. Resting-state brain connectivity in patients with parkinson's disease and freezing of gait. *Parkinsonism & Related Disorders*, 18(6):781 – 787, 2012.

[97] P. Li, S. Li, Z. Y. Dong, J. Luo, H. Y. Han, and H. F. Xiong. Altered resting state functional connectivity patterns of the anterior prefrontal cortex in obsessive-compulsive disorder. *Neuroreport*, 23(11):681–686, 2012.

[98] A. Otti1, H. Guendel, A. Wohlschläger, C. Zimmer, and M. Noll-Hussong. Frequency shifts in the anterior default mode network and the salience network in chronic pain disorder. *BMC Psychiatry*, 13(84):PMID: 23497482, 2013.

[99] A. Otti, H. Guendel, P. Henningsen, C. Zimmer, A. M. Wohlschlaeger, and M. Noll-Hussong. Functional network connectivity of pain-related resting state networks in somatoform pain disorder: an exploratory fmri study. *J Psychiatry Neurosci.*, 38(1):57–65, 2013.

[100] Michael D Fox and Michael Greicius. Clinical applications of resting state functional connectivity. *Frontiers in Systems Neuroscience*, 4(19), 2010.

# 4 Echo Planar Imaging

In medical imaging, image data acquisition speed is one of the crucial parameters that technologists and researchers care about. Echo planar imaging (EPI) is known for its speed of data acquisition. It typically uses a single nuclear spin excitation to acquire entire $k$-space data via rapid switching of readout and phase-encoding gradients [101]. The ability of EPI to acquire an image in few tens of milliseconds has opened doors to a variety of critical medical and scientific applications. Evaluation of cardiac function in real time, mapping of water diffusion in tissue, mapping of organ blood pool & perfusion, and functional imaging of the central nervous system are examples of a few of EPI's applications.

In this chapter, different variants of EPI pulse sequence are explained first. Compared to conventional spin-echo and gradient-echo imaging, EPI is more prone to a variety of artifacts. These commonly encountered artifacts of echo planar images and their cures are discussed next. In the later part of the chapter, a new $k$-space traversal strategy for 3D EPI is presented that encodes two partitions per RF excitation, effectively reducing the number of excitations used to acquire a 3D EPI dataset by half.

## 4.1   Echo Planar Imaging Sequences

Echo planar imaging is a technique that maximally uses the transverse magnetization without additional RF excitation, by creating a series of gradient echoes using a bipolar oscillating readout gradient before the transverse magnetization decays away due to $T_2^*$ relaxation. Phase encoding blips are played in-between each echo readout to encode multiple $k$-space lines with a single RF excitation. The number of gradient echoes produced following an RF excitation is called *echo train length* (or ETL) and is denoted by $N_{etl}$ in this manuscript. Whereas, the interval between two adjacent echoes is known as the *echo spacing* (or ESP), denoted by $t_{esp}$. As can be seen later in this chapter, ETL directly determines the scan-time reduction factor in EPI pulse sequences and has significant impact on a few artifacts seen with EPI such as image distortion, chemical shift displacement, signal loss, and image blurring.

| Field strength | Gray matter | White matter | Caudate | Putamen |
|---|---|---|---|---|
| (T) | (ms) | (ms) | (ms) | (ms) |
| 1.5 | 84.0±0.8 | 66.2±1.9 | 58.8±2.4 | 55.5±2.3 |
| 3.0 | 66.0±1.4 | 53.2±1.2 | 41.3±2.3 | 31.5±2.5 |
| 7.0 | 33.2±1.3 | 26.8±1.2 | 19.9±2.0 | 16.1±1.6 |

**Table 4.1:** *Mean corrected $T_2^*$ values for important brain regions at different magnetic field strengths. Source: [103].*

### 4.1.1 Gradient Echo EPI

A representative 2D gradient-echo EPI (also known as GRE-EPI or GE-EPI) pulse sequence is already introduced in Section 3.2.4. The pulse sequence starts with a selective excitation pulse to produce an FID signal. Under the envelope of the FID, a series of spatially encoded gradient echoes are produced using a train of bipolar readout gradients and phase-encoding gradient blips [102] as shown in Figure 3.11.

In GE-EPI, each $k$-space line along the phase-encoding direction is acquired at a different TE. The amplitude of the corresponding gradient echo, $S(n)$, decays according to:

$$S(n) = S_0 e^{\frac{-\text{TE}(n)}{T_2^*}}$$

(4.1)

where $n$ is the echo index in the echo train and $S_0$ is the signal at time zero, defined as the time immediately after the magnetization is tipped by the applied RF pulse. As seen in Section 3.1.5, image contrast is predominantly determined by the central $k$-space region. Hence in the case of EPI sequence, effective TE ($\text{TE}_{\text{eff}}$) is defined as the TE that corresponds to the central $k$-space line, i.e. $\text{TE}_{\text{eff}} = \text{TE}(k_y = 0)$.

If a long $\text{TE}_{\text{eff}}$ is used with GE-EPI, the image obtained exhibits heavy $T_2^*$ weighting. The $T_2^*$ contrast plays an important role in fMRI (see Section 3.2.5). At higher magnetic fields, the increased magnetic susceptibility effect shortens $T_2^*$. Thus, the $\text{TE}_{\text{eff}}$ must be adjusted accordingly to balance the contrast and SNR of the GE-EPI for functional studies. For example, mean corrected $T_2^*$ values for important brain regions at different magnetic field strengths are shown in Table 4.1.

### 4.1.2 Spin Echo EPI

A basic 2D spin echo sequence has already been introduced in Section 3.2.1. A 2D spin-echo EPI (SE-EPI) pulse sequence essentially uses the same technique to form an echo. It differs in the readout module where a series of spatially encoded gradient echoes are read instead of just a single echo. During a time window around the peak of the spin echo, EPI readout and phase-encoding gradient pulses are played to spatially encode gradient echoes. Like GE-EPI, SE-EPI relies on gradient echoes to sample $k$-space lines, except that the gradient echoes are
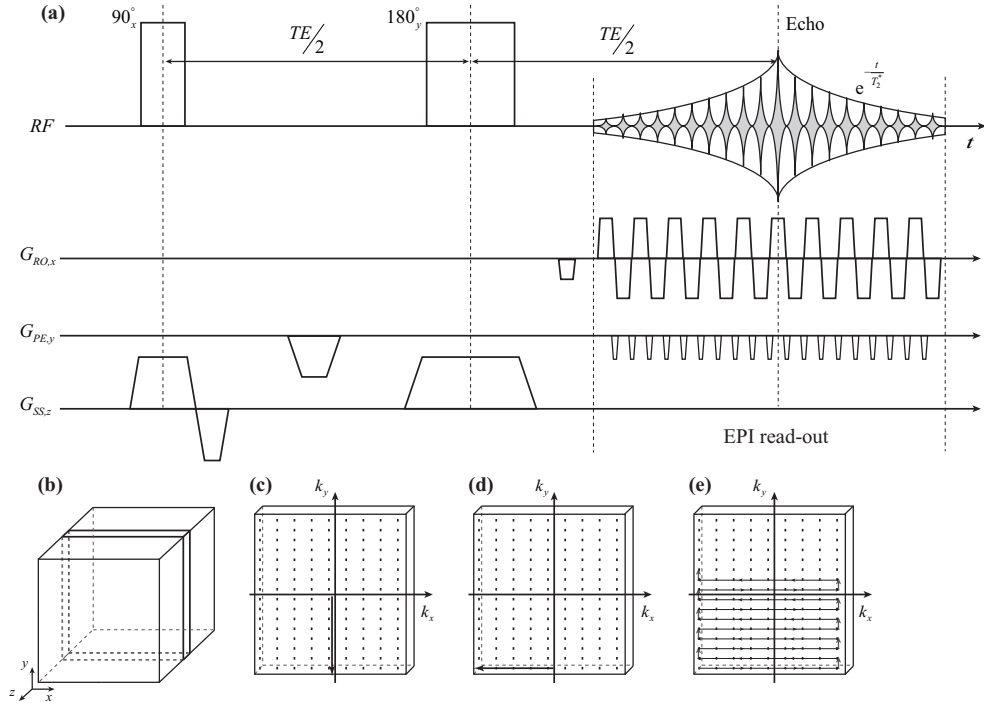
**Figure 4.1:** *(a) Pulse sequence diagram for spin echo based echo planar imaging. The time duration from the center of the* 90° *excitation RF pulse to the center of the echo train length defines TE. (b-e) The resulting k-space sampling scheme.*

formed under the envelope of a spin echo instead of an FID.

Similar to GE-EPI, each gradient echo in SE-EPI is acquired at a different TE. The effective TE of the sequence is also defined as the TE when the central $k$-space line is acquired, i.e. $TE_{eff} = TE(k_y = 0)$. The TE of the spin echo may or may not correspond to $TE_{eff}$. When $TE_{eff}$ coincides with $TE_{se}$, the sensitivity of the sequence to off-resonance effects is substantially reduced and the image becomes predominantly $T_2$ weighted, instead of $T_2^*$ weighted (assuming $TR \gg T_1$ and $TE_{eff} \approx T_2$ or longer), which is useful when $T_2$-weighted echo planar images are desired as in the case of diffusion weighted imaging. However, when sensitivity to $T_2^*$ or off-resonance effects is desired as in the case of functional MRI, $TE_{eff}$ is shifted away from $TE_{se}$.

### 4.1.3 Inversion Recovery EPI

In *Inversion Recovery EPI* (IR-EPI), an inversion recovery module (see Section 3.2.3) is played prior to a GE-EPI or SE-EPI pulse sequence [104]. Among many other uses for it, IR-EPI can also be used to measure tissue perfusion with arterial spin labeling (ASL). The pulse sequence can also be used to prepare a desired tissue contrast as in magnetization-prepared $T_1$-weighted imaging, to attenuate signal from cerebrospinal fluid or to produce a $T_1$ map.

## 4.2 Variants of EPI

### 4.2.1 Standard multi-slice EPI

In *standard multi-slice EPI*, the entire 2D $k$-space data needed for image reconstruction are acquired using an echo train produced by a single RF excitation pulse. If a single slice is imaged, the total scan time is the same as the sequence length $T_{\text{seq}}$:

$$T_{\text{scan}} = T_{\text{seq}} = C + N_{\text{etl}} \times t_{\text{esp}} \tag{4.2}$$

where $C$ is the interval between the start of the sequence and the beginning of data acquisition of the first echo. For multiple slices without signal averaging, the scan time increases to:

$$T_{\text{scan}} = N_{\text{slices}} T_{\text{seq}} = N_{\text{slices}} \left( C + N_{\text{etl}} \times t_{\text{esp}} \right) \tag{4.3}$$

Standard multi-slice EPI is traditionally used for obtaining high temporal resolution echo planar images while being very demanding on the gradient hardware. Typically images produced using multi-slice EPI have low SNR and low spatial resolution and are affected by various types of artifacts. Since $k$-space is sampled under decaying $T_2^*$ envelope, ETL allowed is often not sufficient to sample the entire $k$-space extent even with modern hardware advances which provide a wide receiver bandwidth and higher slew-rates for gradients play-out. Simple techniques such as partial Fourier (PF) acquisition or more advanced parallel imaging approaches (see Chapter 5) are often employed along the phase-encoded direction to reduce ETL and also to reduce the effects of a few artifacts discussed later in this chapter.

### 4.2.2 Multi-shot EPI

With *multi-shot EPI* only a fraction of the required single slice $k$-space data is acquired after each RF excitation. Hence the entire $k$-space data for a single slice is acquired through multiple RF excitations (*multishot*). Since ETL following each excitation is relatively short in the case of multi-shot EPI, it incurs lower artifacts compared to single-shot EPI pulse sequence. Since FID is recreated after each shot, unlike single-shot EPI, the maximum extent of the $k$-space is not limited by the decaying $T_2^*$ envelope and hence multi-shot EPI can produce images of superior spatial resolution at the cost of increased scan-time (which also results in increased sensitivity to motion).

### 4.2.3 Three Dimensional EPI

Three dimensional (3D) approach for EPI, though less commonly used for routine MRI, brings its own pros and cons. A true 3D EPI, called *echo volumar imaging* (EVI) has evolved over time to produce different variants in order to overcome technical challenges imposed by the hardware and the image quality requirements. Some of the benefits of using 3D EPI over

2D EPI include a higher sensitivity per unit scan-time [105, 106], the absence of spin-history artifact [107], and the ability to apply conventional parallel imaging acceleration in the two phase-encoding directions [108], as opposed to only one in case of 2D approach. In this section we shall briefly discuss these variants of 3D EPI approaches.

**Echo Volumar Imaging**

*Echo volumar imaging* traverses entire 3D $k$-space with a single long echo train [109, 110]. Although EVI provides all the 3D approach benefits mentioned above, it requires very long ETL to cover the entire 3D $k$-space. This long ETL imposes constraints on minimum achievable echo time, spatial resolution or has very high demands on the gradients hardware [111]. Increase in ETL can be reduced to some extend by employing parallel imaging in both the phase-encoding directions for a given spatial resolution. However. parallel imaging comes at the cost of reduced SNR, which is discussed in detail in chapter 5. To further overcome the limitations of 3D approach, various recent methods have been proposed such as outer volume suppression, use of surface coils to restrict the actual field of view, or use of 2D/3D RF excitation pulses to restrict excited volume only to the volume of interest (see Chapter 7).

**Multi-slab EVI**

In another 3D approach, called *multi-slab EVI*, the constraints imposed during single-shot EVI acquisitions are alleviated by dividing a thick excitation volume into multiple slabs of lesser thickness and later combining $k$-space data for these thinner slabs to form the required 3D $k$-space [112]. Acquiring the 3D $k$-space in multiple smaller 3D $k$-spaces makes each individual ETL $N_{slab}$ times smaller and demands from gradient hardware is reduced. However, due to imperfect slab-profiles, the slices at the edge of the slabs often have to be discarded. Moreover, thinner slabs reduce the ability to use parallel imaging acceleration on the second phase-encoding direction.

**Segmented 3D EPI**

In yet another approach, called *segmented 3D EPI*, the full 3D $k$-space is acquired in multiple shots [107, 108, 113]. In this approach, each echo train is $N_{shot}$ times smaller than used in 3D EVI to cover the same $k$-space extent (Figure 4.2). Typically, one $k$-space plane is encoded following a single RF excitation in segmented 3D EPI, making achievable echo times comparable to those achievable with single-shot 2D EPI. As a result, echo times comparable to $T_2^*$ could be achieved even at high field strengths ($\geq$ 7T).

The Ernst angle (Equation (3.25)) used during segmented 3D EPI acquisition is lower compared to the one used during 2D EPI acquisition since the TR used for the excitation of the same tissue volume is $N_{slices}$ times lower in the case of segmented 3D EPI, where $N_{slices}$ is the number of slices encoded within a 3D imaging volume. The use of lower flip angle is helpful
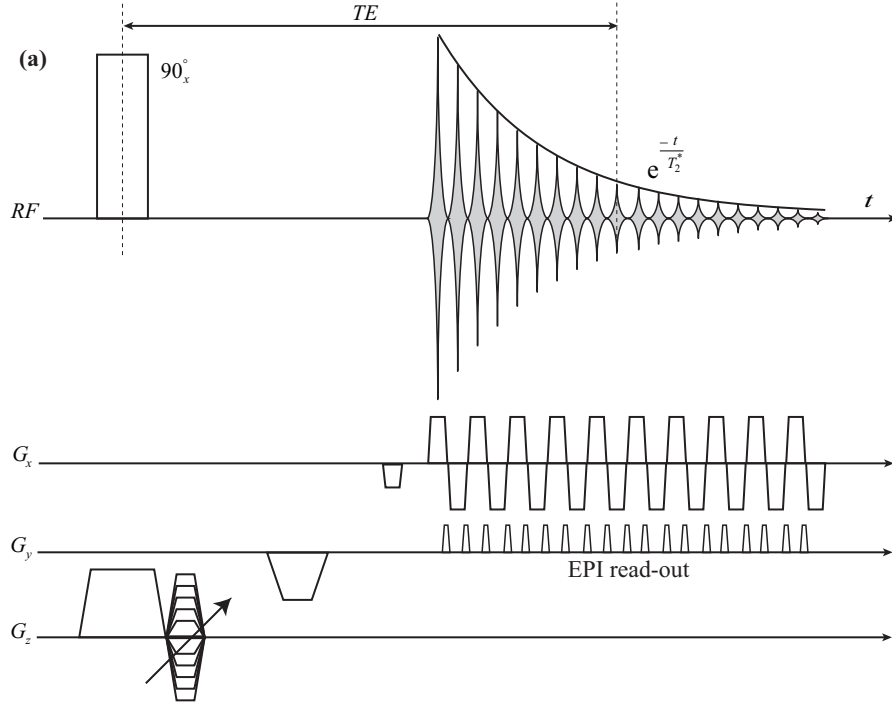
**Figure 4.2:** *Pulse sequence diagram for a gradient echo based segmented 3D EPI sequence. Only one k-space plane is encoded per RF excitation. The phase encoding gradient along partition-encoding direction is combined with slice-select rephaser gradient in the diagram.*

at ultra-high field strengths ($\geq 7$ T) since peak power deposited has quadratic dependence on the flip angle used, making segmented 3D EPI less peak power intensive. Even though a smaller flip angle is used with 3D EPI, a higher signal to noise ratio is reached compared to 2D EPI. This is because though steady state magnetization reached is lower for 3D EPI as given by Equation (4.4), the fact that $N_{\mathrm{slices}}$ more data points contribute to each data point in 3D Fourier reconstruction leads to an intrinsic SNR advantage of $\sqrt{N_{\mathrm{slices}}}$ which increases with increasing slice count.

$$M_{\mathrm{ss}} = \frac{M_0 \sin\alpha \left(1 - e^{\frac{-\mathrm{TR}}{T_1}}\right)}{1 - \cos\alpha \cdot e^{\frac{-\mathrm{TR}}{T_1}}} \tag{4.4}$$

Where $M_{\mathrm{ss}}$ is the steady state magnetization and $M_0$ is the initial longitudinal magnetization. This intrinsic SNR advantage is however counter-balanced to some extent due to the reduced TR and hence reduced $M_{\mathrm{ss}}$. For example, let us consider a volumetric acquisitions consisting of 30 slices or partitions using a standard multi-slice 2D EPI and using a segmented 3D EPI sequence. If 80 ms are required to encode a single $k$-space plane, then according to Equation (3.25) the associated Ernst angles (assuming $T_1 = 1800$ ms) are 75° and 17° for 2D and 3D acquisitions, respectively. Although the resulting steady state magnetization ($M_{\mathrm{ss}}$) values are $0.75M_0$ and $0.15M_0$ for 2D and 3D EPI acquisitions, respectively, the transverse magnetization of 3D EPI acquisition is $0.82M_0$ whereas that of 2D EPI is $0.76M_0$ due to SNR advantage of

$\sqrt{N_{\text{slices}}}$.

As a disadvantage, the maximum available temporal signal-to-noise ratio (tSNR) is reduced compared with single-shot acquisition [105, 108, 114] due to physiological signal fluctuations [114]. This loss in tSNR can be recovered using physiological noise correction techniques [115, 116], and a tSNR superior to 2D EPI can be achieved [117].

Although the scope of this manuscript is limited to Cartesian trajectories, it is worth mentioning that besides Cartesian sampling patterns, different non-Cartesian 3D $k$-space sampling patterns for EPI, e.g. 3D rosette [118] and concentric spheres [119] trajectories, have also been suggested which provide better PSF and more isotropic nature to imaged voxels. However reconstruction algorithms of such non-Cartesian trajectories are computationally intensive.

## 4.3 Artifacts

The cost of increased sampling speed achievable with EPI is paid through its increased susceptibility to various types of artifacts. One of the main reasons for exhibiting this increased susceptibility to artifacts is because of its low bandwidth along the phase-encoding direction. The bandwidth of an MR image refers to the difference in MR frequencies between adjacent pixels, as well as to the total range of frequencies that make up an image. In conventional imaging (using gradient echo or spin echo sequence), the bandwidth per pixel is ordinarily kept comparable to the chemical shift between fat and water. In a 7 Tesla system, for example, a pixel bandwidth of 500 Hz is typical (the fat-water shift is about 1050 Hz). In this case, the fat and water component of a single voxel will be shifted from one another by about 1 pixel, which is an acceptable imaging artifact. At first, one would expect that the pixel bandwidth in EPI would be very high, due to the rapid sampling rate. This is, in fact, true along the readout axis. The continuous encoding scheme used in EPI, however, results in a relatively low bandwidth along the phase encoding axis; 120 Hz/pixel is typical, giving rise to several low-bandwidth related artifacts.

In this section, the nature of the artifacts commonly encountered in EPI is presented. Various methods used, either during experimental setup or during image reconstruction or combination of both, for artifacts reduction in EPI are also discussed.

### 4.3.1 Nyquist Ghosts

*Nyquist ghosting*, also referred to as *N-over-two* ($\frac{N}{2}$) ghost, is one of the typical artifacts seen with echo planar images [120]. The amplitude/phase inconsistencies, which typically alternate between even and odd echoes during bi-polar readout gradient train, give rise to Nyquist ghosts in EPI [121–123]. The inconsistencies may arise from inaccurate timing of the readout gradients, temporal asymmetry of the analog filter, and static field inhomogeneities. Although the first two factors can be minimized with hardware improvement, the last factor depends on

**Figure 4.3:** *Nyquist ghost is shown by arrows in the adjacent echo planar image. The intensity of the ghost is lesser than the main image and the ghost image is shifted by one half of the field of view.*
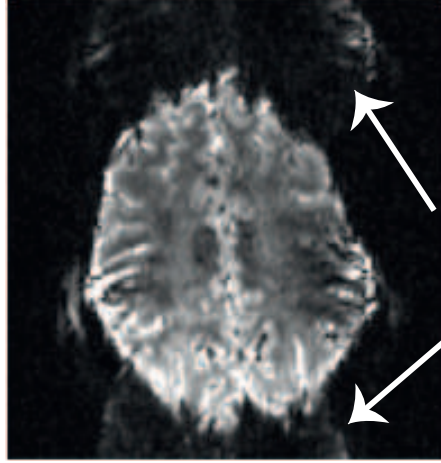
the object being imaged and cannot be readily compensated.

Considering a spatially independent phase error $\phi$ that alternates between odd and even echoes in a single-shot EPI sequence, the $k$-space signal can be expressed as:

$$S'(p,q) = \begin{cases} \sum_l \sum_m I(l,m) \exp\left(-\frac{i2\pi lp}{n_x}\right) \exp\left(-\frac{i2\pi mq}{n_y}\right) \exp\left(-i\phi\right), & \text{if } q \text{ is even} \\ \sum_l \sum_m I(l,m) \exp\left(-\frac{i2\pi lp}{n_x}\right) \exp\left(-\frac{i2\pi mq}{n_y}\right) \exp\left(i\phi\right), & \text{if } q \text{ is odd} \end{cases}$$

(4.5)

where $I$ represents the desired image intensity, $p$ and $q$ are the $k$-space indices along the readout and phase-encoding directions, respectively, and $l$ and $m$ are the corresponding indices in the image domain:

$$\begin{aligned} k_x &= p\Delta k_x \\ k_y &= q\Delta k_y \\ x &= l\Delta x \\ y &= m\Delta y \end{aligned}$$

(4.6)

According to orthonormal properties of Fourier transform, an image $I'$ reconstructed from $S'$ is related to the desired image $I$ by:

$$I'(l,m) = I(l,m)\cos\phi + iI\left(l, m - \frac{N_y}{2}\right)\sin\phi$$

(4.7)

where $N_y$ is the image matrix size in the phase-encoding direction. The first term in Equation (4.7) represents the main image with its intensity uniformly reduced by a factor of $|\cos\phi| \leq 1$. The second term corresponds to the Nyquist ghost whose intensity is given by $I|\sin\phi|$ and whose location is shifted by one half of the FOV along the phase-encoding direction (Figure 4.3), and hence the name N-over-two ghost.

To reduce ghosting artifacts, a number of techniques have been developed. These include

postprocessing techniques with or without the use of a reference scan [121, 124–126]. The commonly used reference scan based technique is to acquire a reference measurement of a few gradient echoes in the absence of the phase-encoding gradient and subsequently align the imaging echoes based on the reference echoes. The correction is achieved either by correcting the phase of the echo and shifting the echo position (corresponding to a constant and linear phase correction in the projection direction) or by nonlinear correction performed on a point-by-point basis in the projection direction [121]. The reference data can also be obtained using a pair of zero phase-encoding echoes [124], eliminating the need for a separate measurement [125]. Because the aplitude of the susceptibility-induced phase shifts increases linearly with $B_0$, the inconsistencies between odd and even $k$-space lines, responsible for Nyquist ghosting, increase with the magnetic field strength. Techniques based on phase-encoded reference scans have been shown to offer better ghost corrections compared to zero phase-encoded techniques [127, 128].

For the echo planar images presented in this manuscript (whenever reconstruction was performed on a standalone computer using MATLAB), the technique used for Nyquist ghost correction was as follow: a reference data was acquired just after each RF pulse excitation with the phase-encoding gradients disabled and just before phase encoded (normal) EPI readout train, which during reconstruction provided a measure of the inconsistent phase errors between odd and even echoes in the echo train. 3 reference lines were acquired with a bipolar readout gradient train, after which an imaging readout echo train was played with required phase-encoding gradients to acquire the entire $k$-space. It should be noted that the reference scan was integrated with the imaging scan, it could as well be acquired as a separate scan. The non-phase-encoded echoes were individually inverse-Fourier-transformed along the readout direction to obtain a set of projections (called projection space and denoted by the letter $P$). Ideally, all projections should have had the same phase because no phase-encoding gradient was applied. Any phase inconsistency could be calculated by comparing the phases among the projections. Only the spatially constant and linear phase errors ($\alpha$ and $\beta$, respectively) were obtained by performing a linear regression:

$$\Delta\phi = \alpha + \beta x \tag{4.8}$$

To carry out phase correction, the EPI $k$-space data were first inverse-Fourier transformed along the readout direction to produce a hybrid data set $P(x, k_y)$ in the projection space. The constant and linear phase errors, $\alpha$ and $\beta$, were removed from $P(x, k_y)$, followed by another one-dimensional inverse Fourier transform along the phase-encoded direction $k_y$ to produce echo planar images.

### 4.3.2 Chemical Shift Artifacts

Chemical shift artifacts in echo planar images, typically, appear in the phase-encoding direction due to lower sampling bandwidth used along this direction. The readout bandwidth used along the readout direction, in the case of EPI, is considerably larger compared to that in

conventional imaging approaches such as spin-echo and gradient-echo imaging. Along the phase-encoding direction, the EPI sampling bandwidth per pixel is given by

$$\Delta \nu_{\text{phase}} = \frac{1}{t_{\text{esp}} \cdot \text{N}_{\text{etl}}} \tag{4.9}$$

where $N_{\text{shot}}$ is the number of RF excitations used to encode a single $k$-space plane. Due to a chemical shift of $\delta$ (in hertz) relative to the receiver frequency, the spatial shift produced along the phase-encoding direction is:

$$\Delta y_{\text{cs}} = \frac{\delta}{\Delta \nu_{\text{phase}}} \text{FOV}_y = t_{\text{esp}} \cdot \delta \cdot \text{FOV}_y \tag{4.10}$$

where $\text{FOV}_y$ is the FOV in the phase-encoding direction. $\Delta \nu_{\text{phase}}$ in Equation (4.10) is typically on the order of 1kHz, because of which the spatial shift along the phase-encoded direction can be substantial in echo planar images. Using saturation pre-pulses for lipid suppression or using water-only excitation pulses are the most commonly used solutions to suppress chemical shift artifacts in echo planar images. Figure 4.9 shows appearance of chemical shift artifact on EPI images.

### 4.3.3 Image Distortion

The EPI technique suffers from a very low bandwidth in the primary phase-encoding direction. Typically, the bandwidth per pixel is <20 Hz, which implies that a local shim inhomogeneity of 200 Hz (as is quite typical close to the frontal sinuses at 7 Tesla) can lead to a mis-location of the signal in that region by 10 pixels. Additionally, when the field homogeneity varies rapidly over a distance, there may be loss of signal for gradient echo sequences (will be discussed in more details in Section 4.3.5). The pixel mis-location in the readout direction of the image is negligible due to relatively high bandwidth (>1000 Hz) used along this direction. So the distortion artifacts in EPI may be regarded as a series of one-dimesion pixel shifts in the phase-encoding direction given by:

$$y = y_0 + \frac{\Delta \nu(y)}{\text{BW}_y} \tag{4.11}$$

where $y$ is the mis-located position, $y_0$ is the correct position, $\Delta \nu(y)$ is the spatial distribution of the static magnetic field in Hz, and $\text{BW}_y$ is the bandwidth per pixel (also in Hz) in the phase-encoding direction. Note that the static magnetic field can be expressed in frequency units (Hz) or magnetic field (Tesla) via the Larmor equation $\nu = \gamma B_0$, where $\gamma$ is the gyromagnetic ratio for hydrogen (42.575 MHz/Tesla).

For the sake of simplicity, the existence of the field homogeneity along a direction can be approximated by existence of a weak background gradient along that direction. For illustration purpose, Figure 4.4 shows the effect of existence of a weak background gradient along the read ($x$) axis of the image.
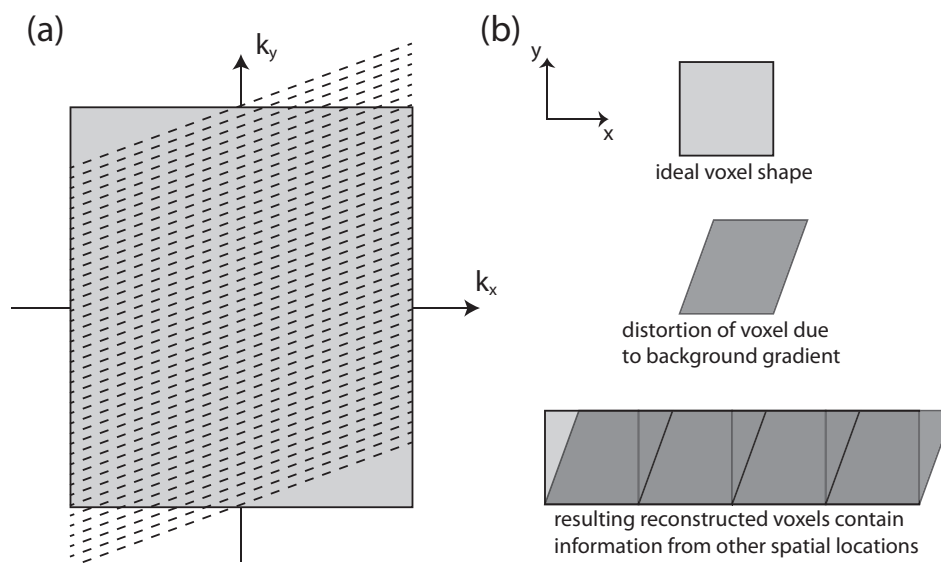
**Figure 4.4:** *Distortion artifact demonstrated using voxel schematic. (a) The k-space coverage in the presence of a background gradient in the y-direction is shown. The ideal k-space coverage is the gray-shaded (solid-fill) region, whereas the dotted lines represent the k-space coverage due to the effect of the background gradient's presence. The read axis (x-axis) is not parallel to $k_x$ in the latter case. (b) The distortion of a single voxel is shown. The final reconstructed image represent square voxels and hence due to the distortion, the signal from one voxel is 'spilled' into the adjacent voxels.*

Among a few methods devised to reduce image distortions in echo planar images, decreasing the echo spacing (thus increasing the sampling bandwidth along the phase-encoding direction) or the echo train length are the most commonly employed ones, albeit with adverse effects of reducing image SNR or incurring limitation on the achievable spatial resolution in single-shot sequences, respectively. This limitation can be partially overcome using parallel imaging techniques [129] (Chapter 5). An example of echo planar image distortion is shown in Figure 4.5. Figure 4.5(a) was acquired without the use of parallel imaging, whereas 4.5(b) was acquired with parallel imaging (GRAPPA) acceleration factor of 2 in the phase-encoding direction, thus reducing the echo train length by half in the latter case. Distortion artifacts are quite evident in the anterior portion of the brain where brain anatomy looks stretched (Figure 4.5(a)). Reducing ETL helped in reducing the distortion (Figure 4.5(b)). Another common solution to image distortion is to first acquire a $B_0$ map and unwarp the image through a phase correction [130].

### 4.3.4 $T_2^*$-*Induced Image Blurring*

Signal acquisition during EPI readout is performed under the envelop of decaying signal whose amplitude is exponentially attenuated with time constant $T_2^*$ (see Equation (4.1)). As a result, image blurring occurs along the phase-encoding direction. The concept of *point spread*

**Figure 4.5:** *Distortion artifact is exemplified through an echo planar imaging acquisition. (a) The anterior part of the brain appears stretched due to relatively long echo train length used for the acquisition. (b) The same image acquired after reducing echo train length by half, by using parallel imaging (GRAPPA) acceleration factor of 2, exhibit considerable reduction in the image distortion.*
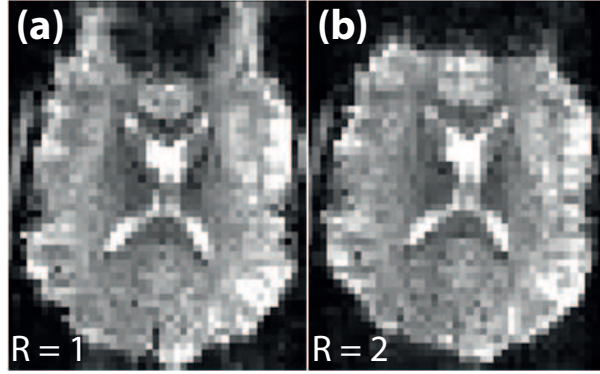
*function* (PSF) discussed in Section 3.1.5 can readily be used to understand the image blurring due to $T_2^*$ effect. The shorter the $T_2^*$ for a given ETL, the more the blurring seen on echo planar images.

Generally, reducing the total duration of the echo train can help alleviate image blurring in EPI. Shortening echo train length or reducing echo spacing are typical approaches employed to restrict the $k$-space acquisition to a narrow time window in which the $T_2^*$ decay is not substantial. Parallel imaging is generally used to reduce echo train length without compromising spatial resolution, however with a penalty on image SNR. Another approach to reduce echo train length without affecting spatial resolution is to make use of multi-shot approach rather than single-shot.

### 4.3.5 Intravoxel Dephasing

EPI as a technique is very susceptible to signal losses due to magnetic field susceptibility variations of the adjacent tissue types within a voxel. *Intravoxel dephasing* is the cause for these signal losses in echo planar images. Even within a single tissue type within a voxel, there will be a small range of magnetic field strengths due to the varying proximity to other tissue types and the varying molecular environment of spins. The precession of the net magnetization vector of each spin isochromat will move in and out of phase with other net magnetization vectors (from other group of spins) within the same image voxel. The position dependent phase term $\phi$ for individual spin isochromat is given by:

$$\phi(d) = -2\pi\gamma G_z \cdot d \cdot \text{TE} \tag{4.12}$$

Equation (4.12) takes into account the dependence only along the $z$-axis for simplicity, but the similar equations can readily be derived for any direction. $G_z$ is the magnetic field gradient along the slice-encoding ($z$-axis) direction, whereas d is the distance from a reference position along the $z$-direction. Due to these accumulated phase differences over distance, when the sub-voxel magnetizations precess out of phase, the overall signal from the voxel is lost because the oscillating magnetic fields produced all cancel out. This phenomenon causes a signal void on echo planar images. Increasing the slice thickness improves the SNR of an image, but a
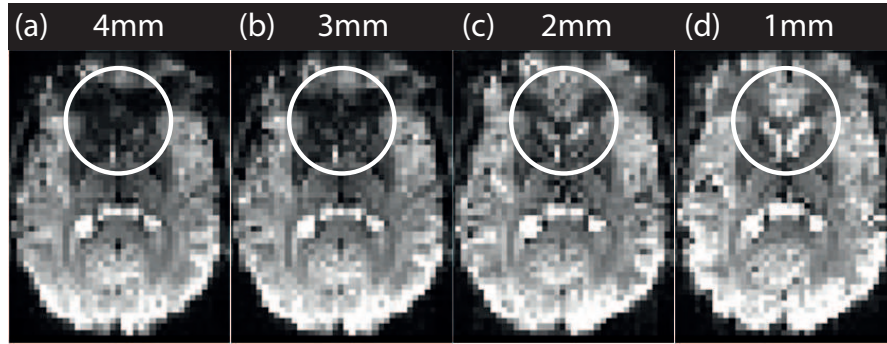
**Figure 4.6:** *Effect of varying voxel size on intravoxel dephasing is demonstrated. The in-plane resolution of all the acquisitions were kept the same at 3.3× 3.3 mm² whereas slice thickness was varied and is indicated at the top of each image. The intravoxel dephasing artifact (signal void outlined by white circle) reduces with reduction in the slice thickness used during acquisitions.*

thicker slice in EPI does not always produce a higher SNR due to greater intravoxel dephasing effects with thicker slices.

Generally, a thinner slice is preferred with EPI to increase global image SNR by avoiding signal loss due to dephasing. For illustrative purpose, echo planar images acquired with 3.3×3.3 mm² in-plane resolution are shown in Figure 4.6. The slice thickness is reduced from 4 mm to 1mm in the steps of 1 mm. As one can notice, the maximum signal loss due to intravoxel dephasing, at the region outlined by a white circle, occurs with the highest slice thickness used. The loss in the signal is gradually reduced as the slice thickness is reduced.

## 4.4 Reduced Excitations EPI

### 4.4.1 Introduction

At high magnetic field strengths ($\geq 7$ T), due to the increased signal available and because of the increased susceptibility-induced artifacts, there is both an opportunity and a need to acquire higher spatial resolution images. Increasing spatial resolution of multi-slice 2D EPI implies an increase not only in the ETL but also in the number of slices needed to achieve the same volume coverage, thereby increasing the minimum TR achievable for whole brain coverage to a point where it becomes comparable to the hemodynamic response. Recently, multi-band excitations have been proposed to accelerate the acquisition of 2D multi-slice imaging [132] and EPI datasets [133–135] in which simultaneously acquired slices can be separated using coil sensitivity profiles [135]. Multiplexed-EPI [136] combines multi-slice excitation with simultaneous echo refocused EPI [137] at the cost of an increased ETL. These recent approaches have shown their potential to provide sub-second temporal resolution.

The aim of developing *3D reduced excitations EPI* (3D RE-EPI), which encodes two *k*-space

---

Text on 3D RE-EPI is adapted from publication [131].

**Figure 4.7:** *Pulse sequence diagram for (a) segmented 3D-EPI, and (b) 3D RE-EPI sequences. In 3D RE-EPI, the primary phase-encode blips are played out after every two readout blips and the partition-encode blips are played out with alternating polarity after every readout blip so that two adjacent partitions are encoded in a single RF excitation. The ETL becomes double than that of the segmented 3D EPI. When the TE is kept constant, the minimum TR for 3D RE-EPI becomes only 25% longer compared with segmented 3D EPI.*
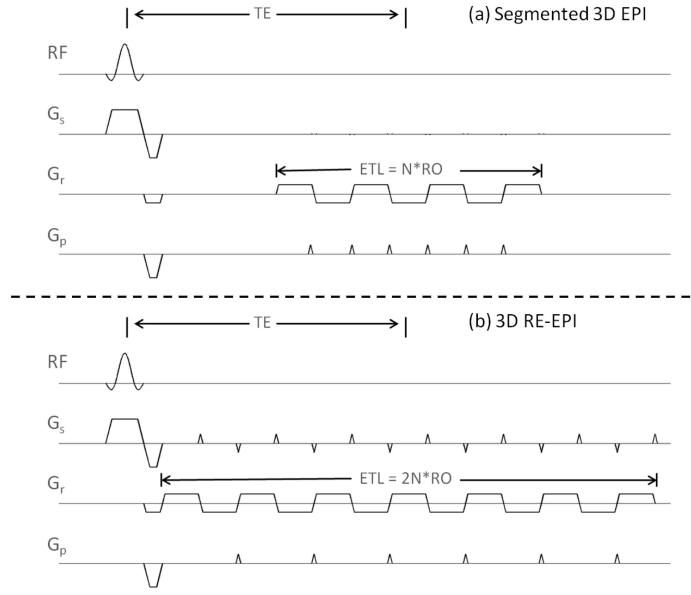


planes per RF excitation (segment), was to reduce the number of segments used to acquire the a 3D dataset by while increasing ETL by a factor of 2 compared to segmented 3D EPI. Image quality assessment was performed for 3D RE-EPI in combination with partial parallel acquisition (PPA) and partial Fourier (PF) with different overall data acquisition speed-up factors. tSNR was assessed using resting state networks (RSN) detection for 3D RE-EPI and compared with segmented 3D EPI and multi-slice 2D-EPI acquisitions. The ability to better characterize physiological signal with 3D RE-EPI was demonstrated through power spectral analysis of physiological data and MR signal.

### 4.4.2 Methods

The proposed sequence 3D RE-EPI (Figure 4.7b) is a modified version of the segmented 3D EPI sequence (Figure 4.7a). In 3D RE-EPI, the primary phase-encode blips are played out after every two readout gradients during the EPI echo train. Partition-encode blips with alternating polarity are played out to encode two successive partitions in a single EPI echo train. Such a $k$-space trajectory reduces the number of excitations and time needed to cover the imaging volume. The acquisition speed-up factor with 3D RE-EPI ($S_{PU}$) can be combined with conventional acceleration methods such as partial Fourier ($A_{PF}$) and parallel imaging ($A_{PPA}$). The speed-up factor (S) due to this novel acquisition technique, which provides a way to acquire 3D dataset faster at the cost of increased ETL, must not be confused with parallel imaging acceleration factors (A), which generally result in a reduction in ETL.

All experiments were conducted according to procedures approved by the institutional review board and all participants provided written informed consents prior to experiments. Six healthy subjects (3 males; average age 25.8 years) were scanned on a 7 T/680 mm head-only

scanner (Magnetom, Siemens, Germany) equipped with a head gradient insert (maximum gradient strength and slew rate: 80 mT/m, 333 T/m/s). A 32-channel RF head coil (Nova Medical Inc., Wilmington, Massachusetts, USA) was used for RF reception.

**Image Quality**

Image quality was evaluated in whole brain images acquired with 3D RE-EPI with 1.2 mm isotropic nominal resolution (using 156×156×120 acquisition matrices for the fully sampled data). The overall 3D RE-EPI speed-up ($S_{OV}$) in the partition-encode direction was varied from 1 to 8 using different combinations of $S_{PU}$, $A_{PF}$, and $A_{PPA}$ ($S_{OV} = S_{PU} \times A_{AF} \times A_{PPA}$). Other acquisition parameters were as follows: TR/TE = 200/30 ms; flip angle (FA) = 17°; readout bandwidth (rBW) = 2190 Hz/pixel; matrix size = 156×156×120; $PPA_{phase}$ = 3; and $PF_{phase}$ = 6/8 in the primary phase-encode direction. Frequency selective fat saturation pulses were applied before each excitation pulse. The partition-encode direction was set to superior-inferior, whereas the primary phase-encode direction was set to anterior-posterior. Image reconstruction was performed entirely online through the vendor-provided software.

An additional low resolution scan was performed on one of the subjects to assess the effect of fat saturation on the chemical shift artifact, typically observed in echo planar images due to the inherent low bandwidth in the phase-encode direction (Section 4.3.2). The protocol parameters were as follows: TR/TE = 40/14 ms; FA = 10°; rBW = 2604 Hz/pixel; matrix size = 80×80×88; nominal resolution = 2.5 mm isotropic; $PPA_{phase}$ = 3, $PF_{phase}$ = 6/8, primary phase-encode = anterior-posterior. Images were obtained with and without a preparatory spectrally selective fat saturation pulse in two separate runs.

**Temporal SNR**

The benefit of improved tSNR with the 3D RE-EPI sequence, compared with multi-slice 2D EPI and segmented 3D EPI sequences, was evaluated through the detection of RSNs. Common protocol parameters for all three sequences: TE = 26 ms, rBW = 2358 Hz/pixel, matrix size = 106×106×60, nominal 2 mm isometric voxels, $PF_{phase}$ = 6/8, $PPA_{phase}$ = 2. Total scan time per sequence was kept constant at 5 min across all the scans. Scans were performed for each subject in a randomized order. Sequence-specific parameters were:

1. Multi-slice 2D EPI: $TR_{volume}$ = 2.920 s; FA = 60°; number of volumes = 102. The TR used was the minimum possible when sampling the same number of slices at the same resolution as with the segmented 3D EPI.
2. Segmented 3D EPI: $TR_{segment}$ = 51 ms; $TR_{volume}$ = 0.816 s; $PF_{slice}$ = 6/8; $PPA_{slice}$ = 3; FA = 13°; number of volumes = 392.
3. 3D RE-EPI: $TR_{segment}$ = 60 ms; $TR_{volume}$ = 0.480 s; $PF_{slice}$ = 6/8; $PPA_{slice}$ = 3; FA = 14°; number of volumes = 667.

Anatomical images were acquired with the MP2RAGE sequence [138] using the following parameters: $TR_{MP2RAGE}$ = 6.0 s; TE = 3.03 ms; inversion time $TI_1/TI_2$ = 0.8/2.7 s; $\alpha_1/\alpha_2$ = 7°/5°; matrix size = 320×320×256 (nominal 0.6×0.6×0.6 $mm^3$ isotropic voxels); partition-encode = left-right; primary phase-encode = anterior-posterior; $PPA_{phase}$ = 3; $PF_{phase}$ = 6/8; $PF_{slice}$ = 6/8. The Sa2RAGE sequence was used for $B_1$ calibration [139].

fMRI data were motion-corrected using the linear image registration tool FLIRT (FMRIB, Oxford, UK). Datasets were first aligned to their high-resolution anatomical images and subsequently to the MNI152 standard space. RSNs were identified via independent component analysis (ICA) using the MELODIC toolbox (FMRIB) [140, 141]. Spatial smoothing of 3-mm full-width-half-maximum was applied prior to ICA. Group analysis was performed with multi-session temporal concatenation. RSNs that consistently appeared in 2D EPI, 3D EPI, and 3D RE-EPI was automatically identified by choosing the components of the 3D EPI and 3D RE-EPI with spatial correlation ≥ 0.35 with the 2D EPI RSNs (after thresholding the component maps at Z = 3). When one or more of the 3D EPI and 3D RE-EPI components passed this criterion, the network was dubbed common or split, respectively. Additional independent components were found after visual inspection. RSNs were named via visual comparison with published data [142–145].

tSNR per unit time in the white matter and gray matter regions were calculated for all subjects for each run using MATLAB (Mathworks, Natick, Massachusetts, USA). Regions of interest containing ~100 pixels each were defined in the corpus callosum and cerebral cortex of the sensory motor regions for each subject, and obtained tSNR per unit time values were averaged across subjects.

**Physiological Signal Characterization**

Respiratory and cardiac data were acquired along with MR data from one of the subjects using 3D RE-EPI with $TR_{volume}$ of 0.528 s and using segmented 3D EPI with $TR_{volume}$ of 0.792 s in two additional runs. Minimum TRs for 3D RE-EPI and segmented 3D EPI were used while keeping TE ~ $T_2^*$ [103]; this corresponds to a penalty on the $TR_{segment}$ by only ~ 1/2 of the ETL for 3D RE-EPI when compared with 3D EPI. Power spectrum analysis was performed using MATLAB on both physiological data and MR signals to evaluate the benefits of sampling at a higher temporal resolution for physiological noise characterization.

### 4.4.3 Results

**Image Quality**

To determine the overall quality of images, 3D RE-EPI acquisitions were performed with three volunteers and compared with images acquired with segmented 3D EPI. Images in three orthogonal planes (through the center of the acquisition volume of a representative dataset) obtained with different acquisition speed-up factors are shown in Figure 4.8. Overall acqui-
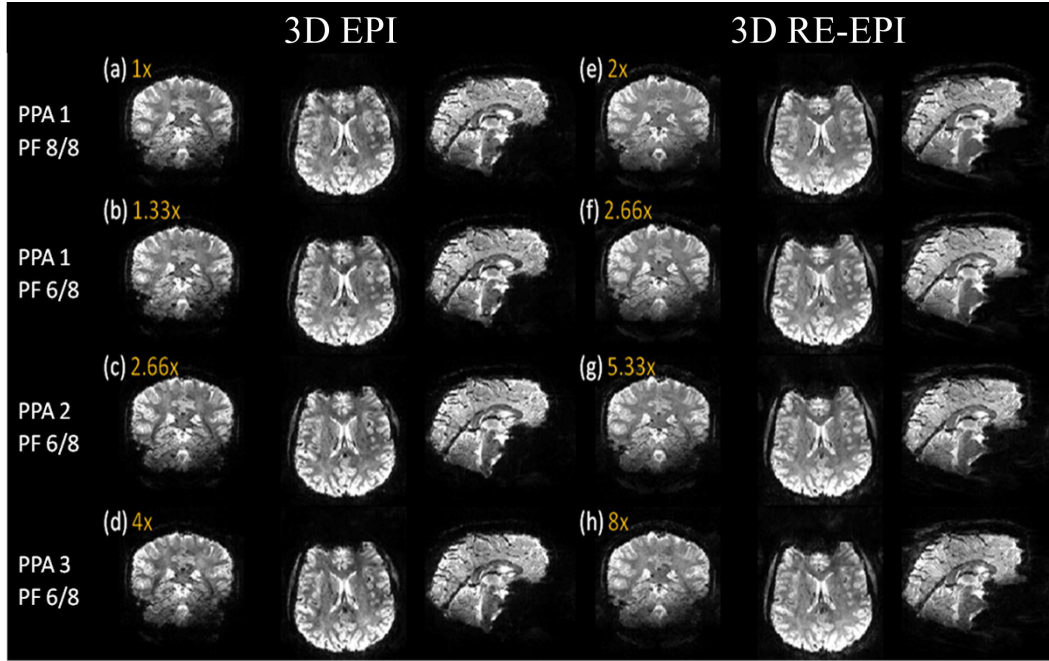
**Figure 4.8:** *Each subpanel shows three orthogonal planes from images obtained using 3D EPI and 3D RE-EPI with different overall partition-direction acquisition speed-up factors ranging from 1 to 8. The in-plane $A_{PF}$ and $A_{PPA}$ were 6/8 and 3, respectively, for all images. Overall partition-direction speed-up factors used for each acquisition are indicated in the top left corner of each subpanel (a-h). PPA and PF acceleration factors used in the partition-direction are indicated on the far left. All the data shown were acquired axially with the readout gradient applied along a left-right orientation.*

**Figure 4.9:** *Chemical shift artifact with 3D RE-EPI (a) without and (b) with spectrally selective fat saturation preparatory pulse played out before each RF excitation. Chemical shift artifacts (indicated by arrows) appear not only shifted in the primary phase-encode direction but also as Nyquist ghost (shifted by $\frac{\text{FOV}}{2}$) in the partition-encode direction, which was left-right in these sagittaly acquired data.*
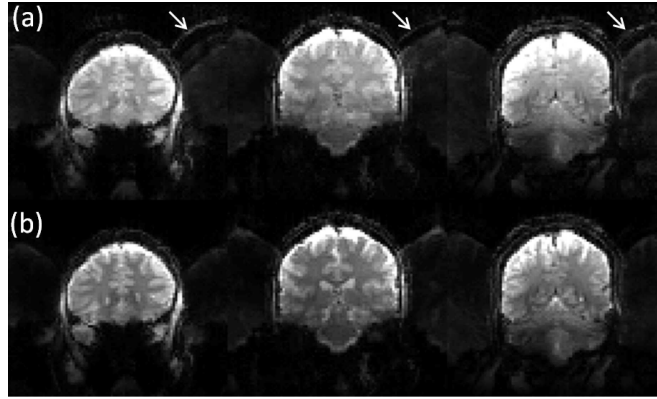


sition speed-up in the partition-encode direction was calculated as $S_{OV} = S_{PU} \times A_{PPA} \times A_{PF}$. Nyquist ghosts were visible in the primary phase-encode direction (anterior-posterior) with segmented 3D EPI and in the partition-encode direction (superior-inferior) with 3D RE-EPI. This resulted from the alternating polarity of the readouts shifting from the primary phase-encode direction (3D EPI) to the partition-encode direction (3D RE-EPI). Due to increased ETL, increased distortions in the primary phase-encode direction (anterior-posterior) were observed.

Figure 4.9 shows coronal slices at three different positions without (Figure 4.9a) and with (Figure 4.9b) a preparatory spectrally selective fat saturation pulse. The chemical shift artifacts appeared not only shifted in the primary phase-encode direction but also as a Nyquist ghost (shifted by FOV/2) in the partition-encode direction, when 3D RE-EPI was used without fat saturation.

**Temporal SNR**

The reduction in $TR_{volume}$ resulted in an increase in the number of time points acquired with 3D RE-EPI (667 time points) compared with multi-slice 2D-EPI (102 time points) and segmented 3D EPI (392 time points), improving the ability to detect RSNs via ICA. The networks detected were divided into three categories: (1) common network, which included medial visual (red-yellow), executive (blue-light blue), default mode (copper), ventral stream (red), sensory motor (green), left lateral (yellow), and right lateral (pink) (Figure 4.10a-c); (2) split networks, which were found split across multiple independent components with increasing temporal resolution (Figure 4.10d-f); and (3) appearing networks, which were found only at a particular temporal resolution and were absent at the other two temporal resolutions (Figure 4.10g-h). The average tSNR per unit scan time values was higher in 3D RE-EPI compared with 3D EPI (an average increase of ~31%) and, compared with multi-slice 2D-EPI (an average increase of ~66%) as shown in Table 4.2.
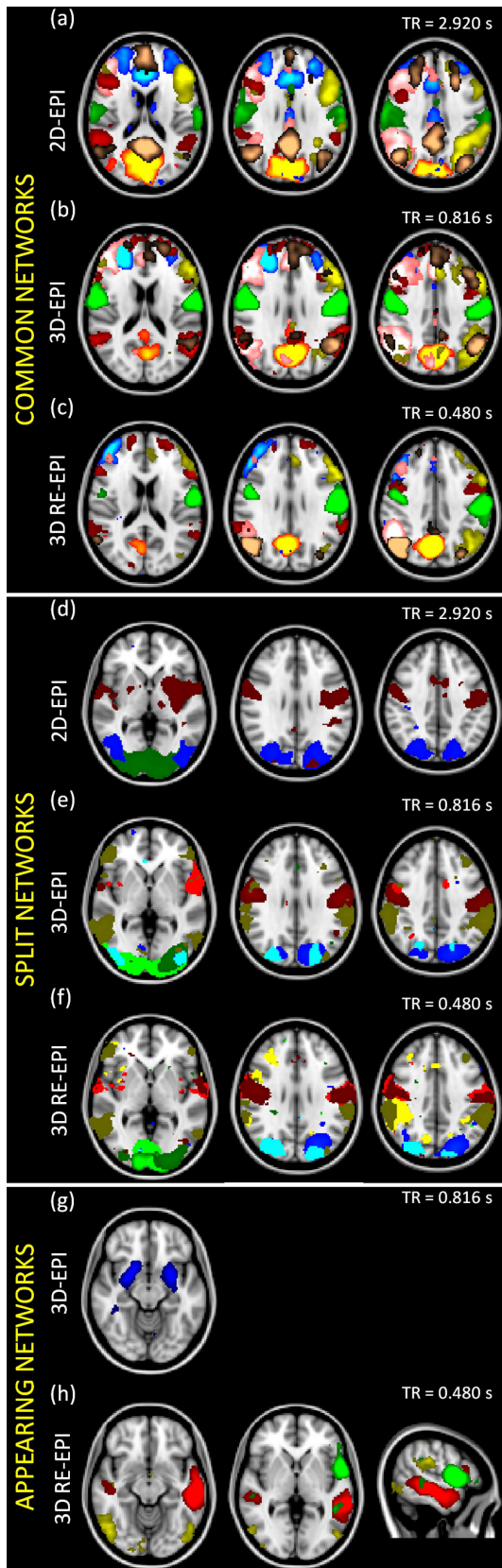
**Figure 4.10:** *Resting state networks shown overlaid on the MNI template. Resting state networks were categorized as common networks (**a**: 2D-EPI; **b**: 3D EPI; **c**: 3D RE-EPI), split networks (**d**: 2D-EPI; **e**: 3D EPI; **f**: 3D RE-EPI), or appearing networks (**g**: 3D EPI; **h**: 3D RE-EPI). **a-c**: Common networks, which were seen in all three acquisitions (medial visual [red-yellow], executive [blue-light blue], default mode [copper], ventral stream [red], sensory-motor [green], left lateral [yellow], and right lateral [pink]) are shown on axial slices at Montreal Neurological Institute (MNI) coordinates z = 18, 28, and 38. **d-f**: Split networks, which appear as multiple components in 3D EPI and/or 3D RE-EPI (lateral visual [dark green, green, and light green], auditory [dark red and light red], precuneus [dark blue and light blue], and task-positive network [brown and light yellow]) are shown on axial slices at MNI coordinates z = 0, 28, and 38. **g**: Appearing network only found in 3D EPI (medial temporal network [blue]) shown at MNI coordinate z = -12. **h**: Appearing networks only found in 3D RE-EPI (language [green], MT-centered visual [yellow], and a bilateral superior temporal sulcus, or secondary auditory network [red]) is shown at MNI coordinates z = -12, 0 and x = -54.*
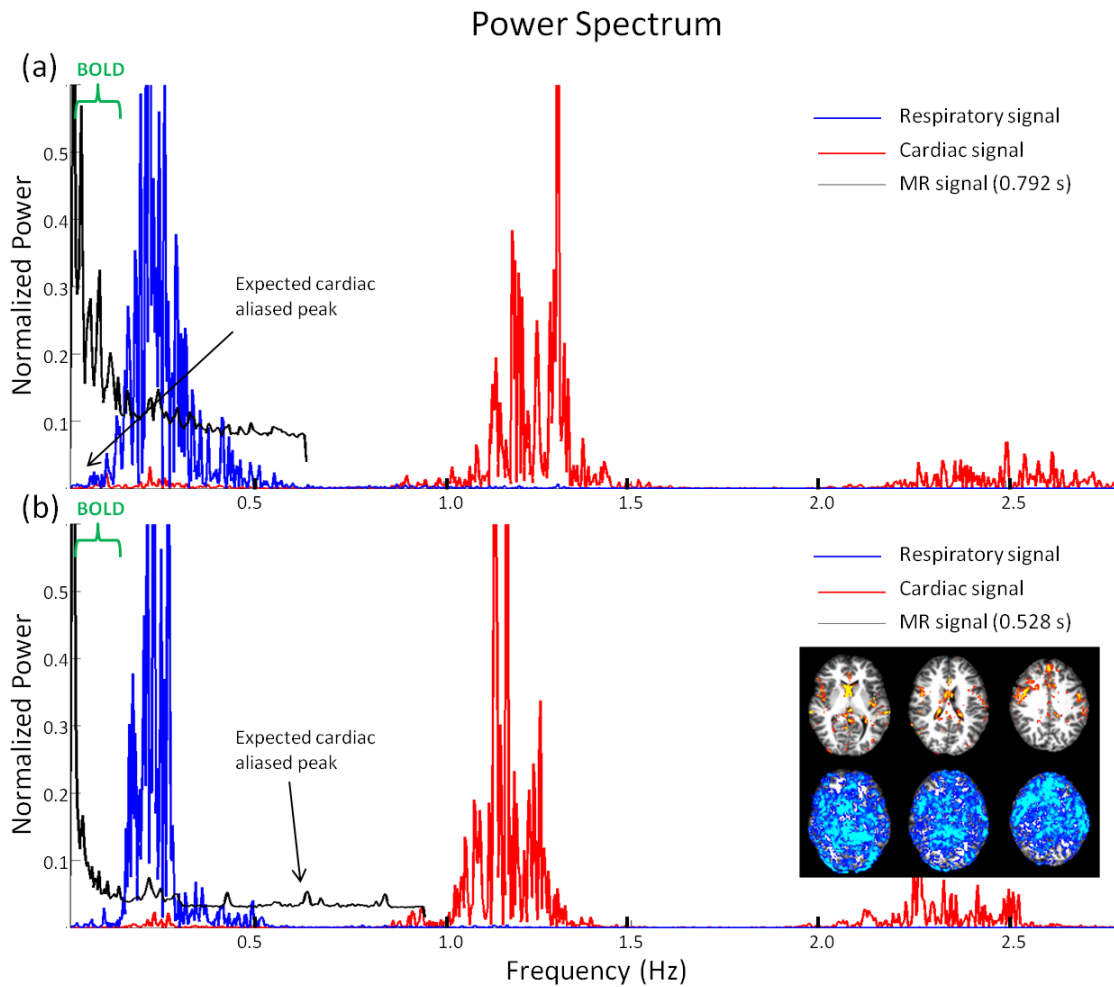
**Figure 4.11:** *Power spectral analysis of MR data acquired with (**a**) 3D EPI at a* $\text{TR}_{volume}$ *= 0.792 s and (**b**) 3D RE-EPI at a* $\text{TR}_{volume}$ *= 0.528 s. Separately acquired power spectra of respiratory activity (blue) and cardiac activity (red) are shown for both experiments. Note that BOLD signals are typically found in the 0.04-0.13 Hz frequency range. Inset: Overlay of pixels contributing signal variations at cardiac rate (upper row) and at respiratory rate (lower row) on three different representative slices from an anatomical dataset. A thresholded power spectrum with a spectral window of 0.66-0.70 Hz was used to create cardiac pixel overlay, whereas respiratory pixel overlay was created using a spectral window of 0.21-0.25 Hz.*

| Pulse Sequence | volume TR (s) | Temporal SNR (Gray matter) | Temporal SNR (White matter) |
|---|---|---|---|
| 2D EPI | 2.920 | $32.22 \pm 0.87$ | $14.71 \pm 1.32$ |
| 3D EPI | 0.816 | $43.78 \pm 3.04$ | $17.48 \pm 2.14$ |
| 3D RE-EPI | 0.480 | $53.81 \pm 3.89$ | $24.28 \pm 3.42$ |

**Table 4.2:** *Average tSNR per unit time values recorded in the gray matter and white matter brain regions using different sampling rates (volume TR) with 3D RE-EPI, 3D EPI, and 2D-EPI.*

**Physiological Signal Characterization**

The power spectra of the physiological signals along with the power spectra for the whole brain averaged fMRI time course are shown in Figure 4.11. Both 0.792 s (segmented 3D EPI, Figure 4.11a) and 0.528 s (3D RE-EPI, Figure 4.11b) sampling rates were sufficient to sample the first harmonic of respiratory signal (~0.23 Hz) without aliasing. The first harmonic of the cardiac signal (~1.20 Hz) was aliased at both the sampling rates. With the $TR_{volume}$ of 0.528 s (i.e. 1.89 Hz), the maximum frequency that could be sampled without aliasing was ~0.94 Hz, making the aliasing peak of the cardiac signal's first harmonic appear at 0.68 Hz (Figure 4.11b) which was away from the BOLD frequency range (0.04-0.13 Hz), whereas for the 3D EPI, the aliasing occurs at 0.06 Hz (Figure 4.11a), overlapping with the BOLD signal. The insets in Figure 4.11 show the thresholded power spectra images. The cardiac power was greater in the cerebrospinal fluid and in the proximity of large arterial vessels. In contrast, respiratory signals were observed throughout the brain, since respiration induced z-gradient variations could be observed over the entire brain region [146].

### 4.4.4 Discussion

3D RE-EPI provides a speed-up factor of 2 in the partition-encoding direction when two partitions per RF excitation are encoded at an expense of increased echo train length. It should be possible to encode more than two partitions per RF excitation if stronger gradients or higher phase-encode acceleration is employed. The total reduction of excitations achieved with 3D RE-EPI, with respect to what can be obtained with segmented 3D EPI, is related with the freedom in distributing the parallel imaging load between the through-plane (partition-encode) and in-plane (primary phase-encode) directions. Even though 3D RE-EPI doubles ETL ($S_{PU} = 2$) compared with segmented 3D EPI, thereby increasing the minimum achievable TR, acquisition speed-up is still achieved for fMRI studies. This is because the minimum TR is largely defined by TE, which should be kept at $\sim T_2^*$ for optimum BOLD signal sensitivity [147], resulting in the minimum TR increment by ETL/2 with 3D RE-EPI. Due to increased ETL, increased distortions are observed in the primary phase-encode direction. However, these distortions may be reduced by using the techniques developed for 2D-EPI [130, 148, 149].

SAR is one of the limiting factors when imaging at ultra-high field strengths. When accelerating 2D EPI by using multi-band excitations, the SAR increases linearly with the number of

simultaneously excited slices, which can limit the maximum SNR achievable. One alternative is to use *power independent of number of slices* (PINS) excitation pulses [142, 150] where the SAR is independent of the number of simultaneously acquired slices, but the number of slices excited simultaneously is infinite along the slice encoding direction (thus limited only by the physical dimension of the object and the coverage of the gradient and RF transmit coil along the slice-encode direction). Here, due to the reduced Ernst flip angles and quadratic dependence of SAR on them, the SAR deposition was reduced ~20-fold when compared with multi-slice 2D-EPI.

In addition to the higher temporal resolution, the new $k$-space sampling strategy results in a reduced number of excitations used to form the same 3D dataset compared to segmented 3D-EPI. This is advantageous because it has been shown that the maximum available temporal SNR with segmented 3D EPI decreases with increasing number of segments used [114]. Compared with the segmented 3D EPI, 3D RE-EPI results in a significant increase in tSNR, which explains the improvement in the detection of the RSNs shown in Figure 4.

To detect activation-induced BOLD responses, reducing the influence of signal fluctuations caused by cardiac pulsation and respiration is especially important at high SNR. The use of short TRs, as possible with 3D RE-EPI, enables better characterization of these nuisance sources that could then be removed: either by simple low-pass filtering or via the physiological noise reduction schemes [115, 116, 151]. The improvement in detection of RSNs with faster imaging by means of increased temporal resolution and tSNR was demonstrated in the multiplexed 2D EPI at 3T [136]. The results with 3D RE-EPI are consistent with those and are the first independent demonstrations at 7T that, with 3D imaging, the same principle holds true.

3D RE-EPI is expected to be of special benefit for fMRI applications where temporal resolution, more than spatial resolution, is a limiting factor [e.g., when studying rapid transient responses [152] or the shape of hemodynamic response function (HRF) or when targeting regions where cardiac pulsation plays an important role [153] not only in terms of signal intensity variation, but also in terms of motion]. Finally, at lower field strength, 3D RE-EPI is expected to perform better due to the reduced magnetic susceptibility effects and due to longer $T_2^*$, allowing acquisition of a larger number of $k$-space planes per segment.

### 4.4.5 Conclusions

We conclude that 3D RE-EPI, a novel acquisition scheme for 3D EPI that encodes two $k$-space planes per RF excitation, yields increased temporal resolution and better physiological signal characterization compared with 3D EPI while producing images with acceptable quality for fMRI studies. 3D RE-EPI (using 32-channel coil, combined with conventional parallel imaging acceleration methods) allowed up to an eight-fold reduction of the number of excitations needed to obtain full brain coverage. This reduction in the number of excitations translated in acquisition acceleration in fMRI studies and improved tSNR per unit time, which ultimately leads to an increase in the number of resting state networks being detected in 7T resting state

fMRI data.

# References

[101] P Mansfield. Multi-planar image formation using nmr spin echoes, 1977.

[102] B. Chapman, R. Turner, R. J. Ordidge, M. Doyle, M. Cawley, R. Coxon, P. Glover, and P. Mansfield. Real-time movie imaging from a single cardiac cycle by nmr. *Magnetic Resonance in Medicine*, 5(3):246–254, 1987.

[103] Andrew M. Peters, Matthew J. Brookes, Frank G. Hoogenraad, Penny A. Gowland, Susan T. Francis, Peter G. Morris, and Richard Bowtell. T2* measurements in human brain at 1.5, 3 and 7 t. *Magnetic Resonance Imaging*, 25(6):748 – 753, 2007. Proceedings of the International School on Magnetic Resonance and Brain Function Proceedings of the International School on Magnetic Resonance and Brain Function.

[104] M. K. Stehling, R. J. Ordidge, R. Coxon, and P. Mansfield. Inversion-recovery echo-planar imaging (ir-epi) at 0.5 t. *Magnetic Resonance in Medicine*, 13(3):514–517, 1990.

[105] Song Lai and Gary H. Glover. Three-dimensional spiral fmri technique: A comparison with 2d spiral acquisition. *Magnetic Resonance in Medicine*, 39(1):68–78, 1998.

[106] Yanle Hu and Gary H. Glover. Three-dimensional spiral technique for high-resolution functional mri. *Magnetic Resonance in Medicine*, 58(5):947–951, 2007.

[107] L. Tugan Muftuler and Orhan Nalcioglu. Improvement of temporal resolution in fmri using slice phase encode reordered 3d epi. *Magnetic Resonance in Medicine*, 44(3):485–490, 2000.

[108] B A Poser, P J Koopmans, T Witzel, L L Wald, and M Barth. Three dimensional echo-planar imaging at 7 tesla. *Neuroimage*, 51(1):261–6, 2010.

[109] Allen W. Song, Eric C. Wong, and James S. Hyde. Echo-volume imaging. *Magnetic Resonance in Medicine*, 32(5):668–671, 1994.

[110] P Mansfield, R Coxon, and J Hykin. Echo-volumar imaging (evi) of the brain at 3.0 t: first normal volunteer and functional imaging results. *J Comput Assist Tomogr*, 19(6):847–52, 1995.

[111] Wietske van der Zwaag, Susan Francis, and Richard Bowtell. Improved echo volumar imaging (evi) for functional mri. *Magnetic Resonance in Medicine*, 56(6):1320–1327, 2006.

[112] Stefan Posse, Elena Ackley, Radu Mutihac, Jochen Rick, Matthew Shane, Cristina Murray-Krezan, Maxim Zaitsev, and Oliver Speck. Enhancement of temporal resolution and bold sensitivity in real-time fmri using multi-slab echo-volumar imaging. *Neuroimage*, 61(1):115–30, 2012.

## REFERENCES

[113] Amir M. Abduljalil, Anthony H. Aletras, and Pierre-Marie Robitaille. 3d echo planar imaging: Application to the human head. *Magnetic Resonance in Medicine*, 34(2):144–148, 1995.

[114] W. van der Zwaag, J. P. Marques, T. Kober, G. Glover, R. Gruetter, and G. Krueger. Temporal snr characteristics in segmented 3d-epi at 7t. *Magnetic Resonance in Medicine*, 67(2):344–352, 2012.

[115] Gary H. Glover, Tie-Qiang Li, and David Ress. Image-based method for retrospective correction of physiological motion effects in fmri: Retroicor. *Magnetic Resonance in Medicine*, 44(1):162–167, 2000.

[116] Marta Bianciardi, Masaki Fukunaga, Peter van Gelderen, Silvina G. Horovitz, Jacco A. de Zwart, Karin Shmueli, and Jeff H. Duyn. Sources of functional magnetic resonance imaging signal fluctuations in the human brain at rest: a 7 t study. *Magnetic Resonance Imaging*, 27(8):1019 – 1029, 2009. Proceedings of the International School on Magnetic Resonance and Brain Function Proceedings of the International School on Magnetic Resonance and Brain Function.

[117] João Jorge, Patrícia Figueiredo, Wietske van der Zwaag, and José P. Marques. Signal fluctuations in fmri data acquired with 2d-epi and 3d-epi at 7 tesla. *Magnetic Resonance Imaging*, 31(2):212 – 220, 2013.

[118] Benjamin Zahneisen, Thimo Grotz, Kuan J. Lee, Sabine Ohlendorf, Marco Reisert, Maxim Zaitsev, and Jürgen Hennig. Three-dimensional mr-encephalography: Fast volumetric brain imaging using rosette trajectories. *Magnetic Resonance in Medicine*, 65(5):1260–1268, 2011.

[119] Benjamin Zahneisen, Thimo Hugger, Kuan J. Lee, Pierre LeVan, Marco Reisert, Hsu-Lei Lee, Jakob Assländer, Maxim Zaitsev, and Jürgen Hennig. Single shot concentric shells trajectories for ultra fast fmri. *Magnetic Resonance in Medicine*, 68(2):484–494, 2012.

[120] Avideh Zakhor. Optimal sampling and reconstruction of mri signals resulting from sinusoidal gradients. *Proc. SPIE*, 1199:1541–1555, 1989.

[121] H. Bruder, H. Fischer, H.-E. Reinfelder, and F. Schmitt. Image reconstruction for echo planar imaging with nonequidistant k-space sampling. *Magnetic Resonance in Medicine*, 23(2):311–323, 1992.

[122] F.H. Epstein, P.E. Licato, J.K. Maier, L.E. Ploetz, and X. Zhou. Method for producing an off-center image using an epi pulse sequence, November 18 1997. US Patent 5,689,186.

[123] G. Goertler and F. Schmitt. Method for suppressing image artifacts in a magnetic resonance imaging apparatus, August 11 1992. US Patent 5,138,259.

[124] A. Jesmanowicz, E. E. Wong, and J. S. Hyde. Phase correction for epi using internal reference lines. In *Proceedings 12th Annual SMRM*, page 1239, 1993.

[125] E. C. Wong. Shim insensitive phase correction for epi using a two echo reference scan. In *Proceedings 11th Annual SMRM*, page 4514, 1992.

[126] A Zakhor. Ghost cancellation algorithms for mri images. *IEEE Trans Med Imaging*, 9(3):318–26, 1990.

[127] Xiaoping Hu and Tuong Huu Le. Artifact reduction in epi with phase-encoded reference scan. *Magnetic Resonance in Medicine*, 36(1):166–171, 1996.

[128] Wietske van der Zwaag, José P. Marques, Hongxia Lei, Nathalie Just, Tobias Kober, and Rolf Gruetter. Minimization of nyquist ghosting for echo-planar imaging at ultra-high fields based on a "negative readout gradient" strategy. *Journal of Magnetic Resonance Imaging*, 30(5):1171–1178, 2009.

[129] Roland Bammer, Martin Auer, Stephen L. Keeling, Michael Augustin, Lara A. Stables, Rupert W. Prokesch, Rudolf Stollberger, Michael E. Moseley, and Franz Fazekas. Diffusion tensor imaging using single-shot sense-epi. *Magnetic Resonance in Medicine*, 48(1):128–136, 2002.

[130] Peter Jezzard and Robert S. Balaban. Correction for geometric distortion in echo planar images from b0 field variations. *Magnetic Resonance in Medicine*, 34(1):65–73, 1995.

[131] Mayur Narsude, Wietske van der Zwaag, Tobias Kober, Rolf Gruetter, and José P. Marques. Improved temporal resolution for functional studies with reduced number of segments with three-dimensional echo planar imaging. *Magnetic Resonance in Medicine*, pages n/a–n/a, 2013.

[132] David J. Larkman, Joseph V. Hajnal, Amy H. Herlihy, Glyn A. Coutts, Ian R. Young, and Gösta Ehnholm. Use of multicoil arrays for separation of signal from multiple slices simultaneously excited. *Journal of Magnetic Resonance Imaging*, 13(2):313–317, 2001.

[133] Kawin Setsompop, Borjan A. Gagoski, Jonathan R. Polimeni, Thomas Witzel, Van J. Wedeen, and Lawrence L. Wald. Blipped-controlled aliasing in parallel imaging for simultaneous multislice echo planar imaging with reduced g-factor penalty. *Magnetic Resonance in Medicine*, 67(5):1210–1224, 2012.

[134] R. Nunes, J. Hajnal, D. Larkman, and X. Golay. Simultaneous slice excitation and reconstruction for single shot epi. In *Proceedings 13th Scientific Meeting, International Society for Magnetic Resonance in Medicine, Seattle*, page 293, 2006.

[135] Steen Moeller, Essa Yacoub, Cheryl A. Olman, Edward Auerbach, John Strupp, Noam Harel, and Kâmil Uğurbil. Multiband multislice ge-epi at 7 tesla, with 16-fold acceleration using partial parallel imaging with application to high spatial and temporal whole-brain fmri. *Magnetic Resonance in Medicine*, 63(5):1144–1153, 2010.

[136] David A. Feinberg, Steen Moeller, Stephen M. Smith, Edward Auerbach, Sudhir Ramanna, Matt F. Glasser, Karla L. Miller, Kamil Ugurbil, and Essa Yacoub. Multiplexed echo

# REFERENCES

planar imaging for sub-second whole brain fmri and fast diffusion imaging. *PLoS ONE*, 5(12):e15710, 2010.

[137] David A. Feinberg, Timothy G. Reese, and Van J. Wedeen. Simultaneous echo refocusing in epi. *Magnetic Resonance in Medicine*, 48(1):1–5, 2002.

[138] José P. Marques, Tobias Kober, Gunnar Krueger, Wietske van der Zwaag, Pierre-François Van de Moortele, and Rolf Gruetter. Mp2rage, a self bias-field corrected sequence for improved segmentation and t1-mapping at high field. *NeuroImage*, 49(2):1271 – 1281, 2010.

[139] Florent Eggenschwiler, Tobias Kober, Arthur W. Magill, Rolf Gruetter, and José P. Marques. Sa2rage: A new sequence for fast b1+-mapping. *Magnetic Resonance in Medicine*, 67(6):1609–1619, 2012.

[140] Christian F. Beckmann, Marilena DeLuca, Joseph T. Devlin, and Stephen M. Smith. Investigations into resting-state connectivity using independent component analysis. *Philosophical Transactions of the Royal Society B: Biological Sciences*, 360(1457):1001–1013, May 2005.

[141] Bharat Biswal, F. Zerrin Yetkin, Victor M. Haughton, and James S. Hyde. Functional connectivity in the motor cortex of resting human brain using echo-planar mri. *Magnetic Resonance in Medicine*, 34(4):537–541, 1995.

[142] P.J. Koopmans, R. Boyacioglu, M. Barth, and Prof.Dr. D.G. Norris. Whole brain, high resolution spin-echo resting state fmri using pins multiplexing at 7 t. *Neuroimage*, 62(3):1939 – 1946, 2012.

[143] F De Martino, F Esposito, PF van de Moortele, N Harel, E Formisano, R Goebel, K Ugurbil, and E Yacoub. Whole brain high-resolution functional imaging at ultra high magnetic fields: an application to the analysis of resting state networks. *NeuroImage*, 57(3):1031 – 1044, 2011.

[144] Ilya M. Veer, Christian Beckmann, Marie-Jose Van Tol, Luca Ferrarini, Julien Milles, Dick Veltman, Andre Aleman, Mark A Van Buchem, Nic J A Van Der Wee, and Serge A R Rombouts. Whole brain resting-state analysis reveals decreased functional connectivity in major depression. *Frontiers in Systems Neuroscience*, 4(41), 2010.

[145] Elena Shumskaya, Teuntje M J C Andriessen, David G Norris, and Pieter E Vos. Abnormal whole-brain functional networks in homogeneous acute mild traumatic brain injury. *Neurology*, 79:175 – 182, 2012.

[146] Pierre-François Van de Moortele, Josef Pfeuffer, Gary H. Glover, Kamil Ugurbil, and Xiaoping Hu. Respiration-induced b0 fluctuations and their spatial distribution in the human brain at 7 tesla. *Magnetic Resonance in Medicine*, 47(5):888–895, 2002.

[147] Wietske van der Zwaag, José P Marques, Martin Hergt, and Rolf Gruetter. Investigation of high-resolution functional magnetic resonance imaging by means of surface and array radiofrequency coils at 7 t. *Magnetic resonance imaging*, 27(8):1011–1018, 2009.

[148] M. Zaitsev, J. Hennig, and O. Speck. Point spread function mapping with parallel imaging techniques and high acceleration factors: Fast, robust, and flexible method for echo-planar imaging distortion correction. *Magnetic Resonance in Medicine*, 52(5):1156–1166, 2004.

[149] Huairen Zeng and R. Todd Constable. Image distortion correction in epi: Comparison of field mapping with point spread function mapping. *Magnetic Resonance in Medicine*, 48(1):137–146, 2002.

[150] David G. Norris, Peter J. Koopmans, Rasim Boyacioğlu, and Markus Barth. Power independent of number of slices (pins) radiofrequency pulses for low-power simultaneous multislice excitation. *Magnetic Resonance in Medicine*, 66(5):1234–1240, 2011.

[151] Marta Bianciardi, Peter van Gelderen, Jeff H. Duyn, Masaki Fukunaga, and Jacco A. de Zwart. Making the most of fmri at 7 t by suppressing spontaneous signal fluctuations. *NeuroImage*, 44(2):448 – 454, 2009.

[152] Onur Afacan, W. Scott Hoge, Firdaus Janoos, Dana H. Brooks, and Istvan A Morocz. Rapid full-brain fmri with an accelerated multi shot 3d epi sequence using both unfold and grappa. *Magnetic Resonance in Medicine*, 67(5):1266–1274, 2012.

[153] A.R. Guimaraes, J.R. Melcher, T.M. Talavage, J.R. Baker, P. Ledden, B.R. Rosen, N.Y.S. Kiang, B.C. Fullerton, and R.M. Weisskoff. Imaging subcortical auditory activity in humans. *Human Brain Mapping*, 6(1):33–41, 1998.

# 5 Parallel Magnetic Resonance Imaging

In the late 1990s, researchers demonstrated that MR imaging could be dramatically accelerated using techniques other than incremental improvements in gradient technology and pulse sequence designs [154, 155]. These new techniques employ sophisticated image reconstruction algorithms and arrays of coils wherein each coil would independently and simultaneously image a given volume — hence the name *parallel imaging*. Parallel imaging is arguably the most striking innovation of last decade in the world of MRI, promising dramatic gains in imaging speed, a reduction in motion and susceptibility artifacts, and ultimately increasing the throughput of clinical and research scanners.

This chapter begins with discussion of founding concepts of *parallel MRI* (pMRI), in which the role of coil arrays in pMRI is explained first. A mathematical treatment of the image aliasing arising due to under-sampling of $k$-space is provided next, followed by parallel imaging reconstruction algorithms used to resolve such image aliasing. While explaining pMRI algorithms, we begin with a simplified example and quickly move towards explaining more advanced parallel imaging techniques. Though a wide range of pMRI techniques have been developed by various research groups, we limit the scope of our discussion to only a few (namely SMASH, SENSE, and GRAPPA) which lay a sufficient foundation to understand other pMRI variants. Later part of the chapter explains the use of controlled aliasing during pMRI acquisition to improve the image SNR by making effective use of coil sensitivity variations provided by array coils.

## 5.1 Basic Concepts of Parallel Imaging

### 5.1.1 Coil Array

Coil array is introduced in Section 2.2.3 of this manuscript. In pMRI, the signal is acquired using an array of $N$ receiver coils with distinct spatial sensitivities (coil array). This brings an additional information about the spatial position of the received signal which is used to partially replace time-consuming Fourier encoding steps achieved through gradient playouts

**Figure 5.1:** *Magnitude images acquired using a 3D GRE sequence with different spatial sensitivity information obtained with 8 independent receiver channels of a 8-channel phased array coil. The combined magnitude image using sum of squares technique is displayed in the center.*
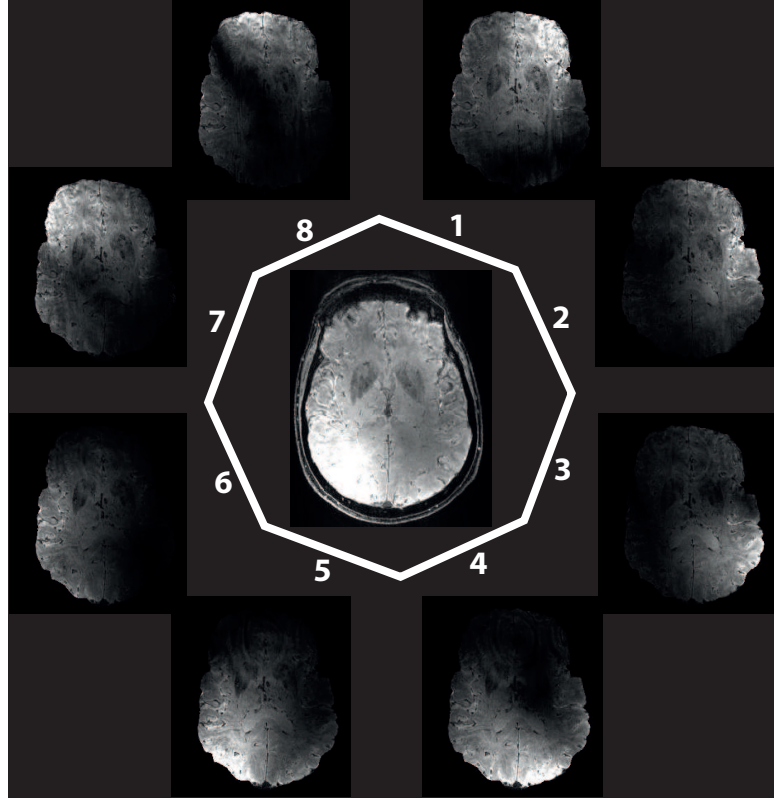
and thus reducing the total time of signal acquisition [156–159]. For multiple channel receiver, all coils simultaneously acquire the signal and hence does not incur any additional penalty in terms of signal acquisition time when compared to the same acquisition performed by a single channel coil. Different channels of a phased array coil acquire signal with different receive sensitivities.

For an ideal receiver array (i.e. for a noiseless reception), the signal $S_n$ received by the $n$-th receiver from the coil array is:

$$S_n(x, y) = S(x, y) C_n(x, y) \tag{5.1}$$

where $C_n(x, y)$ is the sensitivity of the $n$-th receiver and $S(x, y)$ is the signal received by the coil with homogeneous receive sensitivity. Figure 5.1 demonstrates different magnitude images acquired using a 3D gradient echo (GRE) sequence with different spatial sensitivity information obtained with 8 independent receiver channels of a 8-channel phased array coil. The combined magnitude image using *sum of squares* technique [160] is displayed in the center.

90
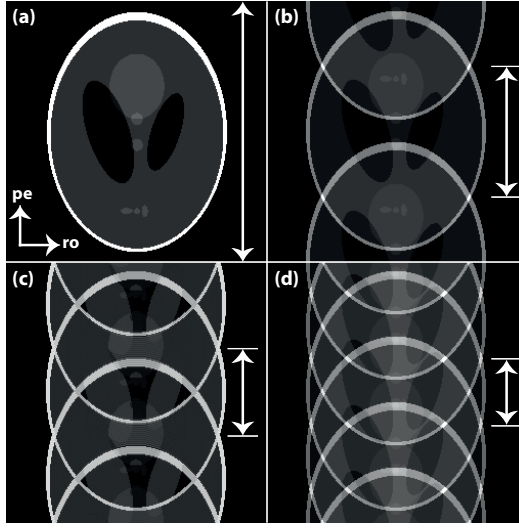
**Figure 5.2:** *Aliasing effects on image due to reduced field of view. The image (a) has full FOV (R = 1). The phase-encoding sampling density is reduced by a factor (b) 2, (c) 3, and (d) 4. This causes aliasing that is visible as a "fold-over" or a "wrap-around" effect in images (b), (c) and (d). The actual span of the FOV is indicated by arrow span on the right of each image.*

### 5.1.2 Aliasing with Parallel MRI

In parallel MRI, the distance between successive the phase-encoding lines ($\Delta k_y$) is increased by an *acceleration factor R,* while keeping the maximum and the minimum extent of the $k$-space unchanged to keep the image spatial resolution the same. As a result of this *under-sampling,* the number of phase-encoding steps $N_{pe}$ is reduced by a factor $R$ but the maximum gradient strength $N_{pe}G_{pe}$ remains the same. Increasing $\Delta k_y$, reduces the field of view according to Equation (3.17) and causes *aliasing* in the image. Different image aliasing patterns caused due to varying acceleration factors used along the phase-encoding direction are illustrated in Figure 5.2.

Image aliasing caused due to $k$-space under-sampling can be explained mathematically by performing inverse Fourier transformation of $k$-space in the read-out direction in advance to simplify the equations. This is possible because 2D Fourier transformation is separable and FOV reduction is expected to occur only the direction of the under-sampling i.e. phase-encoding direction in our case. The aliased image $S_{acc}$ obtained with an acceleration factor $R$ is an inverse Fourier transformation of under-sampled $k$-space $s_{acc}$ in the y-direction (see Equation (3.19)):

$$S_{acc}\left(x, y\right) = DFT_y^{-1} s_{acc}\left(x, k_y\right)$$
$$= \frac{R}{N_{pe}} \sum_{k_y=0,R,2R,...}^{N_{pe}-R} s\left(x, k_y\right) e^{ik_y y} \tag{5.2}$$

Note that only every $R$-th line is taken into account in the equation above. The $k$-space $s$ is

transformed back to the image-domain

$$
\begin{aligned}
S_{\mathrm{acc}}(x,y) &= \frac{R}{N_{\mathrm{pe}}} \sum_{k_y=0,R,2R,\ldots}^{N_{\mathrm{pe}}-R} e^{ik_y y} \sum_{y'=0}^{N_{\mathrm{pe}}-1} S(x,y') e^{-ik_y y'} \\
&= \frac{R}{N_{\mathrm{pe}}} \sum_{y'=0}^{N_{\mathrm{pe}}-1} S(x,y') \sum_{k_y=0,R,2R,\ldots}^{N_{\mathrm{pe}}-R} e^{ik_y y} e^{-ik_y y'} \\
&= \frac{R}{N_{\mathrm{pe}}} \sum_{y'=0}^{N_{\mathrm{pe}}-1} S(x,y') \sum_{k_y=0,1,2,\ldots}^{N_{\mathrm{pe}}/R-1} e^{ik_y y} e^{-ik_y y'}
\end{aligned}
\tag{5.3}
$$

The functions $e^{ik_y y}$ and $e^{-ik_y y'}$ are orthogonal and the sum over $k_y$ for $R=1$ produces zero for all $y \neq y'$. For simplicity, we assume that the function $N_{\mathrm{pe}}/R$ is integer. For $R=1$ the exponential functions are summed to a sum of $R$ Kronecker delta functions in an aliasing equation,

$$
\begin{aligned}
S_{\mathrm{acc}}(x,y) &= \sum_{y'=0}^{N_{\mathrm{pe}}-1} \sum_{r=0}^{R-1} \delta_{\left(y', y \bmod \frac{N_{\mathrm{pe}}}{R} + r \frac{N_{\mathrm{pe}}}{R}\right)} S(x,y') \\
&= \sum_{r=0}^{R-1} S\left(x, y \bmod \frac{N_{\mathrm{pe}}}{R} + r \frac{N_{\mathrm{pe}}}{R}\right)
\end{aligned}
\tag{5.4}
$$

Each value in the aliased image $S_{\mathrm{acc}}$ is a superposition of $R$ successively shifted images, shifted by a factor $\frac{\mathrm{FOV}_y}{R}$.

### 5.1.3 Geometry Factor (g-factor)

When an array coil is used for reception, to take into account possible differences in noise levels and the noise correlation between different coil elements, the receiver noise correlation matrix $\psi$ is included in the reconstruction:

$$
\rho' = \left(C^H \psi^{-1} C\right)^{-1} C^H \psi^{-1} S
\tag{5.5}
$$

where $\rho'$ is the reconstructed estimate of intrinsic signal $\rho$. The matrix $\psi$ is estimated by acquiring noise-only data in the absence of excitation RF pulse. If $\eta_i$ denote the noise-only signal acquired by coil $i$, the $(i,j)^{\mathrm{th}}$ entry of matrix $\psi$ can be calculated using the relation

$$
\psi_{\mathrm{ij}} = \overline{\eta_i \eta_j^*}
\tag{5.6}
$$

where the bar indicates temporal averaging.

Parallel imaging approach, by default, suffers from an SNR loss by a factor of $\sqrt{R}$ due to reduced Fourier averaging. In addition, the SNR of reconstructed images depends upon how well the matrix inversion (Equation (5.5)) can be performed, which in turn depends on how different the coil sensitivities are at the location of the aliased pixels. Therefore, an additional term needs to be taken into account to compare SNR of images obtained with parallel imaging

to that of fully Fourier encoded images. This additional term is mainly dependent on the geometry of the receiver coil array and, therefore, is called *geometry factor* or *g-factor* [154]. Thus, the SNR in the final image acquired with parallel imaging approach is:

$$\text{SNR}_{\text{PI}} = \frac{\text{SNR}_{\text{full}}}{\sqrt{R} \cdot g} \tag{5.7}$$

where $\text{SNR}_{\text{PI}}$ is SNR of images acquired with parallel imaging, $\text{SNR}_{\text{full}}$ is SNR of fully Fourier encoded images, $R$ is the acceleration factor, and $g$ is the g-factor.

The noise amplification described by the g-factor is also related to a property of the matrix $C^H \psi^{-1} C$ that is inverted, called its *conditioning*. If the coil sensitivity values provided by different channels of a receive array coil are almost the same at certain spatial locations, a poorly conditioned matrix can result. A poorly conditioned matrix amplifies the noise in the unwrapped SENSE images. The noise amplification for a poorly conditioned matrix can be reduced by a process called *regularization* [161]. The amount of regularization can be adjusted to reduce noise at the expense of additional uncorrected aliasing. Regularization can be optimized for each pixel to give more uniform SNR.

The g-factor has become a standard method of assessing image fidelity obtained through any parallel imaging reconstruction. For example, when SENSE algorithm is used (see Section 5.2.2), the g-factor $g_p$ at a pixel $p$ can be calculated directly from

$$g_p = \sqrt{\left[\left(C^H \psi^{-1} C\right)^{-1}\right]_p \left[\left(C^H \psi^{-1} C\right)\right]_p} \tag{5.8}$$

A similar quantitative g-factor calculation is discussed for GRAPPA reconstruction algorithm in Section 5.2.5 (see Equation (5.17)).

## 5.2 Parallel Imaging Techniques

### 5.2.1 A Simplified pMRI Example

Let us begin with a simplified example of pMRI which, of course, is never encountered in practice but nonetheless helps in building basic foundations for understanding parallel imaging approach. In this simplified example, an array of 2 independent receiver coils (Figure 5.3(a)), each covering one half of the FOV with a boxcar-type sensitivity profile $C_k$ in phase-encoding direction (Figure 5.3(b)) is considered.

Due to ideal decoupling between coil elements, coil 1 detects only the top half of the object, whereas coil 2 detects only the bottom half (Figure 5.3(c)). Theoretically, only half of the FOV is required to be imaged by these individual coil elements. Coil 1 can acquire top half of the image whereas coil 2 can acquire bottom half (Figure 5.3(c)). In other words, the distance between individual $k$-spaces acquired by these two coils can be increased by a factor of 2 while
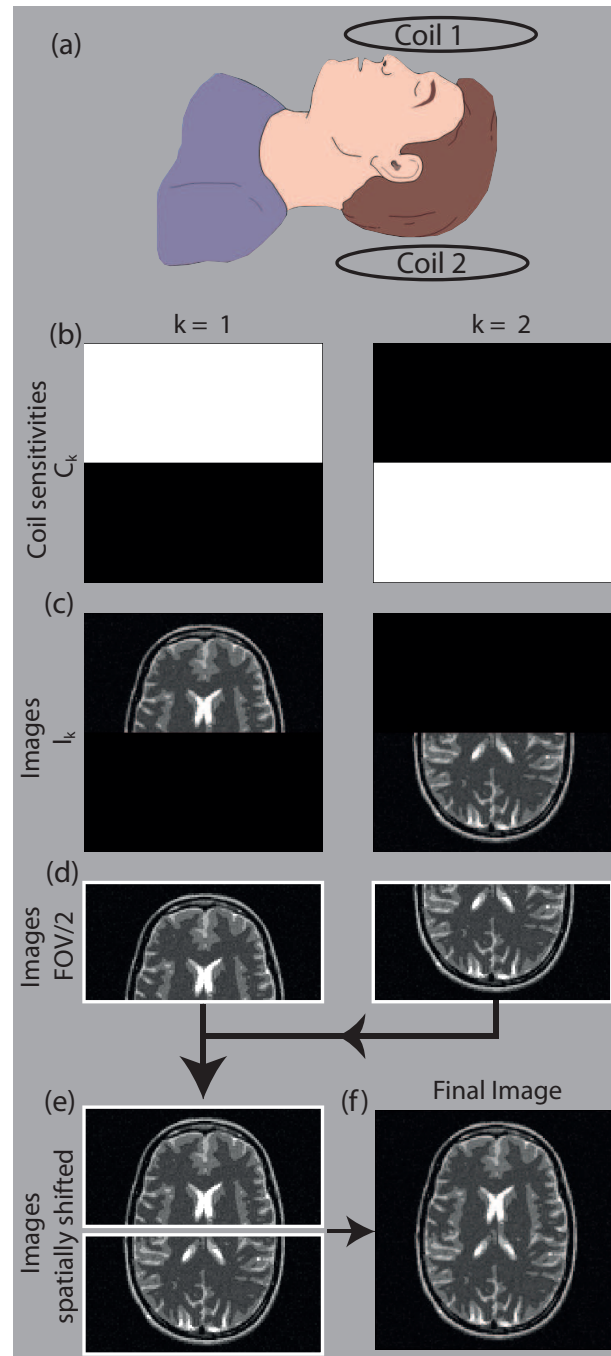
**Figure 5.3:** *(a) Two coil elements are placed in anterior and posterior portion of the human head. (b) Due to ideal decoupling between coil element, the sensitivity profiles of the two coil elements have boxcar shapes. (c) Coil 1 detects only the top half whereas coil 2 detects only the bottom half of the image, making half of the FOV redundant in both the images. (d) Acquisition time of the image can be reduced by half for such a coil array geometry by reducing the FOV by half for each of the coil elements i.e. by increasing the distance between k-space lines by a factor of 2 but still acquiring the full extent of the k-space as before to maintain the image resolution. (e-f) The two half-FOV images can be spatially shifted and combined to create the final desired image in this ideal parallel imaging example.*

keeping the extent of the $k$-spaces intact to maintain the image resolution. Since both these coils operate simultaneously, the required $k$-space data is acquired in half the amount of time as compared to a fully Fourier encoded single coil acquisition to obtain the same image (Figure 5.3(d)). Full FOV image can easily be produced by spatially shifting and concatenating these individual half-FOV images during the final reconstruction step (Figure 5.3(e-f)). An adverse effect of using pMRI is $\sqrt{2}$ reduction in image SNR due to reduction in Fourier encoding steps ($k$-space lines) by a factor of 2.

This example, however, is an idealized one and such boxcar-type sensitivities are never possible to obtain. Though impossible in practice, this example provides an intuitive understanding of parallel imaging.

### 5.2.2  SENSitivity Encoding (SENSE)

As explained in Section 5.1.2, the result of regular under-sampling of Cartesian data is spatial aliasing at regular interval. Under-sampling by a factor $R$ results in signals from $R$ equally spaced spatial locations along the under-sampled direction to overlap in the image. To simplify the discussion, the case of an acceleration factor $R = 2$ with a set of only two coils is considered here. For a pixel at location $(x, y)$ in the aliased image, the signal measured by each of the two coils is given by:

$$
\begin{aligned}
S_1\left(x,y\right) &= C_1\left(x,y\right)\rho\left(x,y\right) + C_1\left(x, y + \frac{\text{FOV}}{2}\right)\rho\left(x, y + \frac{\text{FOV}}{2}\right) \\
S_2\left(x,y\right) &= C_2\left(x,y\right)\rho\left(x,y\right) + C_2\left(x, y + \frac{\text{FOV}}{2}\right)\rho\left(x, y + \frac{\text{FOV}}{2}\right)
\end{aligned}
\tag{5.9}
$$

This system of equations is shown pictorially in Figure 5.4. Here $S$ denotes an aliased signal, $C$ are the coil sensitivities, and $\rho$ is the spin density of the object. The equation above can be written in matrix form as:

$$
S = C\rho
\tag{5.10}
$$

where $C$ is a matrix with a size $N \times R$ (i.e. the number of coils × the acceleration factor). The system of equations as provided by Equation (5.9) is readily solvable if $N \geq R$.

By accurately measuring coil sensitivities $C_1$ and $C_2$, and more importantly if these two coil sensitivity profiles are different, one can solve the system of linear equations mentioned in (5.9). Though for simplicity only two coil array is considered in the discussion here, in general larger number of coils are used in an array, allowing the use of higher acceleration factors to further increase the speed of acquisition. For example, a 32-channel receiver coil is used for reception for experiments discussed in Chapter 6 for a net parallel imaging acceleration factor 10 while still maintaining acceptable image quality. The use of significantly larger number of coils than the acceleration factor employed provides a vastly over-determined systems of
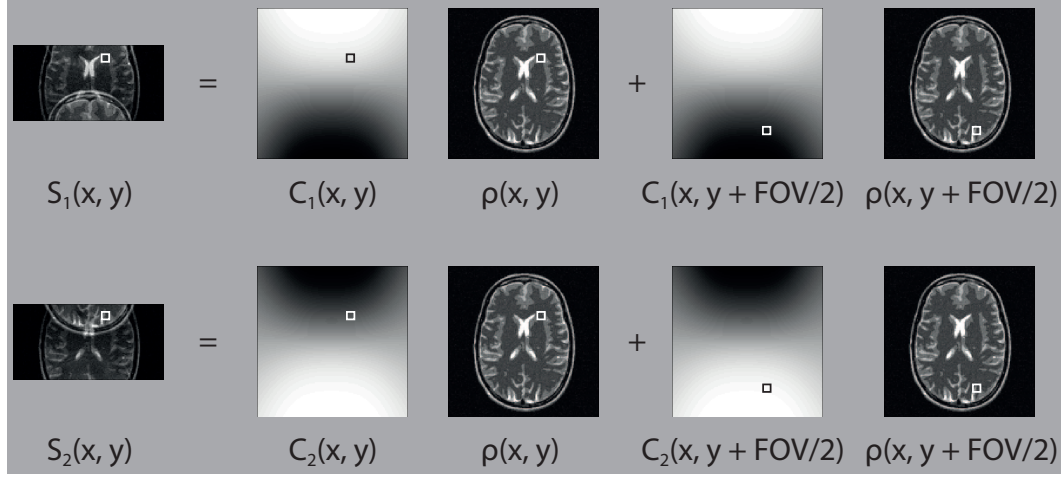
**Figure 5.4:** *A pictorial representation of under-sampled signal obtained using different coil elements of a 2-channel coil array. $S_1(x, y)$ is aliased image obtained from coil 1 whereas $S_2(x, y)$ is aliased image obtained from coil 2. An aliased pixel location in these aliased images contains image information from two separate locations, which are half the field of view distance apart in the under-sampled direction, multiplied by respective coil sensitivity at those locations.*

equations and improves the numerical condition of the matrix inversion.

### 5.2.3 SiMultaneous Acquisition of Spatial Harmonics (SMASH)

The underlying concept used in SMASH algorithm is that a linear combination of the individual coil sensitivities of the receiver array can be used to generate missing phase-encoding steps [155]. In SMASH, the sensitivity values $C_k(x, y)$ are combined with appropriate linear weights $n_k^{(m)}$ to generate composite sensitivity variations of the order m (Figure 5.5):

$$C_m^{comp}(x, y) = \sum_{k=1}^{N_c} n_k^{(m)} C_k(x, y) \cong e^{im\Delta k_y y} \tag{5.11}$$

where $N_c$ is number of coils elements in an array coil. The only unknowns in the Equation (5.11) are the linear weights $n_k^{(m)}$, which can be estimated by fitting (e.g., least square fit) the coil sensitivity profiles $C_k$ to the spatial harmonic $e^{im\Delta k_y y}$ of order $m$. The component coil signal $S_k(k_y)$ in the phase-encoding direction, which is received in coil $k$, is the Fourier transformation of the spin density $\rho(y)$ weighted with the corresponding coil sensitivity profile $C_k(y)$:

$$S_k(k_y) = \int \rho(y) e^{ik_y y} dy \tag{5.12}$$

W = +1    W = +1    W = +1    W = +1          W = +1    W = -1    W = +1    W = -1
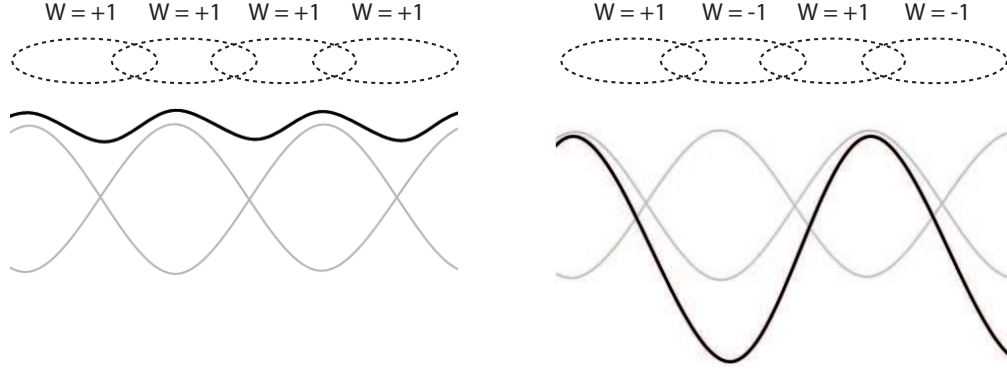
**Figure 5.5:** *A pictorial representation of combining coil sensitivities with appropriate linear weights to generate composite sensitivity as is done for SMASH reconstruction. Four coil elements (dotted ellipses) are assumed which are placed linearly. Left hand side schematic shows an example of low-order composite sensitivity (solid line) generation where thin curves indicate individual sensitivity profiles of underlying coils. Similarly, an example of high order composite sensitivity variation is shown on the right.*

Using Equations (5.11) and (5.12), an expression can be derived to generate shifted $k$-space lines $S(k_y + \Delta k_y)$ from weighted combinations of measured component coil signals $S_k(k_y)$.

$$
\begin{aligned}
\sum_{k=1}^{N_c} n_k^{(m)} \cdot S_k(k_y) &= \int \rho(y) \sum_{k=1}^{N_c} n_k^{(m)} C_k(y) e^{ik_y y} dy \\
&= \int \rho(y) e^{im\Delta k_y y} e^{ik_y y} dy \\
&= S^{\text{comp}}(k_y + m\Delta k_y)
\end{aligned}
\tag{5.13}
$$

Equation (5.13) is the basic SMASH relation and states that linear combinations of component coils can be used to synthesize missing $k$-space lines from adjacent acquired $k$-space lines which otherwise (in case of non-parallel acquisition) would be acquired through application of the phase-encoding gradients.

As one can figure out, this approach is applicable only if the coils are arranged in a linear fashion in an array. The application of SMASH, for this reason, is very limited and further advances based on this concept are discussed next.

### 5.2.4   AUTO-SMASH and VD-AUTO-SMASH

In AUTO-SMASH, the component coil sensitivities are estimated by acquiring a smaller subset of fully sampled central $k$-space region, known as *auto-calibration signal* (ACS) in addition to under-sampled $k$-space data [162]. The AUTO-SMASH approach is illustrated in Figure 5.6(b) for a reduction factor $R = 3$. Typically, $R$-1 ACS lines are acquired in the center of $k$-space at positions $m\Delta k_y y$, where $m$ counts from 1 to $R$-1. The linear weights $n_k^{(m)}$ required to synthesize the missing $k$-space lines are derived from the ACS lines $S_k^{\text{ACS}}$. The component

(a)  Fully sampled k-space          (b)          AUTO-SMASH          (c)          VD-AUTO-SMASH
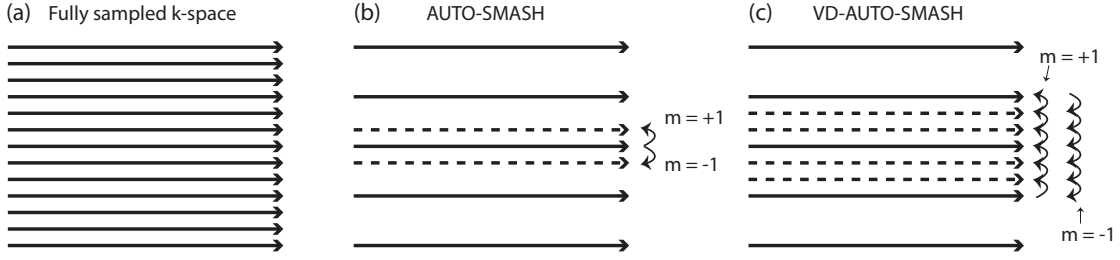


**Figure 5.6:** *(a) A fully sampled k-space is shown with each horizontal arrow indicating a single line of k-space. (b) In AUTO-SMASH, the central R−-1 auto-calibration lines are additionally acquired to derive coil weights for k-space shifts +Δk (m = +1) and -Δk (m = -1). In this example, 2 auto-calibration lines (dotted) are acquired since R is 3. Solid lines forms the under-sampled k-space. (c) In VD-AUTO-SMASH, multiple auto-calibration lines are acquired to derive the coil weights for a k-space shift more accurately.*

coil images which correspond to $k$-space shift of $m\Delta k_y$ should be equal to the weighted combination of auto-calibration profile corresponding to the same shift $m\Delta k_y$.

$$
\begin{aligned}
S^{\text{comp}}\left(k_y + m\Delta k_y\right) &= \sum_{k=1}^{N_c} S_k^{\text{ACS}}\left(k_y + m\Delta k_y\right) \\
&\cong \sum_{k=1}^{N_c} n_k^{(m)} S_k\left(k_y\right)
\end{aligned}
\tag{5.14}
$$

A set of linear weights $n_k^{(m)}$ can be derived by solving Equation (5.14), which can be used to derive missing $k$-space lines. Once all the missing $k$-space lines in an under-sampled $k$-space data are synthesized, a full FOV image can be produced by applying inverse Fourier transformation.

In *Variable Density AUTO-SMASH* (VD-AUTO-SMASH) approach (Figure 5.6(c)) [163], the number of fits to derive the weights $n_k^{(m)}$ are significantly increased by acquiring multiple ACS lines instead of only $R$-1 number of lines as is done in Auto-SMASH approach. Among all the approaches discussed so far, VD-AUTO-SMASH provides the most accurate image reconstruction even in the presence of noise and imperfect coil performance. To add to the image reconstruction quality, acquired ACS lines can be integrated with final $k$-space data thus partially replacing synthesized $k$-space lines by actually acquired $k$-space lines.

### 5.2.5   Generalized Auto-calibrating Partially Parallel Acquisition (GRAPPA)

Unlike SENSE, which is an image domain reconstruction procedure, GRAPPA is a pure $k$-space domain reconstruction method [164]. It is essentially a more generalized approach of parallel imaging reconstruction using the same principles as VD-AUTO-SMASH, except the way linear weights are derived for the desired $k$-space shifts. During GRAPPA reconstruction procedure, the component coil signals $S_k(k_y)$ are fit to just a single component coil ACS signal
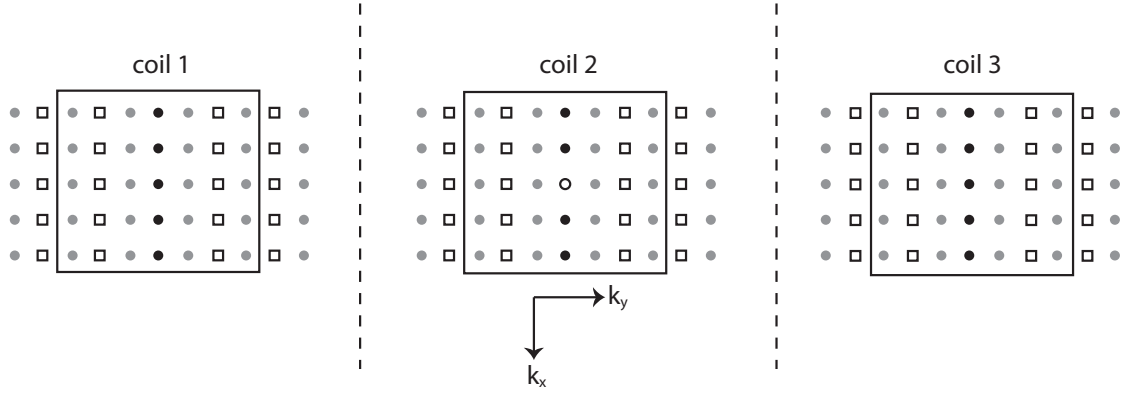
**Figure 5.7:** *An illustration for a 5×4 GRAPPA reconstruction kernel for an acceleration factor of 2 with three coils. Gray dots indicate acquired k-space samples. Black dots indicate auto-calibration signal (ACS) samples acquired, whereas empty squares indicate un-acquired (skipped) k-space samples. Fitting process is performed on the ACS lines to derive weights that relate a particular sample to its neighboring samples. For example, for the kernel size (5×4) shown here, in order to fit central ACS sample point (shown by empty circle) of coil 2, all the points of all the three coils within the black box would be used.*

$S_l^{\mathrm{ACS}}(k_y + m\Delta k_y)$, not a composite signal, thereby deriving the linear weights to reconstruct missing $k$-space lines of each component coil:

$$S_l^{\mathrm{ACS}}\left(k_y + m\Delta k_y\right) \cong \sum_{k=1}^{N_c} n_k^{(m)} S_k\left(k_y\right) \tag{5.15}$$

This procedure is repeated and full $k$-spaces are derived for all the channels of a phased array coil. After Fourier transformation, separate images are produced for each single channel which can be combined finally by, for example, sum-of-squares method [160]. In addition, unlike VD-AUTO-SMASH, GRAPPA uses multiple $k$-space lines from all coils to fit one single coil ACS line and thus provides further robustness to the fitting procedure by making it over-determined. As a result GRAPPA provides better artifacts suppression than VD-AUTO-SMASH.

The original implementation of GRAPPA was later improved by including the points along the $k_x$ direction in the kernel used for determining the coil weights. For example, a kernel of the size 5x4 is illustrated in Figure 5.7. In general, significant weights are from neighboring points and hence smaller block sizes can be used as kernel sizes without much penalties on image quality compared to the case when all the acquired data points are used. The main motivation for using smaller kernel sizes is the reduced computational times and normally the coil sensitivities can be described by a smaller number of Fourier terms.

**G-factor in GRAPPA Reconstruction**

As described in [165], similar to the g-factor definition known from SENSE-type reconstructions (see Equation (5.7)):

$$g = \frac{\text{SNR}_{\text{full}}}{\text{SNR}_{\text{PI}} \cdot \sqrt{R}} \tag{5.16}$$

the GRAPPA g-factor for the coil-combined images can be derived:

$$g = \frac{\sqrt{|(\mathbf{p}^T \cdot \mathbf{W}) \cdot \Sigma^2 \cdot (\mathbf{p}^T \cdot \mathbf{W})^H|}}{\sqrt{|(\mathbf{p}^T \cdot 1) \cdot \Sigma^2 \cdot (\mathbf{p}^T \cdot 1)^H|}} \tag{5.17}$$

where the vector $\mathbf{p}$ can simply be determined from the low-resolution ACS data or the high-resolution accelerated GRAPPA images. In the case of a sum-of-squares (SOS) reconstruction, these coefficients are given for individual coil element $k$ as $p_k = \frac{I_k^*}{I_{\text{SOS}}}$. $\mathbf{W}$ is the GRAPPA weights matrix in the image space and $\Sigma^2$ is the noise covariance matrix for the coil array so that

$$W = \begin{pmatrix} W_{11} & \cdots & W_{1N} \\ \vdots & \ddots & \vdots \\ W_{N1} & \cdots & W_{NN} \end{pmatrix} \tag{5.18}$$

and

$$\Sigma^2 = \begin{pmatrix} \sigma_{11}^2 & \cdots & \sigma_{1N}^2 \\ \vdots & \ddots & \vdots \\ \sigma_{N1}^2 & \cdots & \sigma_{NN}^2 \end{pmatrix} \tag{5.19}$$

where Equations (5.18) and (5.19) are written for N-channel coil array. $\sigma_{ii}$ represents the noise variance in channel $i$ whereas $\sigma_{ij}$ represents the noise covariance between channel $i$ and $j$.

## 5.3 Controlled Aliasing in Parallel Imaging

The assessment of parallel imaging in terms of image quality is made by considering how well a particular parallel imaging algorithm unfolds an aliased image with minimum SNR losses for a given acceleration factor. G-factor (Section 5.1.3) analysis is a widely accepted method for such an assessment. The most essential hardware requirement for optimal parallel imaging reconstruction is optimal design of a multi-channel array coil which can provide different coil sensitivity maps for each channel. Besides optimal design of the array coil, imaging parameters, which influence parallel imaging performance, are field strength, field of view, image plane orientation, acceleration factors, and sampling patterns used during data acquisition. As an illustrative example, Figure 5.8 shows g-factor maps for images acquired with varying acceleration factor R using SENSE reconstruction method. As one can notice,
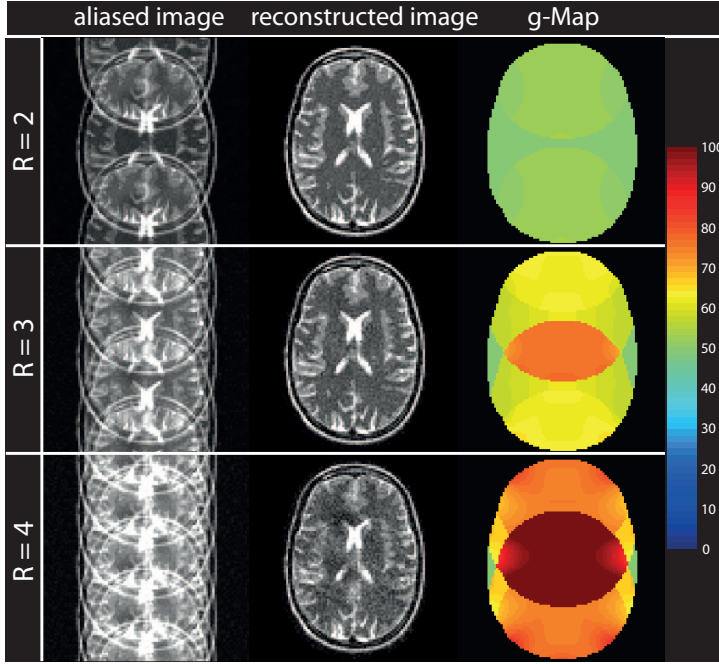
**Figure 5.8:** *An illustrative example of effect of acceleration factor on spatially varying noise amplification during SENSE reconstruction. For convenience, the image aliasing patterns are shown in the first column for respective acceleration factors (R). Noise level significantly varies across the image plane as can be seen from g-factor maps and the final reconstructed images exhibit reduced SNR as acceleration factor is increased.*

the g-factor values increase with increasing acceleration factors used and noise level can vary significantly from pixel to pixel across the image which can potentially be very disruptive to the overall image SNR.

In general, all parallel imaging methods are limited by the fact that aliased pixels must have sufficient sensitivity variations to perform the matrix inversion. Mathematically expressed, if the coil sensitivity values of aliased pixels are nearly identical, then the determinant of the matrix $C$ in Equation (5.10) is zero, making Equation (5.10) unsolvable since the inverse of matrix $C$ would not exist.

### 5.3.1 Controlled Aliasing in Simultaneous Multi-slice Excitation

**Simultaneous Multi-Slice Acquisition (SMS Acquisition)**

For dynamic studies of the brain, such as functional MRI, the speed of acquisition is of paramount importance. Conventionally, these studies rely on single-shot 2D EPI acquisition methods. However, for high resolution imaging where a large number of slices are needed to cover the brain, a long TR is required. This renders the method inefficient compared with 3D encoding methods (Section 3.1.4). Conventional parallel imaging approaches can greatly increase the speed of the EPI encoding by eliminating phase encoding steps. Although beneficial for other reasons such as reducing image distortions by reducing echo train length [166], this does not translate to a significant reduction in TR or acquisition time, as a typical fMRI acquisition needs to use a suitable TE for optimal $T_2^*$ contrast.

In comparison, accelerating the data acquisition using the simultaneous acquisition of multi-

ple slices can be very effective as it directly reduces the amount of time needed to acquire a fixed number of slices [167–169]. Typically, if $N$ imaging slices are acquired per shot instead of one, the total acquisition time decreases directly by a factor of $N$. Furthermore, unlike standard parallel imaging techniques, simultaneous multi-slice (SMS) acquisition methods do not shorten the readout period or omit $k$-space samples. Therefore, they are not subject to a $\sqrt{R}$ penalty on SNR (where $R$ is the acceleration factor) found in conventional parallel imaging acceleration. However, the images reconstructed by direct Fourier transform appear collapsed onto each other and hence advanced reconstruction techniques need to be employed to unfold the aliased slices.

Parallel imaging concepts can readily be applied to un-alias the pixels from slices excited and encoded simultaneously. Unfortunately the aliased slices are generally close to each other due to a comparatively smaller FOV in the slice direction. For example, a 60 slice 2 mm isotropic acquisition with 3x multi-slice acceleration would require un-aliasing pixels 4 cm apart in the slice direction. This pixel separation is equivalent to that of a conventional parallel imaging reconstruction for a brain image with a 20 cm in-plane FOV and R = 5 acceleration. The short distances between aliased pixels place a high demand on the spatial variations in the coil sensitivities and result in un-aliasing artifacts and a high $g$-factor penalty.

### Controlled Aliasing In Parallel Imaging Results IN Higher Acceleration (CAIPIRINHA)

The situation described above can be avoided if the aliasing patterns of the multiple slices are shifted with respect to each other [168, 170–172]. This approach of controlling aliasing patterns to achieve a more readily invertible system of equations for parallel imaging reconstruction is termed as *controlled aliasing in parallel imaging results in higher acceleration* (CAIPIRINHA) technique. Mathematics behind CAIPIRINHA approach can be explained by using the basic Fourier shift theorem. For the sake of simplicity of discussion, let us consider a 1D image $\rho(y)$ which can be expressed as:

$$\rho(y) = \sum_{m=\frac{-N}{2}}^{\frac{N}{2}-1} S(m\Delta k) \cdot e^{im \cdot \Delta k \cdot y} \tag{5.20}$$

where $S$ is the discrete $k$-space signal, $\Delta k$ is the distance between successive $k$-space samples, and index $m$ is the phase encoding step which runs from $(\frac{-N}{2})$ to $(\frac{N}{2}-1)$. Using Fourier shift theorem, a shift in image space can be expressed as:

$$\begin{aligned}
\rho(y-\Delta y) &= \sum_{m=\frac{-N}{2}}^{\frac{N}{2}-1} S(m\Delta k) \cdot e^{im \cdot \Delta k \cdot (y-\Delta y)} \\
&= \sum_{m=\frac{-N}{2}}^{\frac{N}{2}-1} \left( S(m\Delta k) \cdot e^{im \cdot \Delta k \cdot y} \right) \cdot e^{-im \cdot \Delta k \cdot \Delta y}
\end{aligned} \tag{5.21}$$

Thus a spatial shift in the image domain by an amount $\Delta y$ can be achieved by a $\Delta y$-dependent linear phase shift in the $k$-space

$$\theta_m = -im \cdot \Delta k \cdot \Delta y \qquad \text{with} \quad m = \frac{-N}{2}, \frac{-N}{2} + 1, \cdots, \frac{N}{2} - 1 \tag{5.22}$$

For example, to shift the image by half the FOV, $\Delta y = \frac{\text{FOV}}{2}$ and by using $\Delta k = \frac{2\pi}{\text{FOV}}$, Equation (5.22) takes the form

$$\theta_m = -i \cdot m \cdot \pi \tag{5.23}$$

Though the above illustrative calculation is done for a shift of $\frac{\text{FOV}}{2}$, the linear phase modulation $\theta_m$ required for any desired spatial shift $\Delta y$ can be calculated using Equation (5.22). Such spatial shift between simultaneously excited slices can practically be achieved through an RF excitation with varying pulse phases along the phase-encoding direction. Following the nomenclature used in Equation (5.20), a 1D image $\rho(y)$ acquired through simultaneous two-slice experiment can be expressed as:

$$\rho(y) = \sum_{m=\frac{-N}{2}}^{\frac{N}{2}-1} (S_1(m\Delta k) + S_2(m\Delta k)) \cdot e^{i \cdot m \cdot \Delta k \cdot y}$$
$$= \rho_1(y) + \rho_2(y) \tag{5.24}$$

Equation (5.9) poses a problem to resolve the aliasing caused because of under-sampling of $k$-space along the phase-encoding direction whereas Equation (5.24) poses a problem to resolve two simultaneously excited and hence superimposed slices. The spatial shift $\Delta y$ in our two-slice simultaneous excitation experiment for the second slice can easily be adjusted through phase modulation ((5.23)) to be exactly $\frac{\text{FOV}}{2}$, leading to a system of equations which take the form:

$$\begin{pmatrix} S_1(x,y) \\ S_2(x,y) \end{pmatrix} = \begin{pmatrix} C_{11}(x,y) & C_{12}(x, y + \frac{\text{FOV}}{2}) \\ C_{21}(x,y) & C_{22}(x, y + \frac{\text{FOV}}{2}) \end{pmatrix} \cdot \begin{pmatrix} \rho_1(x,y) \\ \rho_2(x, y + \frac{\text{FOV}}{2}) \end{pmatrix} \tag{5.25}$$

Where $S_1$ and $S_2$ are the measured simultaneously excited collapsed images from coil 1 and coil 2 respectively. $C_{ij}$ is the coil sensitivity profile of coil $i$ at location of slice $j$, whereas $\rho_1$ and $\rho_2$ are the spin densities from the two slices excited. Equation (5.25) bears a close similarity to Equation (5.9). Note that the second slice is shifted with respect to the first slice by a factor equal to $\frac{\text{FOV}}{2}$. Generally, the coil sensitivity profiles tend to be very different due to induced spatial shift even if the coil sensitivity profile were the same without any spatial shift. This spatial shift (controlled aliasing) makes the system of equations mentioned above more readily invertible and hence reducing g-factor related SNR losses.

Although, for the sake of simplicity, only a two channel array and two simultaneously excited slices are considered here, the discussion is valid for array containing more number of coil elements and for higher acceleration factors. While g-factor related SNR losses are reduced

due to CAIPIRINHA-style sampling patterns, using it in combination with SMS excitation has an added advantage over accelerations achieved through conventional ($k$-space under-sampling) parallel imaging. Since $N$ slices are simultaneously excited, there is $\sqrt{N}$ times more SNR available while using simultaneous excitation approach to accelerate data acquisition.

Though in the discussion above, appplication of phase modulated RF pulses is used to demonstrate spatial shift in the image domain, an alternate method to induce such a spatial shift would be to apply periodic gradient blips on the slice-encode gradient axis along with conventional phase-encoding gradient blips [172]. This method is more suitable for single-shot pulse sequences such as EPI since the entire $k$-space plane is acquired after a single RF excitation, thus disabling the possibility to use phase-modulated RF pulses to acquire successive $k$-space lines. The periodic playout of gradient blips provides a zigzag appearance (similar to $k$-space patterns described below in Section 5.3.2) to the sampled $k$-space along the slice-encoding direction and results in the spatial shift in the acquired image. This approach is termed as *blipped-CAIPIRINHA* and how a particular amount of spatial shift is induced in this approach can be studied in [172].

### 5.3.2 2D-CAIPIRINHA

The advantage of reduced spatially varying noise amplifications (g-factor) during parallel imaging reconstruction can be brought into 3D imaging approach as suggested by Breuer et al. and is termed as *2D-CAIPIRINHA* [173]. In 2D-CAIPIRINHA, instead of the use of phase-modulated RF pulses to control image aliasing, $k$-space sampling positions are shifted (shift is denoted by a $\Delta$ term as done in [173]) from their normal positions in the under-sampled 2D phase encoding scheme. This simply translates to playing periodic gradient blips on the secondary phase-encoding direction along with the conventional gradient blips that are played on the primary phase-encoding direction during EPI readout train.

A few illustrative examples of different $k$-space sampling patterns and resulting image aliasing patterns are shown in Figure 5.9. In these simulated examples, first a fully sampled $k$-space $yz$-plane is shown, with read direction orthogonal to the plane of the paper (Figure 5.9, column (a)). Standard under-sampling ($\Delta = 0$) of $k$-space results in aliasing patterns shown in column(b) for a net acceleration of 2 (1×2). When CAIPIRINHA-style $k$-space under-sampling is used ($\Delta = 1$), the resulting image aliasing pattern is shown in column (c) of Figure 5.9 for the same net acceleration. Note that the same number of $k$-space samples are acquired for both the under-sampling schemes presented. However with the help of controlled aliasing, lesser part of the image is made susceptible to g-factor losses.

Using this modified strategy, coil sensitivity variations can be exploited more efficiently in multiple dimensions, resulting in a more robust parallel imaging reconstruction with reduced g-factor penalty. Application of 2D-CAIPIRINHA to a segmented 3D EPI sequence is the topic of discussion for the next chapter (Chapter 6) in this thesis. More importantly, the two approaches discussed in this chapter for accelerated data acquisitions, namely simultaneous
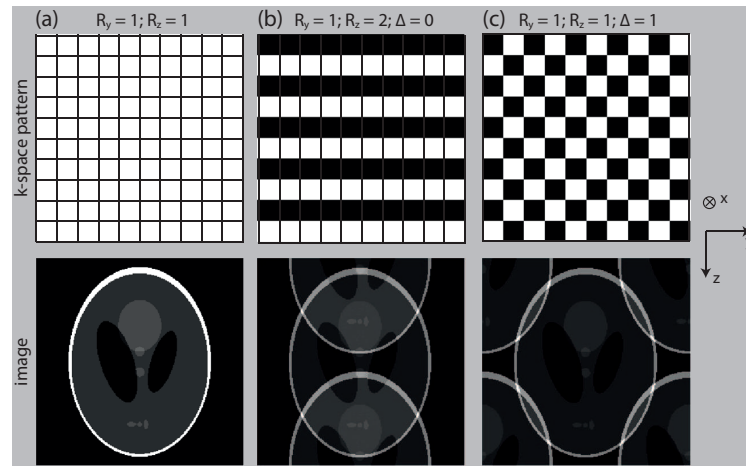
**Figure 5.9:** *Standard versus CAIPIRINHA-style under-sampling of k-space and their effects on image aliasing patterns. Top row shows k-space patterns in which each white square indicates an acquired k-space line, whereas each black square indicates skipped k-space line. Bottom row shows aliasing resulting aliasing pattern. Column (a) is the case when no under-sampling is performed i.e. a fully sampled k-space is acquired. Column (b) shows standard under-sampling ($\Delta = 0$) with $R_y = 1$ and $R_z = 2$, and column (c) shows the same acceleration but with CAIPIRINHA-style under-sampling ($\Delta = 1$) of the k-space.*

multi-slice 2D EPI with blipped CAIPIRINHA and 3D EPI with 2D CAIPIRINHA, are compared quantitatively in terms of performance for functional magnetic resonance imaging studies.

## References

[154] Klaas P. Pruessmann, Markus Weiger, Markus B. Scheidegger, and Peter Boesiger. Sense: Sensitivity encoding for fast mri. *Magnetic Resonance in Medicine*, 42(5):952–962, 1999.

[155] Daniel K. Sodickson and Warren J. Manning. Simultaneous acquisition of spatial harmonics (smash): Fast imaging with radiofrequency coil arrays. *Magnetic Resonance in Medicine*, 38(4):591–603, 1997.

[156] J. W. Carlson. An algorithm for nmr imaging reconstruction based on multiple rf receiver coils. *Journal of Magnetic Resonance*, 74(2):376–380, 1987.

[157] Michael Hutchinson and Ulrich Raff. Fast mri data acquisition using multiple detectors. *Magnetic Resonance in Medicine*, 6(1):87–91, 1988.

[158] J. Kelton, R. M. Magin, and S. M. Wright. An algorithm for rapid acquisition using multiple receiver coils. In *Proceedings 8th Annual SMRM*, page 1172, 1989.

[159] J. B. Ra and C. Y. Rim. Fast imaging using subencoding data sets from multiple detectors. *Magnetic Resonance in Medicine*, 30(1):142–145, 1993.

# REFERENCES

[160] Charles A. McKenzie, Ernest N. Yeh, Michael A. Ohliger, Mark D. Price, and Daniel K. Sodickson. Self-calibrating parallel imaging with automatic coil sensitivity extraction. *Magnetic Resonance in Medicine*, 47(3):529–538, 2002.

[161] William H. Press, Saul A. Teukolsky, William T. Vetterling, and Brian P. Flannery. *Numerical Recipes in C (2Nd Ed.): The Art of Scientific Computing*. Cambridge University Press, New York, NY, USA, 1992.

[162] PeterM. Jakob, MarkA. Grisowld, RobertR. Edelman, and DanielK. Sodickson. Auto-smash: A self-calibrating technique for smash imaging. *Magnetic Resonance Materials in Physics, Biology and Medicine*, 7(1):42–54, 1998.

[163] Robin M. Heidemann, Mark A. Griswold, Axel Haase, and Peter M. Jakob. Vd-auto-smash imaging. *Magnetic Resonance in Medicine*, 45(6):1066–1074, 2001.

[164] Mark A. Griswold, Peter M. Jakob, Robin M. Heidemann, Mathias Nittka, Vladimir Jellus, Jianmin Wang, Berthold Kiefer, and Axel Haase. Generalized autocalibrating partially parallel acquisitions (grappa). *Magnetic Resonance in Medicine*, 47(6):1202–1210, 2002.

[165] Felix A. Breuer, Stephan A.R. Kannengiesser, Martin Blaimer, Nicole Seiberlich, Peter M. Jakob, and Mark A. Griswold. General formulation for quantitative g-factor calculation in grappa reconstructions. *Magnetic Resonance in Medicine*, 62(3):739–746, 2009.

[166] Roland Bammer, Martin Auer, Stephen L. Keeling, Michael Augustin, Lara A. Stables, Rupert W. Prokesch, Rudolf Stollberger, Michael E. Moseley, and Franz Fazekas. Diffusion tensor imaging using single-shot sense-epi. *Magnetic Resonance in Medicine*, 48(1):128–136, 2002.

[167] David J. Larkman, Joseph V. Hajnal, Amy H. Herlihy, Glyn A. Coutts, Ian R. Young, and Gösta Ehnholm. Use of multicoil arrays for separation of signal from multiple slices simultaneously excited. *Journal of Magnetic Resonance Imaging*, 13(2):313–317, 2001.

[168] R. Nunes, J. Hajnal, D. Larkman, and X. Golay. Simultaneous slice excitation and reconstruction for single shot epi. In *Proceedings 13th Scientific Meeting, International Society for Magnetic Resonance in Medicine, Seattle*, page 293, 2006.

[169] K. Setsompop, J. Cohen-Adad, B.A. Gagoski, T. Raij, A. Yendiki, B. Keil, V.J. Wedeen, and L.L. Wald. Improving diffusion {MRI} using simultaneous multi-slice echo planar imaging. *NeuroImage*, 63(1):569 – 580, 2012.

[170] Felix A. Breuer, Martin Blaimer, Robin M. Heidemann, Matthias F. Mueller, Mark A. Griswold, and Peter M. Jakob. Controlled aliasing in parallel imaging results in higher acceleration (caipirinha) for multi-slice imaging. *Magnetic Resonance in Medicine*, 53(3):684–691, 2005.

[171] Gary H. Glover. Phase-offset multiplanar (pomp) volume imaging: A new technique. *Journal of Magnetic Resonance Imaging*, 1(4):457–461, 1991.

[172] Kawin Setsompop, Borjan A. Gagoski, Jonathan R. Polimeni, Thomas Witzel, Van J. Wedeen, and Lawrence L. Wald. Blipped-controlled aliasing in parallel imaging for simultaneous multislice echo planar imaging with reduced g-factor penalty. *Magnetic Resonance in Medicine*, 67(5):1210–1224, 2012.

[173] Felix A. Breuer, Martin Blaimer, Matthias F. Mueller, Nicole Seiberlich, Robin M. Heidemann, Mark A. Griswold, and Peter M. Jakob. Controlled aliasing in volumetric parallel imaging (2d caipirinha). *Magnetic Resonance in Medicine*, 55(3):549–556, 2006.

# 6 Sub-second High Resolution Whole-brain fMRI Using 3D-EPI-CAIPI

To substantially increase the temporal resolution of whole brain fMRI while maintaining low g-factors, the combination of 3D EPI using a 2D controlled aliasing (CAIPIRINHA) with generalized auto-calibrating partially parallel acquisitions (GRAPPA) approach was evaluated. Evaluation was performed on a 7T scanner equipped with a 32 channel receive coil in terms of: (i) image quality – compared to standard parallel imaging accelerated data; (ii) temporal SNR – the ability to detect resting state networks compared to standard 2D-EPI and simultaneous multi-slice blipped 2D-EPI; (iii) temporal resolution – the ability to sample and remove physiological signal fluctuations from the BOLD signal of interest and (iv) the ability to distinguish small changes in HRF dynamics in an event-related fMRI experiment. fMRI data with whole-brain coverage and a voxel size of 2×2×2 mm could be acquired with temporal resolution of 371 ms. 10-fold parallel imaging accelerated 3D-EPI-CAIPI data was shown to lower g-factor losses with respect to standard 3D-EPI. Additional resting state networks were detected using simultaneous multi-slice blipped 2D-EPI and 3D-EPI-CAIPI compared to a comparable 2D-EPI acquisition. This was attributed to the improved statistics due to the higher number of volumes acquired in a given duration and because of the improved characterization of physiological signal fluctuations. Functional MRI with 400 ms temporal resolution allowed the detection of time-to-peak variations in temporal, occipital and frontal cortices HRF due to multisensory facilitation of the order ~200 ms.

## 6.1 Introduction

Echo Planar Imaging (EPI) [174] is the main pulse sequence used for fMRI [175–177] due to its ability to offer high sampling rates. Standard multi-slice 2D-EPI acquires fMRI data at spatial (2-4 mm isotropic) and temporal (2-3 s) resolutions which are sufficient to detect hemodynamic response to the neuronal activities [178]. Both functional connectivity research as well as task-driven functional Magnetic Resonance Imaging (fMRI) benefit from improved statistics attainable through a higher sampling rate [179, 180]. As an additional benefit, higher sampling rates provide a means to separate and filter out physiological signal fluctuations which often contaminate Blood Oxygen Level Dependent (BOLD) signal of interest at lower

temporal resolutions [180–183]. At ultra-high magnetic field strengths ($\geq$ 7T), due to the increased signal available and because of the increased susceptibility induced artifacts, there is both an opportunity and a need to acquire higher spatial resolution images. Increasing the spatial resolution of multi-slice 2D-EPI implies an increase not only in the echo train length (ETL), but also in the number of slices needed to achieve the same volume coverage, thereby increasing the minimum TR achievable for whole brain coverage to a point where it becomes comparable to the hemodynamic response time ( 10-12s).

Recently, multi-band excitations have been proposed to accelerate the acquisition of 2D multi-slice [184–186] in which simultaneously acquired slices are separated using information from sensitivity profiles of the RF coils [187]. To reduce the penalty associated with the geometry factor (g-factor) due to the unfolding of the aliased slices, the use of successive slice shifting in the phase-encoding direction has been suggested [185, 186, 188, 189] to minimize spatial overlap of consecutive slices making full use of the FOV in the phase-encoding direction. In blipped-CAIPI [186] the inter-slice shift in the phase-encoding direction is created using sign- and amplitude-modulated slice-encoding blips simultaneous with the EPI phase-encoding blips. Another technique, Multiplexed-EPI [179] combines multi-slice excitation with simultaneous echo refocused EPI [190, 191] at the cost of an increased echo train length. All these recent approaches have shown their potential to provide sub-second temporal resolution when highly under-sampled detection is used. One of the main penalties of the multi-band excitation approach, especially at high fields, is that multi-band excitations are relatively more power intensive and the peak power of a multi-band RF pulse scales with the square of the number of slices simultaneously excited [192]. Various methodologies have been considered to override this limitation: the use of VERSE excitation pulses comes at the cost of increased RF pulse length and sensitivity to B0 inhomogeneities [193]. By using an optimized set of excitation phases, multi-band RF pulses can be designed for greatly reduced peak RF power relative to uniform phase pulses, approaching a factor of $N$, rather than $N^2$ for $N$ simultaneously excited slices [194]. However, the total pulse power remains unchanged with this approach. The use of PINS excitation pulses results in a SAR which is independent of the number of slices acquired [195, 196]. However, due to the infinite series of excitation profiles along the slice-encoding direction, the number of slices excited using PINS is determined by the object size in the slice-encoding direction - which poses some limitations for fMRI applications where transverse slices are often preferred. The use of time-shifted RF pulses effectively reduces the peak power, but it does not reduce the total energy of the RF pulses [197]. An adverse effect of time-shifting is lengthening of multi-band RF pulses which results in different minimum achievable echo times for the different number of simultaneously excited slices.

Echo Volume Imaging (EVI) or single shot 3D-EPI [198–200] is a technique where a thick slab is excited, as opposed to thin slices in the case of multi-slice 2D-EPI, and the full 3D volume is encoded within the thick slab during readout. However, 3D single-shot acquisitions require long echo trains resulting in compromises in the achievable echo time (TE) and spatial resolution or very high demands on the gradient hardware [200]. One strategy proposed

to reduce the length of the echo train is to perform multi-slab echo volume imaging [183]. By dividing the volume in the partition-encoding direction into $N$ slabs, the number of encoded planes per excitation is reduced by a factor of $N$. This reduces the strain on the gradients but slices at the edge of this slab often have to be discarded because of poor slice-excitation profiles and it reduces the ability to use parallel imaging acceleration in the partition encoding direction due to the reduced field of view. Other highly accelerated acquisitions using computationally intensive iterative reconstructions schemes have been proposed: 3D $k$-space data is acquired using either a concentric shells trajectory [201] with variable density sampling or a 3D rosette trajectory [202] to achieve single excitation whole brain imaging. Another strategy to overcome the limitations of EVI is the acquisition of the 3D volume in several shots [203–206] known as segmented 3D-EPI. In this case, the time needed to acquire one entire 3D $k$-space ($TR_{volume}$) is $TR_{segment}$ times the number of segments, where $TR_{segment}$ is the time between successive excitation of the tissue volume. One single $k$-space plane is typically acquired per excitation (or two segments in the case of 3D RE-EPI [207]), leading to an ETL comparable to those of standard 2D-EPI. Segmented 3D-EPI [205] provides multiple benefits over multi-slice 2D-EPI approach such as a higher sensitivity per unit scan time [208, 209], the absence of a spin-history artifact [204], and the possibility of applying parallel imaging technique readily in two phase-encoding dimensions [205], instead of only one for standard 2D EPI.

3D-EPI is more sensitive to physiological noise than its 2D counterpart [181]. Recent work has shown that with the number of segments used to form the 3D-EPI dataset, the maximum achievable temporal signal-to-noise ratio (tSNR) is reduced [206]. A higher acceleration factor for partially parallel acquisition (PPA) in the partition-encoding direction results in a reduced number of segments used for volume acquisition in segmented 3D-EPI, thus improving tSNR when operating in the physiological-noise dominated regime [206]. The use of parallel imaging techniques is limited by the fact that the performance of these techniques is strongly dependent on several factors, which all contribute to spatially varying noise amplification (characterized by the g-factor) affecting the parallel imaging reconstruction process. The factors contributing to g-factor include the number of receiver coils, the geometry of the coil array, image plane orientation and the $k$-space under-sampling pattern used to achieve the acceleration. Controlled aliasing in volumetric data (2D-CAIPIRINHA) has been proposed [210] as a means to acquire under-sampled $k$-space by introducing a shift between successive acquired sample points which helps to reduce the noise amplification associated with parallel imaging reconstruction. Using this modified sampling strategy, coil sensitivity variations can be exploited more efficiently in multiple dimensions, resulting in a more robust parallel imaging reconstruction.

In this study, periodic gradient blips were applied in the partition-encoding direction along with conventional phase-encoding blips in a 3D-EPI sequence in order to cover the $k$-space with a 2D-CAIPIRINHA pattern. This combination of 3D-EPI and 2D-CAIPIRINHA is subsequently referred to as *3D-EPI-CAIPI* [207]. Image quality assessment for high acceleration factors in the partition-encoding direction (hereafter called $R_z$) was performed via comparisons

of 3D-EPI-CAIPI with highly accelerated standard 3D-EPI in order to evaluate the potential reduction in the number of excitations needed to adequately sample $k$-space, while increasing the achievable temporal resolution. The detection of resting state networks (RSNs) was used to assess the performance of 3D-EPI-CAIPI for functional connectivity studies compared with simultaneous multi-slice (SMS) blipped-CAIPIRINHA EPI (hereafter referred to as SMS-EPI) [186, 211] and with standard (single-band excitation) multi-slice 2D-EPI (hereafter referred to as 2D-EPI). Further, the benefit of higher sampling rate acquisitions to filter out physiological signal fluctuations from functional datasets was evaluated by acquiring datasets at three different sampling rates using 3D-EPI-CAIPI and by performing resting state analysis on them after low-pass filtering to remove physiological signal fluctuations. In the fourth experiment, 3D-EPI-CAIPI with 400 ms temporal resolution and 2 mm nominal spatial resolution was used to demonstrate its ability to detect multisensory facilitation in the primary visual and auditory cortices, which has previously been demonstrated using a long TR, highly jittered[I] fMRI acquisition [212].

## 6.2 Theory

CAIPIRINHA $k$-space sampling patterns can readily be implemented into a standard segmented 3D-EPI sequence [213]. Figure 6.1 shows the standard 3D-EPI sequence diagram and the modifications in the slice-encoding gradient needed in order to modify a standard 3D-EPI trajectory to become 3D-EPI-CAIPI. The standard segmented 3D-EPI sequence is shown in Figure 6.1(a). The required modifications are shown along with resulting $k$-space sampling patterns in Figure 6.1(b-d) for 3 possible trajectories to cover the $k$-space with the same net acceleration $R = 10$, with $R_z = 5$ (to ensure a 5-fold increase in temporal resolution and 5-fold reduction in the number of excitations per volume) and $R_y = 2$ (to ensure reduced image distortions and optimal TE). The solid circles in the sampling patterns (Figure 6.1(b-d), right-hand side) indicate $k$-space sampling points in the yz-plane that are acquired, whereas empty squares indicate un-acquired $k$-space sampling points. Each sampling point in the yz-plane is a $k$-space line along the read direction during the EPI readout with the read direction orthogonal to the yz-plane. 2D-CAIPIRINHA trajectories are characterized by the $\Delta$ term [210], which indicates the shift used along the partition-encoding direction while acquiring each successive $k$-space point in the primary phase-encoding direction. Standard parallel imaging under-sampling strategies as used in 3D-EPI correspond to $\Delta = 0$ (Figure 6.1(b)). When a non-zero $\Delta$ is used (Figure 6.1(c-d)), gradient blips along the partition-encoding direction are played together with the primary phase-encoding blips to shift the $k$-space positions in the partition-encoding direction by $\Delta$. When the cumulative $k$-space shift along the partition-encoding direction is greater than or equal to $R_z$, the partition-encoding gradient moment is rewound and the process is repeated. It is worth noting that the $k$-space sampling trajectories shown in Figure 6.1(b-d) for 3D-EPI-CAIPI are identical to the corresponding trajectories used

---

[I]To obtain sufficient time points to characterize the hemodynamic response function, many different repetitions are sampled with slightly differing lags. This technique is known as 'jittering'.
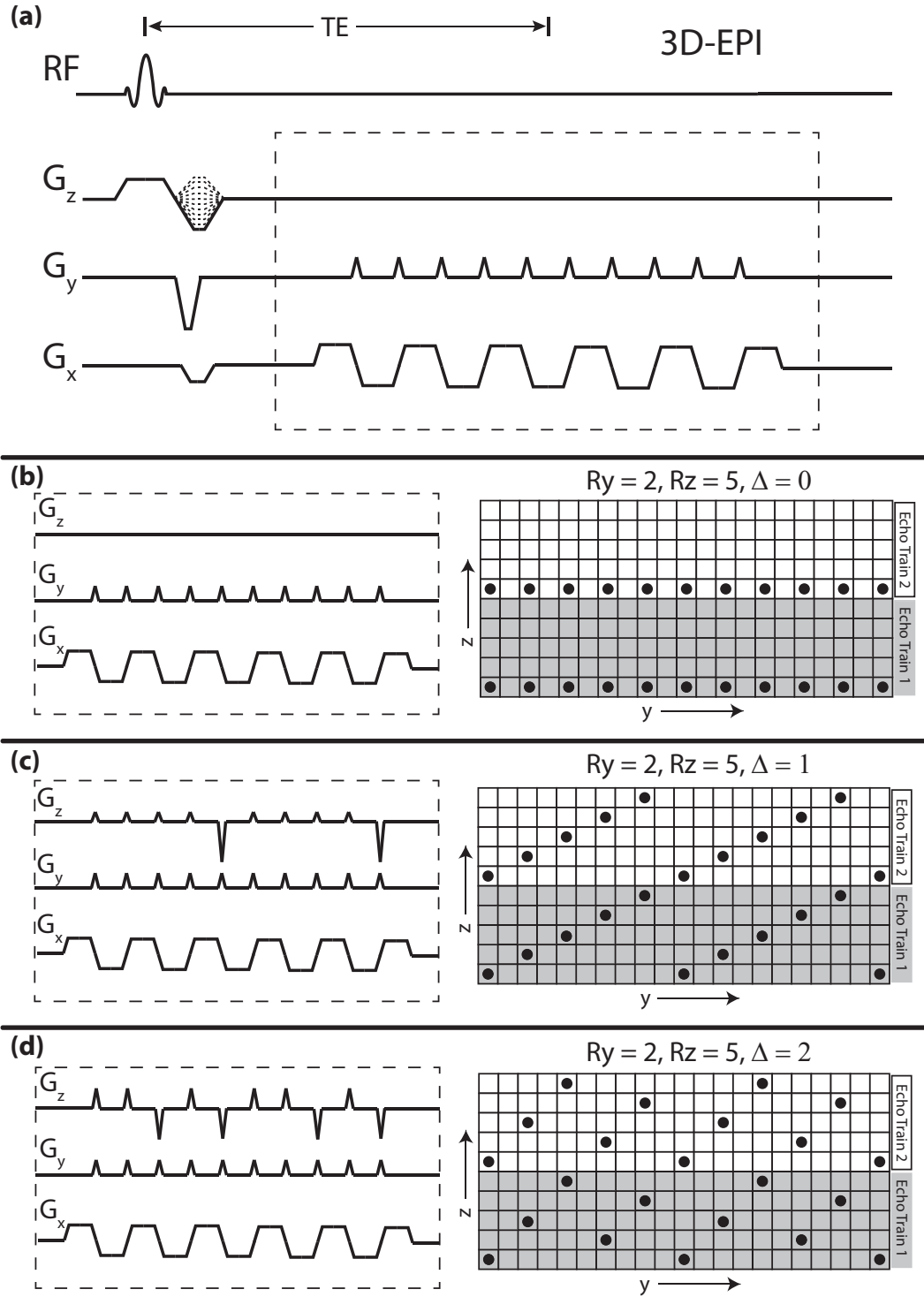
**Figure 6.1:** *(a) Pulse sequence diagram for segmented 3D-EPI pulse sequence. The dotted box outlines partition-, primary phase- and read-gradients (z, y, and x axes respectively) which are modified to shift successive k-space samples in the partition-encoding direction to achieve controlled aliasing. Gradient waveforms and resulting k-space sampling patterns for total acceleration $R = R_y \times R_z = 2 \times 5$ are shown for (b) $\Delta = 0$, (c) $\Delta = 1$, and (d) $\Delta = 2$.*

in simultaneous multi-slice blipped 2D-EPI.

## 6.3 Materials and Methods

All experiments were conducted according to procedures approved by the institutional review board and all participants provided written informed consent prior to the experiments. A 7T/ 680mm head-only scanner (Magnetom 7T, Siemens, Erlangen, Germany) equipped with a head gradient insert (80 mT/m maximum gradient strength, 333 T/m/s maximum slew-rate) and a 32-channel RF-head coil (Nova Medical Inc., MA, USA) was used.

Frequency selective fat saturation pulses were applied during EPI acquisitions before each excitation pulse to reduce chemical shift artifacts. Moreover, when the flip angle was not restricted by SAR, Ernst angle was used assuming an average $T_1$ value of 1800 ms. 3D-EPI-CAIPI image reconstructions were performed on a standalone computer equipped with MATLAB (R2012a, The Mathworks Inc.) using 2D-GRAPPA reconstruction method. G-factor maps were calculated using the general formulation for quantitative g-factor calculations in GRAPPA reconstructions [214]. $B_1$ maps were acquired using the Sa2RAGE sequence [215] to ensure correct RF calibration for all the experiments performed. The average $B_1$ value over the whole-brain was assessed to calibrate reference voltage for each scanning session and was kept the same throughout the session for all scans. Fat suppressed anatomical images were acquired with the MP2RAGE sequence [216] with $TR_{MP2RAGE} = 6.0$ s, TE = 3.03 ms, $TI_1/TI_2 = 0.8/2.7$ s, $\alpha_1/\alpha_2 = 7°/5°$, matrix size = 320×320×256, 0.6×0.6×0.6 mm$^3$ isotropic voxel size, slice encode = L-R, phase encode = A-P, PPA = 3×1, $PF_y = 6/8$ and $PF_z = 6/8$.

### 6.3.1 Image Quality Assessment

Image quality was evaluated in 1.0 mm isotropic whole brain images acquired from a single subject with 3D-EPI-CAIPI with different net accelerations and $\Delta$ values. The acquisition parameters used were: TR/TE = 67/26 ms, flip angle (FA) = 14°, readout bandwidth (rBW) = 1662 Hz/Pixel, matrix size = 188×188×120, reference data = 188×48×48, GRAPPA kernel size = 3×3, $PPA_y = 2$ (acceleration factor for partially parallel acquisition in the primary phase-encoding direction) and $PF_y = 7/8$ (partial Fourier factor in the primary phase-encoding direction). $PPA_z$ (acceleration factor for partially parallel acquisition in the partition-encoding direction) varied from 3 to 5. With $PPA_z = 5$, an acquisition with $PF_z = 6/8$ (partial Fourier factor in the partition-encoding direction) was performed to achieve a total $R_z = 6.66$ and $R = 15.24$, followed by homodyne reconstruction [217, 218]. The partition-encoding direction was set to superior-inferior while the primary phase-encoding direction was set right-left.

### 6.3.2 Comparison of RSN Detection

To assess the benefit of improved tSNR for fMRI studies with the use of the 3D-EPI-CAIPI sequence, when compared to standard 2D-EPI and SMS-EPI sequences, resting state networks were detected with comparable acquisition parameters using six healthy subjects (3 males, avg. age = 28 years). Common protocol parameters used for all three sequences were: Transverse orientation, TE = 26 ms, in-plane matrix size = 106×106, 2 mm isometric voxel size, $PPA_y = 2$, rBW = 2358 Hz/Pixel. Sequence specific parameters were as below:

1. **2D-EPI**: $TR_{volume}$ = 2.92 s, volumes per run = 102, slices = 60, FA = 60° (limited by SAR compared to the Ernst angle of 79°), reference data = 106×44, images were reconstructed using vendor provided in-plane GRAPPA reconstruction method (the specific kernel size used is not specified in the software documentation).
2. **SMS-EPI**: $TR_{volume}$ = 1.08 s, volumes per run = 278, slices = 63, multi-band factor = 3, FOV shift = 1.5 (which resulted in FOV/1.5 shift in the adjacent slices), reference data = 106×44, GRAPPA kernel size = 3×3, FA = 57°, images were reconstructed using vendor provided work-in-progress package which used slice-GRAPPA reconstruction method [186].
3. **3D-EPI-CAIPI**: $TR_{volume}$ = 1.02 s, volumes per run = 294, partitions = 60, $PPA_z = 3$, $\Delta = 1$ (which resulted in FOV/3 shift in the adjacent partitions), reference data size = 106×44×18, GRAPPA kernel size = 3×3, $TR_{segment}$ = 51 ms, FA = 14°, images were reconstructed on a stand-alone computer equipped with MATLAB using in-plane GRAPPA reconstruction method.

Total scan time was kept constant at 5 minutes per run across all the scans. For each subject the acquisition order of the 3 runs was randomized.

All resting state fMRI datasets were motion corrected using MCFLIRT. Temporal drifts were removed using a high-pass filter with a cutoff at 100 s. Datasets from individual subjects were first aligned to their respective high resolution anatomical images and subsequently to the MNI152 standard space using FLIRT [219–221]. Whole-brain tSNR per unit time maps for the three sequences were calculated as the mean divided by the standard deviation along the time dimension divided by square root of the $TR_{volume}$ used for the respective acquisitions. RSNs were identified using the MELODIC toolbox from FSL (http://www.fmrib.ox.ac.uk) which performs Independent Component Analysis (ICA) [222, 223]. Spatial smoothing of 3 mm full-width-half-maximum (FWHM) was applied prior to ICA. Group analysis was performed with multi-session temporal concatenation. RSNs that consistently appeared in 2D-EPI, SMS-EPI and 3D-EPI were automatically identified by choosing the components of the SMS-EPI and 3D-EPI with spatial correlation greater than 0.35 with the 2D-EPI RSNs (after thresholding the component maps at $Z = 3$). Additional components were identified after visual inspection. Names for each RSN were assigned via visual comparison to published data [195, 224–226].

### 6.3.3  Peak RF Power Comparison

To assess implications on peak power deposition while using 3D acquisition compared to multi-band 2D acquisition, a MATLAB simulation was carried out assuming a 60 slices ($N$) acquisition and $TR_{segment}$ = 51 ms. Three types of RF excitation pulses were considered for the simulation: multi-band (MB), multi-band with optimal phase scheduling (MB-PS) [194] and single-band pulse used for 3D acquisitions (3D). The acceleration factor along the slice direction was varied from 1 to 10 and the resulting Ernst angles were calculated assuming $T_1$ = 1800 ms. The peak power values were normalized with respect to peak power required by single-band excitation pulse used for non-accelerated 3D acquisition ($R$ = 1).

### 6.3.4  Physiological Noise

For additional investigation into the ability of shorter $TR_{volume}$ to better characterize respiratory and cardiac induced signal fluctuations, MR data was acquired using 3 different volume TRs from a single subject with simultaneous monitoring of the respiratory and cardiac cycles. Common protocol parameters used for these runs were: TR/TE = 48/26 ms, FA = 13°, matrix size = 106×106×60, 2 mm isometric voxel size, $PPA_y$ = 1, rBW = 3144 Hz/Pixel. Differences in protocol parameters used to achieve different volume TRs were:

1. $TR_{volume}$ = 3.18 s: volumes = 94, $PPA_z$ = 1, $R$ = 1
2. $TR_{volume}$ = 1.060 s: volumes = 283, $PPA_z$ = 3, $\Delta$ = 1, reference data = 106×48×39, kernel size = 3×3, $R$ = 3
3. $TR_{volume}$ = 0.371 s: volumes = 808, $PPA_z$ = 6, $\Delta$ = 2, reference data = 106×48×39, kernel size = 3×3, $PF_z$ = 6/8, $R$ = 8

Two runs at each sampling rate were performed and the order for all runs was randomized. Power spectrum analysis was performed in MATLAB on both physiological data and MR signals. All datasets were temporally low-pass filtered with a cut-off frequency of 0.15 Hz using a $13^{th}$ order Butterworth filter to filter out signal fluctuations due to physiological processes such as respiration and cardiac pulsation. Subsequently, 1.060 s and 0.371 s datasets were temporally under-sampled using cubic spline interpolation to create effective $TR_{volume}$ of 3.180 s producing 94 volumes each. tSNR per unit scan time maps were created pre- and post-lowpass filtering the datasets using the same definition as in the RSN experiment described in section 6.3.2. All datasets were motion corrected using MCFLIRT and averaged tSNR per unit scan time was calculated for 6 different ROIs per dataset containing ~40 pixels each in the gray matter and white matter. Motion-corrected datasets were co-registered with high resolution MP2RAGE anatomical images. ICA was performed using the MELODIC toolbox and RSNs were identified from these datasets using the same technique as used for the RSN experiment (Section 6.3.2).

### 6.3.5   Changes In HRF Dynamics Due To Multisensory Integration

To demonstrate ability of 3D-EPI-CAIPI to detect multisensory facilitation in the primary visual and auditory cortices with short TR, three volunteers (two females) were scanned in the experiment that employed a stimulation paradigm closely mimicking that described in [212]: volunteers were asked to report via a button-press the occurrence of either a visual flash (V, 150 ms, yellow/black checkerboard), a sound presentation (A, 150 ms, white noise burst delivered via Sensimetrics earplugs (Sensimetrics Corporation, MA, USA)) or a simultaneous combination of the two (AV). Per 8-minute run, 30 stimuli were presented using E-prime (Psychology Software Tools Inc., PA, USA), which was also used to record response times. Stimuli were presented every 15-17s.

Data acquisition was performed using the 3D-EPI-CAIPI acquisition with acquisition parameters similar to the $TR_{volume}$ 0.371 s protocol used for the physiological noise characterization experiment, i.e. : $TR_{volume}$ = 400 ms, nominal spatial resolution 2×2×2 $mm^3$, 60 slices/volume, FOV 210x174 mm, TR/TE=57/26 ms, PPA = 1×6, $\Delta$ = 2, $PF_z$ = 6/8, BW = 2774 Hz/Px, slab was AC-PC aligned with the primary phase-encoding direction RL. Two functional runs were acquired, each consisting of 1215 volumes.

SPM8 (http://www.fil.ion.ucl.ac.uk/spm) was used for motion correction, smoothing (FWHM 3 mm) and a GLM analysis with regressors for A, V and AV stimuli and the temporal derivatives thereof. ROIs of ~500 voxels were defined in the auditory, visual and left motor cortices from the AV, VA and f-test over (A,V) respectively. From each ROI, time-courses were extracted, temporally filtered to remove slow drifts and subsequently temporally reordered relative to the stimulus onset. A double gamma function [227] was fitted to the reordered time-courses to allow calculation of the time-to-peak.

## 6.4   Results

### 6.4.1   Image Quality Assessment

Three orthogonal planes of 1 $mm^3$ isotropic resolution images are shown along with their $^1/_g$ maps in Figure 6.2 for different $R_z$. For all the acquisitions, $R_y$ was kept constant at 2 whereas $R_z$ was varied as indicated on the far left of each row along with resulting $TR_{volume}$ for each acquisition. Standard sampling pattern images i.e. $\Delta$ = 0, exhibited greater g-factor losses (Figure 6.2, first column) than those acquired with CAIPIRINHA sampling patterns i.e. $\Delta$  0 (Figure 6.2, center and right column). The average $^1/_g$ values calculated over the whole brain are reported at the top of each $^1/_g$ map panel.

The benefit of using CAIPIRINHA with 3D-EPI acquisitions was in particular noticeable for highly under-sampled acquisitions. For PPA = 2×5 and $\Delta$ = 0, (Figure 6.2I) most of the brain anatomy was not recognizable (especially in the central part of the brain) but was progressively recovered with $\Delta$ = 1 (Figure 6.2J) and $\Delta$ = 2 (Figure 6.2K). The improvements in SNR were
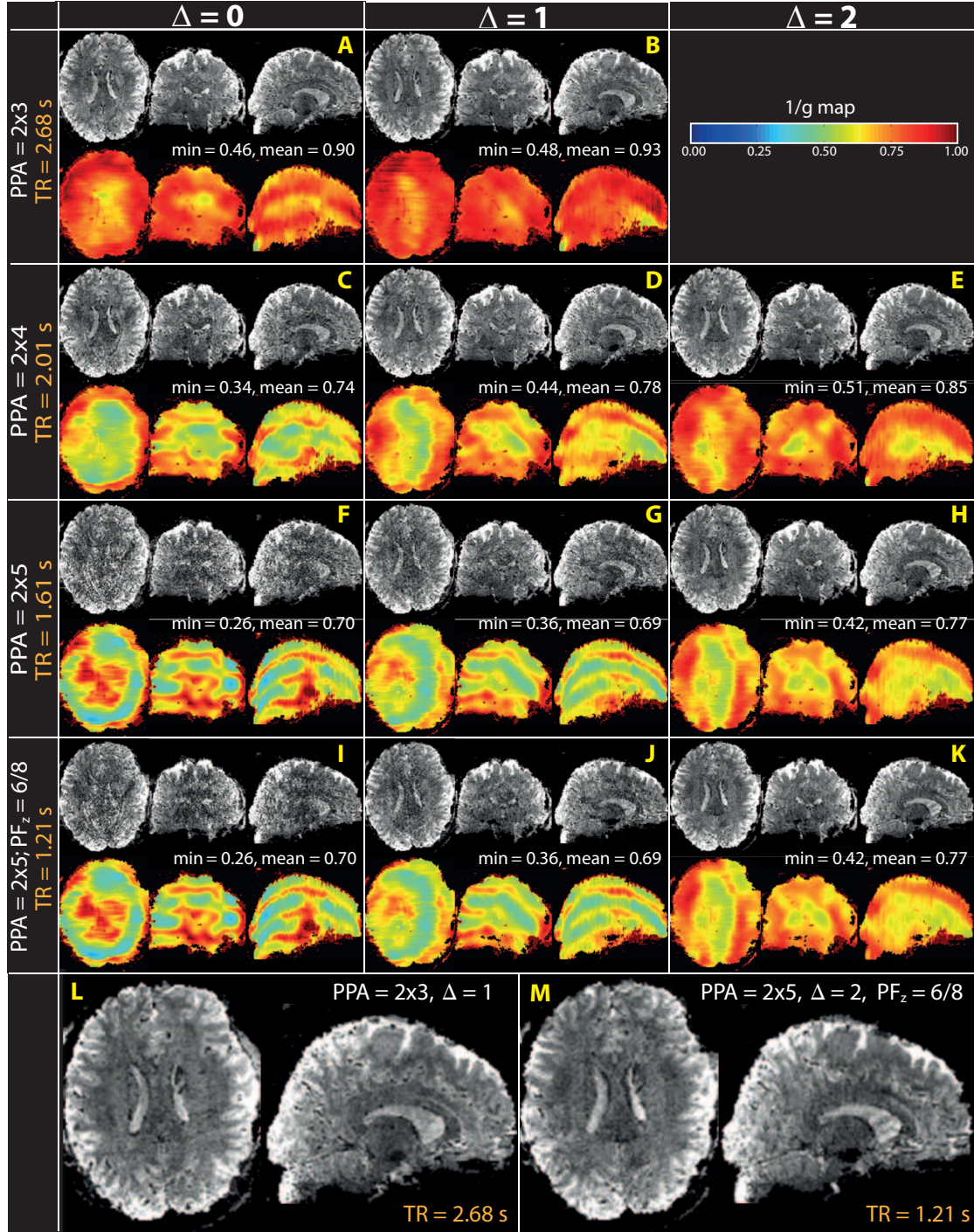
**Figure 6.2:** *Whole-brain echo planar images along with 1/g maps shown in orthogonal planes acquired with 3D-EPI-CAIPI for a single subject. Different parallel imaging acceleration factors used along with resulting volume TRs are indicated on the left of each image row. The left column shows the case of standard parallel imaging (Δ = 0), the middle column shows controlled aliasing with Δ = 1 and the right column shows the Δ = 2 case. The averaged 1/g values are reported on the top right of each 1/g map. Panels (L) and (M) show enlarged transverse and sagittal planes from panels (B) and (K) respectively, for better visualization.*

ascribed to the reduced g-factor. The averaged $^1/_g$ values were 0.70 with $\Delta = 0$ and 0.77 with $\Delta = 2$, corresponding to a 10% improvement over the whole brain. At lower acceleration, reconstruction improvements were not evident from simple visual inspection of the images. However, for the lowest acceleration of 2×3 (Figure 6.2(A-B)), average $^1/_g$ values increased from 0.90 ($\Delta = 0$) to 0.93 ($\Delta = 1$) with the use of CAIPIRINHA, an increase of ~3%. Panel (L) and (M) show transverse and sagittal planes from panel (B) and (K) respectively to help appreciate the comparable image quality obtained even though the latter was obtained with a 2.2-fold decrease in $TR_{volume}$.

### 6.4.2 Comparison of RSN Detection

The reduction in $TR_{volume}$ when using parallel imaging acceleration resulted in an increase in the number of volumes acquired (SMS-EPI and 3D-EPI-CAIPI acquired 278 and 294 volumes respectively) within the same duration when compared to 2D-EPI (102 volumes), improving the ability to detect resting state networks via ICA analysis due to greater statistical power. A total of 74 and 83 ICs were detected from datasets acquired with SMS-EPI and 3D-EPI-CAIPI, respectively, compared to 44 ICs that were detected from 2D-EPI datasets.

The networks detected were divided into three categories. The networks that were found at all three temporal resolutions via spatial cross-correlation (see Methods) were categorized as "common networks". A total of 10 common networks were identified and a few representative common networks are shown in Figure 6.3(a-c) which are: primary visual (red-yellow), sensory motor (blue-light blue), basal ganglia (red), left lateral (green), primary motor (green-yellow), auditory (pink), and medial visual (dark blue) networks. The second category of identified networks was labeled "split networks" as it consisted of networks that were found to be split across multiple ICs in the data sampled at higher temporal resolutions i.e. with SMS-EPI and with 3D-EPI-CAIPI. A total of 8 split networks were identified and a few representative split networks are shown in Figure 6.3(d-f). For example, the lateral visual network (Figure 6.3d, olive green) found as a single component with the 2D-EPI sequence ($TR_{volume} = 2.920$ s) was split across 2 different components (Figure 6.3(e-f), olive green & yellow) for SMS-EPI ($TR_{volume} = 1.080$ s) and for 3D-EPI-CAIPI ($TR_{volume} = 1.020$ s). Similarly the ventral stream network (Figure 6.3d, dark green) was found to split into two separate components (dark green & bright green) both in the SMS-EPI (Figure 6.3e) and 3D-EPI-CAIPI (Figure 6.3f) data. Other representative split networks shown in the figure are listed in the figure caption. Finally, networks which were detected only at higher temporal resolutions and were absent at the lower temporal resolution were categorized as "appearing networks" (Figure 6.3(g-h)). Two appearing networks, namely a language network (Figure 6.3g, green) and a superior temporal network (Figure 6.3g, red), were identified with SMS-EPI whereas a single appearing network, i.e. language network (Figure 6.3h, green), was identified with 3D-EPI-CAIPI. Echo planar images obtained with SMS-EPI and 3D-EPI-CAIPI exhibited visually comparable image quality. For demonstration, transverse and sagittal echo planar images acquired with SMS-EPI (Figure 6.3(i)) and 3D-EPI-CAIPI (Figure 6.3(j)) from one of the subjects are shown.
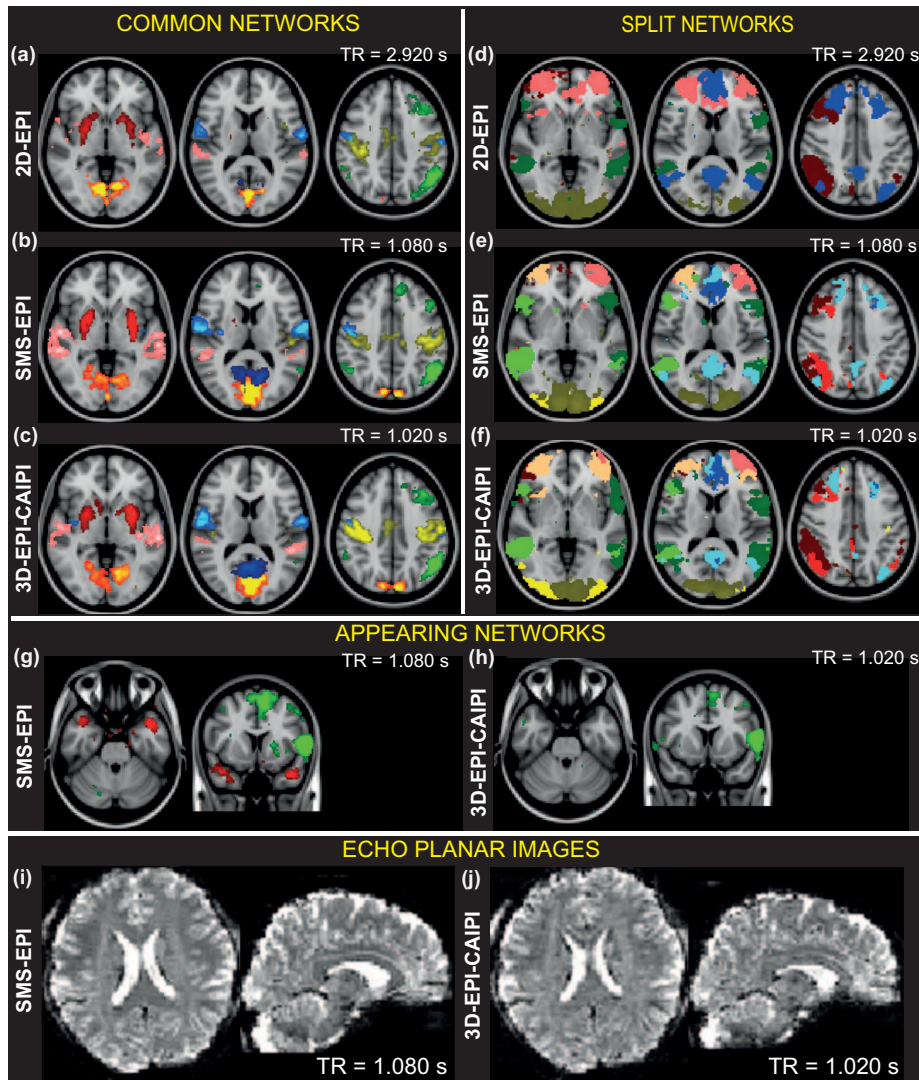
**Figure 6.3:** *Resting state networks shown overlaid on the MNI template. Resting state networks were categorized as common networks (a: 2D-EPI, b: SMS-EPI, c: 3D-EPI-CAIPI); split networks (d: 2D-EPI, e: SMS-EPI, f: 3D-EPI-CAIPI) or appearing networks (g: SMS-EPI, h: 3D-EPI-CAIPI). a-c: Common resting state networks (i.e. identifiable in all 3 acquisitions): primary visual (copper), lateral visual (blue), default mode (green), sensory motor (red-yellow), basal ganglia (red), auditory network (yellow-green), medial visual (blue-bright blue) and left lateral (pink) are shown on axial slices at MNI coordinate z = 6, 34 and 44.*

*d-f: Split networks (i.e. a single network found in 2D-EPI which appears as multiple components in SMS-EPI and 3D-EPI-CAIPI): general visual (olive green and yellow), ventral stream (red and bright-red), Frontal pole (black and pink), primary motor (green and bright-green) and the precuneus network (blue & bright-blue) are shown on shown on axial slices at MNI coordinate z = -8, 6 and 62.*

*g-h: Appearing networks (i.e. identifiable in SMS-EPI and 3D-EPI-CAIPI, but not in 2D-EPI): salience network (red), task positive networks (blue-bright blue) and language network (green) shown at MNI coordinates z = -6, 46 and y = 20.*

*i-j: Representative orthogonal planes of echo planar images acquired with SMS-EPI and 3D-EPI-CAIPI. Average of first 10 volumes with each sequence was used for the image display.*
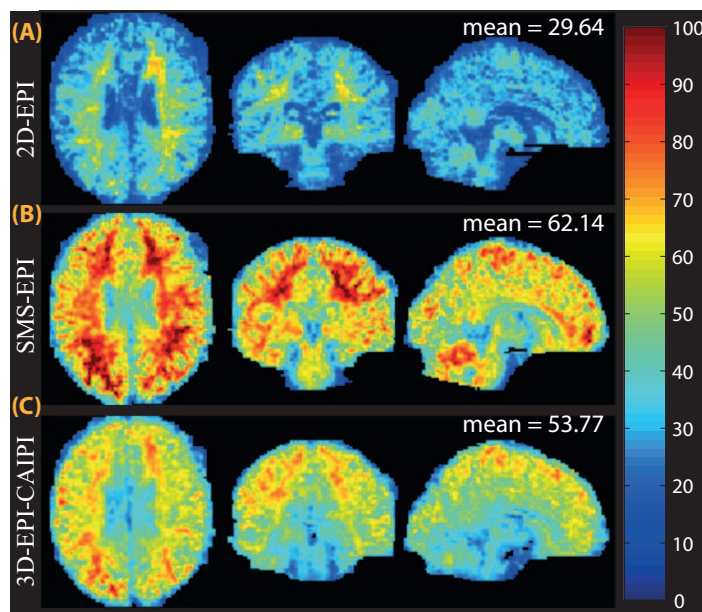
**Figure 6.4:** *Three orthogonal planes displaying averaged whole-brain tSNR per unit time maps calculated for (A) 2D-EPI, (B) SMS-EPI, and (C) 3D-EPI-CAIPI for six subjects. All datasets were motion corrected and aligned to MNI152 standard space prior to calculation of tSNR per unit time. The mean tSNR per unit time values are also reported on the top right of each panel.*

Figure 6.4 shows tSNR per unit time maps calculated for the three sequences used. 2D-EPI exhibited the lowest tSNR per unit time with an average value of 29.6±3.7 calculated for the whole-brain. SMS-EPI exhibited the highest tSNR per unit time with an average value of 62.1±4.4, an increase of nearly 110% compared to 2D-EPI. As expected, 3D-EPI-CAIPI exhibited lower tSNR per unit time than SMS-EPI due to its higher sensitivity to physiological signal fluctuations. However, average tSNR per unit time obtained with 3D-EPI-CAIPI was 53.8±5.3 which was around 81% higher compared to that obtained with 2D-EPI.

### 6.4.3   Peak RF Power Comparison

Unlike SMS-EPI, 3D-EPI-CAIPI achieved parallel acquisitions without any penalty in terms of SAR or peak power requirements. However, due to the reduced TR, SMS-EPI can make use of reduced flip angle (see Equation (3.25)) compared to that used with 2D-EPI when using otherwise similar acquisition parameters. The flip angle used during resting state fMRI experiment for the 2D-EPI was 60° and that for 3D-EPI-CAIPI sequences was 14°. Due to the quadratic dependence of power on the flip angle used, there was a 19 fold reduction in the deposited power with 3D-EPI-CAIPI excitation RF pulses when compared to single-band 2D-EPI when using the same excitation RF pulse shape. In our experimental setup, this reduction in RF power was traded by a more robust fat saturation, though power intensive, based on frequency selective fat saturation pulses (alternatively, binomial excitation pulses could have been used). SMS-EPI was only possible to be run at the optimum Ernst angle once the VERSE design was integrated to the multiple band design and with respect to the standard 2D-EPI resulted in an increased SAR of 62% when the same RF pulse was used.

Table 6.1 shows that for the 3D-EPI-CAIPI there was no effect on peak power with varying $R$ because in the case of 3D-EPI-CAIPI acquisitions, $TR_{segment}$ term is used to calculate the Ernst

| Acceleration Factor (R) | Encoded $k$-planes (N) | Volume TR (sec.) | Ernst angle (deg.) | | Peak power (normalized) | | |
|---|---|---|---|---|---|---|---|
| | | | **2D** | **3D** | **MB** | **MB-PS** | **3D** |
| 1 | 60 | 3.060 | 79 | 14 | 32 | 32 | 1 |
| 2 | 30 | 1.530 | 65 | 14 | 86 | 43 | 1 |
| 3 | 20 | 1.020 | 55 | 14 | 139 | 46 | 1 |
| 4 | 15 | 0.765 | 49 | 14 | 196 | 49 | 1 |
| 5 | 12 | 0.612 | 45 | 14 | 258 | 52 | 1 |
| 6 | 10 | 0.510 | 41 | 14 | 309 | 52 | 1 |
| 7 | 9 | 0.459 | 39 | 14 | 380 | 54 | 1 |
| 8 | 8 | 0.408 | 37 | 14 | 447 | 56 | 1 |
| 9 | 7 | 0.357 | 35 | 14 | 506 | 56 | 1 |
| 10 | 6 | 0.306 | 32 | 14 | 522 | 52 | 1 |

**Table 6.1:** *Comparison table for peak power using three different RF pulse types, namely multi-band (SB), multi-band with optimized phase-scheduling (MB-PS), and single-band sinc pulse used for 3D acquisitions (3D). Peak power values were normalized with respect to RF pulse used for non-accelerated 3D acquisition. Ernst angles were used for peak power calculations taking into consideration resulting* $\mathrm{TR_{volume}}$ *due to acceleration factor (R) used.*

angle, which remains the same irrespective of the acceleration factor (R) used. Whereas in the case of 2D acquisitions, $\mathrm{TR_{volume}}$ term is used which varies depending upon the acceleration factor used along the slice-encoding direction. Due to higher Ernst angles used for 2D acquisitions and also due to quadratic or linear dependence (in the case of multi-band and phase scrambled multi-band respectively) of the peak power on the acceleration factor used, 2D acquisitions require substantially higher peak power compared to 3D acquisitions which only for very large accelerations are compensated by the reduction of the associated Ernst angle (see Equation (3.25)).

### 6.4.4  Physiological Noise

To assess the improvement in physiological noise characterization at higher sampling rates, for each the three different sampling rates, the power spectra of the physiological signals (respiration belt and cardiac signal) and the average power spectra of the whole brain during the fMRI time course were calculated and plotted together (Figure 6.5). With the lowest sampling rate used ($\mathrm{TR_{volume}}$ = 3.18 s or 0.31 Hz), both respiratory and cardiac peaks, which were observed at ~0.28 Hz and ~1.26 Hz respectively, could not be sampled adequately, since the highest frequency signal that could be sampled faithfully was ~0.16 Hz according to the Nyquist criteria. As a result, aliased peaks of respiratory and cardiac signal fluctuations (at ~0.12 Hz and ~0.14 Hz respectively) are likely to interfere with the frequency range of 0.04 Hz – 0.13 Hz where the BOLD signal is usually observed. A $\mathrm{TR_{volume}}$ of 1.06 s sampled a highest frequency of 0.47 Hz and hence could potentially sample the respiratory peak. However, in this subject, the cardiac peak was aliased at ~0.32 Hz, indicated by the arrow in Figure 6.5(b).
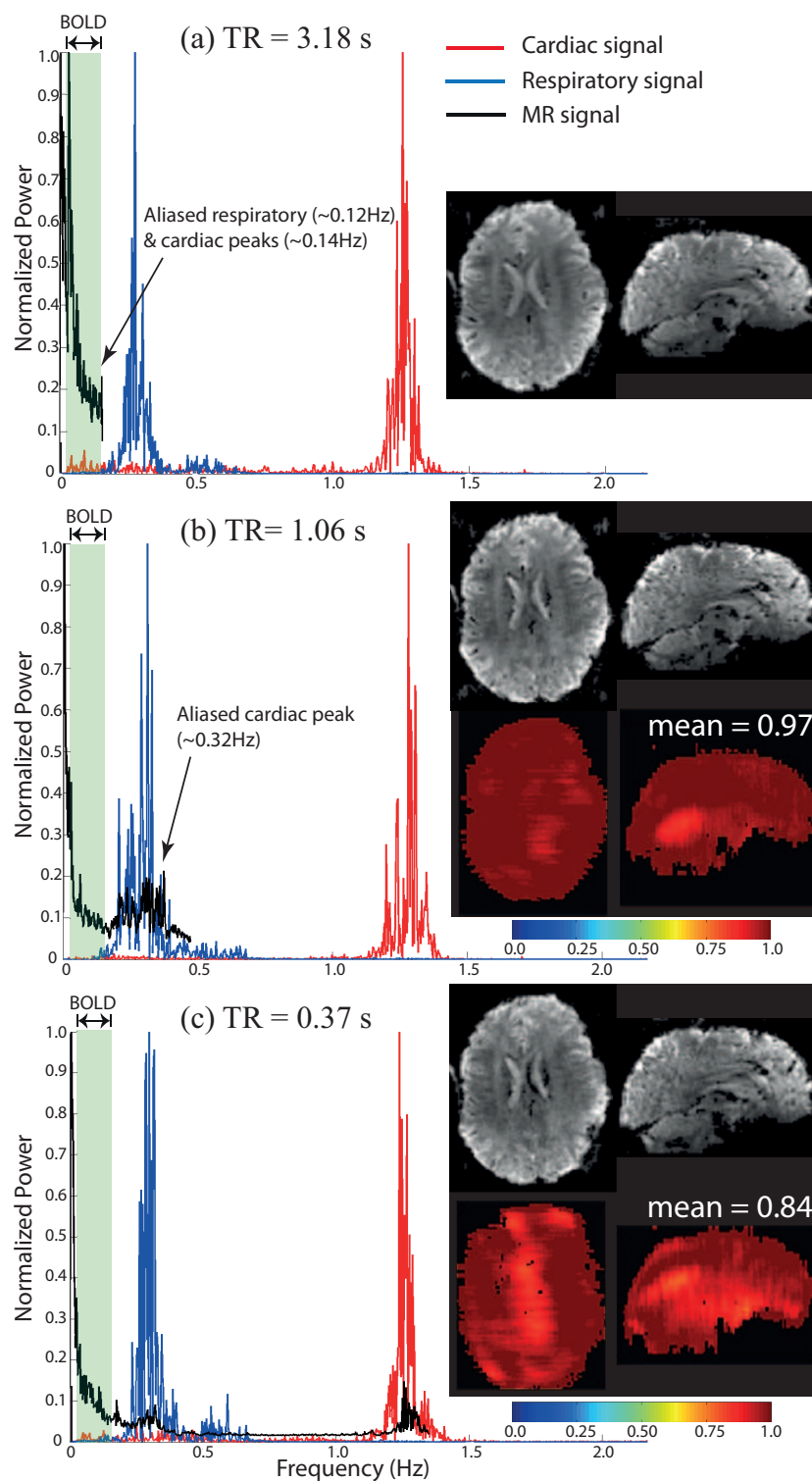
**Figure 6.5:** *Power spectra of the respiratory, cardiac and MR data obtained with* $TR_{volume}$ *of (a) 3.18 s, (b) 1.06 s, and (c) 0.37 s. BOLD signals are typically found in the 0.04 Hz – 0.13 Hz frequency range shown by the green vertical band. Inset: Whole-brain images along with $1/g$ maps shown in orthogonal planes acquired at corresponding sampling rates (only images for 3.18 s dataset). The averaged $1/g$ values are also reported on the top right of each $1/g$ map.*
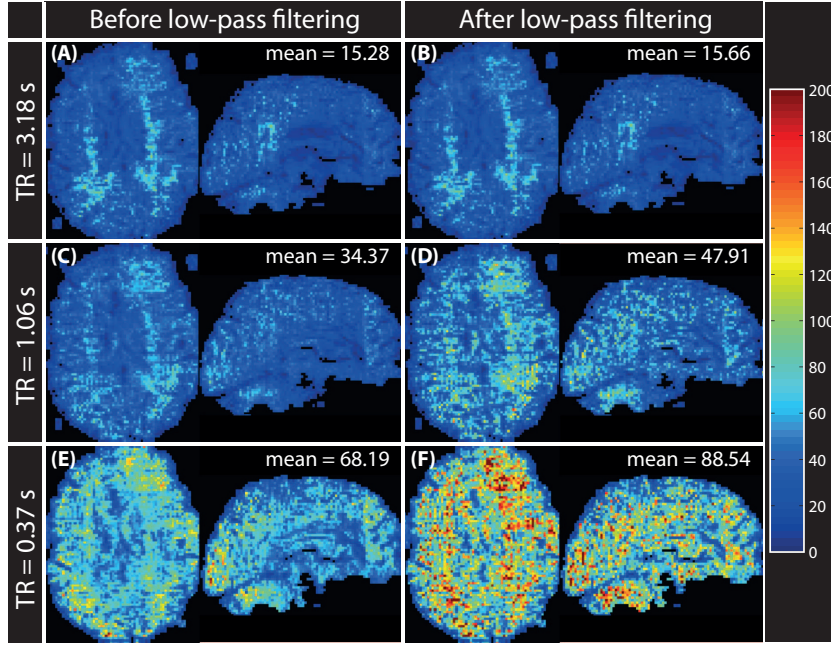
**Figure 6.6:** *tSNR per unit scan time maps for* $TR_{volume}$ *of 3.18 s, 1.06 s and 0.37 s whole-brain data. Panels A, C, and E show maps before low-pass filtering whereas panels B, D, and E show corresponding maps after low-pass filtering the datasets with a cut-off frequency at 0.14 Hz. The mean tSNR per unit scan time values calculated over the whole-brain region are indicated at the top-left of each figure panel.*

With a $TR_{volume}$ of 0.37 s, both the respiratory and cardiac related frequencies were below the Nyquist rate of ~1.34 Hz and hence well-sampled.

The insets in Figure 6.5 show orthogonal slices of the datasets acquired for power spectral analysis. As expected, the 1.06 s dataset (R = 3, Fig. 6.5b) exhibited lower g-factor losses (average $1/g = 0.97$) compared to the 0.371 s dataset (R = 8, Fig. 6.5c, average $1/g = 0.84$). The image quality with both sampling rates was considered acceptable by visual inspection, and the 8-fold acceleration resulted in only ~13% additional g-factor losses compared to 3-fold acceleration, attributed to the 2D-CAIPIRINHA sampling scheme (which was also used for the 3-fold accelerated data).

Figure 6.6 shows tSNR per unit time maps for whole-brain images for all three sampling rates. As expected, no significant improvement in tSNR per unit time values were observed for 3.18 s data since neither of the physiological signals could be filtered out via low-pass filtering from this dataset. Whereas, both 1.06 s and 0.37 s datasets, which already exhibited higher tSNR per unit time values compared to the 3.18 s dataset, benefited with the application of low-pass filtering. tSNR per unit time values showed significant increase due to removal of cardiac and respiratory fluctuations.

Figure 6.7 shows six representative RSNs identified with the three sampling rates used. The
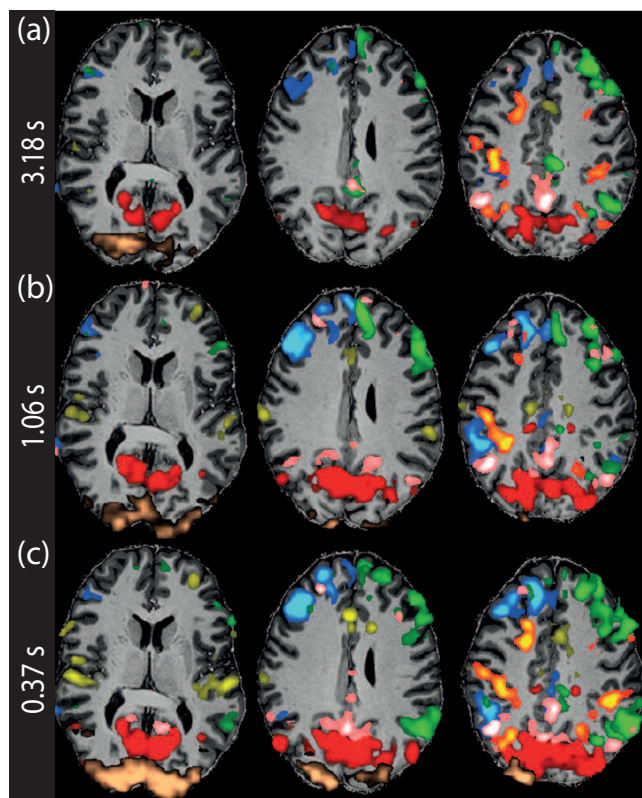
**Figure 6.7:** *Six representative resting state networks identified from datasets acquired with volume TRs of 3.18 s, 1.06 s and 0.37 s. All datasets were low-pass filtered with a cut-off frequency of 0.15 Hz to filter out respiratory and cardiac signal fluctuations. Further, 1.06 s and 0.37 s datasets were temporally under-sampled to produce an effective volume TR of 3.18 s each. All networks were applied a threshold from z = 5 to 10.*

| Resting State Network | Color used | $TR_{volume}$ = 3.18s (voxels/$Z_{max}$) | $TR_{volume}$ = 1.06s (voxels/$Z_{max}$) | $TR_{volume}$ = 0.37s (voxels/$Z_{max}$) |
|---|---|---|---|---|
| Default mode | Pink | 2725/15.83 | 3221/16.27 | 3835/19.11 |
| General visual | Brown | 3432/11.86 | 3968/13.10 | 5634/14.92 |
| Right lateral | Blue | 1871/8.58 | 2629/15.47 | 3792/16.79 |
| Left lateral | Green | 3129/12.82 | 3318/14.45 | 4469/14.48 |
| Medial visual | Red | 3838/16.44 | 4593/29.94 | 5128/32.39 |
| Auditory | Yellow | 829/7.45 | 1545/10.59 | 3749/14.83 |
| Task positive | Red-yellow | 1286/12.57 | 1621/13.84 | 2862/15.66 |
| **Mean** | **-** | **2444/12.22** | **2985/16.24** | **4210/18.31** |

**Table 6.2:** *Names along with sizes (in number of voxels) and maximum z-score ($Z_{max}$) values of resting state networks displayed in Figure 6.7 with volume TRs of 3.18 s, 1.06 s and 0.37 s. The mean activation map size is also indicated in the last row.*
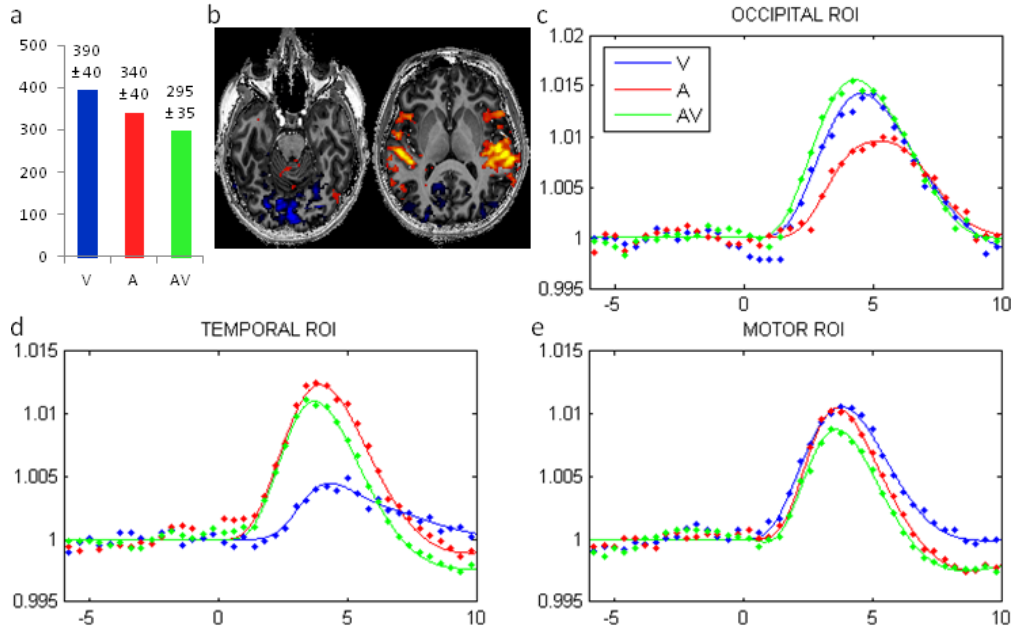
**Figure 6.8:** *(a): Average reaction times to V, A and AV stimuli. ± stderr over runs and volunteers. (b): Example slices from t-score maps (scale 3-10) of a single volunteer for 3D-EPI-CAIPI data. Red/yellow: A V, blue V A. (c): 3D-EPI-CAIPI time-courses reordered relative to stimulus onset and fitted double gamma function in the occipital lobe ROI following delivery of V, A and AV stimuli (d): time-courses and fitted double gamma function from the temporal lobe ROI and (e): time-courses and fitted double gamma function from the left motor cortex ROI. The dots show the 3D-EPI-CAIPI time-courses; the continuous lines indicate the fitted double gamma functions.*

original volume TRs are indicated on the left of each panel. The networks were found to have higher statistical significance, to show larger activated areas and to have higher maximum z-score values (see Table 6.2) using faster sampling when comparing volume TRs 3.18 s, 1.06 s and 0.37 s (top to bottom). The averaged tSNR per unit time values after low-pass filtering for the 0.37 s dataset were 63.2±1.2/95.4±2.5 (reported as: gray matter/white matter), for the 1.06 s dataset were 49.4±5.7/74.2±5.2 and for the 3.18 s dataset were 36.8±4.3/48.7±4.1. This corresponds to an increase in tSNR per unit time of grey matter of 72% and 28% with respect to the datasets with a TR of 3.18 and 1.06 respectively (while in the case of white matter the increase was of 96% and 28%). The improved tSNR per unit time in grey matter was consistent with the greater vasculature when compared to white matter and should correspond mainly to physiological noise suppression rather than stochastic noise.

### 6.4.5   Changes In HRF Dynamics Due To Multisensory Integration

Multisensory facilitation was evident from the recorded reaction times, with significant differences (p < 0.001) in reaction speed between audio-visual (AV) and both auditory (A) and visual (V) stimuli (Figure 6.8a). Martuzzi et al reported longer reaction times for A than for V stimuli,

| Time to Peak (s) | V | A | AV |
|---|---|---|---|
| Occipital | 4.70 | 5.42 | 4.46 |
| Temporal | 4.48 | 4.10 | 3.86 |
| Motor | 3.94 | 3.78 | 3.76 |

**Table 6.3:** *Time to peak of the double gamma function fitted to the HRF for auditory, visual and audiovisual responses in the occipital, temporal and left motor ROIs. Note that AV responses are fastest in all three ROIs.*

but also noted that this differed per subject [212]. The subject pool here was very limited (n=3). An example activation map for a single subject shown overlaid on the MP2RAGE anatomical shows the spatial resolution was sufficient to localize well the BOLD signal changes to the gray matter (Figure 6.8b), while yielding very high BOLD sensitivity; these maps were obtained from A>V and V>A contrasts with only 20 individual 150 $\mu$s events for each stimulus type.

ROI time-courses averaged over runs and subjects are shown in Figure 6.8 for the visual cortex (Fig. 6.8c), auditory cortex (Fig. 6.8d) and motor cortex (Fig 6.8e). The double-gamma function described well the BOLD responses to the different stimuli. The time-to-peak after stimulus onset for the fitted double gamma functions is given in Table 6.3. Positive responses for auditory stimuli were found in the visual cortex and vice versa, albeit significantly delayed compared to the cortex-own stimuli (Table 6.3), as well as much lower in amplitude, as was also reported in [212]. As can be observed from the time courses in Figure 6.8, as well as the times-to-peak in Table 6.3, BOLD responses to the AV stimulus occurred measurably earlier than either of the single-input stimuli, in agreement with [212]. This effect was found in all three ROIs, i.e. AV stimuli were followed by earlier BOLD peaks in the occipital cortex than V stimuli, earlier BOLD peaks in the temporal cortex than A stimuli and earlier BOLD peaks in the left motor cortex than both A and V stimuli. BOLD responses in the motor cortex, with audio-visual BOLD responses fastest and visual BOLD responses slowest, matched the pattern observed in reaction times (AV < A < V, Figure 6.8a) despite the changes in response times only varying by as much as 100 ms.

## 6.5 Discussion

The present study demonstrates that CAIPIRINHA acquisition strategies can readily be implemented in 3D-EPI to improve the parallel imaging reconstruction for high acceleration factors. A net acceleration of 10 fold was shown to be achievable with a 32-channel coil at 7T and was demonstrated to benefit from the CAIPIRINHA sampling pattern. The use of an improved sampling pattern resulted in an increase of SNR of ~10% compared to non-CAIPIRINHA acquisition with otherwise the same protocol parameters.

The same RSNs were detected with CAIPIRINHA enabled 3D-EPI as with SMS-EPI; with both of these short TR$_{volume}$ methods detecting more RSNs than 2D-EPI (see Figure 6.3(g-h)

"appearing networks"). In addition to the examples of 'appearing' networks, it should also be noted that many networks split into separate ICs with higher temporal sampling as shown in Figure 6.3(d-f). As networks are split into more components, the main components appear more spatially specific. Techniques identifying functionally distinct networks by their temporal independence would likely make the most of the increased temporal resolution available with higher sampling rate, as suggested by Smith et al [180] and these techniques are expected to aid network identification for sub-second temporal resolution data. However, further investigation is required to assess if the splitting of the networks was due to the increased dimensionality for IC analysis (due to increased number of volumes) or was a result of the higher sampling rates.

To detect activation-induced BOLD responses, reducing the influence of signal fluctuations caused by cardiac pulsation and respiration is especially important at high SNR [228], as well as in relatively high resolution data at (ultra-) high field [229, 230]. The effects of heartbeat and breathing are aliased to low frequencies at typical volume repetition times (TRs) of 2-3 s and cannot simply be filtered out. The use of short TRs enables better characterization of these nuisance sources which could then be removed: either by simple low-pass filtering or via physiological noise reduction schemes [229, 231, 232]. The improvement in the detection of resting state connectivity networks with faster imaging by means of increased neuronal signal sampling and increased tSNR was demonstrated previously using multiplexed 2D-EPI [179] at 3T and in 3D-EPI at 7T [207]. The results presented here are consistent with those observations. The application of a low pass filtering to the high sampling rate dataset removed much of the physiological noise in grey matter allowing an increase of tSNR of 72% and 28% with respect to the conventional (3.18 s) and mildly accelerated (1.1 s) datasets, respectively. Given that in our second resting state experiment (Figure 6.7 and Table 6.2) the data sets were down sampled to the same TR, the improvement in detection of RSN's was dominated by the improved physiological noise removal rather than increased sampling per se.

The detection of subtle changes in HRF shape and dynamics is difficult with data acquired with a volume TR of 2 seconds or higher, as the HRF remains not fully sampled. To obtain sufficient time points to characterize the HRF, 'jittering' was employed by [212]. Jittering is very sensitive to naturally occurring differences in HRF from event to event and therefore requires a large number of events to be sampled, resulting in long experiments requiring an increased numbers of participants. Sampling each single HRF time-course at sufficient temporal resolution (< 500 ms), reduces this need for averaging, allowing much smaller subject populations to be used. Here, for example, the HRF differences reported by Martuzzi et al. were able to be observed in a group of 3 volunteers rather than 12, and these three subjects only performed 2 runs each, rather than 8 as in the original study [212]. In addition, differences in the HRF time-to-peak were also found in the left motor cortex, as might be expected from the differences in reaction times to the differing stimuli, but no such differences could be reported in the original experiment, suggestive of the larger sensitivity of the high-temporal resolution acquisition at higher field strength. Note that these HRF differences were obtained from different brain regions where the vascular compliance and venous delay times may

have an important effect on the HRF dynamics. For example, in these data the time-to-peak for the motor cortex is shorter than for the occipital lobe or temporal lobe ROIs, while the neural output of the motor cortex evidently happens after the sensory input is received. This difference between brain regions must therefore reflect vasculature differences rather than neuronal processes.

The TRs of ~1 sec used with both short $TR_{volume}$ sequences were sufficient to resolve respiration physiological but not cardiac noise. The temporal SNR values observed were in agreement with those observed in a 2D-EPI vs. 3D-EPI comparison study prior to physiological noise correction [181], where it was demonstrated that this difference can be minimized by the used of physiological correction methodologies [181, 182]. Note that in the experiment presented here, the image reconstruction pipelines used for the two datasets were substantially different, although in theory closer implementations could be used [233, 234]. SMS-EPI had higher order phase correction integrated and the whole parallel imaging reconstruction was different, as mentioned in Section 6.3.2, slice GRAPPA vs. generalized GRAPPA with different kernel sizes and regularization parameters (see Appendix B). Although, in implementation, the image reconstruction of SMS-EPI and 3D-EPI-CAIPI are very distinct, the aliasing patterns used were similar which means that comparable g-factors can be expected for the two approaches - although the correlated noise in SMS-EPI will be limited to the simultaneously acquired slices while in 3D-EPI-CAIPI it is expected to be less localized. Therefore, the main advantage of the 3D-EPI-CAIPI with respect to SMS-EPI, in terms of acceleration, is the ability to use partial Fourier acquisitions in addition to the parallel imaging along the partition-encoding direction followed by homodyne reconstruction [217, 218] if desired. Theoretically, partial Fourier reconstruction can also be used with SMS-EPI but has practical limitations because the number of $k$-space samples along the slice-encoding direction get reduced by a factor equal to number of simultaneously excited slices.

Recently, other groups have started exploring the possibility to use the controlled aliasing in 3D-EPI as a means to obtain higher spatial resolution by translating through-plane sensitivities into in-plane accelerations [235]. In our implementation, the use of 3D-EPI-CAIPI is expected to be of greater benefit for fMRI applications where temporal resolution, more than spatial resolution, is a limiting factor. For example, when studying rapid transient responses [236] or the shape of the hemodynamic response function as done here in the multisensory integration experiment, or when targeting regions such as the brain stem, where cardiac pulsation plays an important role [237] not only in terms of signal intensity variation but also in terms of motion.

## 6.6 Conclusions

We conclude that the standard 3D-EPI can be modified to include controlled aliasing $k$-space coverage acquisition patterns, which allows to increase parallel imaging acceleration in the partition-encoding direction and hence increased temporal SNR and increased temporal

resolution with reduced g-factor penalties compared to standard 3D-EPI. With the increased temporal resolution obtained, a better characterization and removal of the physiological noise is possible, thereby implicitly improving the ability to detect resting state networks and functional activity. Finally, 3D-EPI-CAIPI offers reduced peak power when compared to similar 2D-based techniques, making it an ideal candidate for functional imaging at ultra-high fields.

# References

[174] P Mansfield. Multi-planar image formation using nmr spin echoes, 1977.

[175] Peter A. Bandettini, Eric C. Wong, R. Scott Hinks, Ronald S. Tikofsky, and James S. Hyde. Time course epi of human brain function during task activation. *Magnetic Resonance in Medicine*, 25(2):390–397, 1992.

[176] K K Kwong, J W Belliveau, D A Chesler, I E Goldberg, R M Weisskoff, B P Poncelet, D N Kennedy, B E Hoppel, M S Cohen, and R Turner. Dynamic magnetic resonance imaging of human brain activity during primary sensory stimulation. *Proceedings of the National Academy of Sciences*, 89(12):5675–5679, 1992.

[177] S Ogawa, D W Tank, R Menon, J M Ellermann, S G Kim, H Merkle, and K Ugurbil. Intrinsic signal changes accompanying sensory stimulation: functional brain mapping with magnetic resonance imaging. *Proceedings of the National Academy of Sciences*, 89(13):5951–5955, 1992.

[178] David G. Norris. Principles of magnetic resonance assessment of brain function. *Journal of Magnetic Resonance Imaging*, 23(6):794–807, 2006.

[179] David A. Feinberg, Steen Moeller, Stephen M. Smith, Edward Auerbach, Sudhir Ramanna, Matt F. Glasser, Karla L. Miller, Kamil Ugurbil, and Essa Yacoub. Multiplexed echo planar imaging for sub-second whole brain fmri and fast diffusion imaging. *PLoS ONE*, 5(12):e15710, 2010.

[180] Stephen M. Smith, Karla L. Miller, Steen Moeller, Junqian Xu, Edward J. Auerbach, Mark W. Woolrich, Christian F. Beckmann, Mark Jenkinson, Jesper Andersson, Matthew F. Glasser, David C. Van Essen, David A. Feinberg, Essa S. Yacoub, and Kamil Ugurbil. Temporally-independent functional modes of spontaneous brain activity. *Proceedings of the National Academy of Sciences*, 109(8):3131–3136, 2012.

[181] João Jorge, Patrícia Figueiredo, Wietske van der Zwaag, and José P. Marques. Signal fluctuations in fmri data acquired with 2d-epi and 3d-epi at 7 tesla. *Magnetic Resonance Imaging*, 31(2):212 – 220, 2013.

[182] Antoine Lutti, David L. Thomas, Chloe Hutton, and Nikolaus Weiskopf. High-resolution functional mri at 3 t: 3d/2d echo-planar imaging with optimized physiological noise correction. *Magnetic Resonance in Medicine*, 69(6):1657–1664, 2013.

[183] Stefan Posse, Elena Ackley, Radu Mutihac, Jochen Rick, Matthew Shane, Cristina Murray-Krezan, Maxim Zaitsev, and Oliver Speck. Enhancement of temporal resolution and bold sensitivity in real-time fmri using multi-slab echo-volumar imaging. *Neuroimage*, 61(1):115–30, 2012.

[184] David J. Larkman, Joseph V. Hajnal, Amy H. Herlihy, Glyn A. Coutts, Ian R. Young, and Gösta Ehnholm. Use of multicoil arrays for separation of signal from multiple slices simultaneously excited. *Journal of Magnetic Resonance Imaging*, 13(2):313–317, 2001.

[185] R. Nunes, J. Hajnal, D. Larkman, and X. Golay. Simultaneous slice excitation and reconstruction for single shot epi. In *Proceedings 13th Scientific Meeting, International Society for Magnetic Resonance in Medicine, Seattle*, page 293, 2006.

[186] Kawin Setsompop, Borjan A. Gagoski, Jonathan R. Polimeni, Thomas Witzel, Van J. Wedeen, and Lawrence L. Wald. Blipped-controlled aliasing in parallel imaging for simultaneous multislice echo planar imaging with reduced g-factor penalty. *Magnetic Resonance in Medicine*, 67(5):1210–1224, 2012.

[187] Steen Moeller, Essa Yacoub, Cheryl A. Olman, Edward Auerbach, John Strupp, Noam Harel, and Kâmil Uğurbil. Multiband multislice ge-epi at 7 tesla, with 16-fold acceleration using partial parallel imaging with application to high spatial and temporal whole-brain fmri. *Magnetic Resonance in Medicine*, 63(5):1144–1153, 2010.

[188] Felix A. Breuer, Martin Blaimer, Robin M. Heidemann, Matthias F. Mueller, Mark A. Griswold, and Peter M. Jakob. Controlled aliasing in parallel imaging results in higher acceleration (caipirinha) for multi-slice imaging. *Magnetic Resonance in Medicine*, 53(3):684–691, 2005.

[189] Gary H. Glover. Phase-offset multiplanar (pomp) volume imaging: A new technique. *Journal of Magnetic Resonance Imaging*, 1(4):457–461, 1991.

[190] David A. Feinberg, Timothy G. Reese, and Van J. Wedeen. Simultaneous echo refocusing in epi. *Magnetic Resonance in Medicine*, 48(1):1–5, 2002.

[191] Thomas Loenneker, Franciszek Hennel, and Jürgen Hennig. Multislice interleaved excitation cycles (music): An efficient gradient-echo technique for functional mri. *Magnetic Resonance in Medicine*, 35(6):870–874, 1996.

[192] S. Müller. Multifrequency selective rf pulses for multislice mr imaging. *Magnetic Resonance in Medicine*, 6(3):364–371, 1988.

[193] Steven Conolly, Dwight Nishimura, Albert Macovski, and Gary Glover. Variable-rate selective excitation. *Journal of Magnetic Resonance (1969)*, 78(3):440 – 458, 1988.

[194] E.C. Wong. Optimized phase schedules for minimizing peak rf power in simultaneous multi-slice rf excitation pulses. In *Proceedings 20th Scientific Meeting, International Society for Magnetic Resonance in Medicine, Melbourne*, page 2209, 2012.

## REFERENCES

[195] P.J. Koopmans, R. Boyacioglu, M. Barth, and Prof.Dr. D.G. Norris. Whole brain, high resolution spin-echo resting state fmri using pins multiplexing at 7 t. *Neuroimage*, 62(3):1939 – 1946, 2012.

[196] David G. Norris, Peter J. Koopmans, Rasim Boyacioğlu, and Markus Barth. Power independent of number of slices (pins) radiofrequency pulses for low-power simultaneous multislice excitation. *Magnetic Resonance in Medicine*, 66(5):1234–1240, 2011.

[197] Edward J. Auerbach, Junqian Xu, Essa Yacoub, Steen Moeller, and Kâmil Uğurbil. Multi-band accelerated spin-echo echo planar imaging with reduced peak rf power using time-shifted rf pulses. *Magnetic Resonance in Medicine*, 69(5):1261–1267, 2013.

[198] P Mansfield, R Coxon, and J Hykin. Echo-volumar imaging (evi) of the brain at 3.0 t: first normal volunteer and functional imaging results. *J Comput Assist Tomogr*, 19(6):847–52, 1995.

[199] Allen W. Song, Eric C. Wong, and James S. Hyde. Echo-volume imaging. *Magnetic Resonance in Medicine*, 32(5):668–671, 1994.

[200] Wietske van der Zwaag, Susan Francis, and Richard Bowtell. Improved echo volumar imaging (evi) for functional mri. *Magnetic Resonance in Medicine*, 56(6):1320–1327, 2006.

[201] Benjamin Zahneisen, Thimo Hugger, Kuan J. Lee, Pierre LeVan, Marco Reisert, Hsu-Lei Lee, Jakob Assländer, Maxim Zaitsev, and Jürgen Hennig. Single shot concentric shells trajectories for ultra fast fmri. *Magnetic Resonance in Medicine*, 68(2):484–494, 2012.

[202] Benjamin Zahneisen, Thimo Grotz, Kuan J. Lee, Sabine Ohlendorf, Marco Reisert, Maxim Zaitsev, and Jürgen Hennig. Three-dimensional mr-encephalography: Fast volumetric brain imaging using rosette trajectories. *Magnetic Resonance in Medicine*, 65(5):1260–1268, 2011.

[203] Amir M. Abduljalil, Anthony H. Aletras, and Pierre-Marie Robitaille. 3d echo planar imaging: Application to the human head. *Magnetic Resonance in Medicine*, 34(2):144–148, 1995.

[204] L. Tugan Muftuler and Orhan Nalcioglu. Improvement of temporal resolution in fmri using slice phase encode reordered 3d epi. *Magnetic Resonance in Medicine*, 44(3):485–490, 2000.

[205] B A Poser, P J Koopmans, T Witzel, L L Wald, and M Barth. Three dimensional echo-planar imaging at 7 tesla. *Neuroimage*, 51(1):261–6, 2010.

[206] W. van der Zwaag, J. P. Marques, T. Kober, G. Glover, R. Gruetter, and G. Krueger. Temporal snr characteristics in segmented 3d-epi at 7t. *Magnetic Resonance in Medicine*, 67(2):344–352, 2012.

[207] Mayur Narsude, Wietske van der Zwaag, Tobias Kober, Rolf Gruetter, and José P. Marques. Improved temporal resolution for functional studies with reduced number of segments with three-dimensional echo planar imaging. *Magnetic Resonance in Medicine*, pages n/a–n/a, 2013.

[208] Yanle Hu and Gary H. Glover. Three-dimensional spiral technique for high-resolution functional mri. *Magnetic Resonance in Medicine*, 58(5):947–951, 2007.

[209] Song Lai and Gary H. Glover. Three-dimensional spiral fmri technique: A comparison with 2d spiral acquisition. *Magnetic Resonance in Medicine*, 39(1):68–78, 1998.

[210] Felix A. Breuer, Martin Blaimer, Matthias F. Mueller, Nicole Seiberlich, Robin M. Heidemann, Mark A. Griswold, and Peter M. Jakob. Controlled aliasing in volumetric parallel imaging (2d caipirinha). *Magnetic Resonance in Medicine*, 55(3):549–556, 2006.

[211] K. Setsompop, J. Cohen-Adad, B.A. Gagoski, T. Raij, A. Yendiki, B. Keil, V.J. Wedeen, and L.L. Wald. Improving diffusion {MRI} using simultaneous multi-slice echo planar imaging. *NeuroImage*, 63(1):569 – 580, 2012.

[212] Roberto Martuzzi, Micah M Murray, Christoph M Michel, Jean-Philippe Thiran, Philippe P Maeder, Stephanie Clarke, and Reto A Meuli. Multisensory interactions within human primary cortices revealed by bold dynamics. *Cereb Cortex*, 17(7):1672–9, 2007.

[213] Mayur Narsude, José P. Marques, Daniel Gallichan, and Rolf Gruetter. Superior grappa reconstruction with reduced g-factor noise using 2d caipirinha for 3d epi. In *Proceedings 21st Scientific Meeting, International Society for Magnetic Resonance in Medicine, Salt Lake City*, page 3705, 2013.

[214] Felix A. Breuer, Stephan A.R. Kannengiesser, Martin Blaimer, Nicole Seiberlich, Peter M. Jakob, and Mark A. Griswold. General formulation for quantitative g-factor calculation in grappa reconstructions. *Magnetic Resonance in Medicine*, 62(3):739–746, 2009.

[215] Florent Eggenschwiler, Tobias Kober, Arthur W. Magill, Rolf Gruetter, and José P. Marques. Sa2rage: A new sequence for fast b1+-mapping. *Magnetic Resonance in Medicine*, 67(6):1609–1619, 2012.

[216] José P. Marques, Tobias Kober, Gunnar Krueger, Wietske van der Zwaag, Pierre-François Van de Moortele, and Rolf Gruetter. Mp2rage, a self bias-field corrected sequence for improved segmentation and t1-mapping at high field. *NeuroImage*, 49(2):1271 – 1281, 2010.

[217] Mark Bydder and Matthew D. Robson. Partial fourier partially parallel imaging. *Magnetic Resonance in Medicine*, 53(6):1393–1401, 2005.

[218] E.M Haacke, E.D Lindskogj, and W Lin. A fast, iterative, partial-fourier technique capable of local phase recovery. *Journal of Magnetic Resonance (1969)*, 92(1):126 – 145, 1991.

## REFERENCES

[219] Douglas N. Greve and Bruce Fischl. Accurate and robust brain image alignment using boundary-based registration. *NeuroImage*, 48(1):63 – 72, 2009.

[220] Mark Jenkinson, Peter Bannister, Michael Brady, and Stephen Smith. Improved optimization for the robust and accurate linear registration and motion correction of brain images. *NeuroImage*, 17(2):825 – 841, 2002.

[221] Mark Jenkinson and Stephen Smith. A global optimisation method for robust affine registration of brain images. *Medical Image Analysis*, 5(2):143 – 156, 2001.

[222] Christian F. Beckmann, Marilena DeLuca, Joseph T. Devlin, and Stephen M. Smith. Investigations into resting-state connectivity using independent component analysis. *Philosophical Transactions of the Royal Society B: Biological Sciences*, 360(1457):1001–1013, May 2005.

[223] Bharat Biswal, F. Zerrin Yetkin, Victor M. Haughton, and James S. Hyde. Functional connectivity in the motor cortex of resting human brain using echo-planar mri. *Magnetic Resonance in Medicine*, 34(4):537–541, 1995.

[224] F De Martino, F Esposito, PF van de Moortele, N Harel, E Formisano, R Goebel, K Ugurbil, and E Yacoub. Whole brain high-resolution functional imaging at ultra high magnetic fields: an application to the analysis of resting state networks. *NeuroImage*, 57(3):1031 – 1044, 2011.

[225] Elena Shumskaya, Teuntje M J C Andriessen, David G Norris, and Pieter E Vos. Abnormal whole-brain functional networks in homogeneous acute mild traumatic brain injury. *Neurology*, 79:175 – 182, 2012.

[226] Ilya M. Veer, Christian Beckmann, Marie-Jose Van Tol, Luca Ferrarini, Julien Milles, Dick Veltman, Andre Aleman, Mark A Van Buchem, Nic J A Van Der Wee, and Serge A R Rombouts. Whole brain resting-state analysis reveals decreased functional connectivity in major depression. *Frontiers in Systems Neuroscience*, 4(41), 2010.

[227] Gary H. Glover. Deconvolution of impulse response in event-related {BOLD} fmri1. *NeuroImage*, 9(4):416 – 429, 1999.

[228] J. Bodurka, F. Ye, N. Petridou, K. Murphy, and P.A. Bandettini. Mapping the {MRI} voxel volume in which thermal noise matches physiological noise—implications for fmri. *NeuroImage*, 34(2):542 – 549, 2007.

[229] Marta Bianciardi, Peter van Gelderen, Jeff H. Duyn, Masaki Fukunaga, and Jacco A. de Zwart. Making the most of fmri at 7 t by suppressing spontaneous signal fluctuations. *NeuroImage*, 44(2):448 – 454, 2009.

[230] C. Hutton, O. Josephs, J. Stadler, E. Featherstone, A. Reid, O. Speck, J. Bernarding, and N. Weiskopf. The impact of physiological noise correction on fmri at 7t. *NeuroImage*, 57(1):101 – 112, 2011.

[231] Marta Bianciardi, Masaki Fukunaga, Peter van Gelderen, Silvina G. Horovitz, Jacco A. de Zwart, Karin Shmueli, and Jeff H. Duyn. Sources of functional magnetic resonance imaging signal fluctuations in the human brain at rest: a 7 t study. *Magnetic Resonance Imaging*, 27(8):1019 – 1029, 2009. Proceedings of the International School on Magnetic Resonance and Brain Function Proceedings of the International School on Magnetic Resonance and Brain Function.

[232] Gary H. Glover, Tie-Qiang Li, and David Ress. Image-based method for retrospective correction of physiological motion effects in fmri: Retroicor. *Magnetic Resonance in Medicine*, 44(1):162–167, 2000.

[233] Benjamin Zahneisen, Benedikt A. Poser, Thomas Ernst, and V. Andrew Stenger. Three-dimensional fourier encoding of simultaneously excited slices: Generalized acquisition and reconstruction framework. *Magnetic Resonance in Medicine*, pages n/a–n/a, 2013.

[234] K. Zhu, A. Kerr, and J. Pauly. Autocalibrating caipirinha: Reformulating caipirinha as a 3d problem. In *Proceedings 20th Scientific Meeting, International Society for Magnetic Resonance in Medicine, Melbourne*, page 518, 2012.

[235] B.A. Poser, V.G. Kemper, D. Ivanov, S.A. Kannengiesser, K. Uludag, and M. Barth. Caipirinha-accelerated 3d epi for high temporal and/or spatial resolution epi acquisitions. In *Proceedings of the 30th Annual Scientific Meeting of ESMRMB, Toulouse, France*, page 226, 2013.

[236] Onur Afacan, W. Scott Hoge, Firdaus Janoos, Dana H. Brooks, and Istvan A Morocz. Rapid full-brain fmri with an accelerated multi shot 3d epi sequence using both unfold and grappa. *Magnetic Resonance in Medicine*, 67(5):1266–1274, 2012.

[237] A.R. Guimaraes, J.R. Melcher, T.M. Talavage, J.R. Baker, P. Ledden, B.R. Rosen, N.Y.S. Kiang, B.C. Fullerton, and R.M. Weisskoff. Imaging subcortical auditory activity in humans. *Human Brain Mapping*, 6(1):33–41, 1998.

# 7 Spiral Excitation 3D EPI

Slice selective RF excitation, introduced in Section 3.1.1, is spatially selective in only a single direction. A single plane (i.e. a slice) of spins is excited by the 1D RF pulse accompanied by slice-select gradient and this scheme is often followed by a refocusing gradient lobe to refocus the dephased spins known as the *refocusing gradient*. A multidimensional RF pulse is spatially selective in more than one direction. For example, using a 2D RF pulse [238, 239], a long strip or cylinder can be selectively excited whereas a 3D RF pulse [240], due to its selectivity in three directions, can excite a voxel of spins. However due to their long pulse durations, 3D RF pulses are less commonly used than their 2D counterpart.

This chapter starts with expanding $k$-space interpretation to the excitation of a RF pulse (we have interpreted $k$-space traversal during acquisition in Chapter 3). Before moving on to explaining $k$-space interpretation of 2D RF excitation, we familiarize ourselves with the $k$-space approach of understanding RF excitation by analyzing 1D selective excitation pulse. Once the founding concepts for 2D RF pulse and its $k$-space interpretation are explained, design and application of 2D RF excitation pulse in combination with 3D-EPI-CAIPI [241] readout module is demonstrated for localized fMRI acquisition.

## 7.1 $K$-space Interpretation of Radio-frequency Excitation

A general solution to the Bloch equation (see Equation (2.33)) can be derived for the transverse magnetization ($M_{xy}$) as

$$M_{xy}(x) = i\gamma M_0 \int_0^T B_1(t) e^{ix \cdot k(t)} \mathrm{d}t \tag{7.1}$$

Where $M_{xy}$ is defined as in Equation (2.21) ($M_{xy} = M_\perp$), whereas $B_1$ is defined as

$$B_1 = B_{1,x} + i B_{1,y} \tag{7.2}$$

The solution in Equation (7.1) is derived for the small-tip angle approximation, which assumes that the longitudinal magnetization $M_z$ remains equal to its equilibrium value $M_0$ since the excitation pulse rotates the magnetization vector **M** by only a small angle from the $+z$-axis. Hence,

$$M_z \approx M_0 = \text{constant} \tag{7.3}$$

The initial state of the spin system is assumed to be $(0, 0, M_0)$ for the derivation of Equation (7.1). The term $k(t)$ describes the $k$-space trajectory, i.e. the path on which $k$-space is traversed during the application of an RF pulse, and is defined by

$$k(t) = -\gamma \int_t^T \mathbf{G}(t')\, \mathrm{d}t' \tag{7.4}$$

This definition differs from the one commonly used in MRI (see Equation (3.12)) in that the integration is from the time $t$ to the end of the applied gradient (**G**) duration $T$. We can write exponential in Equation (7.1) as an integral of a three-dimensional delta function:

$$M_{xy}(x) = i\gamma M_0 \int_0^T B_1(t) \int_K {}^3\delta(k(t) - k) e^{ix\cdot k} \mathrm{d}k \mathrm{d}t \tag{7.5}$$

Exchanging the order of integration,

$$M_{xy}(x) = i\gamma M_0 \int_K \left\{ \int_0^T B_1(t) {}^3\delta(k(t) - k) \mathrm{d}t \right\} e^{ix\cdot k} \mathrm{d}k \tag{7.6}$$

The term in the braces is the three-dimensional path which can be assigned a new function $p(k)$:

$$p(k) = \int_0^T B_1(t) {}^3\delta(k(t) - k) \mathrm{d}t \tag{7.7}$$

Resulting in following expression for transverse magnetization which is simply the Fourier transformation of the weighted $k$-space trajectory.

$$M_{xy}(x) = i\gamma M_0 \int_K p(k) e^{ix\cdot k} \mathrm{d}k \tag{7.8}$$

The expression in Equation (7.8) can further be simplified by normalizing the delta function in Equation (7.7) by multiplying it with derivative of its argument. To balance the equation, we must divide by the same factor. i.e., we multiply delta function by $|\frac{\mathrm{d}k}{\mathrm{d}t}|$ and divide $B_1(t)$ by $|\gamma \mathbf{G}(t)|$ since $\frac{\mathrm{d}k}{\mathrm{d}t} = \gamma \mathbf{G}(t)$.

Now, defining a spatial weighting function $W(k(t))$ as

$$W(k(t)) = \frac{B_1(t)}{|\gamma \mathbf{G}(t)|} \tag{7.9}$$
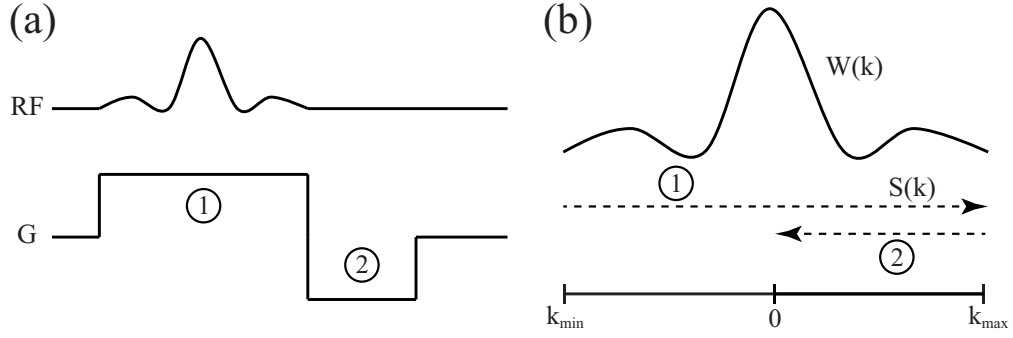
**Figure 7.1:** *K-space interpretation of the slice-selective excitation. (a) A sinc pulse is played together with a slice-select gradient. At the end of the sinc pulse, a refocusing gradient lobe with area equal to half the area of slice-select gradient but with opposite polarity is played to refocus the excited magnetization. (b) RF weighting $W(k)$ and sampling function $S(k)$ is illustrated for the 1D slice-selective excitation. Notice the symmetric RF weighting about the k-space origin and that the refocusing gradient brings the sampling position back to the center of the symmetric RF weighting (path 2) in order to refocus the magnetization. The slice profile is simply the Fourier transformation of the weighting function.*

and a sampling path function $S(k)$ as

$$S(k) = \int_0^T \left\{ {}^3\delta(k(t) - k) \, | \, \dot{k}(t) \, | \right\} \mathrm{d}t \tag{7.10}$$

make Equation (7.8) take the form

$$M_{xy}(x) = i\gamma M_0 \int_K W(k)S(k)e^{ix \cdot k}\mathrm{d}k \tag{7.11}$$

Equation (7.11) simply states that the resulting transverse magnetization is the Fourier transform of a spatial frequency weighting function $W(k)$ multiplied by a spatial frequency sampling function $S(k)$. This expression allows to determine the sampling path to be followed and the weighting of the RF energy across the spatial frequency space while designing a 2-dimensional RF pulse for selective excitation. Although the discussion above is carried out using a small-tip angle approximation, it has been shown by Pauly et al. that the results can be valid for flip angles as large as 90° under spatial symmetry considerations [242].

### 7.1.1  Conventional Slice-selective Excitation: *k*-space Interpretation

A slice-selective excitation module was introduced in Section 3.1.1. As shown in Figure 7.1(a), during slice-selection, a constant gradient is applied along the slice-encoding direction (*z*-axis to follow the nomenclature) while a sinc RF pulse is applied simultaneously. At the end of the sinc pulse, a gradient-refocusing lobe with opposite polarity is added to refocus the through-slice dephased magnetization. The area of this refocusing gradient is half of the area of the main slice-select gradient.

The $k$-space interpretation of this conventional slice-selective excitation is as follows (see Figure 7.1(b)): According to Equation (7.4), the location of the $k$-space at time $t$ is the integral of the *remaining* gradient waveform. Hence considering the entire slice-select process (including the refocusing gradient), the position in $k$-space at the beginning of application of the RF pulse is at $k_{min}$. The center of the $k$-space (origin) is reached when the positive and the negative gradients balance each other out which occurs halfway through the RF pulse. During the application of the remaining half of the RF pulse, the $k$-space position shifts away from the origin towards $k_{max}$, and causes dephasing. The negative gradient lobe (refocusing gradient) brings the $k$-space position back to the origin, which is also the center of the applied symmetric RF weighting. The slice profile is thus simply the Fourier transformation of the applied RF weighting. In general for a symmetric weighting of the $k$-space, if the final $k$-space position ends up at the center of the symmetric weighting, the excited magnetization is automatically refocused.

## 7.2 Circularly Symmetric Gaussian Localized Excitation

In this section we describe an analytical approach for designing an inherently (auto-) refocused two-dimensional selective excitation RF pulse based on [243]. Following the understanding developed in the previous section, it becomes clear that designing a RF pulse requires a spatial frequency weighting function $D(k)$ whose Fourier transformation is the desired excitation profile. Moreover the auto-refocusing requirement implies that $D(k)$ is symmetric and that the $k$-space sampling ends at the center of the weighting function. The frequency weighting function $D(k)$ can be written as a multiplication of a weighting function $W(k)$ and a spatial frequency sampling function $S(k)$ (sampling trajectory); i.e. $D(k) = W(k)S(k)$ [242].

For a circularly symmetric Gaussian localization excitation, the desired spatial frequency weighting also has to be a circularly symmetric Gaussian function. Moreover, since the design specification demands an auto-refocused excitation, the sampling position must end at the center of the symmetric weighting function; i.e. at the origin and hence sampling starts at the edge of the spiral and moves towards the center along the spiral. Note that, it is also possible to obtain the same excitation profile with a spiral-out trajectory with the same weighting function but it would require a refocusing lobe at the end of the RF pulse.

The required $k$-space trajectory for a spiral in sampling can be written as

$$k_x(t) = A\left(1 - \frac{t}{T}\right)\cos\left(\frac{2\pi n t}{T}\right)$$
$$k_y(t) = A\left(1 - \frac{t}{T}\right)\sin\left(\frac{2\pi n t}{T}\right)$$

(7.12)

where the amplitude $A$ in Equation (7.12) above determines the maximum $k$-space extent of the spiral trajectory designed for $n$ cycles in a time $T$. The gradient waveforms required to produce this spiral trajectory can be computed by simply taking the derivative of Equation
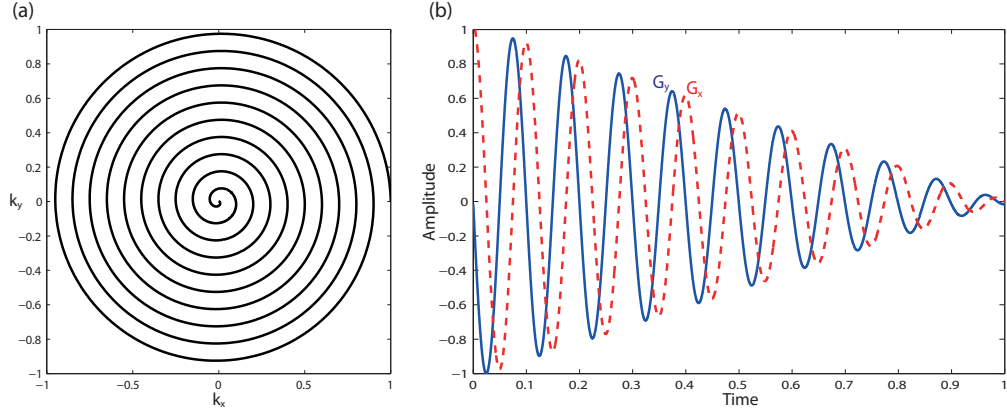
**Figure 7.2:** *(a) Spiral $k$-space trajectory and (b) the required gradient waveforms to traverse inward path along the trajectory (Equation (7.13)).*

(7.4) and rearranging the terms.

$$
\begin{aligned}
G_x(t) &= -\frac{A}{\gamma T}\left[2\pi n\left(1-\frac{t}{T}\right)\sin\left(\frac{2\pi n t}{T}\right)+\cos\left(\frac{2\pi n t}{T}\right)\right]\\
G_y(t) &= \frac{A}{\gamma T}\left[2\pi n\left(1-\frac{t}{T}\right)\cos\left(\frac{2\pi n t}{T}\right)-\sin\left(\frac{2\pi n t}{T}\right)\right]
\end{aligned}
\tag{7.13}
$$

An example spiral $k$-space trajectory and associated gradient waveforms are shown in Figure 7.2 for $n = 10$.

Now that the spatial sampling function $S(k)$ has been determined and presuming that the spiral trajectory is traversed with sufficient density, the required spatial frequency weighting $W(k)$ needs to be determined: As discussed in Section 7.1.1, the Fourier transformation of the applied RF weighting in $k$-space gives the slice-profile of the excited magnetization. The required spatial weighting function $W(k)$ for obtaining a Gaussian localized excitation can be written as:

$$
W(k) = A_G e^{-\sigma^2\left(k_x^2+k_y^2\right)/A^2}
\tag{7.14}
$$

where $A_G$ is an overall scale factor which determines the excitation flip angle, and $\sigma$ is linearly proportional to the Gaussian pulse width and hence influences the spatial resolution of the selective volume.

141
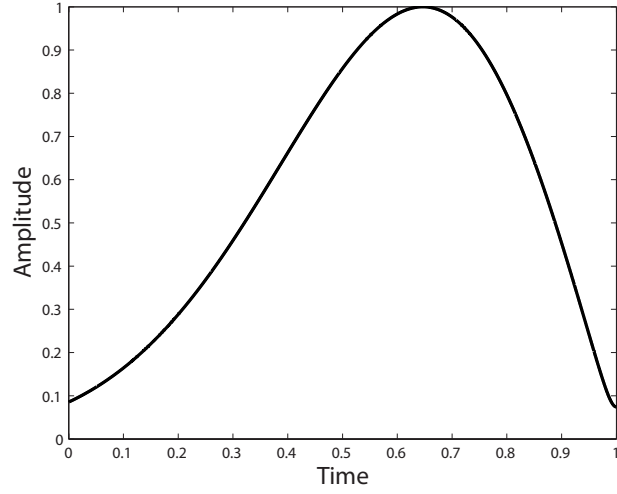
**Figure 7.3:** *An example Gaussian RF pulse shape to produce a cylindrical Gaussian weighting of k-space. Gradients waveforms, as given in Equation (7.13), have to be played during application of this RF pulse. The RF pulse shown here is calculated using equation (7.15) for σ = 2 and n = 10.*

Recalling Equation 7.9 and combining with Equations (7.13) & (7.14) with it, results in

$$
\begin{aligned}
B_1(t) &= W(t)\,|\,\gamma G(t)\,| \\[1mm]
&= A_G e^{-\sigma^2\left(k_x^2 + k_y^2\right)/A^2}\,\gamma \frac{A}{T}\sqrt{\left[2\pi n\left(1 - \frac{t}{T}\right)\right]^2 + 1} \\[1mm]
&= \gamma A_G \frac{A}{T} e^{-\sigma^2\left(1 - \frac{t}{T}\right)^2}\sqrt{\left[2\pi n\left(1 - \frac{t}{T}\right)\right]^2 + 1}
\end{aligned}
\tag{7.15}
$$

An example RF pulse shape with $\sigma = 2$, for gradients given in Equation (7.13), is illustrated in Figure 7.3. This $B_1$ field applied in combination with gradients described in Equation (7.13) results in a circularly symmetric Gaussian localized excitation.

The thickness $d$ of the 2D profile (i.e. the diameter of the cylindrical excitation profile) can be expressed as the ratio of the dimensionless time-bandwidth product of the Gaussian pulse and the maximal $k$-space radius obtained by the sampling trajectory:

$$
d = \frac{T\Delta f}{2K_r}
\tag{7.16}
$$

where the quantity $t\Delta f$ is the time-bandwidth product of the Gaussian RF pulse whereas $K_r$ is the maximum radial extent of the spiral $k$-space from the $k$-space origin.

As with the data acquisition part, where significant attention is provided to sampling density in order to avoid image aliasing, extra care needs to be taken to ensure sufficient $k$-space sampling density during the excitation part to limit excitation aliasing (i.e., undesired excitation). For simplicity, the spiral $k$-space trajectory can be considered as a set of equidistant concentric rings separated by $\Delta k_r$ in the radial direction. The Fourier tranformation of of such discrete $k$-space sampling is of infinite extent and consists of a central peak with additional ring lobes appearing at distances of integer multiples of $\frac{1}{\Delta k_r}$. The distance of adjacent lobes in the excitation profile is equivalent to the field-of-view definition in the imaging domain
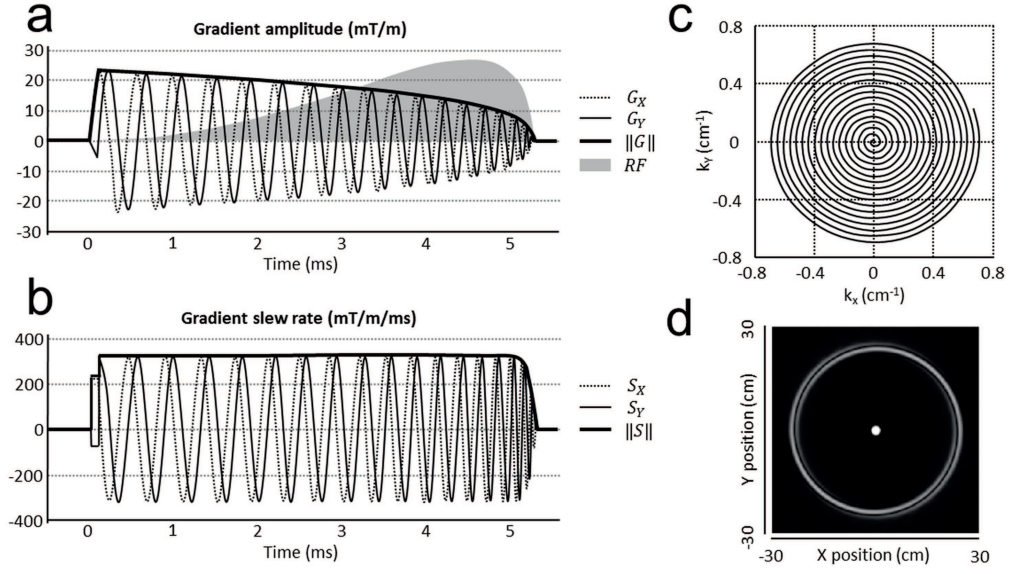
**Figure 7.4:** *(a) Spiral gradient waveform (5.17 ms) generated using an exponential slew-rate recovery model [244] and RF shape (gray area, arbitrary units) exciting a 0.7 cm cylinder radius. (b) Following hardware limitations, the gradient time-derivative shows that the gradient system is working in the slew-rate limited regime (330 mT·m$^{-1}$·ms$^{-1}$), and further constrained near the k-space center. (c) Corresponding excitation k-space. The maximum extent in k-space $k_{max}$ and the interval between two consecutive spiral turns characterize the cylinder radius and position of the first aliasing lobes of the excitation profile (see Equations (7.16) and (7.17)). (d) The simulated excitation profile (FA = 30°, FOV 30 × 30 cm$^2$, arbitrary units). Source: [245].*

and may be termed field-of-excitation (FOX) in analogy. The lobes are important in that they characterize the aliasing patterns of the RF pulse outside the FOX. Thus, an RF pulse may generate transverse magnetization also outside the FOX if longitudinal magnetization is present. The excitation aliasing due to insufficient $k$-space sampling will occur at a spatial radius larger than:

$$r_{\text{alias}} > \frac{1}{\Delta k_r} \tag{7.17}$$

where $\Delta k_r$ is the largest radial spacing in the spiral trajectory as the angular distance is increased by $2\pi$. It is interesting to note that with spiral sampling function, the aliasing is cylindrical rather than a replication of excited volume which is the case when under-sampling occurs during Cartesian $k$-space traversal. Similarly, due to the approximate circular $k$-space coverage of a spiral trajectory, all system imperfections give rise to radially symmetric broadening of the central lobe of the excitation profile, which results in a blurred excitation profile.
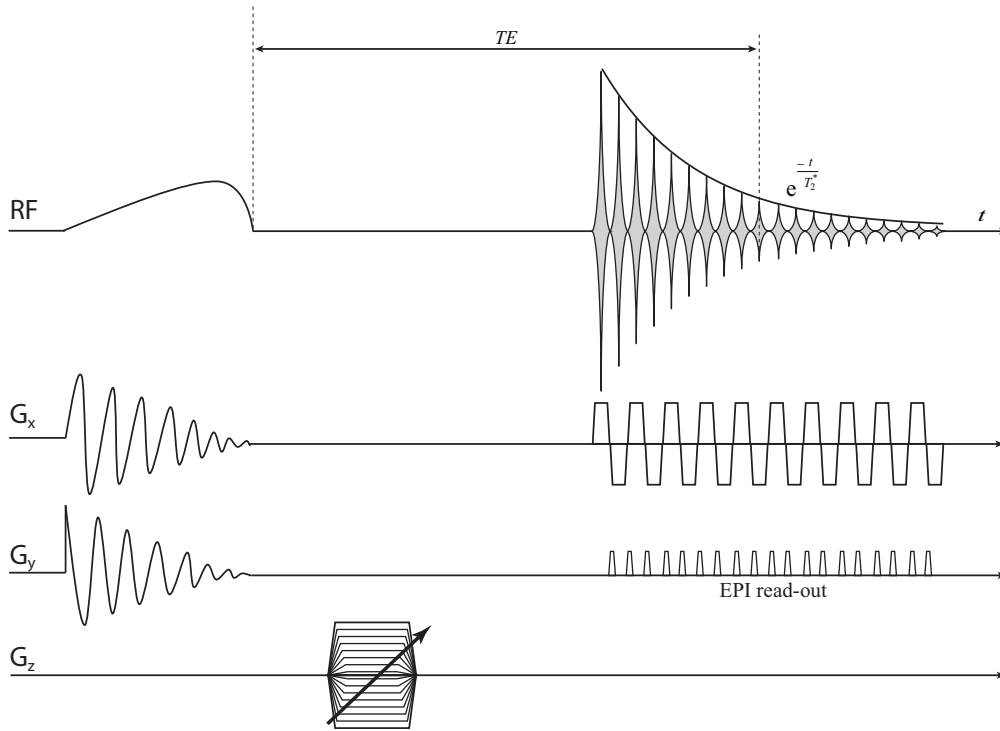
**Figure 7.5:** *Pulse sequence diagram for combination of spiral excitation and segmented 3D EPI sequence. Notice that the refocusing gradient required immediately after the slice-selection gradient (compare with Figure 3.11) is absent in this case since the excited magnetization is expected to be refocused at the end of the RF pulse due to spiral-in trajectory. Because of the same reason, the TE in this case is defined as the duration from the end of the RF pulse to the center of the EPI read echo train.*

## 7.3 3D-EPI-CAIPI With Spiral Excitation

The spiral-in trajectory and the required $B_1$ field can readily replace conventional slab-selective sinc RF pulse used in 3D-EPI-CAIPI sequence [241] to explore the benefits of restricted-field-of-view imaging for functional MRI studies of brain activation. The very same spiral-in design as used in Reynaud et al [245] was integrated with 3D-EPI-CAIPI. To briefly summarize the design considerations: instead of using linear gradient waveform described by Ahn et al and Pauly et al [242, 246, 247] for spiral trajectory, a different approach to spiral-in gradient waveforms using exponential [244] and polynomial slew-rate recovery [248] around $k$-space center was adapted.

The gradient waveforms were designed (see Figure 7.4) after taking into consideration the maximum gradient strength of 80 mT·m$^{-1}$, and maximum slew-rate of 330 mT·m$^{-1}$·ms$^{-1}$ offered by the 7T Siemens magnetom head-only system available at our facility. The gradient waveforms were calculated with a 10 $\mu$s time interval to match the raster-time of the waveform generator and the $k$-space trajectory was resampled onto a 1 $\mu$s raster to meet the dwell-time of the RF amplifier.

144

Figure 7.5 shows pulse sequence diagram resulting from combining spiral excitation module with segmented 3D EPI readout module. As discussed in Chapter 6, a segmented 3D EPI pulse sequence can easily be converted into a 3D-EPI-CAIPI sequence by applying periodic gradient blips along the $z$-gradient axis. The main advantage that the spiral-in trajectory offers is the speed of imaging, which can be applied for a wide range of studies such as cardiac imaging, functional brain imaging, and flow measurements [248, 249]. More recently, spiral-in trajectory has been demonstrated to be useful to minimize the RF energy and time spent for automated shimming using projection mapping at high field [245].

The idea of combining spiral-in excitation with 3D-EPI-CAIPI was to develop an ultra-fast sequence with restricted-field-of-view to be able to perform functional MRI studies on localized brain regions with high spatial resolution as well as temporal resolution. For example, the brain-stem is located in the inferior part of the brain and contains many important nuclei that connect sensory parts of the brain with the body. It further regulates the cardiac and the respiratory functions. Motion of the brain-stem with cardiac pulsations, overall subject motion, and other noise sources make it very difficult to obtain meaningful data for functional analysis. Due to these sources of noise and also because of very small sizes of nuclei of interest it becomes important to obtain fMRI data with high temporal (< 1 s) and spatial (< 2 mm) resolution. Whole-brain (full-FOV) fMRI acquisition at high spatial resolution would require very long volume acquisition times ($TR_{volume}$) due to long echo train lengths employed and because many partitions need to be encoded for full FOV coverage along partition-encoding direction.

In Chapter 6, use of parallel imaging with controlled aliasing while acquiring 3D EPI datasets was demonstrated to yield sub-second temporal resolution with sufficient spatial resolution (2 mm). Restricted-field-of-view excitation can further reduce spatial/temporal resolution by reducing echo train length or number of partitions required. As an example, two different acquisitions, one with full-FOV and the other with restricted-FOV is shown in Figure 7.6. The protocol parameters used for these acquisitions were:

- **Full-FOV acquisition**: Transverse orientation, matrix size = 100×100×72, voxel size = 2×2×2 mm$^3$ isotropic, $R_y \times R_z$ = 1×4, CAIPIRINHA-$\Delta$ = 2, reference data = 100×24×48, GRAPPA kernel size = 3×3, $TR_{segment}$ = 55 ms, TE = 25 ms, flip angle = 10°, readout bandwidth = 2942, number of measurements = 300.
- **Restricted-FOV acquisition**: Sagittal orientation, matrix size = 88×88×64, voxel size = 1.5×1.5×1.5 mm$^3$ isotropic, $R_y \times R_z$ = 1×4, CAIPIRINHA-$\Delta$ = 2, reference data = 88×12×48, GRAPPA kernel size = 3×3, $TR_{segment}$ = 62 ms, TE = 25 ms, flip angle = 10°, readout bandwidth = 2272, number of measurements = 300. *Spiral excitation parameters*: cylinder radius = 20 mm, aliasing ring radius = 22.4 cm.

The time required for a single volume acquisition for full-FOV acquisition mentioned above was 990 ms whereas almost the same time (992 ms) as required by restricted-FOV acquisition where the acquisition was performed with 2.4 times higher spatial resolution.
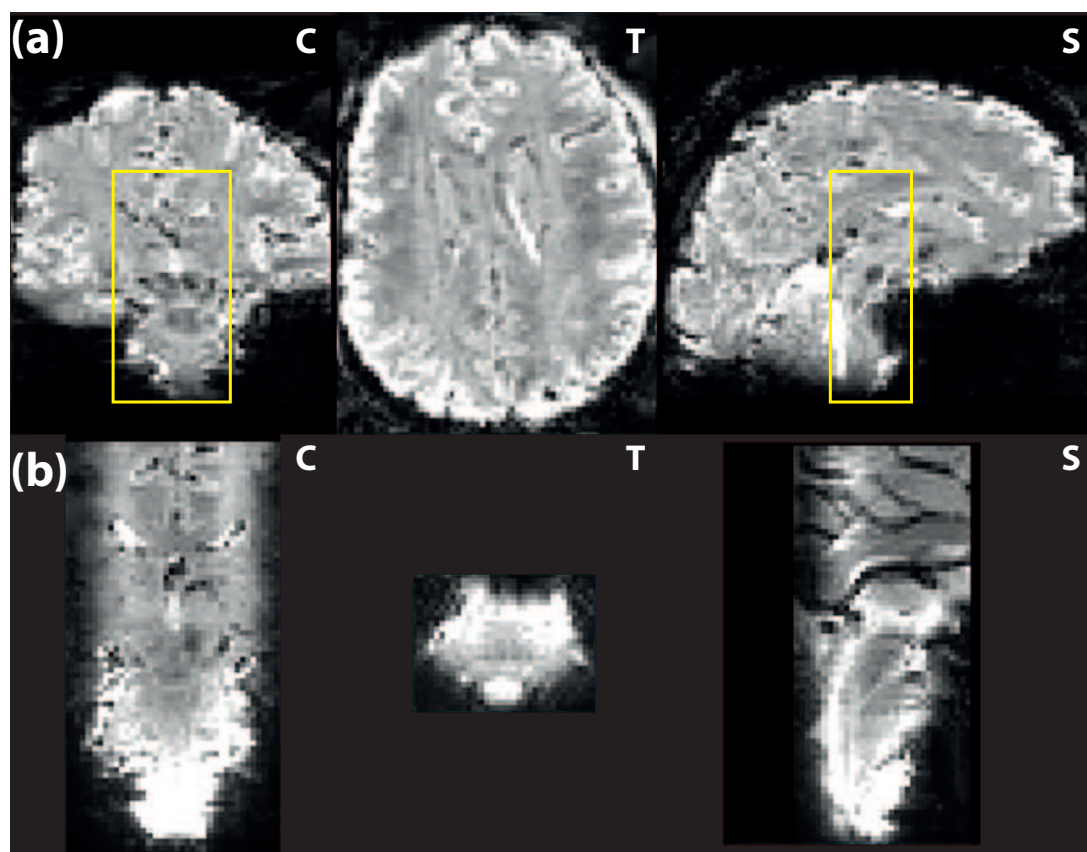
**Figure 7.6:** *Three mutually orthogonal image planes from: (a) Whole-brain acquisition using full-FOV slab-selective sinc excitation 3D-EPI-CAIPI and (b) Restricted-FOV acquisition using spiral excitation 3D-EPI-CAIPI. The image-planes have been marked as C (coronal), T (transverse), and S (sagittal) on top-right corner. The approximate restricted field of view used has been delineated on C and S planes of full field of view images with yellow boxes.*
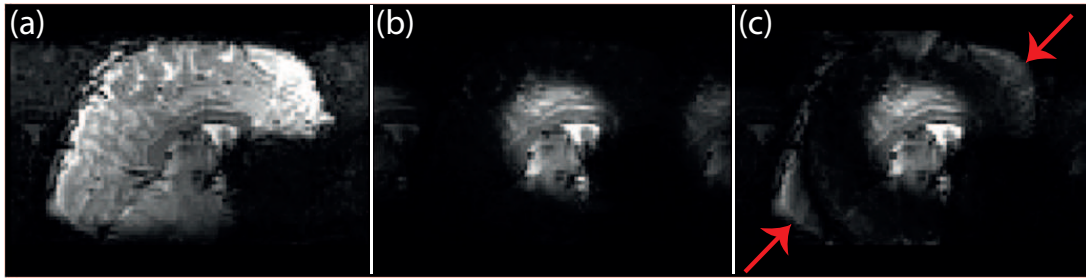
**Figure 7.7:** *Excitation aliasing with spiral excitation 3D-EPI-CAIPI. (a) A sinc excitation 3D-EPI-CAIPI acquisition showing whole-brain sagittal image plane. (b) A spiral excitation 3D-EPI-CAIPI acquisition used to excite cylindrical region (long axis: L-R) with a radius of 2.5 cm without causing excitation aliasing. (c) The same acquisition performed as in (b) but with insufficient $k$-space sampling density to cause excitation aliasing (indicated with arrows) at a radial distance of 10 cm.*

### 7.3.1 Excitation Aliasing Artifact

As discussed before in Section 7.3, insufficient $k$-space sampling density during the excitation causes undesired excitation outside of FOX, called excitation aliasing. Figure 7.7 illustrates excitation aliasing caused due to insufficient $k$-space sampling during spiral excitation with 3D-EPI-CAIPI readout. Figure 7.7(a) shows sagittal slice of a full FOX (sinc excitation) wheras Figure 7.7(b) shows the same acquisition performed with a spiral excitation to excite only a central cylindrical region of 2.5 cm radius with long axis along left-right direction. The $k$-space sampling density in this case was sufficient to prevent excitation aliasing. Figure 7.7(c) shows excitation aliasing, indicated by arrow marks, with a radius of 10 cm caused due to insufficient spiral sampling of the $k$-space.

## 7.4 Future Scope

As demonstrated in Section 6.4.4 of Chapter 6, fast acquisitions ($\leq$ 1s) can be used to reduce the influence of physiological signal fluctuations from the acquired fMRI data, thus increasing statistical significance of fMRI analysis by increasing tSNR per unit time. Restricted-FOV acquisitions for fMRI studies aid in targeting brain areas which pose difficulties in obtaining meaningful due to various sources of signal fluctuations (cardiac pulsations, respiration, subject movement etc.) and inherent physiology (small sizes of functionally important nuclei). Due to reduced field of view, high spatial resolution data can be acquired from such regions without sacrificing temporal resolution. Moreover, application of controlled aliasing while employing parallel imaging during acquisition helps to reduce g-factor losses, maintaining acceptable image quality.

## 7.5  Conclusion

Spiral excitation enabled 3D-EPI-CAIPI sequence offers a promising way to explore the difficult-to-image brain regions. Localized excitation helps to focus only on the region of interest and provides an opportunity to acquire images with high spatial and temporal resolutions, which may enable functional studies of very small brain nuclei.

## References

[238]  Paul A. Bottomley and Christopher J. Hardy. Two-dimensional spatially selective spin inversion and spin-echo refocusing with a single nuclear magnetic resonance pulse. *Journal of Applied Physics*, 62(10):4284–4290, 1987.

[239]  C.J. Hardy and H.E. Cline. Broadband nuclear magnetic resonance pulses with two-dimensional spatial selectivity. *Journal of Applied Physics*, 66:1513–1516, 01 1989.

[240]  V. Andrew Stenger, Fernando E. Boada, and Douglas C. Noll. Multishot 3d slice-select tailored rf pulses for mri. *Magnetic Resonance in Medicine*, 48(1):157–165, 2002.

[241]  Mayur Narsude, José P. Marques, Daniel Gallichan, and Rolf Gruetter. Superior grappa reconstruction with reduced g-factor noise using 2d caipirinha for 3d epi. In *Proceedings 21st Scientific Meeting, International Society for Magnetic Resonance in Medicine, Salt Lake City*, page 3705, 2013.

[242]  John Pauly, Dwight Nishimura, and Albert Macovski. A k-space analysis of small-tip-angle excitation. *Journal of Magnetic Resonance*, 213(2):544 – 557, 2011. Magnetic Moments Groundbreaking papers from the pages of the Journal Magnetic Resonance - and recollections from the scientists behind them.

[243]  Peter Börnert and Bernd Aldefeld. On spatially selective {RF} excitation and its analogy with spiral {MR} image acquisition. *Magnetic Resonance Materials in Physics, Biology and Medicine*, 7(3):166 – 178, 1998.

[244]  T Zhao, Y Qian, Y-K Hue, TS Ibrahim, and F Boada. An improved analytical solution for variable density spiral design. In *Proceedings 16th Scientific Meeting, International Society for Magnetic Resonance in Medicine, Toronto, Canada*, page 1342, 2008.

[245]  Olivier Reynaud, Daniel Gallichan, Benoit Schaller, and Rolf Gruetter. Fast low-specific absorption rate b0-mapping along projections at high field using two-dimensional radiofrequency pulses. *Magnetic Resonance in Medicine*, pages n/a–n/a, 2014.

[246]  C. B. Ahn, J.H. Kim, and Z.H. Cho. High-speed spiral-scan echo planar nmr imaging-i. *Medical Imaging, IEEE Transactions on*, 5(1):2–7, March 1986.

[247]  John Pauly, Dwight Nishimura, and Albert Macovski. A linear class of large-tip-angle selective excitation pulses. *Journal of Magnetic Resonance (1969)*, 82(3):571 – 587, 1989.

[248] Gary H. Glover. Simple analytic spiral k-space algorithm. *Magnetic Resonance in Medicine*, 42(2):412–415, 1999.

[249] Jeff H. Duyn and Yihong Yang. Fast spiral magnetic resonance imaging with trapezoidal gradients. *Journal of Magnetic Resonance*, 128(2):130 – 134, 1997.

# 8 Conclusions and Outlook

This thesis introduced many different novel techniques to increase the temporal resolution of 3D EPI scans for fMRI at ultra-high magnetic field strengths ($\geq$ 7 T). A very simple but innovative idea of 3D RE-EPI, requiring no additional efforts to be taken on image reconstruction front, was introduced at first. Although 3D RE-EPI provided an effective way to increase temporal resolutions of fMRI acquisitions, it suffered from high g-factors related SNR losses when very high parallel imaging acceleration factors were used. As a solution to which 3D-EPI-CAIPI was introduced, by combining segmented 3D-EPI with CAIPIRINHA-style $k$-space trajectory, to reduce the g-factors related SNR losses when using parallel imaging acceleration factors. Finally, reduced FOV excitation using 2D RF pulses with spiral $k$-space excitation trajectory combined with 3D-EPI-CAIPI was introduced as a potential candidate localized fMRI studies.

In this chapter, a consolidated summary and future outlook of the principal findings of this thesis is presented.

## 8.1 Principle Findings and Conclusions

Section 4.4 in Chapter 4 presented the work on 3D RE-EPI which provides a speed-up factor of 2 in the partition-encoding direction when two partitions per excitation are encoded at an expense of increased echo train length. It should be possible to encode more than two partitions per excitation if stronger gradients or higher phase-encoding direction acceleration is employed. 3D RE-EPI yields increased temporal resolution and better physiological noise characterization compared to 3D EPI while producing images with acceptable quality for functional MRI studies. 3D RE-EPI (using 32 channel coil, combined with conventional parallel imaging acceleration methods) allowed up to an 8-fold reduction of the number of excitations needed to obtain full brain coverage. This reduction in the number of excitations, translated in acquisition acceleration in fMRI studies and improved temporal SNR per unit time which ultimately lead to an increase in the number of resting state networks being detected at 7 Tesla rs-fMRI data.

Chapter 6 demonstrated that CAIPIRINHA acquisition strategies can readily be implemented in 3D EPI to improve the parallel imaging reconstruction for high acceleration factors. The standard 3D EPI sequence was modified to include CAIPIRINHA-style $k$-space acquisition patterns, which allowed the increase of parallel imaging acceleration in the partition-encoding direction and hence increased temporal SNR per unit time and increased temporal resolution with reduced g-factor penalties compared to standard 3D EPI. With the increased temporal resolution obtained, a better characterization and removal of the physiologcal noise is possible, thereby implicitly improving the ability to detect resting state networks and functional activity. Finally, 3D-EPI-CAIPI offers reduced peak power deposition when compared to similar 2D-based techniques, making it an ideal candidate for functional imaging at ultra-high field strengths ($\geq 7$ T).

Chapter 7 introduced reduced field-of-view imaging with 2D RF pulse using spiral $k$-space excitation trajectory and 3D-EPI-CAIPI readout module. The potential of spiral excitation enabled 3D-EPI-CAIPI sequence to offer a promising way for exploring the difficult-to-image brain regions was discussed. It was further argued that the localized excitation could help to focus only on the region of interest and provide an opportunity to acquire images with high spatial and temporal resolutions, which might enable functional studies of very small brain nuclei.

## 8.2  Future Research

The techniques presented in this thesis are expected to be of special benefit for fMRI applications where the temporal resolution, more than the spatial resolution, is a limiting factor. For example, when studying rapid transient responses or the shape of the HRF as done in Chapter 6 in multisensory integration experiment, or when targeting regions where cardiac pulsation plays an important role not only in terms of signal intensity variations but also in terms of motion as mentioned in Chapter 7.

Faster sampling rates resulted in resting state networks splitting into more components, compared to slower sampling rates. Techniques identifying functionally distinct networks by their temporal independence would likely make the most of the increased temporal resolution available with higher sampling rate and these techniques are expected to aid network identification for sub-second temporal resolution data. However with regard to the resting state networks result presented in this thesis, a further investigation is needed to assess if the splitting of the networks was due to the increased dimensionality for IC analysis (due to increased number of volumes) or was a direct result of the higher sampling rates.

Moreover, a restricted-FOV fMRI study utilizing 2D RF pulse is due for demonstrating the benefits of localized excitation combined with 3D-EPI-CAIPI readout module (Chapter 7). Restricted-FOV with 3D-EPI-CAIPI readout is expected to aid in fMRI studies targeting brain areas which pose difficulties in obtaining meaningful due to various sources of signal fluctuations (cardiac pulsations, respiration, subject movement etc.) and inherent physiology (small

sizes of functionally important nuclei).

# A Convolution Operation

## Convolution of Two Functions

The concept of *convolution* is central to Fourier theory and the analysis of linear systems. In fact the convolution property is what really makes Fourier methods useful. In one dimension the convolution between two functions, $f(x)$ and $h(x)$ is defined as:

$$g(x) \quad = \quad f(x) \otimes h(x) \quad = \quad \int_{-\infty}^{+\infty} f(s)\, h(x-s)\, \mathrm{d}s \tag{A.1}$$

where $s$ is a dummy variable of integration. This operation may be considered as the area of overlap between the function $f(x)$ and spatially reversed version of the function $h(x)$. The result of the convolution of two simple one dimensional functions is shown in Figure A.1. The *Convolution Theorem* relates the convolution between the real space domain to a multiplication in the Fourier domain, and can be written as:

$$G(u) \quad = \quad F(u)\, H(u) \tag{A.2}$$

where

$$
\begin{aligned}
G(u) \quad &= \quad \mathscr{F}\{g(x)\} \\
F(u) \quad &= \quad \mathscr{F}\{f(x)\} \\
H(u) \quad &= \quad \mathscr{F}\{h(x)\}
\end{aligned}
$$

This is one of the most important properties of Convolution operation and used extensively in signal/image processing. Now few of the simple properties of convolution operation will be presented.
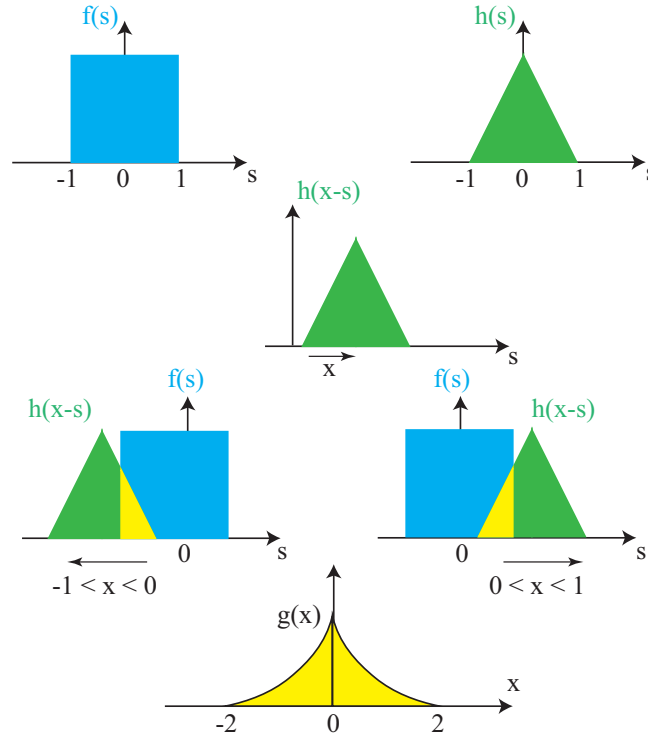
**Figure A.1:** *Convolution of two simple functions. The result of two simple one dimensional functions $f(x)$ and $g(x)$ is shown as function $g(x)$.*

## Simple Convolution Properties

The convolution is a linear operation which is distributive, so that for three functions $f(x)$, $g(x)$, and $h(x)$ we have that

$$f(x) \odot \big(g(x) \odot h(x)\big) \quad = \quad \big(f(x) \odot g(x)\big) \odot h(x) \tag{A.3}$$

and commutative, so that

$$f(x) \odot h(x) \quad = \quad h(x) \odot f(x) \tag{A.4}$$

If the two functions $f(x)$ and $h(x)$ are of finite extent (are zero outside a finite range), then the extent (or width) of the convolution $g(x)$ is given by the sum of the widths of the two functions. For example, in Figure A.1 both $f(x)$ and $h(x)$ are non-zero over the finite range $x = \pm 1$ while the convolution result $g(x)$ is non-zero over the range $x = \pm 2$. This property has practical implications (such as blurring) of convolution filters used in digital image processing.

## Two Dimensional Convolution

As with Fourier transformation, the extension to two-dimensions is simple:

$$g(x, y) \quad = \quad f(x, y) \odot h(x, y) = \iint f(s, t) h(x - s, y - t) \, ds \, dt \tag{A.5}$$

which in the Fourier domain leads to an important result

$$G(u, v) = F(u, v) H(u, v) \tag{A.6}$$

This relationship is fundamental to and is extensively used in image processing. Thus the key duality property of convolution is

Multiplication in Real Space $\Longleftrightarrow$ Convolution in Fourier Space

Convolution in Real Space $\Longleftrightarrow$ Multiplication in Fourier Space

## Convolution With a Dirac Delta Function

The special case of the convolution of a function with a delta function. By definition, $\delta$-function is non-zero only where its argument is equal to zero so $\delta(t - \tau)$ "exists" only where $t = \tau$. Therefore, the convolution of a signal, $f(t)$ with $\delta(t)$ is:

$$\int_{-\infty}^{+\infty} f(\tau) \delta(t - \tau) \, d\tau = f(t) \tag{A.7}$$

Thus, convolution with a delta function initially centered at the origin identically returns back the original function, $f(t)$. This is easily visualized as a result of a unit-amplitude spike sliding past a signal so that multiplication (and integration) of the two functions simply leaves the original signal unchanged. If the delta function was not initially at the origin, e.g., $\delta(t - t_0)$, a delta function at $t = t_0$, the convolution integral gives

$$\int_{-\infty}^{+\infty} f(\tau) \delta(t - t_0 - \tau) \, d\tau = f(t - t_0) \tag{A.8}$$

Here, we see that convolution by a delta function with arbitrary arguments ends up placing its argument in the original argument of the function $f(t)$. This is a *shifting* operation.

## Convolution With a Dirac Comb

The act of digitizing a continuous signal into discrete values can be imagined as a multiplication of a string of delta functions spaced $\Delta t$ apart. The string of delta functions so constructed is called a *Dirac comb* (expressed using the symbol Ш, pronounced *shah*). It looks like a comb you use in hair except that it has an infinite number of teeth, $\Delta t$ apart, each approaching zero
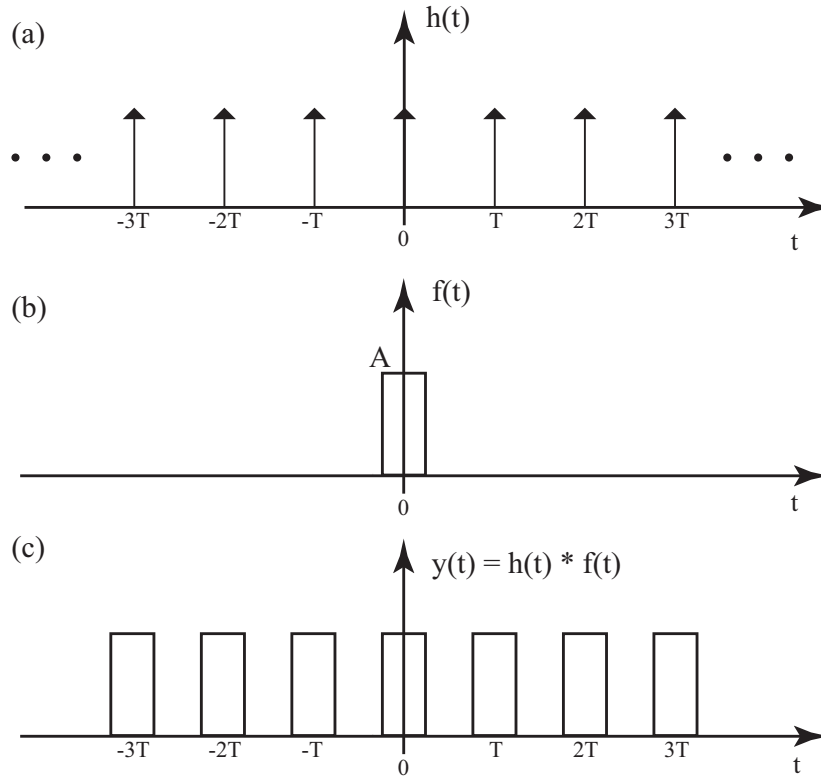
**Figure A.2:** *(a) Dirac comb function when convolved with (b) a finite function yields (c) an infinite periodic series of replicas of the finite function with a period equal to the spacing between the teeth of Dirac comb function.*

width! It is expressed mathematically as

$$\text{III} = \sum_{k=-\infty}^{+\infty} \delta(t - k\Delta t) \tag{A.9}$$

Convolution of a signal, $f(t)$ with a Dirac comb (Equation (A.9)) is

$$y(t) = f(t) * \sum_{k=-\infty}^{+\infty} \delta(t - k\Delta t) \tag{A.10}$$

Combining Equation A.8 and A.10 yields

$$\sum_{k=-\infty}^{+\infty} f(t)\delta(t - k\Delta t) = \sum_{k=-\infty}^{+\infty} f(t - k\Delta t) \tag{A.11}$$

So, convolution with a Dirac comb yields an infinite series of replicas of the original function with period $\Delta t$, the spacing of the teeth of the comb (Figure A.2). The result of convolution with a Dirac comb is the basis for understanding aliasing discussed throughout this manuscript. Basically, aliasing occurs when the teeth of the Dirac comb are closer together than the width of $f(t)$ and the replicas overlap.

# B Supplementary Experiment For g-factors Calculation

The noise amplification described by the geometry factor (g-factor), as defined in Equation 5.8 for SENSE reconstruction, is also related to a property of the matrix $C^H \psi^{-1} C$ that is inverted, called its *conditioning*. Noise amplification results from a poorly conditioned matrix during unwrapping of images acquired using parallel imaging. A poorly conditioned matrix can be *regularized* to produce unwrapped images with reduced noise amplification. This reduction in the noise amplification using regularization comes at the expense of additional uncorrected aliasing. It, therefore, is crucial to use correct regularization factor during parallel imaging reconstruction to ensure an optimum trade-off between noise amplification and residual image aliasing is achieved.

## B.1    Methods

An additional experiment was conducted to assess the improvement in image quality, and to determine acceptable regularization factor, with the use of CAIPIRINHA-style $k$-space under-sampling patters ($\Delta > 0$) compared to standard under-sampling patterns ($\Delta = 0$). The protocol parameters used were the same as in Section 6.3.1 in Chapter 6. Specifically, parameters used were as below:

> Image quality was evaluated in 1.0 mm isotropic images acquired with 3D-EPI-CAIPI with different net accelerations and $\Delta$ values. The acquisition parameters used were: TR/TE = 67/26 ms, flip angle (FA) = 14°, readout bandwidth (rBW) = 1662 Hz/Pixel, matrix size = 188×188×120, reference data = 188×48×48, GRAPPA kernel size = 3×3, $PPA_y = 2$, and $PF_y = 7/8$. $PPA_z$ varied from 3 to 5. The partition-encoding direction was set to superior-inferior while the primary phase-encoding direction was set right-left.

$1/g$ maps were calculated using two different approaches in order to cross check the patterns and range of values obtained, first with quantitative g-factor calculations in GRAPPA reconstructions [250] and then with the pseudo-replica method using 100 replicas [251].
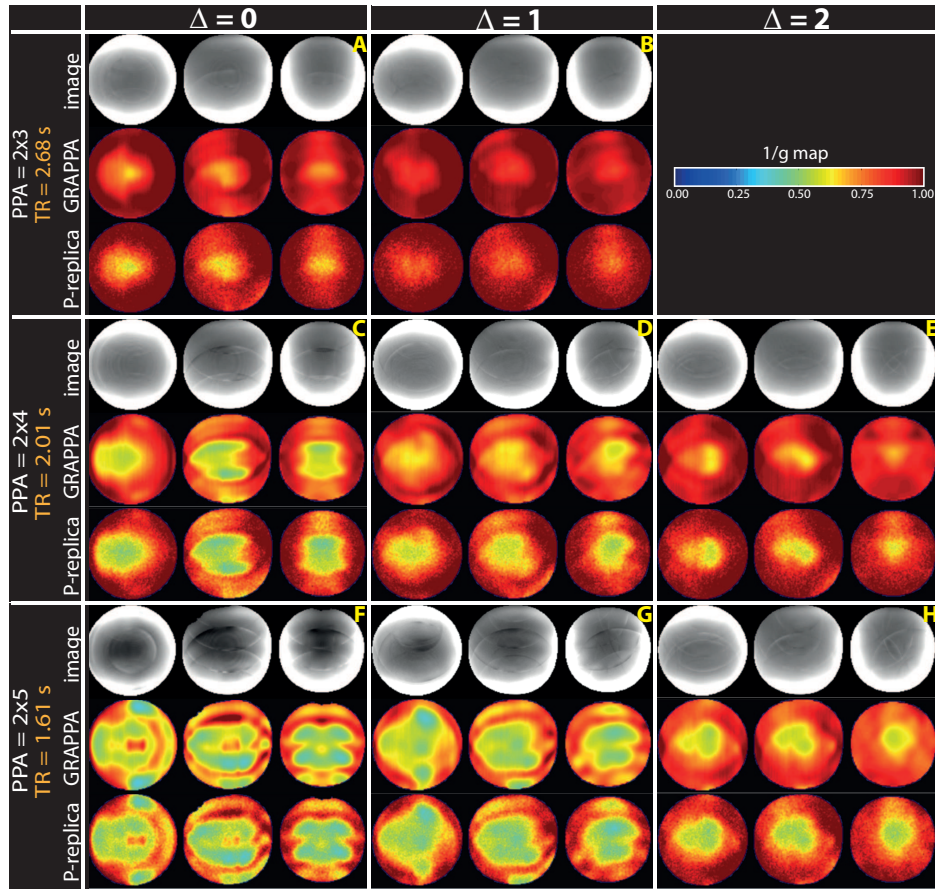
**Figure B.1:** *Comparison of g-factor maps with a homogeneous phantom using general formulation for quantitative g-factor calculation in GRAPPA reconstruction [250] and using Pseudo-replica method (100 replicas) [251]. The net acceleration used is shown on the far left of each row. Different columns of panels correspond to different values of $\Delta$ used. Each panel consist of three rows: the first row displays three orthogonal images of the homogenous phantom, the second row displays $^1/_g$ maps calculated using Breuer's method whereas the third row displays $^1/_g$ maps as calculated using Robson's method.*

## B.2 Results

Figure B.1 shows various panels (A-H), each for different overall accelerations and $\Delta$ values used. Each panel consists of three rows: the first row displays three orthogonal images of the homogenous phantom, the second row displays $^1/_g$ maps calculated using Breuer's method whereas the third row displays $^1/_g$ maps as calculated using Robson's method. As can be seen, these $^1/_g$ maps using both methods are in good agreement with one another, and the range of values and spatial distribution is similar to that presented in the literature [250–252].

Finally, Breuer's method was used to calculate $^1/_g$ maps shown in Figure 6.2 of Chapter 6 since this method is particularly applicable for g-factor calculations for GRAPPA reconstruction.

# References

[250] Felix A. Breuer, Stephan A.R. Kannengiesser, Martin Blaimer, Nicole Seiberlich, Peter M. Jakob, and Mark A. Griswold. General formulation for quantitative g-factor calculation in grappa reconstructions. *Magnetic Resonance in Medicine*, 62(3):739–746, 2009.

[251] Philip M. Robson, Aaron K. Grant, Ananth J. Madhuranthakam, Riccardo Lattanzi, Daniel K. Sodickson, and Charles A. McKenzie. Comprehensive quantification of signal-to-noise ratio and g-factor for image-based and k-space-based parallel imaging reconstructions. *Magnetic Resonance in Medicine*, 60(4):895–907, 2008.

[252] Kawin Setsompop, Borjan A. Gagoski, Jonathan R. Polimeni, Thomas Witzel, Van J. Wedeen, and Lawrence L. Wald. Blipped-controlled aliasing in parallel imaging for simultaneous multislice echo planar imaging with reduced g-factor penalty. *Magnetic Resonance in Medicine*, 67(5):1210–1224, 2012.

# C The Gaussian Radio-frequency Pulse Shape

The RF ($B_1$) field for a Gaussian pulse in the rotating frame is given by the expression:

$$B_1(t) = A_G e^{-\frac{t^2}{2\sigma^2}} e^{i\Delta\omega_{\mathrm{rf}}t} \qquad \text{(Gaussian pulse centered at t = 0)} \qquad (C.1)$$

where $A_G$ is an overall scale factor which determines the excitation flip angle, and $\sigma$ is linearly proportional to the Gaussian pulse width. $\Delta\omega_{\mathrm{rf}} = 2\pi\Delta f_{\mathrm{rf}}$ dictates the off-resonance frequency in case an off-resonance excitation is desired, i.e. for an on-resonance excitation $\Delta\omega_{\mathrm{rf}} = 0$. An example Gaussian function as given by Equation (C.1) is shown in Figure C.1 for the case when $\Delta\omega_{\mathrm{rf}} = 0$, $\sigma = 1$, and $A_G = 1$.

From the expression of the Gaussian function (see Equation C.1), it is clear that the Gaussian function is non-zero (theoretically) for all values of $t$ although it falls very rapidly for $t\sigma$. For practical purposes, the RF pulse is terminated when the magnitude of the $B_1$ field reaches below a pre-determined threshold. For example, at $t = \pm 3.717\sigma$, the envelope of the RF field is $A_G/1000$, that is, a 60-dB attenuation. Thus, the pulse width of a Gaussian pulse is approximately:

$$T_G \approx 2 \times 3.717\sigma = 7.434\sigma \qquad (C.2)$$

The Fourier transformation of the above Gaussian is another Gaussian function (desired excitation profile). Assuming zero frequency offset

$$\mathrm{FT}[B_1] = A_G\sigma\sqrt{2\pi}e^{-2(\pi\sigma f)^2} \qquad (C.3)$$

The rapid fall-off and the lack of side lobes in the frequency response of Equation (C.3) are the main advantages of the Gaussian pulse over a sinc pulse. The FWHM of the frequency response is given by $\Delta f_G = 0.3748/\sigma$, which is a measure of the RF bandwidth. Thus, the dimensionless time-bandwidth product of any Gaussian is independent of $\sigma$ and given by:

$$T_G\Delta f_G \approx 7.434\sigma \times \frac{0.3748}{\sigma} \approx 2.8 \qquad (C.4)$$
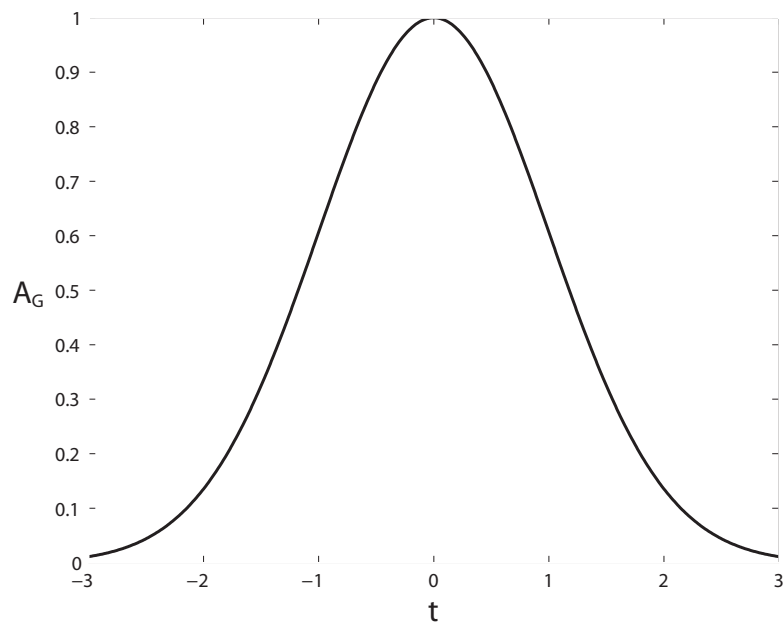
**Figure C.1:** *A normalized Gaussian pulse shape calculated for $\sigma = 1$. The Gaussian function is centered at $t = 0$.*

In Chapter 7, we demonstrate the use of circularly symmetric Gaussian RF pulse to selectively excite a cylinder as opposed to a planar excitation achieved using sinc RF pulse.

# List of Publications

## Journal Papers

- **Mayur Narsude**, Daniel Gallichan, Wietske van der Zwaag, Rolf Gruetter, and José P. Marques. *Sub-second High-Resolution Whole-brain fMRI Using Controlled Aliasing 3D-EPI*. NeuroImage 2014 (submitted)
- Roy Solomon, Jana Darulova, **Mayur Narsude**, and Wietske van der Zwaag. *Comparison of an 8-Channel and a 32-Channel Coil for High-Resolution fMRI at 7 T*. Brain Topography, March 2014, Volume 27, Issue 2, pp 209-212
- **Mayur Narsude**, Wietske van der Zwaag, Tobias Kober, Rolf Gruetter, and José P. Marques. *Improved temporal resolution for functional studies with reduced number of segments with three-dimensional echo planar imaging*. Magnetic Resonance in Medicine, 2013, DOI: 10.1002/mrm.24975

## Conference Papers

- **Mayur Narsude**, Wietske van der Zwaag, Daniel Gallichan, Rolf Gruetter, and José P. Marques. *Resting State Networks Detection, the Importance of High Temporal Resolution: A comparison Study Between 2D-EPI, SMS 2D-EPI, and 3D-EPI-CAIPI Acquisitions*. Proc. of ISMRM-ESMRMB 2014 - Joint Annual Meeting of International Society for Magnetic Resonance in Medicine and European Society for Magnetic Resonance in Medicine and Biology, Milan, Italy, 2014
- Wietske van der Zwaag, **Mayur Narsude**, Roberto Martuzzi, and José P. Marques. *Using Wholebrain, High Temporal Resolution, 3D-EPI-CAIPI to Observe Multisensory Interaction in Primary Sensory Cortices*. Proc. of ISMRM-ESMRMB 2014 - Joint Annual Meeting of International Society for Magnetic Resonance in Medicine and European Society for Magnetic Resonance in Medicine and Biology, Milan, Italy, 2014
- **Mayur Narsude**, Daniel Gallichan, Wietske van der Zwaag, Rolf Gruetter, and José P. Marques. *Whole Brain fMRI in 370ms: Exploring the Benefits of High Temporal Resolution 3D-EPI-CAIPI*. Proc. of ISMRM-ESMRMB 2014 - Joint Annual Meeting of International Society for Magnetic Resonance in Medicine and European Society for Magnetic Resonance in Medicine and Biology, Milan, Italy, 2014

- **Mayur Narsude**, José P. Marques, Daniel Gallichan, and Rolf Gruetter. *Superior GRAPPA Reconstruction with Reduced G-Factor Noise Using 2D CAIPIRINHA for 3D EPI*. Proc. of ISMRM 2013 - 21st Annual Meeting of International Society for Magnetic Resonance in Medicine, Salt Lake City, Utah, USA, 2013

- Wietske van der Zwaag, **Mayur Narsude**, Joao Jorge, José P. Marques, and Rolf Gruetter. *High Temporal resolution and physiological noise removal improve BOLD detection in the brainstem and auditory cortex.* 4th Conference on Auditory Cortex, Lausanne, Switzerland, 2012

- **Mayur Narsude**, José P. Marques, Wietske van der Zwaag, Tobias Kober, and Rolf Gruetter. *PACEUP-3DEPI: A Highly Accelerated 3D-EPI Sequence for fMRI at 7T*. Proc. of ISMRM 2012 - 20th Annual Meeting of International Society for Magnetic Resonance in Medicine, Melbourne, Australia, 2012

- Wietske van der Zwaag, **Mayur Narsude**, Joao Jorge, José P. Marques, and Rolf Gruetter. *High Temporal resolution and physiological noise removal improve BOLD detection in the brainstem and auditory cortex at 7T*. Proc. of ISMRM 2012 - 20th Annual Meeting of International Society for Magnetic Resonance in Medicine, Melbourne, Australia, 2012

- **Mayur Narsude**, José P. Marques, Wietske van der Zwaag, Tobias Kober, and Rolf Gruetter. *PACEUP-3DEPI: A Highly Accelerated 3D-EPI Sequence for fMRI at 7T*. Proc. of ESMRMB 2012 - 29th Annual Scientific Meeting of European Society for Magnetic Resonance in Medicine and Biology, Lisbon, Portugal, 2012

- **Mayur Narsude**, José P. Marques, Florent Eggenschwiler, and Rolf Gruetter. *Mapping Inversion Efficiencies of Adiabatic Pulses at 7 T*. Proc. of ISMRM 2011 - 19th Annual Meeting of International Society for Magnetic Resonance in Medicine, Montreal, Canada, 2011

- Joao Jorge, Patricia Figueiredo, Wietske van der Zwaag, **Mayur Narsude**, and José P. Marques. *Sources of signal fluctuations in single-shot 2D EPI and segmented 3D EVI acquisitions for fMRI at 7T*. Proc. of ISMRM 2011 - 19th Annual Meeting of International Society for Magnetic Resonance in Medicine, Montreal, Canada, 2011

- Joao Jorge, Patricia Figueiredo, Wietske van der Zwaag, **Mayur Narsude**, and José P. Marques. *Correlated noise correction in 2D and 3D fMRI at 7 Tesla*. Proc. of HBM 2011 - 17th Annual Meeting of the Organization for Human Brain Mapping, Quebec City, Canada, 2011

## Personal Information

| | |
|---|---|
| Name | Mayur Narsude |
| Date of Birth | 05th November 1981 |
| Place of Birth | Mumbai, India |
| Nationality | Indian |
| E-mail address | mayur@iitbombay.org |
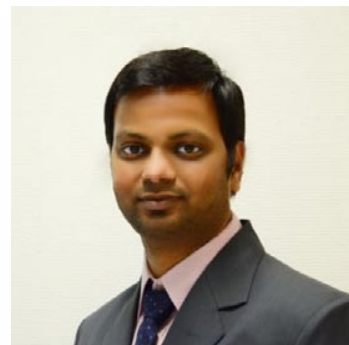
## Education

| | |
|---|---|
| Ph.D. Studies 08/2009 – today | University of Lausanne, Lausanne, Switzerland Doctoral program of Physics under the supervision of Prof. Rolf Gruetter, Director, Laboratory for functional and metabolic imaging (LIFMET) |
| M.S. 08/2003 – 08/2005 | University of Texas at Arlington and University of Texas South Western medical center, USA Master of Science in Bioengineering |
| B.Tech. 07/1999 – 05/2003 | Indian Institute of Technology, Mumbai, India Electrical Engineering |

## Work Experience

| | |
|---|---|
| Senior Design Engineer 12/2005 – 02/2009 | General Electric Healthcare, Bangalore, India Pulse sequence developer, Team leader for Installed base and Excite Plus (11.1) programs |
| Intern 05/2002 – 07/2002 | Air India, Mumbai, India Responsible for developing an automated flight status updating software using C |